An Exploration of Prominent Cusped-Field Thruster Phenomena: The Hollow Conical Plume and Anode Current Bifurcation

by
Taylor Scott Matlock

Submitted to the Department of Aeronautics and Astronautics
in partial fulfillment of the requirements for the degree of
Doctor of Philosophy
at the
MASSACHUSETTS INSTITUTE OF TECHNOLOGY
September 2012

Author .....
Department of Aeronautics and Astronautics
Aug 15, 2012

Certified by .....
Manuel Martinez-Sanchez
Professor of Aeronautics and Astronautics
Thesis Supervisor

Certified by .....
William A. Hargus, Jr.
Research Scientist, Air Force Research Laboratory
Committee Member

Certified by .....
Paulo Lozano
Associate Professor of Aeronautics and Astronautics
Committee Member

Certified by .....
Markus Zahn
Thomas and Gerd Perkins Professor of Electrical Engineering
Committee Member

Accepted by .....
Eytan H. Modiano
Professor of Aeronautics and Astronautics
Chair, Graduate Program Committee

An Exploration of Prominent Cusped-Field Thruster Phenomena: The Hollow Conical Plume and Anode Current Bifurcation

by

Taylor Scott Matlock

Submitted to the Department of Aeronautics and Astronautics
on Aug 15, 2012, in partial fulfillment of the
requirements for the degree of
Doctor of Philosophy

Abstract

A low power plasma thruster, initially dubbed the Diverging Cusped-Field Hall Thruster, was built at MIT in 2007 with the aim of providing an alternative to comparably sized conventional Hall thrusters able to provide enhanced lifetimes and thus deliver higher total impulses. The initial design was constrained in some respects by availability and inexpensiveness of materials rather than on experience based optimization due in part to the dearth of literature available for similar devices. While experiments suggest that the prototype Diverging Cusped-Field Thruster performs as well as mature Hall thruster designs, they have also revealed several operational quirks which could potentially pose problems for spacecraft integration. Dominant among these peculiarities are the existence of at least two distinct operational modes, marked by a steep jump in anode current and current oscillation amplitude, and, somewhat separately, the coalescence of the ion plume into a hollow cone-like structure with peak fluxes around 30 degrees from the thruster axis.

This thesis describes the experimental and numerical work undertaken in an attempt to uncover the physical underpinnings of these two prominent cusped-field thruster phenomena. Stratification of the plasma plume into a wide-angle conical shell represents both a loss in thrust efficiency and a potential hazard for beam impingement on spacecraft surfaces. A method was envisaged to decrease the divergence of the beam using an external solenoid to re-contour the magnetic field near the thruster exit, where measurements suggest the critical ion acceleration occurs. Implementation of this method demonstrated clear vectoring of a large portion of the ion beam towards smaller angles in line with hypothesized effects, however a distinct, low-density, outer shell remained at the initial angle of divergence.

Separately, the observed bifurcation in operational mode at normal conditions represents both a physically interesting display of plasma dynamics in the thruster discharge chamber and a potentially highly problematic feature, as operational envelopes in a particular mode have been observed to change unpredictably with experimental

conditions. Attempts are made to experimentally isolate the factors which lead to bifurcation. The steady-state characteristics of the two modes are investigated using infrared thermography to monitor chamber temperatures while the unsteady behavior is monitored with an AC current probe on the discharge power supply. A thermal model of the thruster, using commercial finite-element-analysis software, is developed to validate plasma power deposition estimates from the thermography experiments.

A prominent feature of the bifurcation is observed in the anode current spectrum, which changes from a quiescent mode to one exhibiting a strong relaxation oscillation at a fundamental frequency of several kilohertz. The nature of the oscillatory mode, and its transition to a highly damped state, is investigated through parametric scans of the thruster operating conditions. The main oscillation appears, from experiment, to be a breathing mode similar to those observed in Hall thrusters. An unsteady 1-D fluid code is adapted from the Hall thruster literature to model the interaction of neutral gas flow with the magnetically-limited electron current believed to be the main source of the instability. Trends in stability of the breathing mode with both thruster and model parameters, such as propellant flow rate, anode voltage, magnetic field, electron mobility and discharge chamber divergence are examined. A turbulent shear model is introduced to capture the effects of a time-evolving cross-field electron mobility on mode transitions and is shown to reproduce the experimentally observed oscillation damping at high voltages if the eddy turnover times are allowed to increase by modest intervals. The shear model is also able to naturally reproduce a feature of the anode current waveform, where a series of possible ionization avalanche events are muted before eventually leading to a large burst in current, which has not been captured by prior models.

Thesis Supervisor: Manuel Martinez-Sanchez
Title: Professor of Aeronautics and Astronautics

Acknowledgments

I think I should start by thanking my advisor, Professor Manuel Martinez-Sanchez, for his guidance throughout this endeavor. He has always been an invaluable and accessible resource, and a role model for the type of scientist I would like to one day become. I will always be grateful for his mentorship.

Many thanks are due to my committee, Professor Markus Zahn, Professor Paulo Lozano, and Dr. William Hargus Jr., for all the helpful suggestions along the way. An added thanks is due to Dr. Hargus, and to Dr. C. William Larson, for their guidance and support as I applied to graduate schools while still an extremely green researcher at the EP lab at Edwards AFB. I am also grateful to my thesis readers Dr. Vlad Hruby and Dr. Daniel Courtney for taking the time to comb through this document and provide some much appreciated feedback.

Much of the work described here would not have been possible without the generous assistance of various laboratories. The thermal camera was graciously lent to us by Professor Brad King of Michigan Tech University, whom I'd like to thank along with the members of the Isp Lab, EJ Meyer and Jason Makela, who helped with logistics and instructions. Dr. Hargus of the AFRL lent us the ZnSe viewports and adapter flanges used for the thermal imaging experiment. Dr. Jim Bales of the Edgerton Lab at MIT lent us the high speed camera used to image thruster oscillations and took the time to train us on the equipment as well. I am also very grateful to Dr. Serge Barral of the Institute of Plasma Physics and Laser Microfusion whose extensive work on Hall thruster oscillations is relied upon heavily here and whose suggestions and encouragements in regards to the 1-D modeling were extremely helpful.

I am indebted to the rotating cast of SPL members over the years for their friendship, guidance, assistance and support. I'd like to thank, in particular, Nareg Sinenian, Murat Celik and Dan Courtney for teaching me the ropes in the laboratory as a Master's candidate and novice experimentalist. I've received a great deal of assistance in performing the experiments which make up this thesis from Dan Courtney, Stephen Gildea, Fuzhou Hu and Anthony Pang among others who have pitched in along the

way. Steve has also been a tremendous resource as a friend, colleague and office mate, often taking the time to listen to my various misguided theoretical musings and help me figure out where I went wrong. I have also benefited from the friendship and commiseration of my former roommates Greg O'Neill and Tim Fedkiw.

I have always received the utmost support from my parents, Richard and Bonnie Matlock. I'd like to dedicate this work to them, for instilling in me all the values which have allowed me to reach this point. And finally, I'd like to thank my beautiful and caring wife, Andrea. Her patience and thoughtfulness smoothed out the roughest parts of this process and for that I will always be grateful.

This research was made possible through funding from the Air Force Office of Scientific Research under a grant monitored by Dr. Mitat Birkan.

Contents

List of Figures

List of Tables

Chapter 1

Introduction

The advantage which electric devices have over their chemical counterparts for in-space propulsion is largely in their high obtainable propellant exhaust speeds which make them far more fuel efficient, a true boon for any long range or long duration mission. The main drawback is sub-Newton thrust at normal power levels meaning much longer burn times are necessary for the same orbital maneuver, making the thruster lifetime (or more precisely the total impulse deliverable) a vital feature of most electric propulsion devices. The Diverging Cusped Field Thruster (DCFT) is a 100-W class plasma thruster under development at the MIT Space Propulsion Laboratory. Its intended performance is as a lower wall loss, and consequently longer lifetime, alternative to conventional Hall effect thrusters, which have been utilized effectively for tasks ranging from orbital maintenance to near lunar orbit attainment.

The DCFT consists of a conical discharge chamber lined by a ceramic insulator which uses three ring magnets of alternating polarity to create a multiple-cusp[a] magnetic field designed to limit plasma loss to the ceramic wall and increase propellant ionization by strongly confining the electrons provided to the chamber by an external hollow cathode. In a conventional Hall thruster the magnetic field is nearly perpendicular to the chamber walls allowing only electrostatic confinement of the plasma electrons away from the walls by the formation of plasma sheaths. The fields in the DCFT, on the other hand, are largely parallel to the chamber surfaces, leading to

[a]In a broad sense a cusp is a point, line or ring to which magnetic field lines converge

much stronger electron confinement in these locations. At the ring cusps, where the field is nearly perpendicular to the wall, plasma wall losses are limited by strong electron mirroring, with mirror ratios many times larger than those found in typical Hall thrusters.

An unoptimized prototype of the DCFT was first tested in 2007 and, though it performed comparably to a similar class Hall thruster, was seen to exhibit several somewhat unexpected and unwanted features. The ion beam emitted by the thruster is strongly peaked at an angle around 30° off the thruster axis, with a substantial flux of high energy ions found at even higher angles. This feature is harmful not only from an efficiency view, due to use of applied energy to accelerate particles in directions not contributing to thrust, but from a spacecraft integration standpoint, as the impingement of high energy ions on spacecraft structures is often highly undesirable. The peak ion flux in an annular Hall thruster, for comparison, is generally within a couple degrees of the axis, with 90% of the beam falling within 40-50°. Through experimentation with the external magnetic field, described here, we have come to a notional understanding of the mechanism behind this divergence, though a complete quantitative theory is left as future work.

The thruster also exhibits bifurcating modes of operation, which are often hysteretic and result in a steep jump in the anode current and its oscillation amplitude when the anode voltage drops below a certain point (around 300-400 V depending mostly on propellant flow rate). Thrust measurements suggest little change in thruster efficiency at the transition from high current (HC) to low current (LC) mode [1, 2], but the occurrence of an uncontrolled jump in operating power and anode current spectral density features at an applied voltage typical for high thrust-to-power operation is certainly cause for alarm from the standpoint of spacecraft application. Similar bifurcations have been observed in annular Hall thrusters only at either much lower (<115 V [3]) or much higher (>540 V [4]) anode voltages, while no bifurcation at all has been found yet in a smaller, cylindrical variant of the DCFT [5]. We currently have no complete theory to explain the mode change and characteristic fluctuations, though some ideas have been forwarded to describe the oscillation cycles [6].

More recent measurements have revealed that, at least in the highly oscillatory, high anode current mode, the peak erosion of the discharge chamber ceramic occurs in the central wall cusp [7], while the majority of the ion acceleration occurs near the exit cusp [8, 6]. It is currently unclear whether this is an effect of the current oscillations or if it is a commonality of the design in either operating mode due perhaps to the main ionization zone occurring in the point cusp just upstream of the exit as originally posited for the (very similar) HEMP thruster [9] or in the second ring cusp itself. The ionization and acceleration regions have been shown to be intrinsically linked in annular Hall thrusters [10], and if the opposite is occurring in the DCFT this disparity ought to be reconciled.

Clear steps forward have been made in understanding the complex phenomena underlying the DCFT operation during the course of the research to be presented in this thesis. The shape of the magnetic field near the thruster exit has been actively altered to decrease the divergence of the plume matching a simple theoretical framework for the electric field formation. A broad characterization of the anode current spectral properties has been undertaken which shows repeated trends in the nature of current oscillations as the thruster is brought from a stable high current mode to the point of bifurcation. These anode current oscillation patterns have also now been reproduced using a simple 1-D fluid model of the cross-field flow of electrons opposite that of the neutral propellant, accounting for the effect of flow properties on turbulent electron transport.

1.1 Motivation for Research

In a broad sense, this research is motivated by the interest in small spacecraft. More diverse and affordable launch opportunities are available as spacecraft size and mass decrease, but the options for propulsion become narrower. Large mass savings can be had in the form of reduced propellant requirements using electric propulsion instead of chemical, as long as a large propulsive event is not required to occur in a short amount of time.

The various electric propulsion options, such as electrosprays, arcjets, ion engines, and Hall thrusters, to name some common choices, generally service their own niche based on specific mission requirements. A Hall thruster might be the unit of choice when a robust device with high thrust-to-power ratio is desired, while electrosprays may be your best bet for a high-precision low-impulse maneuver. The difficulty for small spacecraft comes when the mission requirements fit best with a plasma thruster, as such devices are intrinsically difficult to scale to low power levels while maintaining high efficiencies.

The reason for the poor scaling of plasma-based thruster options is the requirement to confine electrons in the small volume containing the neutral propellant long enough to allow for efficient ionization, while also minimizing the loss of power which occurs when the plasma impinges on the ionization chamber walls. Electron confinement is achieved through the use of magnetic fields, which strongly confine electrons to travel along the applied lines of flux. Low operating powers are generally achieved by decreasing the propellant flow rate which often necessitates a decrease in the ionization chamber cross section to maintain a high enough neutral particle density to sustain ionization. A small chamber cross-section requires a stronger magnetic field to allow for the same degree of electron confinement while also resulting in an increased ratio of chamber wall surface area to volume available for ionization.

The enhanced difficulty of confining the plasma in a smaller thruster leads to generally lower efficiencies. While a 10 kW Hall thruster might operate near a 70% efficiency, a typical 200 W Hall thruster seldom achieves much above 40%. An increased plasma impingement on discharge channel walls combined with the lower volume of the insulating material which separates plasma from the magnetic circuit also results in significantly lower thruster lifetimes at lower power levels [7].

Non-conventional magnetic fields may be necessary to mitigate these shortcomings. This is the impetus behind the low-power DCFT which models its magnetic field topology after the HEMP-Thruster, a recently developed device operated at >1 kW anode powers and asserted to experience virtually no erosion of its insulating walls [11]. The DCFT operates at efficiencies essentially equivalent to those of a

well-developed, flight tested Hall thruster of the same power level [1, 2] and has been recently shown to exhibit beginning-of-life erosion rates which linearly extrapolate to a thruster lifetime matching that of heritage Hall thrusters as well [7].

Though the thruster has not been seen to necessarily outperform thrusters of the same class the motivation to further study the device stems from the fact that the first prototype, designed without any of the kinds of established best practices available to Hall thruster developers, performed just as well. It is hoped that future DCFT designs, based on knowledge gained from recent research aimed at uncovering the physical underpinnings of its unique operation, may result in significant improvements in efficiency and lifetime. The use of open-ended, multi-cusp confinement systems for low power propulsion is still in its nascent stages and may yet yield a way forward for plasma thruster miniaturization.

1.2 Research Contributions

The scope of this research has been quite broad from the outset, taking a new thruster with many interesting features and a fairly small amount of data and looking for clues as to why it operates the way it does. The main focus of the work described here is discerning why the peak ion flux in the thruster plume is found at a high angle from the thrust axis and why the thruster bifurcates between a quiescent, low anode current mode at high voltages and a strongly oscillating, high current mode at low voltages.

A heuristic theory to explain the shape of the plume has been developed based on experimental work which has shown that a reduction in the convexity (in relation to the anode) of the magnetic field lines near the thruster exit can effectively aim the main ion beam to lower angles with respect to the thrust axis. The field line which separates the external field (with positive flux lines for example) from the internal field (with negative flux lines) is shown to anchor the potential structure, through measurements of the nearby plasma potential and ion flux topography.

A parametric study of the discharge oscillations and thruster thermal state in its

different modes of operation is performed which clearly elucidates some previously unknown trends. A somewhat broadband fluctuation in the low current mode, with a peak power spectral density between 25-100 kHz, is shown to crop up at conditionally stable operating points near the transition to high current mode. The cathode position and strength of the external magnetic field are shown to have an effect both on the mode of operation and on the frequency of oscillations.

The first thermal measurements of the DCFT are obtained, using a thermocouple affixed to the outer surface of the discharge chamber insulating cone and a thermal camera monitoring the internal chamber surfaces. The anode is found to be the hottest surface in the thruster during operation, and is seen to exhibit an apparent jump in its proportional heating when the thruster switches into high current mode. A thermal model of the thruster is constructed using commercial finite element analysis software which suggests that around 30% of the input anode power is deposited on the discharge chamber walls.

An unsteady 1-D fluid code, following a model developed for Hall thrusters [12], is used to describe the interaction between the slowly progressing front of neutral propellant with the cross-field flow of electrons from cathode to anode. The code is shown to reproduce the main features of the large amplitude anode current oscillations observed in the high current mode and a parametric study performed to examine the various mechanisms for oscillation excitation predicted by the model. An unsteady model is developed to capture changes in the presupposed turbulent transport of electrons across a radial magnetic field due to axial shear in azimuthal electron currents, which is based on models used in the tokamak literature to describe transitions from modes of low-to-high plasma confinement [13, 14, 15]. This model is shown, for the first time, to reproduce the features of the mode transition observed in the DCFT, though further experimental work is required to validate conclusions drawn from the highly simplified code.

1.3 Thesis Content

The thesis begins by defining the metrics for plasma thruster performance followed with an overview of several related plasma thruster variants, focusing on those exhibiting cusped magnetic topographies. The fundamental physics describing plasmas in cusped fields are reviewed along with the first devices to use cusps to contain plasmas. The general derivation of the plasma fluid equations from the kinetic equation is presented and subsequently applied to the problem of 1-D plasma flow to a wall, which is an essential component of both plasma probe theory and the theory of thruster operation. The background chapter is concluded with a discussion of electron transport across a magnetic field, as this is one of the key problems for any plasma-containing device.

Chapter 3 is devoted to the external dynamics of the thruster. The divergent, hollow plume is discussed as a nearly universal feature for gridless cusped-field thrusters with strong external magnetic fields. A heuristic theory is presented which attempts to explain the high angle of ion beam focusing based on the intrinsic magnetic topography of these devices. Experiments using an external trim coil to alter the magnetic field are discussed which seem to validate our main hypothesis, but also result in an unexpected stratification of the plume.

Chapter 4 is dedicated to the exposition of experimental evidence regarding the bimodal operation of the DCFT. Discharge current bifurcations found in similar devices are reviewed and compared to that of the DCFT, with a common thread of mode changes resulting in the cessation of high amplitude oscillations. The main discharge current oscillation found in the DCFT high current mode is identified as a breathing instability which is discussed in both theoretical and experimental contexts. The bulk of the chapter is dedicated to a characterization of the mode transition and attendant discharge current oscillations in our thruster through a scan of various parameters. Thermal measurements accompanying the parametric study are presented as well.

Chapter 5 discusses an unsteady 1-D model of a Hall thruster discharge which is adopted from the literature to characterize the various avenues towards the excita-

tion of non-linear breathing modes, similar to those presented for the DCFT in the preceding chapter. A time-dependent model of the electron cross-field transport is added to the model and results presented which capture the trends in anode current waveform accompanying the approach to mode transition.

The final chapter reiterates conclusions drawn from preceding chapters with a look at how the different pieces of the DCFT puzzle might fit together. Recommendations for future work are presented which conclude the main portion of the thesis.

Chapter 2

Background

2.1 Electric Propulsion Overview

We will begin with an abridged discussion of electric propulsion devices, constricted, for the sake of brevity, to those which resemble the cusped-field thruster under study. Before discussing the properties of the various thrusters we discuss a system of metrics by which a grid-less plasma thruster may be judged. The system is outlined for this specific case as it is the most applicable to our device, however the general concepts involved may be easily transplanted to the description of a broad range of plasma thrusters.

2.1.1 Figures of Merit

It is important to establish a clear set of thruster performance metrics in order to compare the DCFT to other plasma propulsion devices and to assess where improvements can be obtained. The main indicators for rocket performance are the thrust produced, T, and the specific impulse, I_{sp}, which is a measure of the mass of propellant required to obtain a given change in orbital velocity, where a higher specific impulse means a lower necessary propellant mass. The two parameters are related by $T = g_e I_{sp} \dot{m}$, where g_e is the acceleration due to gravity at the earth's surface and $\dot{m}$ is the propellant mass flow rate.

The remaining figures of merit for the DCFT can be borrowed from the Hall thruster literature due to the similarity between the two devices. A recent thorough architecture for Hall thruster efficiency analysis related to experimentally accessible quantities was presented by Larson *et al* [28] and expounded upon by Brown [29], while a simplified version is described here. The total thrust efficiency can be defined as the fraction of input power used to produce thrust, $\eta_t = T^2/(2\dot{m}P_{in})$. The anode efficiency is often found in the Hall thruster literature instead, which is generally of the form,

$$\eta_a = \frac{T^2}{2\dot{m}_a P_a} \tag{2.1}$$

where any mass flow through the external cathode and any power delivered to the cathode keeper are no longer counted against the efficiency. Here, the mass flow rate through the anode is denoted $\dot{m}_a$ and the anode power, $P_a = I_a V_a$. This can be a misleading figure as the DCFT (among other thrusters) is sometimes run with cathode flow rates and keeper powers approaching half those applied to the anode. For clarity, the anode mass flow rate refers to the input neutral propellant mass flux at the discharge chamber inlet.

Thrust, in terms of plume properties, is obtained by integrating in spherical coordinates, with the origin at the intersection of the thruster axis of symmetry and the exit plane, the axial ($z = rcos\theta$) component of propellant mass flux through a hemisphere external to the thruster. The contribution of unionized propellant to thrust is neglected, as usual, due to neutral flow speeds typically being several orders of magnitude lower than that of the ions resulting in the expression,

$$T = \int\int v_{iz} m_i n_i \mathbf{v}_i \cdot \mathbf{dA} = 2\pi R^2 m_i \int_0^{\pi/2} n_i v_{ir}^2 cos\theta sin\theta d\theta \tag{2.2}$$

where $\mathbf{v_i}$ is the ion velocity averaged over the ion velocity distribution function, n_i is the local ion density, the z direction lies along the thruster axis and r points in the direction of the spherical radius, R. Defining the mass flux averaged ion velocity and the momentum flux averaged $cos\theta$ as,

$$< v_{ir} >_m = \frac{\int\int v_{ir} m_i n_i \mathbf{v}_i \cdot \mathbf{dA}}{\int\int m_i n_i \mathbf{v}_i \cdot \mathbf{dA}} = \frac{\int\int v_{ir} m_i n_i \mathbf{v}_i \cdot \mathbf{dA}}{\dot{m}_i} \tag{2.3}$$

$$< cos\theta >_{mv} = \frac{\int\int v_{ir} cos\theta m_i n_i \mathbf{v}_i \cdot \mathbf{dA}}{\dot{m}_i < v_{ir} >_m} \tag{2.4}$$

allows the expression and subsequent segmentation of the anode efficiency in terms of measurables, replacing the different brackets with overbars for economy,

$$\eta_a = \frac{(\dot{m}_i \overline{v}_{ir} \overline{cos\theta})^2}{2\dot{m}_a P_a} = \frac{\frac{1}{2} m_i \overline{v}_{ir}^2}{eV_a} \frac{e\dot{m}_i/m_i}{I_a} \frac{\dot{m}_i}{\dot{m}} \overline{cos\theta}^2 \tag{2.5}$$

This expression for anode efficiency can be regrouped into more familiar terms by introducing the mass flow averaged ionic charge, Q, which is defined in relation to the total ion current in the beam, I_b, by the expression, $m_i I_b \equiv Qe\dot{m}_i$. The anode efficiency becomes,

$$\eta_a = \frac{1}{Q^2} \left(\frac{\frac{1}{2} m_i \overline{v}_{ir}^2}{eV_a} \right) \left(\frac{I_b}{I_a} \right) \left(\frac{I_b}{e\dot{m}/m_i} \right) \overline{cos\theta}^2 = \frac{1}{Q^2} \eta_v \eta_b \eta_u \overline{cos\theta}^2 \tag{2.6}$$

where we introduce the voltage efficiency, η_v, the beam efficiency, η_b, and the utilization efficiency, η_u, which describe respectively the efficiency with which the ions are accelerated by the applied voltage, the amount of anode current which contributes to thrust, and the amount of propellant used to create the ion beam. The beam current, and $cos^2\theta$ loss can be straightforwardly measured by electrostatic probing in the plume while the anode mass flow rate, voltage and current are part of the thruster telemetry. The multiply averaged ion velocity is less experimentally accessible, but can be estimated and bracketed using a simple potential analyzer. The extraction of any of these properties is actually mainly hampered by facility effects, where a finite neutral gas backpressure in the vacuum chamber is ingested by the thruster and undergoes resonant processes with the plume ions which can not easily be deconvolved from natural interactions with unionized propellant [24].

Measurements in the plume of the DCFT performed by Gildea at the Air Force Research Laboratory [18] indicate the thruster was operating less efficiently than it

had during thrust measurements on the original prototype. At anode conditions of 300 V, 0.53 A and 0.83 mg/s of Xe, the integrated beam current was estimated to be 0.38 A leading to a beam efficiency, $\eta_b = 0.72$, and a propellant utilization efficiency, $\eta_u = 0.87$. The momentum flux weighted divergence angle was an estimated 56° leading to a combined efficiency of about 20% not including the voltage and charge efficiencies, which are expected to be reasonably close to unity. The thruster ran at 0.62 A for an anode efficiency of 40% in the Courtney measurements made at the same thruster inputs and a similar vacuum chamber backpressure, with the thruster operating in the highly oscillatory mode in both cases.

One obvious difference between the two experiments is that the anode was made of stainless steel instead of graphite during thrust measurements, while subsequent testing is done almost exclusively using a graphite cap to limit sputtering and redeposition of anode materials on the boron nitride cone. Perhaps the intense sputtering of the steel anode is leading to a beam current contribution by ionized iron (the ionization potential for Fe is well below that for Xe) which is unaccounted for in efficiency estimates.

Perhaps the discrepancy in thruster performance is instead due to deficiencies in the estimate method based on plume measurements. It is shown, for example, in Sec. 3.3.3 that a similar estimate of the anode efficiency from ion flux measurements (taken at a radius of 30 cm from an origin at the thruster exit plane) is about 2/3rd of the efficiency estimated using a more appropriate coordinate system for data reduction.

2.1.2 Ion Engines

Ion engines levy the principles utilized by multidipole (or equivalently multipole) chambers to create a highly uniform, magnetic field free plasma–a thorough description of multidipole chambers is deferred to a later section after some of the basic physics is presented. A set of closely spaced grids bound the plasma chamber on one side and accelerate the impinging thermal ion flux through an applied potential difference of the order of a kilovolt to create a high velocity jet, providing thrust. An external neutralizer cathode emits electrons into the ion beam to create a charge

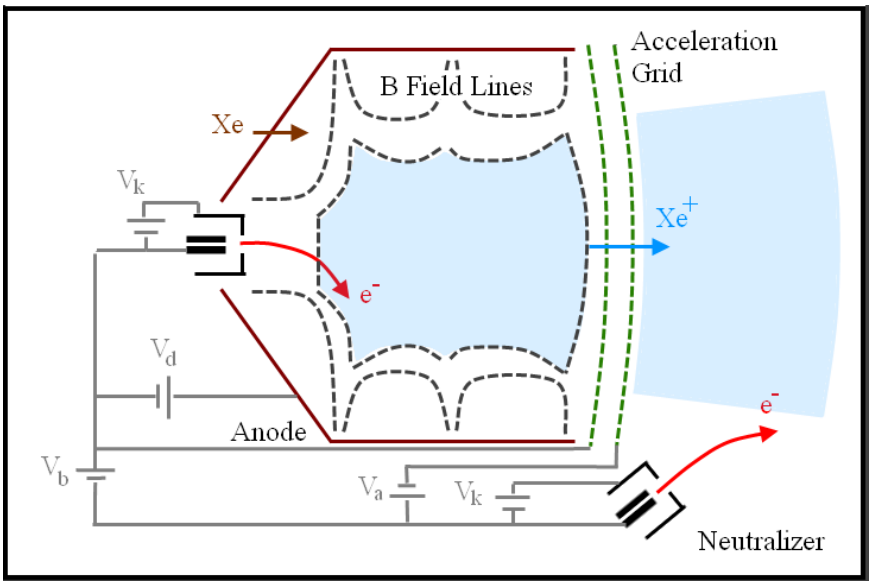

Figure 2-1: Schematic of a typical electron bombardment ion engine with a cusped magnetic field configuration

neutral plasma jet, preventing the build up of space charge. A simplified schematic of a typical ion engine is shown in Figure 2-1 in which the cusped-type magnetic configuration is illustrated. The figure displays some of the power supplies required for electron bombardment ion engine operation in which a discharge cathode supplies electrons to the ionization chamber, where they remain long enough to efficiently ionize an incoming flow of neutral propellant due to confinement by the applied magnetic field.

Plasma electrons stream to the discharge chamber walls faster than ions causing an electron repelling sheath to form there, and the main plasma to equilibrate at a potential slightly above the applied discharge voltage, V_d, which is usually on the order of 20-60 V. Primary electrons emitted by the discharge cathode gain a significant amount of energy as they accelerate from the applied keeper potential, V_k ~15 V, to the bulk plasma potential allowing them to actually ionize more than one neutral atom on average before cooling to a temperature near that of the ensemble of secondary electrons which were produced in each ionization event. The high efficiency with which the neutral gas is ionized along with the spatial uniformity of the resulting ion beam compound to make ion engines an efficient form of electric propulsion. For

example, the NSTAR engine which flew on the 1998 Deep Space 1 mission operated at a total efficiency of 63% for an input power of 2.1 kW, providing 83 mN of thrust at a specific impulse of 3200 seconds [81].

The walls of the discharge chamber, in the simplified picture presented, also act as the anode through which the discharge current must run to sustain the plasma. A magnetic field is then desired which can provide long confinement times for the energetic primary electrons (which dominate the neutral gas ionization), but allow thermalized electrons (secondaries from ionization and primaries which have undergone an inelastic collision) to flow to the anode easily enough to maintain a stable discharge, a task to which cusped magnetic fields are ideally suited. Thermalized electrons reach the anode at the cusps in a manner maintaining quasineutrality with the unmagnetized ions, which only feel the effects of the magnet mirror there indirectly through electrostatic interaction with electrons. The low density population of primary electrons are generally of a high enough energy to be unaffected by self-consistent electric fields which mediate the bulk plasma and thus leak through the cusps dependent only on their pitch angle [82, 83].

The use of a multidipole type field in an ion engine discharge chamber was described in 1969 by Moore [84] who place conducting strips in between cusps to act as the anode. More conventional ring cusp type magnetic field configurations are discussed as early as 1976 by Beattie and Wilbur [85] and further developed by Sovey [86] in 1984 for an inert gas thruster, where the discharge current is largely collected at the cusps.

The NSTAR thruster, mentioned earlier, also utilizes a ring-cusp configuration in the discharge chamber, which is 30-cm in diameter. Typical plasma parameters in the NSTAR device include neutral densities of $10^{18} - 10^{19} m^{-3}$, plasma densities of $10^{16} - 10^{17} m^{-3}$, secondary electron temperatures of around 4 eV and a primary electron energy near 20 eV [87]. A spatially uniform ion density near the grids is desired in order to obtain a flat ion beam profile, which avoids highly localized grid erosion and maximizes thrust. In order to obtain such a profile the magnetic field is designed to be fairly weak within much of the chamber volume, avoiding the strong density

gradients set up by inhibited cross-field electron transport. The field in the NSTAR chamber is below 20 G across most of the chamber radius, but increases to several hundreds of Gauss near the magnets to prevent rapid ambipolar diffusion across field lines to the anode. The electrons are still highly magnetized, even near the center of the chamber, while the ions are not, with Coulomb collisions (small-angle deflections of one charged particle interacting with another through the Coulomb force) being negligible compared to collisions with neutral particles due to the comparatively low plasma densities. This regime of plasma properties is very similar to that found in the more general multidipole devices discussed later, as well as those expected in the DCFT.

2.1.3 Cusped Field and Hall Thrusters

HEMP-Thrusters

The High Efficiency Multi-Stage Plasma (HEMP) Thruster developed by THALES Electron Devices GmbH is the main precursor to DCFT. The device is based on the company's experience with traveling wave tubes consisting of a periodic permanent magnet structure. The cartoon in Figure 2-2 shows the basic layout of the device which consists of a rear mounted anode through which a neutral gas is input at a steady rate. An external hollow cathode provides electrons, which due to confinement by the periodic spindle-cusp type fields–a magnetic field marked by a ring cusp sandwiched between two point cusps which is further discussed in the multidipole section–efficiently impact ionize the neutral gas. The early HEMP devices had purely cylindrical discharge chambers, insulated by boron nitride walls with magnetic fields provided by three permanent ring magnets of alternating polarity but identical size [9].

In the first report of thrust measurements on a HEMP-T (Model DM3a) in 2003 the authors explain that the applied potential is seen by the plasma in discrete drops from one point cusp to the next [88]. Energy measurements in the plume indicated that ions at angles between 15° and 50° from the thruster angle were accelerated

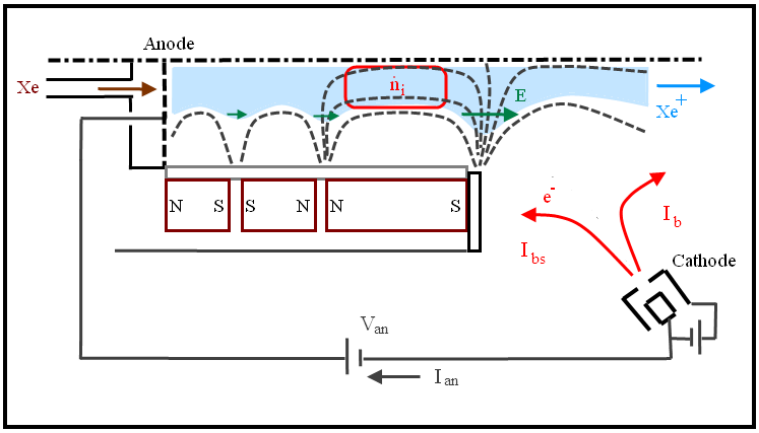

Figure 2-2: Cross sectional schematic of a basic HEMP type thruster as described in [9]

to nearly the applied potential, while those found between 55° and 65° only received around half of that. The authors posited that the hollow jet which formed from 15-50° is from ions created near the point cusp just downstream of the anode which receive the full 500 V, while ions found at 55° in the plume are born at 270 V near the second downstream point cusp and those from 60-65° are born at 150 V near the last point cusp upstream of the exit. Near the axis the plume was less dense and believed to be dominated by charge exchange ions. The efficiency of the early prototypes peaked at 31% for a thrust of 24 mN and specific impulse of 1682 seconds operating at 550 V and 1.16 A on the anode and a xenon mass flow rate of 1.46 mg/s (15 sccm). The ion current in the plume peaked at around 35° from the thruster axis in this 3cm diameter thruster.

In a review paper by Kornfeld, Koch and Harmann [9], the interesting history of HEMP-T development is discussed, detailing some of the lessons learned while trying out a wide variety of designs. Through the use of Berkley's OOPIC plasma simulation code and the collisionless trajectory code KOBRA the team found that the original chamber diameter of 1 cm was too small to prevent high wall losses and so a move to larger diameter thrusters led to the development of the 2-cm HEMP DM-6. Another design change incorporated into the DM-6 was the lengthening of the third (most downstream) magnet compared to the inner two, creating a long region where the B field is largely parallel to the thruster wall. This change came about

based upon the idea that the steepest potential drop (i.e. largest electric field) would be at the exit ring cusp where the mirror ratio is highest, the neutral density lowest and therefore the high electron Hall parameter (the ratio of electron gyrofrequency to electron-neutral collision frequency) leads to a peak in axial electron impedance. Cathode emitted electrons passing this region of high electric field and largely radial magnetic field would enter the next upstream cell close to the thruster axis and with a much increased average energy, leading to high ionization rates in that region. By extending this zone they may be able to increase the overall ionization of the incoming neutrals and accelerate the created ions almost uniformly across the exit potential drop. The discussed OOPIC simulations are said to have identified this and the next upstream region of axial magnetic field as the main regions of ionization, although the results are not presented. Attempts to probe the plasma along the axis were apparently unsuccessful as they led to noticeably large disruptions of the plasma.

The main advantage touted for the HEMP type thruster is its lack of insulator erosion. A 250 hour test of the DM7 version of the thruster is reported to reveal only 10 μm deep erosion of the 1.5 mm thick ceramic at the location of the middle cusp [11] which extrapolates linearly to a lifetime of greater than 30000 hours. This variant has both the extended third magnet and an almost bell nozzle shaped chamber downstream of the middle cusp. A later paper describes this increase in the relative dimensions of the exit cusp section as motivated by a proposed link between decreasing the exit neutral pressure and reducing the plume divergence through a combined lowering of the plasma potential in the plume and of the proportion of charge exchange ions [89]. This paper also suggests an increase in electron confinement can be had by increasing the ratio of the radial field at a wall cusp to the axial field at the next downstream point cusp. The more recent DM9 variant of the HEMP-T, which has an inner diameter of 22.5 mm at the upstream magnets and a diameter of 45 mm at the downstream magnet, is shown to no longer exhibit a hollow plume structure, with a peak in ion current measured on the thruster axis and ion energies near the applied voltage (600 V) within around 50° of the axis [90].

Hall Thrusters

A conventional Hall thruster consists of an annular discharge chamber in order to accommodate the central pole of the magnetic circuit, making it possible to create a largely radial field, with a peak strength of several hundred Gauss near the exit, using solenoids. A largely axial electric field is applied between an anode (which sometimes doubles as the propellant injector) in the rear of the chamber and an external hollow cathode, with typical potential drops of around 200-600 V. The magnetized electrons execute closed azimuthal ExB drifts independent of the unmagnetized ions (this is the Hall effect current which lends its name to the device), with the centrifugal force of the electron ensemble motion largely balanced by an electron-repelling sheath which forms on the discharge chamber walls. The confinement of electrons by the Hall effect along with the energy they gain moving towards the anode allows for efficient ionization of an input neutral propellant flow, creating plasmas with typical peak densities around $\sim 10^{18}\ m^{-3}$, electron temperatures ~ 20 eV and ion temperatures of < 2 eV [25].

Since the motion of electrons from the cathode to the anode (electron backstreaming) is impeded by the perpendicular magnetic field, a self-consistent electric field forms near the peak in B_r which accelerates ions out of the device. The majority of the electron current pumped through the hollow cathode (which in total equals the anode current) goes into neutralizing the ion plume, while the remaining fraction makes up the backstreaming current necessary to sustain ionization. Though the backstreaming current, $I_{bs} = I_a - I_b$, is necessary for thruster operation it reduces thruster efficiency as power is expended in pumping a current over the anode voltage which does not contribute to thrust.

Some concavity to the magnetic field lines near the exit is used as an ion lens which promotes the convergence of the ejected ions into a narrow plasma plume, strongly peaked on the thruster axis. The plume divergence is often significantly larger than found in modern ion engines however, due to such factors as imperfect focusing, high electron temperatures (which lead to large radial electric fields near

the wall) and resonant charge exchange from accelerated ions to unionized propellant (which is in greater abundance in a Hall thruster plume). Despite having higher plume divergences than in ion engines, modern kiloWatt level Hall thrusters have similar efficiencies of around 60-70% [91] and are generally much easier to construct due to the lack of closely spaced acceleration grids.

Two major classes exist for conventional Hall thrusters based on the electrical properties of the discharge chamber wall. In one class, usually referred to as Thrusters with Anode Layer (TAL), the channel wall is conducting and sometimes set to the cathode potential. TAL-type thrusters often operate at relatively high electron temperatures and electric fields, with a thin layer of plasma near the anode and an acceleration region that is often downstream of the thruster exit. In the other class of Hall thruster, often designated as Stationary Plasma Thrusters (SPT), the walls are insulated, both thermally and electrically, often by ceramics such as Boron Nitride (BN), Borosil ($BN - SiO_2$) or Alumina (Al_2O_3). The discharge chamber in SPT's are typically much longer than in TAL's, with a magnetic field that diminishes approaching the anode. The relatively high secondary electron yield from ceramics lead to reduced potential drops in the wall sheath and correspondingly higher plasma loss to the wall than in a TAL (though the plasma lost is at lower energies). The ionization and acceleration regions are also more internalized in SPT-type thrusters which leads to higher levels of ion bombardment erosion of the insulating material, localized near the exit. The ceramic piece insulating the inner wall of the discharge chamber is often the life limiting material in an SPT due in part to its lower volume. Once the inner wall is eroded through, the plasma contacts the magnetic circuit, the degradation of which will lower the thruster performance and ultimately lead to its failure.

Cylindrical Hall Thruster The Cylindrical Hall thruster (CHT) developed at Princeton is a low power Hall thruster in which the normal annular configuration is eschewed in favor of a largely cylindrical one, which effectively increases the volume to surface area ratio in the discharge chamber. The CHT, in a manner similar to the

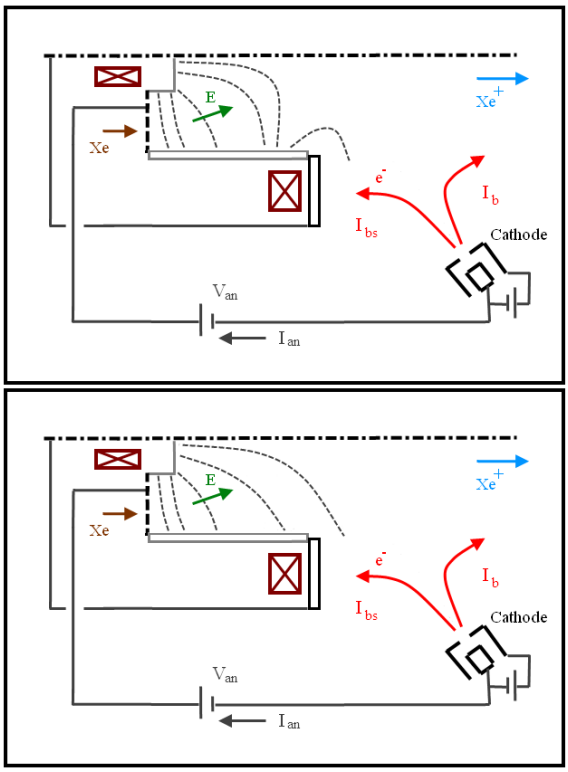

Figure 2-3: Cross sectional schematic of CHT in (top) cusp and (bottom) direct configuration

End-Hall thruster before it [92], maintains the closed Hall drift without the central pole piece. One of the main stated reasons for moving to a cylindrical design instead of coaxial one was to enable efficient miniaturization for low power operation. For Hall thrusters low power generally equates to lower propellant mass flow rates and in order to maintain a high enough neutral density and electron confinement for efficient ionization, the cross sectional area is reduced and the magnetic field made stronger. Increasing the field strength and decreasing the size of the central pole becomes difficult due to magnetic saturation of the pole material, while retaining the central pole size would exacerbate the problem of increased surface-to-volume ratio (which may lead to enhanced wall losses) inherent to the miniaturization.

The original design of the CHT actually still contains a short coaxial region stretching from the anode/gas distributor to roughly the length of the mean free path for neutral ionization downstream before becoming fully cylindrical. The magnetic field is supplied by an inner solenoid which surrounds a short central pole at the base of the thruster and an outer solenoid, located near the exit, which is used to either create a ring cusp in this region or to guide the field lines to run almost parallel with the wall (this is called the 'direct' configuration in the literature). In either configuration the field is predominantly radial in the short annular region, while the cylindrical region has a large axial component and a point cusp at its base. The two configurations are illustrate schematically in Figure 2-3.

The first prototype had a 9 cm diameter discharge chamber and a peak field strength of only around 150 G [93]. Emissive probe measurements of the plasma potential internal to the device showed that the main acceleration region was located just downstream of the coaxial section, where the majority of the ionization was expected to occur. As the anode voltage was increased from 200 to 300 V the location of the peak electric field was measured to shift downstream by several millimeters (in an annular Hall thruster the peak is seen to move upstream with voltage [30]). Scans of the solenoid currents showed that an optimum ratio of the outer and inner coil strengths resulted in a minimum discharge current, revealing that a continual increase in the field strength does not result in a continually decreasing anode current, but

rather at some threshold field strength the current actually begins to increase. The half-angle containing 90% of the ion current in the plume was larger in the prototype CHT than in conventional Hall thrusters, being 60° compared to 45-50°, and the overall efficiency was a lower 40% compared to 50% for power levels around 500-700 W.

A 2.6 cm diameter CHT was soon developed with a much stronger magnetic field. A peak radial field of over 600 G is obtained just upstream of the start of the cylindrical section and a field strength of around 1500 G is found at the point cusp [94]. Internal plasma potential measurements on this thruster reveal a longer acceleration region than in the 9 cm case, though it is still mostly contained within the cylindrical region, with a plasma potential of 100 V at the exit for an applied voltage of 250 V. Despite having propellant utilization efficiencies exceeding unity (possible if the beam contains a significant fraction of doubly charged ions), the CHT did not perform as well as a normal annular-type Hall thruster, registering anode efficiencies from 15%-32% in the power range of 90-320 W [95], compared to the 42% efficient BHT-200-X2B which operates at 200 W [96].

More recently, reports were published on a permanent magnet version of the 2.6 cm CHT, which more closely resembles the DCF and HEMP thrusters[22]. The maximum field strength in this device is roughly 2-2.5 kG, found at the internal point cusp, but the main difference with the solenoid-based version is the strong field external to the discharge chamber. At the location of the channel radius, 1 cm downstream of the exit, the field is still nearly 300 G in the permanent magnet variant, where it is normally less than 20 G. The most striking result of the CHTpm (as the permanent magnet variant is called) testing is the appearance of a hollow, conical plume as is found in the DCFT and early HEMP-T devices. The ion current profile begins to fill in at low angles when the anode voltage is increased above around 400 V, but RPA measurements show that the ions there have a large spread in energies all at least 100 V below the applied potential.

In the cusp configuration the peak ion current density is found at around 40-50°, while in the direct configuration, which in this case exhibits a ring cusp on

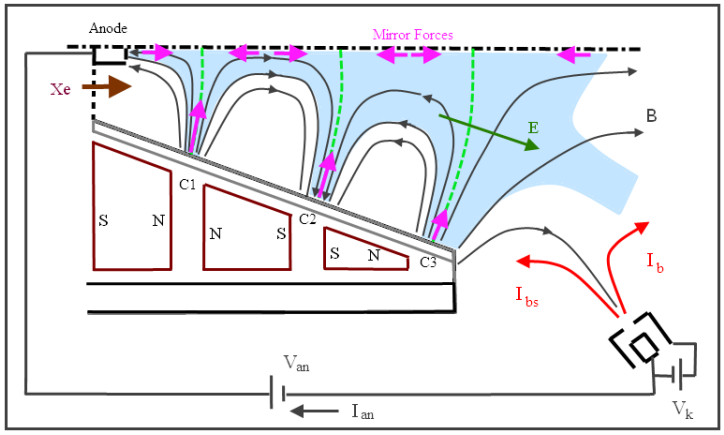

Figure 2-4: Cross sectional schematic of the DCFT thruster

the walls that is further downstream, the current density maximum occurs around 60-70°. Among the main differences between the cusp and direct configurations are that, in the cusp mode, the external magnetic field is significantly weaker and the ring cusp is deeper inside the channel. A follow-on study has shown that the normal, peaked-on-axis plume can be recovered from the CHTpm by using a magnetic shield to reduce both the internal and external field strengths to those more typical of the electromagnet version of the CHT [97].

Fully cylindrical Hall thrusters have also been designed and tested by groups in Korea [98] and Japan [99]. Internal probing of a 5.6 cm diameter CHT built at Osaka University [99] has shown that the plasma density peaks in the center of the device near the point cusp at around $5\text{x}10^{18}$ m^{-3}, where the plasma potential is actually at a radial minimum, at a flow rate of 0.5 mg/s. The majority of the acceleration appears to start at a point only a few millimeters from the annular anode and proceeds in a diagonal path towards the thruster axis at the exit. The measured electron temperature is around 20 eV in the near-anode region, but the flux lines still appear to be very nearly equipotentials as well.

DCFT

The DCFT design, shown schematically in Figure 2-4, is based largely on the HEMP thruster developed at THALES Electron Devices GmbH and the Cylindrical Hall

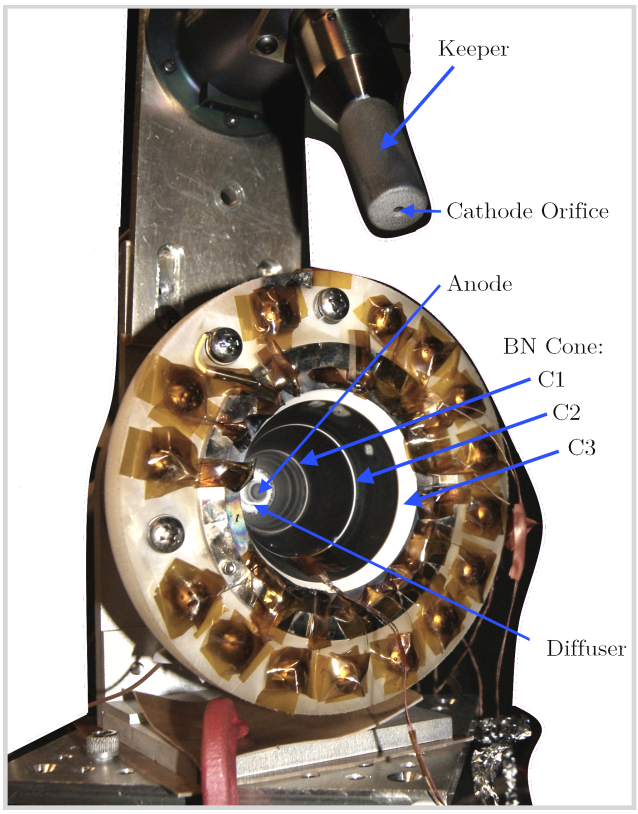

Figure 2-5: Labelled picture of the Instrumented DCFT thruster with Busek Hollow Cathode.

Thruster of Princeton. Both devices are cylindrical with magnetic shielding of the insulated chamber walls and to some extent the conducting anode. The HEMP thruster is most similar to the DCFT as they share a magnetic circuit design marked by three or more alternating polarity ring magnets. The DCFT differs most obviously from its predecessors in its divergent chamber and on-axis anode placement.

The divergence was initially motivated by the observation of Hall thruster erosion patterns in which the slightly defocused ion beam leads to a large degree of insulator sputtering near the exit of the discharge channel. The strongly localized ion impingement in Hall thrusters has led to the common practice of chamfering the exit edge of the insulator, but since ionization was expected to occur much closer to the anode in the multi-cusped DCFT the entire length of the boron nitride insulator was set to angle away from the expected ion beam. This novel discharge chamber shape also allowed for the straightforward use of beveled ring magnets of diminishing size to gradually reduce the magnetic field strength in the chamber as the ionized propellant accelerated out of the device, which was hoped to decrease any effect the sharply diverging external magnetic field might have on the axial collimation of the ion beam.

The central, graphite anode is mounted at the upstream end of the discharge chamber backed by a thick magnetic steel core used to guide flux lines towards the axis and in doing so create a strong axial bottle in front of the anode to meter the backstreaming electron current. Similar point cusps exist on axis between the most upstream ring cusp (C1) and the central ring cusp (C2), between C2 and the exit ring cusp (C3), and between C3 and the cathode plane, as labeled on Figure 2-4 where pink arrows denote locations of strong mirroring. A boron nitride cone is used to insulate the magnetic circuit from the plasma, and though initially white, the cone becomes covered in a dark layer of deposited material after several hours of operation in our vacuum chamber. The dark deposition is absent in the ring cusps as seen in the picture of a DCFT prototype outfitted with internal probes in Fig. 2-5.

A potential, V_a, is applied between the anode and the electron emitting insert of an external hollow cathode of anywhere from 200 to 600 V. The applied electric field imparts energy to backstreaming electrons from the cathode which are confined

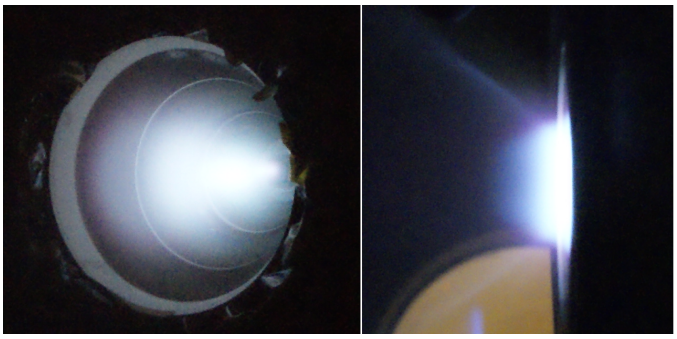

Figure 2-6: Images of DCFT thruster firing viewing (left) into the discharge chamber (right) perpendicular to the exit plane

away from the chamber walls by transverse magnetic fields between ring cusps and a combination of magnetic mirroring and wall sheaths at the cusps. Neutral xenon propellant is fed through a porous, steel frit surrounding the anode (the diffuser labelled in Fig. 2-5) at a flow rate of 0.39 mg/s to 0.98 mg/s, where the inner diameter of the chamber is only 15 mm resulting in an inlet neutral density of around 10^{20} m^{-3} at the maximum flow rate. The chamber is 5 cm long and diverges at a 22.5° half angle, so that the chamber diameter is 5.3 cm at the exit and if the neutral flow were unionized and negligibly accelerated the density there would be 10^{19} m^{-3} at a flow of 0.98 mg/s. The large neutral densities lead to a high collisional frequency with electrons, causing the smaller particle to diffuse somewhat across magnetic field lines, leak through bottles[a], and luckily to ionize a substantial fraction of the neutral propellant. Electrons which gain enough energy from the electric field can ionize multiple times before being lost to the chamber surfaces or anode. The secondary electrons knocked off of atoms by ionizing collisions can also contribute to subsequent ionization events.

The initial backstreaming electron current (likely small) gains a substantial flux in the discharge chamber through ionization and contributes to a DC current at the anode of around 0.2 A to 0.7 A. The counter-streaming ions are accelerated through

[a]Electrons with pitch angles outside the point cusp loss cone may be trapped between point and wall cusps until collisions with heavy particles give them the proper pitch to leak through. However, there is perhaps a competing effect due to the electric field, which forms to keep ions close to the magnetically funneled electrons, tending to increase the perpendicular (with respect to **B**) energy of electrons upon collision with a neutral, and thus making them more susceptible to mirroring.

a potential drop, recently measured by the author and others to occur mainly just downstream of the exit separatrix [8, 6]. A separatrix is simply a line which divides cells of different magnetic vector potential polarity. The exit separatrix is a convenient conceptual anchor for the electric field since electrons emitted from the cathode must travel across a strong magnetic field to reach it but once upstream are already on a flux line of low vector potential and are able to stream relatively easily toward the anode along that line until reaching the next cusp. The separatrix also marks the region to which electrons are funneled by the magnetic field lines, so one may expect the peak plasma densities to occur nearby.

Visually, a luminous bulb appears during thruster operation which extends just past the exit, similar to the appearance of a Hall thruster exit, but instead of coalescing into a central spike, a distinct jet appears pointed near 30° off-axis, which is coincident with the peak ion flux measured by electrostatic probes. The bulb and jet can be seen in Figure 2-6 alongside an image of the discharge chamber illuminated by the plasma during thruster operation.

The ion jet is neutralized by electrons supplied by the same hollow cathode used to initiate (and maintain) the discharge. The hollow cathode is a complicated plasma device in itself and much research is still ongoing to discern and describe the main phenomena involved in its operation and coupling to a variety of systems. The main component of a hollow cathode is the low work function insert (which is where the cathode potential is referenced) which is generally some mixture of tungsten and various oxides. A coil heats the insert to temperatures where thermionic emission of electrons can commence, an effect which is aided by an electric field supplied by a positively biased keeper electrode. The keeper for modern hollow cathodes, as used on the DCFT, is a cylindrical enclosure which is used to initiate the extraction of electrons from the cathode. The electrons emitted from the insert actually ionize a noble propellant gas, creating a plasma which allows large currents to be drawn without space charge limitation. Ideally, the keeper electrode can be deactivated once the discharge is initiated, but it is often maintained to ensure a steady operation through an odd disruption.

A thorough description of the design process and initial test results for the DCFT can be found in the Masters thesis of Courtney [1] from 2008. This thesis also documents the first direct thrust measurements obtained on the thruster, which were taken at flow rates ranging from 0.68 mg/s to 0.98 mg/s corresponding to chamber pressures between 3.2x10^{-6} and 4.3x10^{-6} Torr. The best measured performance was obtained at 0.83 mg/s of Xe, 550 V and 0.44 A on the anode, yielding 13.4 mN of thrust for an anode efficiency of $44.5\% \pm 8\%$ and an I_{sp} of 1650 s. These, and other metrics are defined in the preceding section for clarity. The lowest measured performance of 6 mN of thrust at $25.5\% \pm 9\%$ efficiency and 900 s occurred at an anode flow rate of 0.68 mg/s, 300 V and 0.34 A.

Stanford DCFT

A variant of the DCFT was recently designed and built at Stanford which has a magnetic field topology similar to the MIT thruster, but with a largely cylindrical discharge chamber, which flares out over a short section near the exit [5]. The Stanford DCFT is also smaller than the MIT prototype, with a chamber diameter of 14.3 mm and a length of 39.7 mm, compared to the DCFT's mean diameter of 26.4 mm and length of 49.5 mm, resulting in an 88% reduction in volume. The anode (which is slightly larger than the DCFT's) is also placed in a point cusp near the rear of the discharge chamber which is said to have a typical mirror ratio of 1.6, while for the DCFT it is greater than 3.8. Unfortunately, the only published experimental results for this thruster to date have used krypton as the propellant gas instead of xenon which makes comparison to similar devices less straightforward. Krypton has a mass about 64% that of xenon, which equates to a 20% reduction in ion gyroradius and a 25% increase in ion velocity for the same energy. The first ionization energy threshold is also higher for krypton than xenon, which is one of the reasons for its generally lower performance in Hall thrusters [108].

Thrust measurements indicate anode efficiencies ranging from around 7 to 23 % for power levels ranging from 40 to 240 W. Surprisingly, the 40 W case resulted in the highest effiiciency, while at the highest power tested the efficiency was just below

20%. A scan of the cathode position showed a strong dependence of thruster efficiency on where the cathode was placed in the magnetic field. The efficiency varied from 24%, when the cathode was 1 cm radially from the axis, to about 15% at a radial position of 10 cm with a local minimum at a radius of 4 cm. The position of the local minimum appeared to stay between 3 and 5 cm over a range of operating conditions. Another interesting trend is that the anode current appeared to drop monotonically as the cathode was moved further from the axis, to regions of higher magnetic vector potential. The authors posit that the general reduction in performance between cathode positions of 2 and 6 cm from the axis is related to the emitted electrons approaching the critical pitch angle for entering the wall loss cone as the cathode moves to field lines which are increasingly parallel to the cathode axis. It does not seem like this would be a dominant effect, however, since electron emission from hollow cathodes is not generally considered to be a collimated beam and the critical pitch angle at the walls of these thrusters is very small regardless of cathode orientation.

It seems more plausible to this author that the non-monotonic trends in thrust with cathode radial position are due to an interplay between increased ionization with increased electron confinement and decreasing ion acceleration efficiency as possibly more ions are born at lower potentials. It would be interesting to check the importance of the initial pitch angle on thruster performance by rotating the cathode pointing vector.

Faraday probe measurements of the ion current profile in the plume reveal a similar hollow cone distribution to that found in the MIT DCFT peaked at around 34°, confirming that the characteristic peak angle in ion flux is not due, in the case of the latter, to the diverging shape of the discharge chamber. The integrated beam current is found to be 0.226 A with the anode at 300 V and 0.361 A for 8.2 sccm of krypton, resulting in a beam efficiency of 63% and a utilization efficiency of 60%. Considerable asymmetry is noted in the beam profile on the cathode side, where the beam divergence is lower along with the total integrated current.

Plasma potential measurements in the plume show a substantial portion of the total potential drop occurring downstream of the thruster exit. The potential also

exhibits local maxima in the region of peak ion flux at a roughly 30° angle, and along the thruster axis. Interestingly, the thruster is only observed to run in a mode analogous to the low anode current mode of the DCFT, with no large amplitude anode current oscillations and a visually stratified plume.

2.2 Plasmas in Cusped Magnetic Fields

The DCFT is not the first device to leverage the benefits of a cusped magnetic field topology to create a dense plasma, or even to use that plasma for propulsion. Many years have been spent researching the various intricacies of plasma phenomena in these fields under widely varying experimental conditions. Several of the most germane applications of cusped magnetic fields are presented in the following sections to serve as an introduction, first to the historical establishment of the main physics involved, and secondly to their integration into the space propulsion community.

One of the main features of a magnetic cusp which will be discussed is the mirroring effect. The effect is often derived starting from the view of a single electron orbiting, and moving laterally along a magnetic field in a direction of changing field strength. A simple case is presented to illustrate the effect, starting with the divergence of a magnetic field in cylindrical coordinates shown below.

$$\nabla \cdot \mathbf{B} = \frac{1}{r}\frac{\partial}{\partial r}(rB_r) + \frac{\partial B_z}{\partial z} = 0 \tag{2.7}$$

We can find the mirror force on a charged particle gyrating around the z-axis with a Larmor radius, ρ_L, and a speed of gyration, $v_\perp$, using Newton's second law and the definition of the Lorentz force,

$$F_{||} = m\frac{dv_{||}}{dt} = qv_\perp B_r \tag{2.8}$$

where the subscripts, $||$ and $\perp$ refer to vector components parallel and perpendicular to the magnetic field respectively. If the magnetic field strength changes negligibly over the period of one Larmor gyration, then the magnetic moment $\mu = 1/2mv_\perp^2/B$ is

an adiabatic invariant (not proven here), and Equation 2.7 can be integrated taking $\partial B_z/\partial z$ constant and evaluated at the Larmor radius,

$$B_r = -\frac{\rho_L}{2}\frac{\partial B_z}{\partial z} \tag{2.9}$$

and the result substituted into Equation 2.8 along with the definition, $\omega_c = qB/m = v_\perp/\rho_L$ to yield,

$$F_{||} = -q\frac{v_\perp \rho_L}{2}\frac{\partial B_z}{\partial z} = -\mu\frac{\partial B_z}{\partial z} \tag{2.10}$$

which shows that a magnetic field which increases slowly as the particle travels along it results in a decelerating force. A more complete formulation can be found in many introductory plasma physics texts [31] along with a justification for the constancy of μ.

The adiabatic invariant can also be used to show when a charged particle will be decelerated to the point of reflection based on its initial conditions. The conservation of energy in the absence of an electric field is used to equate the velocity and magnetic field strength at some starting point to the field and velocity at the point of reflection, where the parallel velocity component reaches zero.

$$\frac{1}{2}mv_{||_0}^2 + \mu B_0 = \mu B_f \tag{2.11}$$

where B_f is the field strength at the reflection point. The initial angle between the parallel and perpendicular velocities (the pitch angle, $tan\theta = v_\perp/v_{||}$) of a particle which is just reflected at the cusp defines the loss cone. All particles with initial pitch angles within the loss cone will pass through the cusp without being reflected. The loss cone angle can be found in terms of the mirror ratio, $R = B_f/B_0$,

$$tan^2\theta_m = \frac{1}{R-1} \tag{2.12}$$

where θ_m is the loss cone angle.

If all charged particles within the cusped field can be treated with an adiabatic

invariant magnetic moment then loss through a strong cusp will only occur as quickly as particles diffuse in velocity space to the loss cone. If, however, the ions of a plasma gyrate on length scales greater than the cusp length, the electric field-free loss cone analysis will not apply and some self-consistent state ought to be achieved in which the loss rates of the two species balance to maintain quasi-neutrality.

Interestingly, the mirror force can be shown to cancel out of the fluid equations for an isotropic distribution of electrons flowing into a cusp [62]. As the flux tube containing the electrons constricts the total pressure gradient force which acts on the high-B side of the fluid element becomes smaller than that on the low-B side, which in the isotropic case exactly balances the oppositely-directed force due to mirroring and the normal Boltzmann relation is obtained. A unique (to the author's knowledge) derivation of the electron momentum equation parallel to a field line is shown in Appendix E.

2.2.1 Magnetic Mirror Confinement Fusion

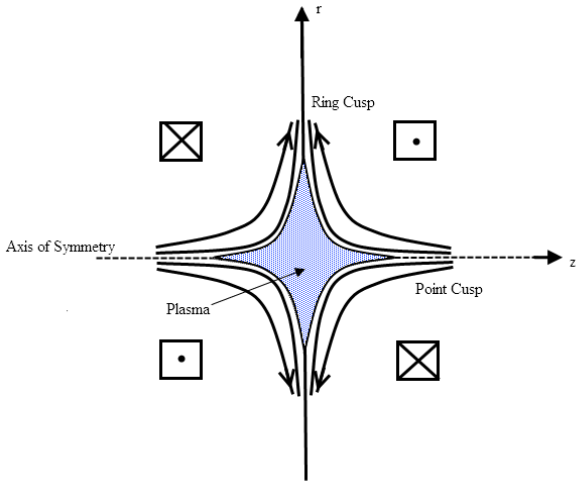

Figure 2-7: Cartoon schematic of spindle cusp magnetic field confining a plasma

Much of the early theoretical work on plasma interactions with a cusped magnetic field came from the fusion community where it was considered a promising method for ion confinement. Simple analysis taking the magnetic moment as invariant shows how

strong parallel gradients in the magnetic field can lead to nearly complete confinement (as discussed in the previous section). This lead to the idea of using a magnetic bottle for plasma containment, with a point cusp at each end to reflect charged particles back to the mid plane of the device. Unfortunately, it was found that particles continually diffuse into the loss cone through Coulombic collisions, making substantial power gains virtually impossible [31]. A historical overview of mirror fusion development up to the 1980's is given by Damm [33], where the use of cusped fields to quell low frequency instabilities is presented.

The problem of mirror machine instabilities led to the examination of cusped geometries, perhaps the most basic of which (and incidentally the most closely related to the DCFT) being the spindle cusp shown if Figure 2-7, due to the inherent macroscopic stability afforded by keeping the radius of curvature of the confining field everywhere outside of the plasma [34]. The spindle cusp, consisting of a ring cusp at the mid plane and point cusps along the axis on either side, is similar to the magnetic cells of the DCF and HEMP thrusters, though many of the early experiments utilized them to contain plasmas of pressures near the applied magnetic pressure [35]. Plasma pressures in the DCFT are expected to be much lower than that of the applied field, indeed around 1 Pa compared to the 4 kPa provided by a field of 1 kG.

The analysis of particle motion in an idealized spindle cusp was undertaken by several authors in the early days of its consideration as a confinement scheme for nuclear fusion, usually considering the conservation of canonical angular momentum and particle energy, and neglecting electric fields and collisions in order to make the problem analytically tractable [38, 39, 40, 41, 42, 43, 44]. The ideal cusp field is modeled in cylindrical coordinates (r,z) by the out-of-plane magnetic vector potential $A_\theta = ar^2z$ where a is an arbitrary coefficient used to set the magnitude of the field strength. A ring cusp occurs at $z = 0$ and two point cusps are formed on either side of the midplane where $r = 0$. There is zero field at the origin of the spindle which allows charged particles to stream through if they are injected close enough to the axis. The conditions for this streaming is derived by Schmidt [39] and later expounded on by Shinano and Ito [42], who find an analytical formula for the change in the magnetic

moment, μ, as a particle passes the midplane.

Expressions have been derived under various assumptions for the reflection point of particles injected from the $-z$ side of the spindle for various initial r positions [41, 43] as well as their confinement time within the cusp[43]. The high energy, one species, collisionless cases often considered do not ultimately bear much similarity with the DCFT however, due to the large differences between these regimes. An early review by Luk'yanov and Podgornyi [40] brings together some of the early theories on plasma confinement by a spindle cusp and tabulates the results of multiple experiments. The presented results include experiments performed with plasma densities comparable to those expected internal to the DCFT ($\sim 10^{18} m^{-3}$) and show clearly that the plasma density is sharply peaked on the axis of symmetry for both the point and ring cusps. The characteristic size (in the z direction for the ring cusp, r direction for point cusps) of the density distributions are described as 'leak widths', or 'magnetic gaps' in the high pressure cases, and are shown in one low pressure experiment to scale nearly inversely with magnetic field strength.

Experimental study of spindle cusps can be categorized by injection scheme as well as by the ratio of plasma to applied magnetic pressure. In many experiments a high energy source of electrons, ions or both is pointed along the z axis of a spindle, upstream of one of the point cusps [38, 43, 40]. Alternatively, a plasma can be introduced in the cusped field near the null point [45] as was done by Bosch and Merlino [46], who used a filamentary electron source to ionize a background neutral Argon gas. The effect of the experimental conditions on the resulting leak widths and electron confinement times is discussed further in the appendix.

The 'picket fence' magnetic field arrangement has also been widely studied for plasma confinement [47, 48, 49, 50, 51, 52, 53] and typically consists of a periodic array of line cusps. In this configuration the confinement properties of a cusped field can be investigated relatively easily by creating a plasma on one side of the 'fence' and comparing its properties with those of the plasma leaking through to the other side. The experiments cited all utilize a negatively biased, heated filament as a source of high energy primary electrons which ionize a background noble gas [47, 48, 49].

The picket fence itself is always inside a vacuum vessel which is lined with permanent magnets of alternating polarity, creating a 'multidipole' field which acts to prevent plasma from streaming to the walls everywhere but the cusps. Since leak widths are generally observed to scale inversely with the field strength, the total leak width area can be made to be a small fraction of the total exposed area of the containing vessel simply by using strong magnets.

Experimental characterization of multidipole chambers by themselves has also been undertaken by a number of researchers [66, 67, 68, 69, 70, 71, 72, 73, 74] due to their capability to create a large volume of moderately dense, magnetic field free plasma in the central region of the device, good for studying various plasma phenomena. Plasma densities obtained vary from around $10^{14} - 10^{17} m^{-3}$ at neutral pressures around 0.01-1 mTorr, with electron temperatures on the order of several eV and ion temperatures about ten times less. These devices are similar in many ways to the discharge chambers of common ion engines, which are discussed in the following section. In both devices the magnetic field strengths are large enough to magnetize the electrons, but not the far heavier ion species.

The interaction of a field-free low pressure plasma with a cusped magnetic field, which was the many concern of early confinement experiments, has been extensively investigated both numerically [50, 52, 76] and analytically [51, 77, 78, 80]. The early 2-D particle-in-cell simulations of a plasma in a picket fence field by Marcus *et al* [50], despite reducing the ion mass by over two orders of magnitude and using a simulation domain less than 20 Debye lengths long, recover several of the main experimentally observed features, including the strong confinement of electrons to field lines near the cusp and the funneling of ions towards the regions of high electron density by a potential valley running down the cusp. An analytical basis for the shape of the potential valley was introduced by Knorr and Willis [51] who find asymptotic solutions to Poisson's equation at the throat of a picket fence type cusp considering 1-D solutions to Vlasov's equation along the cusp width direction. The resulting perpendicular potential distribution is several times the electron temperature deep and several times the geometric mean of electron and ion Larmor radii wide. This geometric mean of the

Larmor radii is commonly referred to as the hybrid gyroradius, and is often called upon in the cusp leak width literature since it incorporates the inertia of the ions into the electrostatically coupled electron gyration length.

If a wall is introduced at the throat of the cusp, as in a multidipole chamber, then the parallel electric field of the Debye sheath must be considered. Martinez-Sanchez and Ahedo [80] find solutions to a collisionless 1-D kinetic model in the direction along the cusp perpendicular to the wall. Separate cases of either magnetized or unmagnetized ions are analyzed with a background population of electrons following the Boltzmann relation, with both cases yielding similar results which differ only slightly from the normal plasma presheath. Though the ion flux increases approaching the wall, the area through which it passes decreases at the same rate due to the conservation of magnetic flux $\Phi = BA$.

This point is sometimes overlooked when considering the 1-D case of electrons streaming towards a wall and calculating the incoming flux by integrating the electron distribution function over only those particles within both the magnetic mirror loss cone and with enough energy to pass the sheath [54]. The relation obtained for the wall impinging flux from an infinitely far away bulk population is the normal one divided by the mirror ratio. A purely 1-D magnetic field gradient cannot exist, however, making the problem inherently two dimensional. Though the flow (particles per second) from infinity is reduced by the inverse mirror ratio it is through an area which is greater than the area at the wall by the mirror ratio and thus the two factors cancel and the wall impinging flux (particles per second per unit area) is just the normal one (i.e. $\Gamma_w = e^{-1/2} n_{e\infty} c_s$).

Though the wall impinging flux of ions is not altered much by the presence of the cusp, the net ion current to the wall is clearly reduced. This is due to the restricted area through which the plasma is funneled. Combining continuity (where the cross-field flux of electrons is neglected) with conservation of magnetic flux shows that the ratio of flux containing areas from bulk plasma to wall is equal to the mirror ratio, but does not by itself set a value for either area. The wall area is set by the balance between the magnetic confinement of electrons and electrostatic confinement

of ions and is often estimated using a semi-empirical leak width as discussed further in Appendix B.

2.3 Plasma Modeling Basics

The self-consistent modeling of a plasma in externally applied magnetic and electric fields is a difficult task. In theory, one can track the motion of each of the many constituent particles by solving the equations of motion with given initial conditions. In practice, however, some averaging over many particles, along with an assortment of other techniques outside the scope of the present work, must be used to make the problem numerically feasible [109]. This is the basic premise of the fully kinetic, particle-in-cell (PIC) modeling undertaken, for example, by Gildea *et al* [106, 107] to simulate DCFT operation and though it has advantages in being able to reproduce 2-dimensional plasma phenomena with reasonable confidence, it is hindered by long computational run-times which even then are only made possible by some tinkering with physics, such as increasing the free space permittivity and reducing the mass of the ions.

Analytical approaches to the modeling of plasmas rely on statistical methods to describe the macroscopic properties of the system. In kinetic theory, each particle species is represented by a distribution function which gives the relative number of particles which exist in a differential volume of phase space, that is, within an infinitesimal range of velocities and position. The dependence of the distribution function on velocity, position and time is approximated by the Boltzmann equation, derived, for example, by Bittencourt [110], which accounts for interactions between particles by assuming all intermediation is through binary collisions. In general, the collisional term of the Boltzmann equation is analytically intractable and a successive approximation must be made.

The relaxation model of Bhatnagar, Gross and Krook [111] may be used when binary collisions between particles of like masses dominate, as is the case for ions in a weakly ionized gas, which models interactions as a smoothing towards an equilibrium

distribution over a relaxation time scale. The assumption that particle interactions are mediated by binary collisions is reasonable for weakly ionized plasmas where charged particles collide more frequently with neutral particles than each other, but breaks down when Coulombic interactions become important. The Fokker-Planck equation can be used to approximate the collisional term of the Boltzmann equation as the sum of a succession of many weak interactions, in order to more closely resolve the effects of Coulomb collisions.

By itself, the kinetic, or Boltzmann, equation is difficult to interpret intuitively and it is typically converted to macroscopic, averaged properties by integrating the equation times some order of velocity over the entire velocity space. The familiar fluid continuity equation is obtained when multiplying the kinetic equation by velocity to the zeroth power. Multiplying the kinetic equation by velocity to the first power yields the momentum conservation equation and by velocity to the second power yields the energy conservation equation. Integrating over the n^{th} power of velocity is commonly referred to as taking the n^{th} moment of the Boltzmann equation, with each moment resulting, in general, in a term (e.g. pressure in the momentum equation and heat flux in the energy equation) which can be solved for by taking the next moment. Rather than taking an infinite amount of moments an assumption is usually made about the pressure or heat flux term. A weakly ionized plasma with no directed motion, for example, can be approximated with an electron heat flux term in the form of Fourier's law of conduction, with the conduction coefficient dependent on electron temperature and electron-neutral collision frequency [110].

This process of taking averages over the distribution function, demonstrated in the following section, and simplifying the collision term can be used to derive a fluid model for each species in the plasma, which describes the evolution of the average properties of the system in time and space. A fluid treatment of the plasma relies on the subdivision of the system into small fluid elements each containing a large number of particles which are described by their distribution averaged, macroscopic properties. This description is only well applied to situations in which the particles within a fluid element are confined spatially, so that they form a coherent set [31]. In

low density plasmas the mean free path for collisions is much larger than any useful fluid element size, but the Larmor radius of electrons is typically small allowing the reasonable use of fluid descriptions of motion perpendicular to a magnetic field.

A further simplification used to describe electrons in both kinetic and fluid modeling is the assumption of a Maxwellian distribution. It can be shown that a spatially homogeneous plasma, free from external forces, will always tend to an equilibrium, Maxwellian distribution, with like particle collisions promoting a Maxwellian distribution within each species, unlike particle collisions tending to equalize the properties of the two interacting species and inelastic collisions acting to create an equilibrium in the internal energy states of the plasma constituents [112]. The efficiency of each process is dependent on the masses of the colliding particles, their velocities and the frequency of collisions. Electrons tend to reach local equilibrium the fastest due to their low mass making them the most mobile species, while the equilibration of ion and electron properties is quite slow for a weakly ionized gas due to low collisionality and the large disparity in masses.

Several other analytical models are used to describe plasmas in certain conditions. The magnetohydrodynamic (MHD) model unifies fluid equations for ions and electrons by assuming that collisional momentum exchange only occurs by Coulomb collisions between the two and results in a set of single fluid equations where the charged particle current is carried by electrons and momentum is carried by the ions [31]. This simplification is justified for a fully ionized plasma, which thruster plasmas are generally far from, and is quite useful for determining the stability of various configurations in this limit. The analysis of the guiding center motion of a charged particle in applied fields is also a useful analytical tool for describing the various drifts which occur in a plasma, but is somewhat tricky to apply self-consistently to an ensemble.

2.3.1 Derivation of Plasma Fluid Equations

As described above, the derivation of the fluid equations begins with the Boltzmann equation for species s,

$$\frac{\partial f_s}{\partial t} + \mathbf{w} \cdot \nabla f_s + \frac{\mathbf{F}_s}{m_s} \cdot \nabla_w f_s = \sum_r \mathbb{C}_{sr} \tag{2.13}$$

where f_s is the particle distribution function in phase-space, $\mathbf{w}$ is the particle velocity coordinate, ∇ is the spatial gradient, $\mathbf{F}_s$ is the external force on the particles, ∇_w is the velocity gradient, and $\mathbb{C}_{sr}$ is the collision integral for interactions of species s with species r [32]. The moment equations are obtained by integrating Eqn. 2.13 times some function ϕ over all velocities yielding,

$$\frac{\partial}{\partial t}(n_s \langle \phi \rangle_s) - n_s \left\langle \frac{\partial \phi}{\partial t} \right\rangle_s + \nabla \cdot (n_s \langle \phi \mathbf{w} \rangle_s) - n_s \langle \mathbf{w} \cdot \nabla \phi \rangle_s - n_s \left\langle \frac{\mathbf{F}_s}{m_s} \cdot \nabla_w \phi \right\rangle_s = \sum_r \Delta_{sr}[\phi] \tag{2.14}$$

where use is made of the notations,

$$n_s \equiv \int f_s d\mathbf{w} \tag{2.15}$$

$$\langle g(\mathbf{x}, \mathbf{w}, t) \rangle_s \equiv \frac{1}{n_s} \int g f_s d\mathbf{w} \tag{2.16}$$

$$\Delta_{sr}[g] \equiv \int g \mathbb{C} d\mathbf{w} \tag{2.17}$$

which define the number density of species s, n_s, as well as the ensemble average of function g over species s, where the integrals are over all velocity space. The final term in Eqn. 2.13 is simplified in Eqn. 2.14 by the assumption that the product of the distribution function and the force or the velocity (to any power) go to zero at infinity.

The species continuity equation is obtained by setting ϕ=1, so that all derivatives go to zero, resulting in,

$$\frac{\partial n_s}{\partial t} + \nabla \cdot (n_s \mathbf{u}_s) = \sum_r \Delta_{sr}[1] \tag{2.18}$$

where $\mathbf{u}_s$ is the ensemble averaged velocity. The collision integral is left in its general form for the current derivation.

The s-momentum conservation eqution is obtained by setting $\phi = m_s \mathbf{w}$ and inserting the Lorentz force, $\mathbf{F}_s = q_s(\mathbf{E} + \mathbf{w} \times \mathbf{B})$, to yield,

$$\frac{\partial n_s m_s \mathbf{u}_s}{\partial t} + \nabla \cdot (n_s m_s \mathbf{u}_s \mathbf{u}_s) + \nabla \cdot \overrightarrow{\overrightarrow{P}}_s - n_s q_s(\mathbf{E} + \mathbf{u}_s \times \mathbf{B}) = \sum_{r \neq s} \Delta_{sr}[m\mathbf{w}] \tag{2.19}$$

where the pressure tensor is defined as $\overrightarrow{\overrightarrow{P}}_s \equiv n_s m_s \left\langle \mathbf{c}_s \mathbf{c}_s \right\rangle_s$ and the random velocity as $\mathbf{c}_s = \mathbf{w} - \mathbf{u}_s$. The spatial and time derivatives of ϕ are zero in this case since w is an independent variable.

The energy conservation equation is similarly found using $\phi = \frac{1}{2} m_s w^2$ with the result,

$$\frac{\partial}{\partial t}\left(\frac{1}{2} n_s m_s u_s^2 + \frac{3}{2} n_s T_s\right) + \nabla \cdot \left[n_s \mathbf{u}_s (\frac{1}{2} m_s u_s^2 + \frac{3}{2} T_s)\right] + \nabla \cdot \left[\mathbf{q}_s + \mathbf{u}_s \cdot \overrightarrow{\overrightarrow{P}}_s\right] - n_s q_s \mathbf{u}_s \cdot \mathbf{E} = \sum_{r \neq s} \Delta_{sr}[\frac{1}{2} m w^2] \tag{2.20}$$

where the temperature, T_s, is defined through $\frac{3}{2} T_s \equiv \left\langle \frac{1}{2} m_s c_s^2 \right\rangle_s$ and the heat flux vector, $\mathbf{q}_s \equiv \frac{n_s m_s}{2} \left\langle c_s^2 \mathbf{c}_s \right\rangle_s$, is introduced.

Evaluation of the collision terms, $\Delta[\phi]$, is a tricky business and the reader is referred to the book of Mitchner and Kruger for a detailed introduction [32]. Here we replace them with some common form elastic collision frequencies.

$$\Delta_{sn}[m\mathbf{w}] = \mu_{sn} n_s (\mathbf{u}_n - \mathbf{u}_s) \nu_{sn} \tag{2.21}$$

$$\Delta_{sn}[\frac{1}{2}mw^2] = \mu_{sn} n_s \left[\frac{m_n \mathbf{u}_n + m_s \mathbf{u}_s}{m_s + m_n} \cdot (\mathbf{u}_n - \mathbf{u}_s) + \frac{3}{m_s + m_n}(T_n - T_s) \right] \nu_{sn} \quad (2.22)$$

Equations 2.21 & 2.22 give examples of the forms taken by the collision operators, considering collisions between a charged particle s and neutral particle n where the frequency with which an s particle collides with the n particle background is ν_{sn}. The reduced mass, μ_{sn}, is defined as $\mu_{sn} \equiv m_s m_n/(m_s + m_n)$.

2.3.2 1-D Plasma Flow to a Wall

The behavior of a plasma near a wall is of importance both for probe theory and for the workings of any device which tries to contain a plasma. The critical feature of the interaction between the plasma and the wall is the formation of an electron repelling sheath which arises due to the much faster flow of the more mobile electrons towards the wall than the ion species, creating a layer of net positive charge adjacent to the boundary. The sheath shields the potential of the wall from the bulk plasma, with the non-neutral region extending a distance on the order of several Debye lengths from the wall.

This thin layer is generally much smaller than any collision mean free paths allowing a collisionless treatment. The electron momentum equation (in the limit where any possible magnetic field effects can be neglected) reduces to a balance of electron pressure gradient and electric field terms, resulting in the Boltzmann relation,

$$n_e(\phi) = n_{e_{sh}} e^{\frac{e(\phi - \phi_{sh})}{T_e}} \quad (2.23)$$

where the subscript sh refers to values at the sheath edge and the electron temperature gradient is neglected, being much smaller than the density gradient in all practical cases. Also implicit in this relation is the assumption of an isotropic pressure tensor so that its divergence component in the wall direction is $\partial P_{xx}/\partial x = \partial(nT)/\partial x$. A similar relation can be defined in the case of a more general pressure tensor.

All ions which enter the sheath are accelerated by the electron-repelling electric field and impact the wall. A stringent requirement on the energy of ions entering the sheath is found in solutions of the sheath problem known as the Bohm criterion, which simplifies when $T_e >> T_i$ to,

$$v_{i_{sh}} \geq \sqrt{\frac{T_e}{m_i}} \tag{2.24}$$

where the right-hand-side is recognizable as the isothermal ion sound speed, c_{si}. The ion energy requirement then translates to the necessity of a generally much larger layer, called the presheath, through which the cold ions are accelerated to the sound speed. The size of the presheath ranges from the mean free path for ion collisions to half the distance between the plasma-containing walls.

When the walls are insulating, the electron and ion fluxes to the wall are equal and the potential difference between the bulk plasma and the wall is set by the electron energy. The general derivation of this relation follows from the 1-D consideration of a plasma far from the wall with cold ions and Maxwellian electrons. Only electrons with enough energy to pass through the sheath can actually reach the wall, and this condition may be used as a limit of integration to find the one-sided flux of electrons which reach the wall from afar.

$$n_e u_{ez}|_z =< w_z >_e = \int_{-\infty}^{\infty}\int_{-\infty}^{\infty}\int_{\sqrt{\frac{-2e\phi(z)}{m_e}}}^{\infty} w_z f_\infty(w) dw_z dw_x dw_y \tag{2.25}$$

$$f_\infty(w) = n_\infty (\frac{m}{2\pi T})^{3/2} e^{\frac{-mw^2}{2T}} \tag{2.26}$$

This derivation procedure is started in Eqn. 2.25 in which z is taken as the wall direction, ϕ is the potential at point z where the flux is being evaluated (the potential at infinity is set to zero) and f_∞ is the distribution function for the electrons far from the wall. Inserting the Maxwellian distribution function, defined in Eqn. 2.26, for

the electrons in Eqn. 2.25 results in,

$$n_e u_{ez}|_z = n_{e\infty}\sqrt{\frac{T_e}{2\pi m_e}}e^{-\frac{e\phi(z)}{T_e}} \tag{2.27}$$

which is just the density at z found using the Boltzmann relation times one quarter of the mean thermal speed of electrons, $\overline{c}_e/4 = \sqrt{T_e/(2\pi m_e)}$. The potential at the sheath edge is necessarily $\phi(z_{sh}) = -T_e/2$ to satisfy the Bohm criterion. Assuming quasineutrality at the sheath edge, $n_i(z_{sh}) = n_e(z_{sh}) = n_{e\infty}e^{-1/2}$, the ion flux to the wall is simply,

$$n_i u_{iz}|_{z_{sh}} = n_{e\infty}e^{-1/2}\sqrt{\frac{T_e}{m_i}} \tag{2.28}$$

which when equated to the electron flux at the wall (with potential ϕ_w) to ensure the insulating boundary condition yields the potential at the wall with respect to the bulk plasma,

$$\frac{\phi_w}{T_e} = \frac{1}{2} + \ln\left(\sqrt{\frac{2\pi m_e}{m_i}}\right) \tag{2.29}$$

which includes the presheath drop of $T_e/2$. This analysis does not include the possibility of the emission of secondary electrons from the surface of the wall due to impact from either plasma species. Such an effect would result in a lessened potential drop from bulk plasma to wall since the net flux of negative charge carriers through the sheath is reduced. The flux of secondary electrons emitted from a wall divided by the flux of primary electrons incident on the wall is called the secondary electron yield (SEY) and is given the symbol Γ here. The SEY depends on the wall material and the energy of the incident electrons. Atomic impact (charged or not) can also result in secondary electron emission, but this is negligible for the materials and ion energies relevant to our device.

The ceramics generally used as wall material for cusped-field and SPT-type thrusters have high secondary electron emission yields for electron temperatures on the order

of tens of eV, which increase almost linearly with the energy of the incident electrons. If the incident electron population is at a high enough temperature the secondary electron yield can approach unity and the sheath potential needed to satisfy the insulating condition at the wall is greatly reduced from its normal, secondary-free value. The measured yield from a beam of test electrons has also been shown to significantly exceed unity at high energies, however for the case of a static electron-repelling plasma sheath this regime is never attained. Instead, a space charge saturated regime is entered where the build-up of negative charge near the wall limits the possible current of secondary electrons. This was first derived by Hobbs and Wesson to occur at a secondary yield of

$$\Gamma_{max} \cong 1 - 8.3\sqrt{\frac{m_e}{m_i}} \tag{2.30}$$

which for xenon is 0.9831, based on analysis considering cold ions, a Maxwellian population of plasma electrons and secondaries which are emitted from the wall with negligible energy [137]. Under the guidelines of the analysis of Hobbs and Wesson, the insulating wall condition can easily be re-derived from

$$n_{i_{sh}} v_{i_{sh}} = n_{e1} v_{e1}(1-\Gamma) = n_{e2} v_{e2} \frac{1-\Gamma}{\Gamma} \tag{2.31}$$

$$n_{e2} = n_{i_{sh}} v_{i_{sh}} \frac{\Gamma}{1-\Gamma} \sqrt{\frac{m_e}{2e(\phi - \phi_w)}} \tag{2.32}$$

$$n_{e1} = (n_{i_{sh}} - n_{e2_{sh}}) e^{e(\phi - \phi_{sh})/T_e} \tag{2.33}$$

$$\left[1 - \frac{\Gamma}{1-\Gamma}\sqrt{\frac{m_e T_{sh}}{m_i e(\phi_{sh} - \phi_w)}}\right] e^{-e(\phi_{sh}-\phi_w)/T_e} \sqrt{\frac{T_e}{2\pi m_e}} = \frac{1}{1-\Gamma}\sqrt{\frac{2T_{sh}}{m_i}} \tag{2.34}$$

where the subscript sh refers to values at the sheath edge, w refers to the wall, n_{e1} is the incident thermal electron density, n_{e2} is the local secondary electron density

and $T_{sh} = 1/2 m_i v_{i_{sh}}^2$ is the ion kinetic energy at the sheath edge. The derivation of the modified Bohm condition is also straightforward but is omitted here for brevity and given as

$$\frac{T_e}{2} \leq T_{sh}\left[1 - \frac{\Gamma}{1-\Gamma}\sqrt{\frac{m_e T_{sh}}{m_i e \Delta\phi_{sh}}}\right] - \frac{T_e}{2}\frac{\Gamma}{1-\Gamma}\sqrt{\frac{m_e}{m_i}}\left(\frac{T_{sh}}{e\Delta\phi_{sh}}\right)^{3/2} \tag{2.35}$$

where $\Delta\phi_{sh} = \phi_{sh} - \phi_w$. Several fits exist for Γ as a function of temperature, which allow equations 2.34 & 2.35 to be solved for T_{sh} and $\Delta\phi_{sh}$. The ions are found to enter the sheath at the normal Bohm condition, $T_{sh} = T_e/2$, when the secondary yield is small, with a small increase in the entrance speed required at higher yields, reaching $T_{sh} = 1.15(T_e/2)$ at the space charge saturation condition, regardless of the fit used.

The above analysis shows $n_{e1_{sh}} c_s / n_{i_{sh}} v_{i_{sh}} \approx 1$, since the secondary electron density is almost negligibly small, even in the space charge saturated limit, where $n_{e2_{sh}} = 0.0825 n_{i_{sh}}$, and the ions enter the sheath very near the Bohm velocity. Substituting the Bohm criterion in for T_{sh} in Eqn. 2.34 one obtains,

$$\frac{e(\phi_{sh} - \phi_w)}{T_e} \approx \ln\left[(1-\Gamma)\sqrt{\frac{m_i}{2\pi m e}}\left\{1 - \frac{\Gamma}{1-\Gamma}\sqrt{\frac{m_e T_e}{2 m_i e(\phi_{sh} - \phi_w)}}\right\}\right] \tag{2.36}$$

where the braced term within the logarithm is very near unity (within 12% based on the condition of Eqn. 2.30).

In order to properly capture the effects of secondary electron emission (SEE) on the cooling of the plasma a reliable model of the SEE yield for the material under investigation is required. Unfortunately, there is not much data on the SEE of ceramics at low electron energies due to difficulties in extricating the yield from the effects of surface charging. It seems that a large part of the Hall thruster literature relies on either a fit to Russian data presented by Fife *et al* [157] (and later represented slightly differently by Choueiri [57]) or on data collected by Viel-Inguimbert [55] but

reproduced in the more oft cited work of Bugeat [58], Jolivet & Roussel [59] or Gascon *et al* [4]. A more recent experiment by Dunaevsky *et al* [60] claims lower uncertainties than previous work, and perhaps most importantly, uses the same grade of Boron Nitride (HP grade) from the same manufacturer (Saint-Gobain) as is used on the DCFT.

The Russian data for BN is modeled by Fife as following a simple power law ($\Gamma_{BN} = 0.141 E_p^{0.576}$) based on the energy of the electron beam, E_p, and then integrated over a Maxwellian distribution of primary electrons (with temperature T_p) to yield an effective emission of $\Gamma_{BN} = 0.198 T_p^{0.576}$. For this fit the crossover energy (where the yield becomes unity) is 30 eV (or for a Maxwellian a temperature of 16.64 eV), compared to early, high energy experiments by Dawson which indicate a crossover at 50 eV [56]. Viel-Inguimbert obtained secondary yields for quite a few ceramics, including BN, $BNSiO_2$, Al_2O_3 and SiC, with beam electron energies as low as 20 eV. Data were also obtained at an increased sample temperature and at different incidence angles, with both cases showing little effect on the yield at low (<100 eV) incident energies. Power law fits to the data of Viel-Inguimbert are given by Goebel & Katz ([81] pg. 349) for several of the materials mentioned, including $\Gamma = 0.207 T_p^{0.549}$ for BN, with several linear fits given by Barral *et al* [61], who present $\Gamma = .45 + .55(E_p/53)$ for BN-SiO_2. The data of Dunaevsky *et al* are also well fit by linear regression, yielding $\Gamma = .54 + .46(E_p/40)$ for BN, compared to a linear fit of the Viel-Inguimbert data for BN, $\Gamma = .59 + .41(E_p/30)$.

The energy distribution of the electrons leaving the wall may be fairly complex, due to backscattering of the incident electrons, either elastic or inelastic, leading to a spread of energies up to that of the incident particle. In the measurements of SEE yield cited above, the flux of 'true' secondaries (electrons actually emitted from the material) is lumped in with the flux of backscattered electrons, so that the energy composition of the quoted SEY is left fairly ambiguous. At low incident energies, especially, backscattering is expected to contribute a substantial portion to the emitted energy spectrum.

2.3.3 Cross-Field Diffusion

The precise nature of the electron flow across field lines is one of the least well understood topics in plasma physics. A great deal of literature is dedicated to investigating cross-field transport, but here we briefly summarize some of the most applicable aspects. The ambipolar diffusion of a plasma across a magnetic field can be straightforwardly modeled with electron collisions with unlike particles allowing their displacement from one field line to the next, yielding a diffusion coefficient which is roughly proportional to $1/B^2$ [113]. Unfortunately, most experiments find the plasma diffuses across the field at a much higher rate [119]. Bohm famously suggested that the anomalously large diffusion was due to plasma oscillations and that the static balance between perturbation growth and damping by cross field diffusion came at a diffusion coefficient of roughly,

$$D_\perp \approx \frac{kT_e}{16eB} \tag{2.37}$$

a relation which is based on an unpublished theory [113]. An interesting anecdote is related in Chen's book [114] in which plasma physics luminary Lyman Spitzer is said to have tracked down David Bohm in Brazil, many years after Bohm's seminal paper describing anomalous diffusion, to ask him the origin of the 1/16 factor in his proposed diffusion coefficient, only to learn that the famous quantum physicist had entirely forgotten. In his paper, Bohm notes, however, that the factor should depend on the experimental conditions which determine the amplitude of oscillations, and claims an uncertainty of a factor of 2 or 3.

Spitzer himself derives a Bohm-type diffusion coefficient based on electric field fluctuations normal to the magnetic field, seemingly under the assumption of ergodicity, finding $D_\perp$ equal to twice the ensemble average of the squared electric field fluctuation amplitude over the squared magnetic field strength multiplied by the correlation time of the perturbations [115]. Spitzer suggests the r.m.s. value of electric field fluctuations is proportional to the temperature of whichever species drives the oscillation over the Larmor radius and that the correlation time is inversely propor-

tional to the gyrofrequency. Yoshikawa and Rose derive a diffusion coefficient based on density fluctuations in the Hall current direction which approaches the classical one when the Hall parameter, $\Omega = \omega_{ce}/\nu_e$, and the oscillation amplitude are both low, but has a Bohm-like form, with a coefficient of $\pi/4$ times the average square deviation of the density, when the mean squared oscillation amplitude times the Hall parameter is much greater than unity [116]. Some notable early reviews of the topic of anomalous transport are given by Hoh [118] and Boeschoten [119].

The first measurements of anomalous diffusion in a Hall thruster type device may be attributable to Janes and Lowder [117]. The ion current crossing an axial plane is measured and subtracted from the total discharge current to find the cross-field electron flux, which is too high to be explained by the classical collision-based diffusion. Bohm diffusion is called upon to explain the discrepancy, with a factor ranging from 1/3 to 1/10 instead of Bohm's 1/16 being measured. The reported 1/3 through 1/10 coefficients are actually just the ratios of axial to azimuthal electron current measured along the discharge chamber, which are classically equivalent to the inverse Hall parameter for a crossed axial electric field and radial magnetic field. These 'effective' inverse Hall parameters being measured are much lower than expected from the calculated cyclotron and heavy particle collision frequencies.

Langmuir probe measurements at different azimuthal positions revealed a rotating spoke perturbation in the ion density, rotating at around 20% of the electron Hall current drift speed. A correlated plasma potential fluctuation was similarly measured and a simple calculation performed which showed the product of density and electric field oscillations could be integrated azimuthally to yield values of the axial to Hall electron current ratio close to those measured. The theory of Yoshikawa and Rose was also demonstrated to predict values in close agreement with the experiment.

A more modern set of measurements, described in a paper by Meezan et al [120], use both optical and electrostatic diagnostics to examine the evolution of electron cross-field mobility in a Hall thruster. The effective inverse Hall parameter is shown to range from around 1/3 to 1/270 for discharge voltages between 100 and 200 V. A minimum exists in the electron mobility near the location of the peak magnetic

field (coincident with the Hall current peak) which approaches the classical limit, except at a discharge voltage of 100 V. The 100 V case is shown to strongly match the anomalous diffusion coefficient predicted by the theory of Yoshikawa and Rose based on measurements of the ion density fluctuations in the discharge chamber. The uncertainty in the inverse Hall parameter profiles are noted to be quite large, however, making the measurements far from conclusive.

Several others have performed similar measurements of the ratio of azimuthal to axial electron current [30, 121, 122] with varying results, though all maintain the existence of a peak effective Hall parameter near the peak magnetic field, though the precise location depends on such parameters as discharge voltage [120, 30] and propellant mass flow rate [122]. Indeed, the peak effective Hall parameter appears to coincide mainly with the location of the maximum axial electric field (generally coincident with maximum Hall current) which moves downstream with increasing propellant flow rate or decreasing anode voltage. Of the various measurements, none yield an electron mobility profile that can be fit by one theory, be it anomalous diffusion, classical collisional or wall collision based.

It was noted in the late 1960's by Morozov that the enhanced cross field diffusion could be due to electron collisions with the channel walls in a manner similar to collisions with heavy particles, since the inter-wall distance is generally much shorter than the electron-neutral mean free path. Morozov and Savelev later expanded on this theory of near-wall conductivity [25, 123] using the Vlasov equation and assuming a wall sheath thickness much less than an electron Larmor radius. The model is derived in slab geometry with the magnetic field running perpendicularly between two channel walls and the electric field running parallel (i.e. axially). A Maxwellian distribution of secondary electrons are emitted from the wall (results are also shown for a 'flat-top' distribution) at some temperature and accelerated solely by the sheath into the plasma bulk. The resulting equation describes the axial electron current oscillating about zero current along the magnetic field pointing direction. When the contribution of secondary electron current from one wall is integrated from the wall to infinitely far away the axial current density is found to equal the incident electron current to

the wall times the secondary electron yield, Γ, multiplied by the Hall drift speed over the electron cyclotron frequency ($i_{ez} = \Gamma j_{ew} E/(\omega_{ce} B)$) [25]. The authors also cite previous experimental work which found qualitatively similar spatial oscillations in axial electron current transverse to the wall to corroborate this theory, with the experiments, however, showing most of the current concentrated near the outer wall.

Several authors have expanded upon the theory of Morozov to include such effects as magnetic mirroring [124], cylindrical geometry [125] and a theorized oscillating sheath [126]. Recent experiments have demonstrated a dependence of the anode current on the wall material which is typically hypothesized to be due to the change in secondary electron yield properties [170, 127], though a full accounting for anode current from near-wall conductivity has yet to be shown. Various authors find the current contribution from near-wall conductivity to be an order of magnitude too low to explain the observed discharge currents [122, 129]. Alternative descriptions of cross field transport in Hall thrusters have been proposed, based on specialized experimentation [128] and 3-D PIC modeling [130], for example.

The cross field transport problem is certainly not cut and dried and a thorough examination of the extensive literature is outside the practical scope of the present investigation. In many models the cross field transport enters as a sort of fitting parameter, as in the 1-D Hall thruster model which is re-derived in Sec.5.1, with a scaling with B^{-1} delineating anomalous from classical or near-wall conductivity based transport, which scale with B^{-2}. An important aspect of the transport problem, also discussed in a later section, is the finding in toroidal fusion devices of a mechanism for the reduction of turbulence-induced transport, used to explain a change in plasma confinement from low to high (L to H) modes [14].

Chapter 3

External Dynamics of the DCFT

3.1 Hollow-Cone Plumes in Cusped Field Thrusters

Among the various cusped-field devices, the Thales HEMP-thruster [9], Princeton's permanent magnet CHT [22] and the Diverging Cusped Field Thruster (DCFT) being investigated in different forms at MIT [16] and Stanford [5], there has been the collective observance of a nearly hollow, conical plume structure, where the ion beam is largely focused into a shell which is peaked on the order of 30° to 50° from the thruster axis-of-symmetry (though this is no longer the case in more recent versions of the HEMP-T [90] and permanent magnet CHT [97]). The ions within this shell have been measured by many to be accelerated by nearly the entire applied potential, while in several cases, retarding potential analyzers (RPA's) revealed the ion fluxes nearer to the centerline to be of a generally lower energy composition [88, 22, 18].

A conventional Hall thruster plume, in comparison, is peaked within a few degrees of the thruster axis and decays roughly exponentially at higher angles. In a simplified sense, the magnetic flux lines in a Hall thruster can be considered to very roughly coincide with lines of equipotential, with some defocussing due to electron pressure and wall interaction, as presented in a review of Hall thruster physics by Morozov and Savelev [25]. Under these premises it is clearly advantageous to shape the flux lines near the ionization/acceleration region of the channel in a manner which can focus the ion beam towards the centerline [26, 27].

The near equivalence of magnetic field lines with equipotentials is based on the oft-cited concept of thermalized potential. Electrons are extremely mobile along field lines, but are highly restricted in their motion across field lines, leading to the effective shielding of potential differences parallel to the field but not perpendicular. This concept can be put on mathematical footing using the parallel component of the electron momentum equation, given in Eqn. 3.1, neglecting electron inertial and collisional terms in comparison to the electric field and pressure gradient. Equation 3.1 is straightforwardly manipulated to find Eqn. 3.2 in the electroquasistatic case. The electron temperature gradient is neglected compared to the density gradient to find Eqn. 3.3, which shows the potential as a function of its position along the field line, ξ, is the sum of the potential at some reference location along the line and a term which depends mildly on the local plasma density as a fraction of the density at the reference point. Unless the electron temperature is significant compared to ϕ_0, or the electron density gradients along the field line are very large, the plasma potential is roughly constant, according to this analysis.

$$0 = en_e E_{||} + \nabla_{||}(n_e T_e) \tag{3.1}$$

$$d\phi = \frac{d(n_e T_e)}{en_e} \tag{3.2}$$

$$\phi(\xi) = \phi_0 + \frac{T_e}{e} \ln \frac{n_e(\xi)}{n_{e0}} \tag{3.3}$$

The magnetic field topology of the DCFT, shown in Fig. 3-5, differs quite distinctly from that in a conventional Hall thruster and initially it was unclear where the main region of ionization or acceleration would occur. Emissive probe measurements in the near-field of a cylindrical variant of the DCFT performed by Young *et al* [5] showed a drop in the plasma potential downstream of the exit accounting for a significant portion of the applied voltage. Similar measurements were then made on the DCFT at MIT which also suggested the majority of the potential drop sits near the exit and a hypothesis for the role of the magnetic topology in anchoring acceleration

to this region was discussed [8].

The crux of the argument is that electrons are expected to have a difficult time crossing the strong magnetic field at the exit to gain access to the internal discharge chamber, but once inside they are already on a field line which connects directly to the next upstream separatrix. The high local impedance to axial electron motion then allows an electric field to form across the field lines leading from cathode to the exit separatrix. An additional effect which may help tie the electric field to the separatrix is its possible role as a turbulent transport barrier due to the likely shear of azimuthal electron flow there, with azimuthal shear being strongly linked to the reduction of turbulence-induced electron transport [188]. Azimuthal shear may be expected at a normal ring cusp since the funneling of electrons creates electric field and pressure gradient forces which point away from the separatrix, causing a change in direction of the azimuthal electron drifts about this line.

A slightly different explanation was forwarded in an earlier paper by Kornfeld *et al* to account for the observed peak in electric field at the exit of the HEMP Thruster [9], where the low neutral density and peak mirror ratio at the exit ring cusp were given as the main impediments to axial electron flow. Whatever the mechanism for cross field electron transport, it seemed clear to us that the commencement of the large potential drop should lie close to the ultimate separatrix, upstream of which electrons are relatively free to flow axially until perhaps being mirrored further on by the internal point cusp. Indeed this has been borne out by recent laser induced fluorescence (LIF) measurements of the ion velocity in the near-exit region of the DCFT by MacDonald *et al* [6], which show a rather pronounced localization of ion acceleration around the final separating flux line. It is the focus of the experiment described below to attempt to lower the divergence of the ion plume in the DCFT by making the downstream separatrix less convex (in relation to the anode), and thus hopefully forcing a more axially pointing peak electric field.

Recent experiments at Princeton on a permanent magnet CHT (CHTpm) show that the halo shaped plume usually observed can be altered drastically using a ferromagnetic circuit to shield out the external magnetic field [97, 100]. The plume

becomes strongly peaked on axis, with a bell-curve type angular distribution of ion current similar to that found in annular Hall thrusters, when the magnetic shielding is in place and the propellant utilization more than doubles.

Further, measurements of the plasma potential using emissive probes [100] and ion velocity map using LIF [101] show that the magnetic shield results in a substantial upstream shift in the electric field despite the exit separatrix moving in the opposite direction. Hollow cone plume shapes were also obtained with a normal CHT (no permanent magnets) using an additional electromagnet, which encircles the thruster, in conjuction with a magnetic shield to gradually raise the magnetic field strength downstream of the thruster exit [100]. The authors conclude that a strong axial magnetic field external to the device is necessary to create a hollow cone-type plume, though the axial field strengths do not appear to differ by much for cases which yielded either hollow or filled plumes in the presented figures.

The magnetic shielding concept was adopted by researchers developing a miniature HEMP thruster who also found that the addition of a ferromagnetic housing around their device would result in a peak ion current density around 20° from the thrust axis which would otherwise be around 60° off-axis [102]. The HEMP 3050 DM9.1 is shown to have an on-axis peak in ion current density in the plume, as well as an apparent hump in the density profile between 10 and 20° [90], though the reason for the change from the normal hollow cone plume is not discussed explicitly in the literature.

A decrease in the external magnetic field strength was achieved on the DCFT using a magnetic steel encasement (or collar), but did not result in a filling-in of the hollow plume [8]. Instead, the angle of the peak ion current density was observed to move slightly away from the thruster axis and the global plasma potential in the plume was found to decrease by more than 10 V, though this second effect is at least partially due to a tripling of the keeper current needed to stabilize the shielded thruster. An obvious difference between the magnetic shielding attempted on the DCFT and that used on the CHTpm is that in the latter case the exit separatrix changes from being largely internal to the device, to being entirely external and in a region of relatively low magnetic field strength. The separatrix is barely affected at

all in the shielded DCFT experiment, remaining in a region of strong (>100 G) fields. The author has found it difficult to achieve a similar weakening of the separatrix in Maxwell simulations of the DCFT, unless the support structure of the device is redesigned.

It is suspected that the shielding concept works by effectively removing the importance of the exit cusp. When the ultimate downstream separatrix is placed in a region of weak magnetic fields outside the thruster, as occurs naturally in annular Hall thrusters [105], cathode-emitted electrons can stream across it with relative ease compared to the field lines they must cross in the strong internal field. With the exit separatrix no longer acting as an anchor for the potential structure, the electric field is free to move upstream to wherever the new main barrier to electron transport occurs in their march towards the anode. The description above is likely too strong an oversimplification of the myriad details which result in the potential and density distributions observed, but may be a convenient starting point for understanding the complex interplay of the plasma with the applied magnetic and electric fields.

3.2 Magnetic Field Topographies

The aim of this section is to lend some concrete examples to the varying field topographies discussed above, by simulating some simple magnetic circuits. The applied magnetic field is defined by two of Maxwell's equations, reproduced as Eqns. 3.4 and 3.5 in the magnetoquasistatic limit, where μ_0 is the vacuum permeability and J the current density. For magnetic circuits consisting only of permanent magnets and ferromagnetic pieces the J in Eqn. 3.5 is zero. The field can be described by the magnetic vector potential, $\mathbf{A}$, defined by $\mathbf{B} = \nabla \times \mathbf{A}$ and a gauge such as $\nabla \cdot \mathbf{A} = 0$. The flux function, $\psi = rA_\theta$, is often more convenient than the vector potential for systems with cylindrical symmetry.

$$\nabla \cdot \mathbf{B} = 0 \tag{3.4}$$

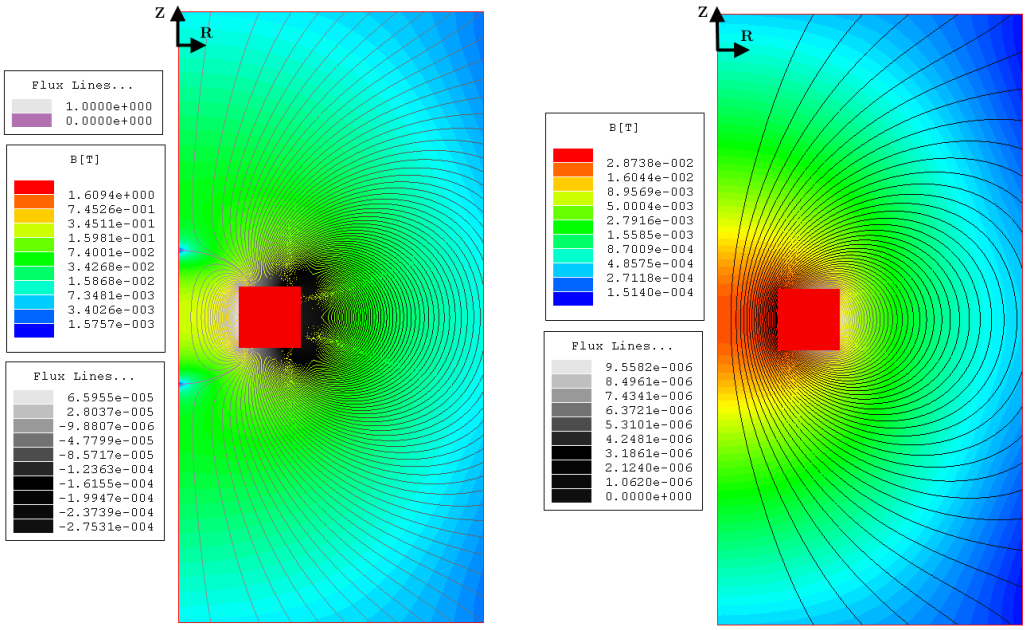

(a) (b)

Figure 3-1: Maxwell 2D simulations of (a) permanent ring magnet (b) electromagnet with 1000 A-turns, where the magnets are shown as solid red boxes

$$\nabla \times \mathbf{B} = \mu_0 \mathbf{J} \tag{3.5}$$

The magnetic fields created by an axially magnetized ring magnet and an electromagnet passing current through the same cross section are compared in Fig. 3-1, where both magnets have an inner radius of 2 cm, outer radius of 4 cm and length of 2 cm. The separatrices of the permanent magnet field are delineated by purple curves which emanate from the north and south poles of the magnet and separate the regions of positive ψ (in this case the region just inside of the magnet) from regions of negative ψ. The magnetic field strength goes to zero where the separatrices meet the axis of symmetry since the axial field component changes direction across this line and the radial field component must equal zero along the axis. The electromagnet creates a much different topography and does not exhibit any separatrices since ψ is positive everywhere.

Adding one or more ring magnets of alternate polarity to the circuit of Fig. 3-1a does little to the shape of the separatrices on either of the axial bounds of the new

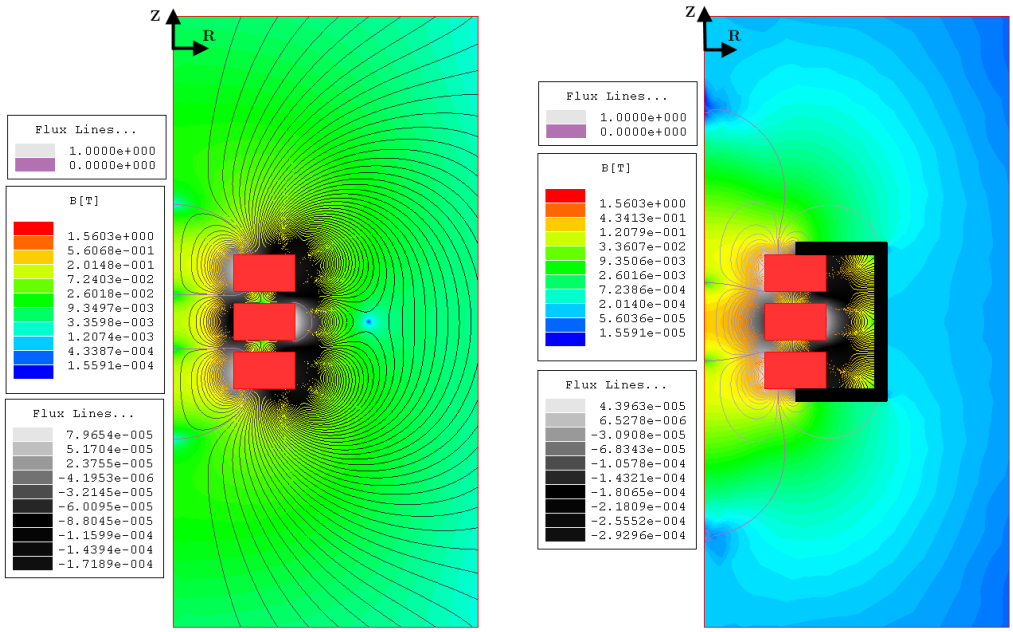

(a) (b)

Figure 3-2: Maxwell 2D simulations of 3 axially magnetized permanent ring magnets of alternating polarity (a) unshielded (b) shielded by c-shaped iron piece shown in black

circuit, as shown in Fig. 3-2a, but creates an additional internal separatrix for each added magnet. The internal separatrices denote the locations of new ring cusps. The field internal to the magnets in Fig. 3-2a is on the order of several kiloGauss leading to electron gyroradii on the order of 10 microns, while the ion gyroradii may be several millimeters. The external field strength is still several hundred Guass in Fig. 3-2a which leads to electrons being still strongly magnetized with sub-mm gyroradii. The stray field is reduced in Fig. 3-2b using a ferromagnetic shield, similar to what is used to enhance CHTpm performance [97], while the separatrices on either end are extended outwards to regions of lower field strength.

A magnetic circuit which is more resemblant of the DCFT is shown in Fig. 3-3a due to the inclusion of a base core used to enhance the magnetic mirror at the centrally mounted anode. Figure 3-3b demonstrates the use of an external electromagnet to make the separatrix furthest from the base nearly radial by opposing the field of the nearest permanent magnet and adding to the stray field. This separatrix could be flattened using a permanent ring magnet polarized opposite to the adjacent magnet,

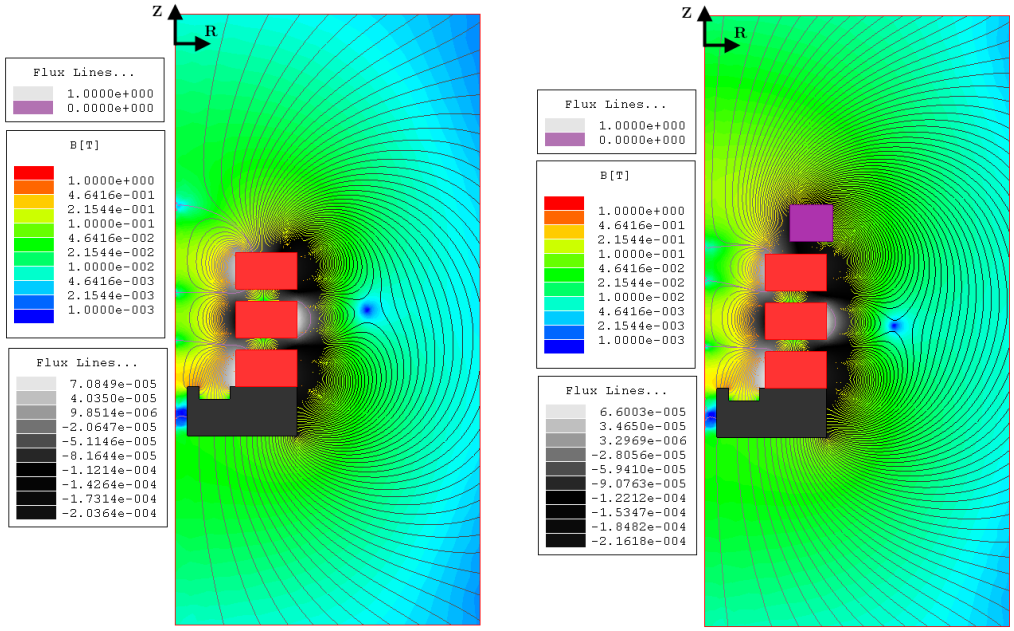

(a) (b)

Figure 3-3: Maxwell 2D simulations of (a) permanent ring magnet circuit (b) circuit containing one electromagnet with 5000 A-turn applied, where iron pieces are shown in black, permanent magnets in red and electromagnets in purple

but this would just lead to the creation of an extra separatrix outside of the new magnet. The electromagnet is able to alter the shape of this outer separatrix without adding a new one of its own, and may also do so in an actively adjustable way, making it an excellent experimental tool.

A potential circuit design is shown in Fig. 3-4a which does not rely on additional magnets to flatten the last separatrix, but instead passively does so by using a c-shaped core to shield the first two magnets and an internal ferromagnetic guide to funnel the field lines from the third magnet to a point where it can connect radially to the axis. Figure 3-4b demonstrates an implementation of the magnetic shielding concept on the circuit from Fig. 3-3a, though the shielding in this case is strong enough to entirely soak up the last separatrix.

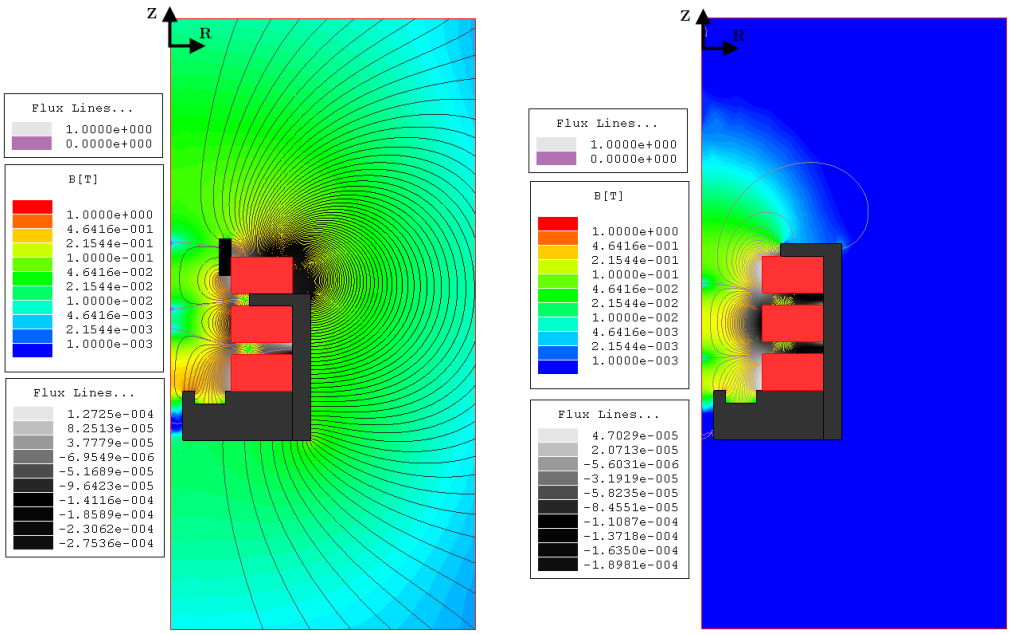

(a) (b)

Figure 3-4: Maxwell 2D simulations of permanent ring magnet circuits with (a) separatrix guide (b) magnetic shield, where iron pieces are shown in black and permanent magnets in red

3.3 Control of the DCFT Plume Structure

The experiments described below involve the use of an external electromagnet to reduce the average angle of the exit separatrix (with respect to the radial direction) by adding a magnetic field opposed to that of the most downstream permanent magnet. Electrostatic probes are used to measure changes in the ion current density, ion voltage distribution function and plasma potential structure in the plume as the strength of the external field is varied. The purpose of these experiments is to determine whether a flattening of the exit separatrix can lead to an axially pointed ion beam with a high energy content. The efficiency of the combined thruster/electromagnet system is not considered, as the intent is not to propose such a packaged device, but rather to suggest potential avenues for magnetic field topologies of new thruster designs.

3.3.1 Experimental Setup

Tests are performed using the original DCFT, constructed by Dan Courtney, the design of which is detailed in Courtney's Masters thesis [1]. The earliest DCFT testing, described in [1], used a stainless steel anode, however, excessive sputtering of the steel anode resulted in a switch to graphite as the anode material. All subsequent testing by Courtney, and all testing described in this thesis was performed with a graphite anode.

The thruster body is left electrically floating, while the anode and cathode keeper potentials are applied with respect to the common chamber and facility ground. The anode voltage is set by an Agilent N5772A Programmable Power Supply, while the keeper current is set by a Sorensen DCS 600-1.7. Flow control and measurement to the anode and cathode is provided by two Omega FMA-A2400 series mass flow controllers, allowing 0-10 mL/min flows calibrated for xenon. The cathode is generally run at a 0.5 A keeper current with 0.1 mg/s of xenon, however keeper currents of up to 1.3 A and cathode flows of up to 0.2 mg/s are sometimes required to ensure stable operation in LC mode.

All experiments were performed inside the MIT Space Propulsion Laboratory ASTROVAC vacuum chamber. The chamber is roughly 1.5 by 1.6 m with a pumping speed of about 7500 L/s on Argon obtained using two CTI-Cryogenics cryopumps (CT10 and OB400). Pressure in the chamber is monitored using an inverted magnetron gauge, and is seen to vary between pressures of around 20 to 50 μTorr at the flow rates of xenon used in the experiment described here. A Busek Inc. hollow cathode is used as an electron source to initiate the discharge and neutralize the resulting ion beam.

Probes are positioned within the chamber by a stack of two linear translation stages forming an X-Z system and a rotational stage driven by a set of stepper motors. The X stage positions the probes to a certain radial distance from the thruster centerline and has a total travel length of 30 inches. The 40 in-long Z stage controls the axial position of the probe with the face of the aluminum cap bolted to the

thruster exit taken as Z=0. The step resolution of both stages is 5μm.

The stages are controlled through LabView using a Velmex Inc. VXM motor controller. There is no encoder to provide positional telemetry, instead the commanded motion is assumed to have been carried out. Post-experiment positions were typically measured to be within a few mm of this assumption after many motions. Many of the experiments described here use the three stages to mimic a swinging boom with its pivot at a point on the intersection of the exit plane and the thruster axis of symmetry.

3.3.1.1 External Electromagnet

Equipped with the idea that the main ion acceleration is tied to the properties of the magnetic field near the exit, an experiment was devised in which the field would be altered in a variety of ways using an external electromagnet. Magnetostatic simulations, using Ansoft's 2D Maxwell Student Version, demonstrated that a reasonably sized electromagnet, placed flush with the exit cap of the thruster, could be used to turn the majority of the exit separatrix back towards the anode, or alternatively pull it further out of the thruster into regions of weaker magnetic fields.

The shape of the electromagnet was designed in Maxwell with the intent of minimizing plume impingement while maximizing impact on the field topology at moderate total currents. The final design was constructed using roughly 30 turns of enamel-coated copper coil around an 8 cm inner diameter support structure, of roughly 2 cm in length. The electromagnet is powered by an Agilent N5761A to not much in excess of 25 A in order to avoid overheating.

In what will be referred to as the positive polarity the magnet is able to provide a sufficient counter-field to bend the field lines near the thruster exit back towards the anode as shown in Fig. 3-5 where Maxwell is used to predict the flux line topology for different electromagnet (EM) input currents, I_{mag}, corresponding to a total of $\sim 30 I_{mag}$ amp-turns. The figure also shows that the electromagnet has little effect on the shape of the separatrix near the discharge chamber walls where the field is much higher than that the coil can produce. Measurements of the magnetic field in the

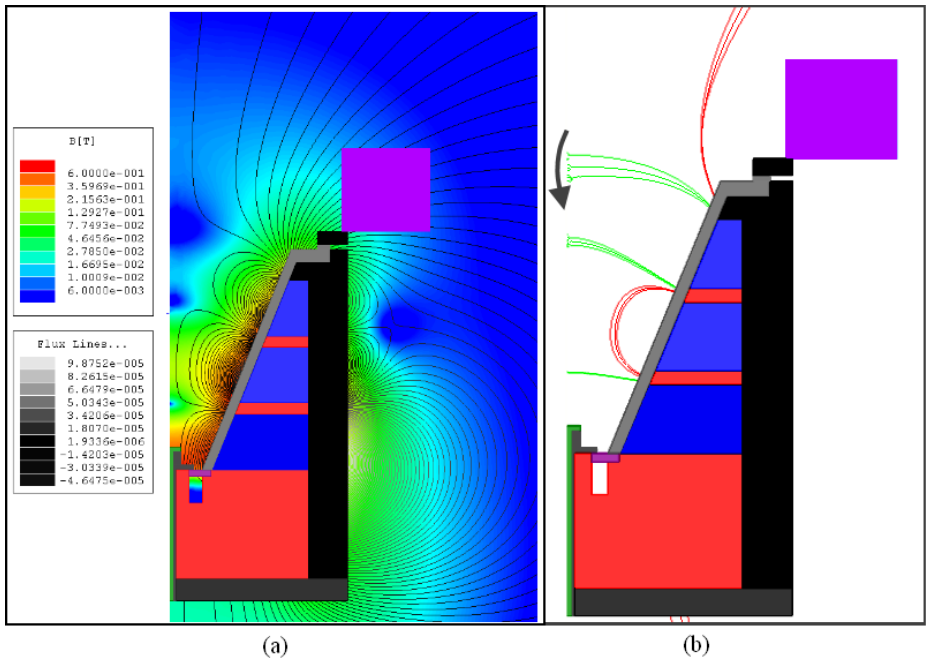

Figure 3-5: Ansoft Maxwell SV simulations of the DCFT outfitted with electromagnet (shown in purple). Field strength and flux lines are shown in (a) with 0 A to magnet and (b) with just flux lines highlighting the separatrices at various magnet currents in green. An arrow shows the direction the exit separatrix moves as the magnet current is increased from 0 A to 10 A then 20 A.

thruster at different coil currents have been performed with an AlphaLabs Inc. DC Gaussmeter and are shown in Appendix A along with separate Maxwell simulations for four of the main EM currents utilized.

Of course, the EM not only changes the shape of the separatrices, it significantly alters the strength of the magnetic field near the exit. A positive EM current strengthens the field downstream of the exit, while weakening the point cusp just upstream of the exit. A strong exit magnetic field has been hypothesized as the culprit for large beam divergence in a permanent magnet CHT [22], so the effects of the change in topology and change in field strength may be mixed in our experiment. The inner surface of the electromagnet is covered with Kapton tape to provide thermal and electrical insulation to the magnet support structure, and perhaps most importantly to prevent sputtering and redeposition of the conductive aluminum.

A two-axis stage is used to position the cathode during experiments. The nominal cathode position is about 7 cm radially from the thruster axis, and 3 cm downstream

of the exit. The electromagnet occludes the flux line which connects this nominal cathode location to the discharge chamber and so a different position is needed. The stages allow *in situ* adjustment of the cathode position which demonstrably affects the stability of the different regimes of thruster operation. In fact, much of the RPA data in LC mode are taken with the cathode very nearly on the edge of the main jet emanating at roughly 30°, as moving the cathode much closer to or much farther from the axis was found to result in a highly repeatable change into HC mode (as discussed further in Sec. 4.4.4).

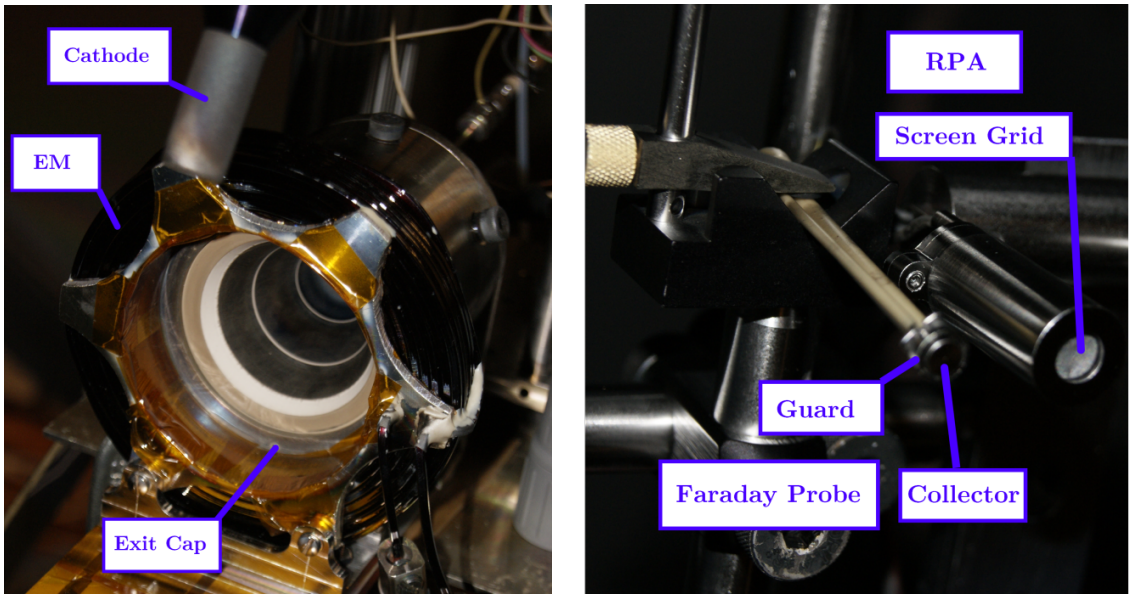

(a) (b)

Figure 3-6: (a) Picture of the DCFT with external EM in ASTROVAC with hollow cathode mounted on a 2-axis stage (b) Picture of the Faraday probe and Retarding Potential Analyzer used in the following study

A picture of the DCFT with external EM is shown in Fig. 3-6a where the hollow cathode and electromagnet are labeled along with the exit cap which serves as the exit plane from which our measurement coordinate system is referenced. The Faraday probe and RPA used in the following study are pictured in Fig. 3-6b. The thruster coordinate system is displayed in Fig. 3-7 which shows the Cartesian coordinates in blue and the polar coordinates in red.

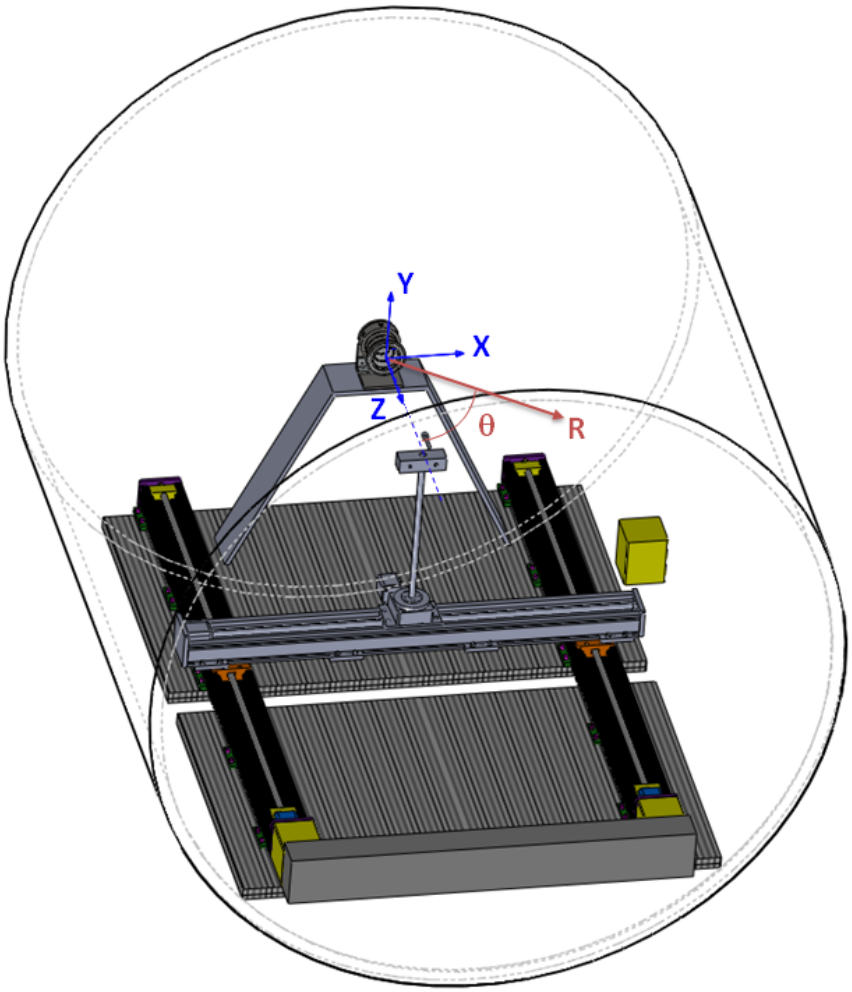

Figure 3-7: SolidWorks model of the thruster mounted in the vacuum chamber with a probe positioned by the 3-axis system. Probe measurement coordinates are shown with the origin at the intersection of the thruster axis (Z) and the plane containing the exit cap face

3.3.1.2 Faraday Probe

Faraday probes provide a simple and accurate means of measuring the ion current density in the plasma plume. A flat conducting plate is often used to collect the so-called ion saturation current when biased far enough below the local plasma potential. Electrons are almost all repelled when the conductor is several times the electron temperature below the floating potential, while ions free fall down the potential drop and are collected by the plate.

As the potential difference between plasma and conductor grows the size of the

plasma sheath grows as well. A bare conductor will collect all ions which intercept the sheath edge and so a large sheath can lead to a large, typically unknown, collection area. The Faraday probe concept circumvents this ambiguity by surrounding the collector with a conductive guard ring, which is biased to the same potential to ensure an essentially flat sheath in front of the collector, making 2D sheath effects relevant only to the guard ring.

The separation between the guard ring and the collector must be less than the minimum sheath thickness of the plasma being probed in order to maintain a continuous sheath across the pair. A simple 1-D consideration yields an estimate of the sheath thickness for a floating body in a xenon plasma of around 6-7 times the Debye length [23]. A lower bound for the Debye length in the far field DCFT plume of 105 μm is estimated using a fairly high plasma density (10^{16} m^{-3}) and a low electron temperature (2 eV), which would require a spacing of less than 0.7 mm between guard and collector. The probe used here has a 0.45 mm spacing which is expected to be sufficient over a broad spatial range, external to the thruster.

The maximum density external to the thruster can be estimated assuming a beam current of 0.3 A emanates from the thruster exit at roughly the ion sound speed. The radius at the channel exit is 28 mm and the sound speed at 10 eV is 2700 m/s, resulting in a rough ion density of 2.8×10^{17} m^{-3}. If the floating potential at the exit is 10 V above ground (it's usually well above this), then a probe biased 27 V below ground would be 95 V below the plasma potential, corresponding to a sheath thickness estimate of about 0.48 mm [23].

The Faraday probe used here, shown schematically in Fig. 3-8, collects current on a 4.5 mm diameter circular plate of 316 stainless steel. The design of this probe, as well as of the Retarding Potential Analyzer described in the following section, is detailed by Azziz [24]. The guard ring and collector are biased 27 V below ground using a series of 9 V batteries and the current to the collector is measured on the high side of the applied voltage through either a 2 kΩ resistor using a Fluke 77 IV handheld meter or with a Keithley 2410 High Voltage Source Meter.

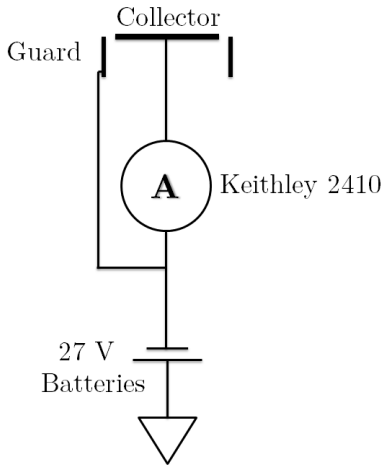

Figure 3-8: A schematic of the Faraday probe used in all studies, depicting electrical connections and associated electronics.

3.3.1.3 Retarding Potential Analyzer

Ideally, all ions in the thruster plume are accelerated over the full applied anode potential, with any deviation from this situation resulting in an inefficiency, characterized in the merit system outlined in Section 2.1.1 by the voltage efficiency. An estimate of this efficiency can be gleaned from the relatively simple use of a Retarding Potential Analyzer (RPA), which operates by separating plasma electrons from ions before passing the ions through a grid biased to selectively repel those below a certain energy per charge ratio (E/q).

The ion current which is energetic enough to pass through the retarding grid is collected on a conducting plate downstream. In the ideal case the full ion current (reduced by grid transparencies) which is intercepted by the RPA is collected on this downstream plate until the retarding potential is brought above the anode voltage at which point the current drops to zero.

A simple 1D analysis can be used to show that the first derivate of the collected current with respect to the applied ion retarding voltage is proportional to the ion energy per charge distribution function [23]. A smoothing spline is often fit to the raw current vs. retarding voltage curve before differentiation to avoid amplification of noise at low voltages.

A schematic of the RPA used here is given in Fig. 3-9, in which the three grids are denoted by number, and a full description of its design presented by Azziz [24]. Grid 1 is left floating, while grid 2 is biased to 27 V below ground using a string of 9 V batteries, in order to repel the majority of the electron population while allowing a large fraction of the ions to pass. Grid 3 is the ion retarding grid which is biased up to 325 V above ground using a Bertan 230S High Voltage Power Supply. A collector plate marks the downstream end of the RPA and is grounded through a Keithley 2410 Source Meter which also measures the current collected by this plate at different ion retarding potentials. The Keithley 2410 averages the current from 10 samples at each retarding voltage.

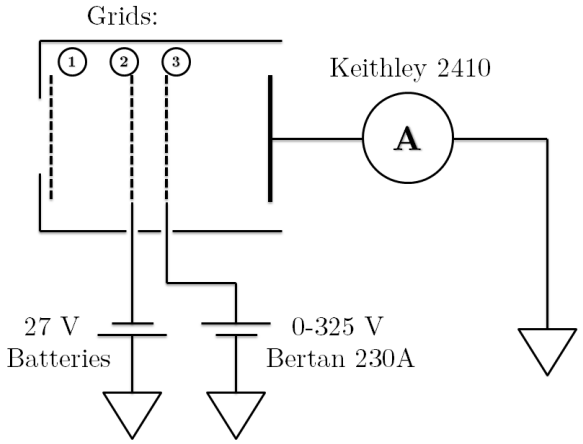

Figure 3-9: A schematic of the Retarding Potential Analyzer used in all studies, depicting electrical connections and associated electronics.

The grids are made of molybdenum with a 72% open area, consisting of 0.14-mm wide hexagonal openings. The openings must be smaller than plasma sheath to ensure the plasma cannot shield out the repelling potential. The estimates of sheath thickness described in the Faraday probe section may be readily applied here to see that the 0.14-mm opening width ought to be sufficiently small for the expected plasma conditions in the DCFT plume.

Letting the first grid float minimizes the impact of the RPA on the surrounding plasma and also reduces the plasma density incident on the electron repelling grid.

The electron repelling grid is spaced only 0.5 mm from the ion retarding grid in order to avoid space charge effects which can alter the probe characteristics [23].

The grids are separated by boron nitride spacers with the entire assembly encased in a 12.7 mm diameter tube made of 316 stainless steel with a 6.35 mm diameter aperture preceding the floating grid. The collector is 15.75 mm downstream of the aperture, resulting in a collimating effect which selectively repels ions with trajectories originating outside the probe's line of sight.

3.3.1.4 Emissive Probe

Emissive probes are electrostatic probes used to measure the local plasma potential based in some fashion on the increase in the apparent ion collection when a probe, heated to emit a thermionic electron current, is at a potential below that of the surrounding [131]. If the probe were above the plasma potential the emitted electrons would be recollected by the probe. Several methods exist for applying emissive probes to measure potential [132, 133] with a comparison of the main techniques given by Sheehan *et al* [134].

The present study makes use of the floating emissive probe technique, often used in studies of the internal potential maps in Hall thrusters [135, 136], due to its simplicity and minimal impact on thruster operation. This method involves the heating of an electrically floating, low work function wire, which is exposed to the plasma, until a thermionic electron current is emitted. As the emitted electron current increases the wire floats increasingly close to the local plasma potential. This effect eventually asymptotes as the emitted electrons create a space charge saturated sheath in front of the probe.

According to the 1-D theory of Hobbs and Wesson, an electron emitting, floating body can only come as close as $1.05T_e$ to the plasma potential before the sheath becomes space charge saturated [137]. Sheehan notes that an inclusion of the presheath potential drop puts the floating potential of planar surface with a space charge saturated sheath roughly $1.8T_e$ below the local plasma potential [134]. The emissive probe study described here only interrogates the plume region of the thruster which

is expected to be largely comprised of supersonic ions, likely not necessitating the formation of a presheath in order for probe impinging ions to meet the Bohm criterion.

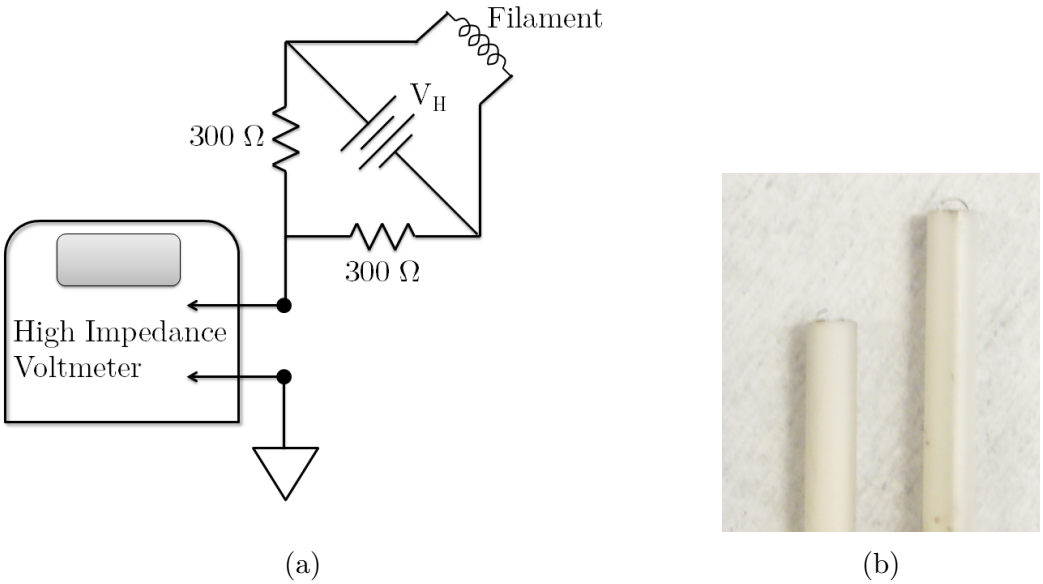

(a) (b)

Figure 3-10: (a) A schematic of the Emissive Probe used in the present study, depicting electrical connections and associated electronics (b) Picture of the tips of two emissive probes

The emissive probes used here are constructed from 0.125-in outer diameter, double bore alumina rods fit with stainless steel wire leads connected to 0.125-mm diameter 1% thoriated tungsten wire. The radius of curvature of the tungsten filament is roughly 1-mm on all probes, with example probe tips shown in Fig. 3-10b. The bored out alumina is covered in the front of the probe using a castable alumina putty. Connections of the steel leads to the tungsten filaments were made a variety of ways, the least effective of which was by pressure fitting the bores with extra tungsten. More reliable connections were made by either crimping the filaments to nickel leads which were then soldered to the stainless wire or by directly spot welding tungsten to steel.

The tungsten filament was heated to thermionic emission by an Agilent E3634A DC power supply, providing the V_H in Fig. 3-10a, capable of floating up to 240V. The floating potential of the probe is measured on a Fluke 77 IV multimeter. The

filament has a resistance at the heating supply of about 6 ohms and a heating current of around 2.4 A was typically found to result in the saturation of the floating potential of the probe.

3.3.2 EM Effects on Operation

A general trend manifested in early experiments is a decrease in the anode current as a positive (external field strengthening) EM current is increased. At high EM currents the anode current will either reach a minimum and begin to increase slowly or switch suddenly to a significantly higher current. These trends can be seen in Fig. 3-11, which shows the anode current versus EM current for a range of anode voltages at constant mass flow rates of 5 sccm of xenon on the anode and 1 sccm of xenon on the cathode, with a 1 A keeper current. The thruster is in LC mode for EM currents below 25 A.

Figure 3-11 also shows that the minimum anode current in the tested range of EM currents is reached at progressively lower EM currents as the anode voltage is increased. The way the EM current value corresponding to a minimum anode current changes with voltage is reminiscent of the optimization procedure in Hall thrusters, where the solenoid current is varied at each operational point until a minimum anode current is achieved. The value of EM current which minimizes the anode current at each anode voltage is given in Fig. 3-12a while the percent reduction in the nominal anode current is shown at each voltage in Fig. 3-12b.

3.3.3 Faraday Probe Results

An increased EM current is also seen to have a visible effect on the plume structure in LC mode, with a clear stratification of the previously solitary conical shell into nested shells. The inner shell of luminosity can be seen to emerge at gradually less divergent angles as the positive EM current is increased. This effect is just as stark in Faraday probe measurements, such as those displayed in Fig. 3-13 which shows the ion current versus angle of the probe with respect to the thruster axis at various EM

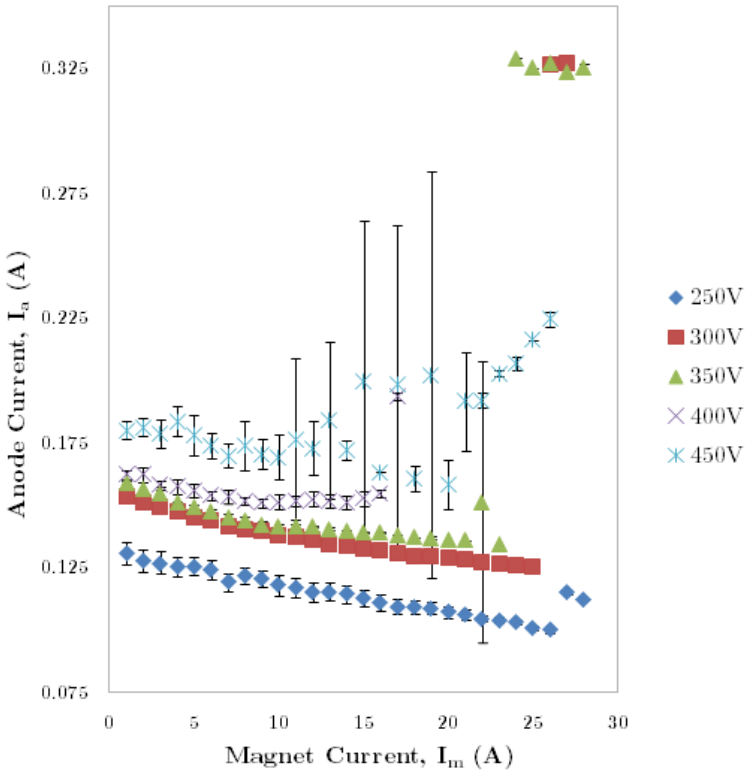

Figure 3-11: Anode current versus applied EM current at various values of the anode voltage for an anode mass flow rate of 0.49 mg/s, cathode flow rate of 0.098 mg/s and a keeper current of 1A.

currents with a constant anode voltage of 350 V and flow rate of 5 sccm of xenon. The DCFT is in LC mode, but with substantially higher anode currents than those at the same anode voltage and flow in Fig. 3-11 due to the higher cathode flow, keeper current and background pressure.

The ion current density peaks 30° from the thruster axis when the EM is unenergized, with an apparent hump around 38° as well. The peak moves inward to 25° when 20 A are applied to the EM, with a fairly constant change in peak location by 0.25°/A for EM currents in between. The hump which appears with no current on the EM becomes a resolved secondary peak, located at a 38-40° angle from the axis, when a positive EM current is applied. A small tertiary peak is also apparent with positive EM current located around 8° which is instead located on-axis when the electromagnet is unenergized.

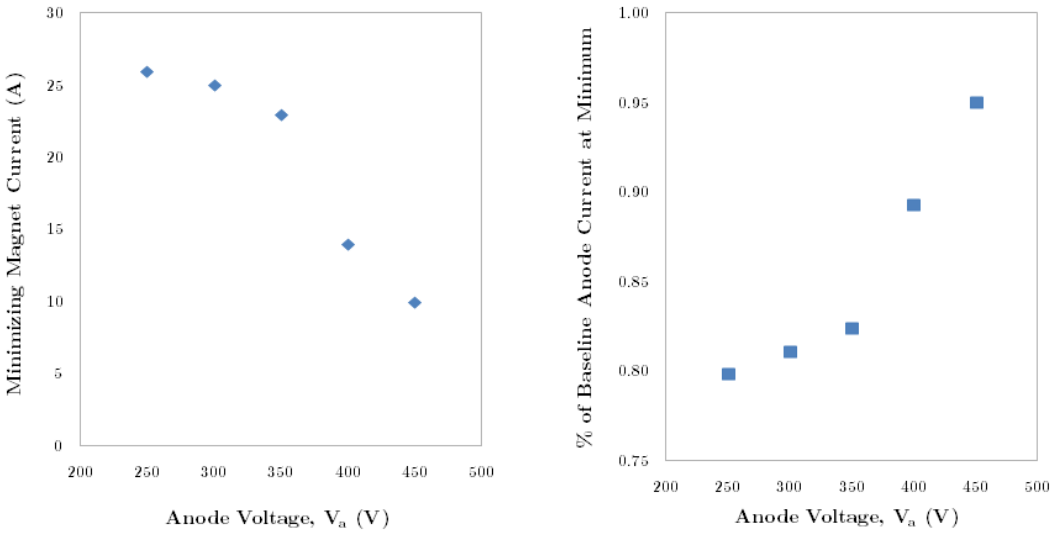

(a) (b)

Figure 3-12: Measurements showing the (a) EM current at which the anode current reaches its minimum and (b) the ratio of the minimum anode current to the anode current with no EM current as a function of anode voltage for an anode mass flow rate of 0.49 mg/s, cathode flow rate of 0.098 mg/s and a keeper current of 1A

An increase in EM current from 0 to 20 A leads to an 8% increase in ion current density at 0°, a 17% increase at 8°, and a 27% decrease at 38°. The ion current density remains relatively unchanged at all EM currents at angles between 40° and 46°, but is seen to decrease at angles >46° as the current is set to higher positive values.

The various efficiencies related to the ion beam can be estimated by integrating over the profiles displayed in Fig. 3-13 to estimate the beam current (through Eqn. 3.6) and momentum averaged $\cos\theta$ (through Eqn. 3.7), with the results compiled in Fig. 3-14. The beam and cosine-squared efficiencies, shown in Figs. 3-14a & 3-14b, increase with EM current as can generally be expected since both the anode current (increasing η_b) and the angle containing the peak ion current density (increasing $< \cos\theta >$) are decreased as the external field is strengthened and separatrix bent back towards the anode.

$$I_b = 2\pi R^2 \int_0^{\pi/2} J_i(\theta) \sin\theta d\theta \tag{3.6}$$

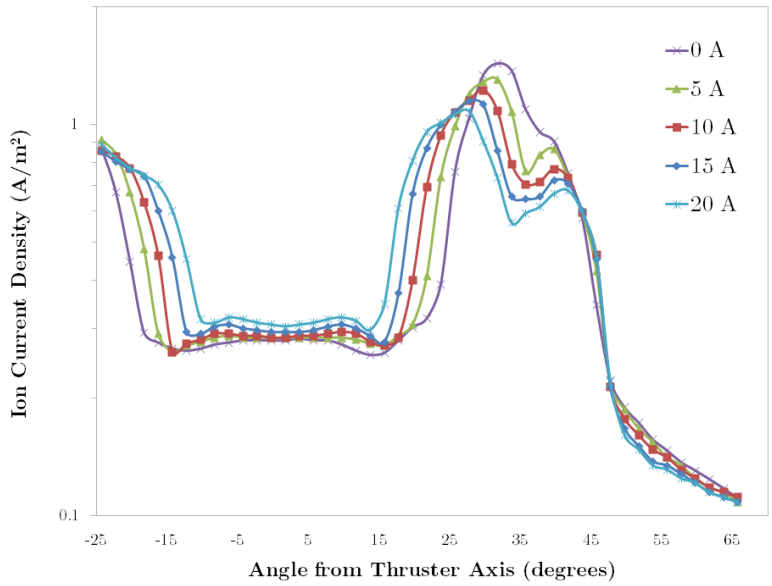

Figure 3-13: Faraday probe measurements of ion current density versus angle from thruster axis at R=38 cm at various applied EM currents. Thruster operating at 350 V and 0.49 mg/s on the anode with 0.2 mg/s on the cathode and a 1.365 A keeper current.

$$< cos\theta > \approx \frac{2\pi R^2}{I_b} \int_0^{\pi/2} J_i(\theta) \cos\theta \sin\theta d\theta = \frac{I_{bz}}{I_b} \tag{3.7}$$

Somewhat unexpectedly, the utilization efficiency, shown in Fig. 3-14c, decreases enough to offset gains from the other two efficiencies resulting in a net efficiency, shown in Fig. 3-14d which is actually somewhat lower (by about 1%) at 20 A of EM current than 0 A. It is not presently known exactly why the beam current is decreasing as the external magnetic field is strengthened. Perhaps a decrease in the electron current reaching the internal region of the device leads to a drop in ionization, or the collapse of the point cusp just upstream of exit separatrix causes a reduction in plasma confinement. The utilization efficiency is calculated using only the anode mass flow rate in the denominator, as opposed to the total flow through anode and cathode.

The uncertainty in these Faraday probe measurements is estimated as half of the resolution of the hand-held Fluke meter used to measure current (in this case 0.05 mV for a 0.1 mV resolution), which corresponds to 1.6 mA/m^2. The error bars in Figs.

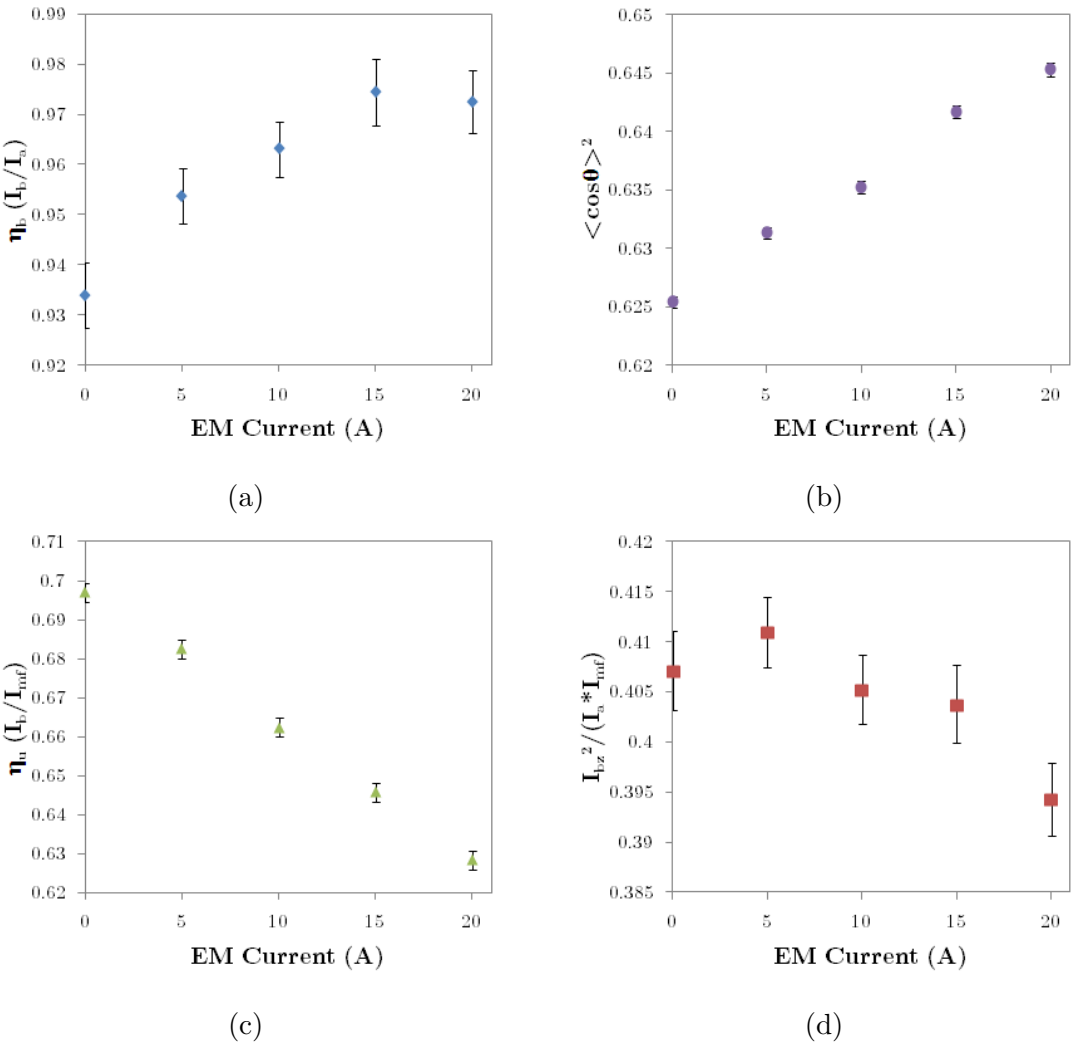

Figure 3-14: Integrated Faraday probe measurements of ion current density versus angle from thruster axis at R=38 cm at various applied EM currents to estimate (a) beam efficiency (b) cosine-squared efficiency (c) utilization efficiency (d) product of (a), (b) and (c). Thruster operating at 350 V and 0.49 mg/s on the anode with 0.2 mg/s on the cathode and a 1.365 A keeper current.

3-14(a)-(b) reflect the uncertainty of the Faraday probe data combined with standard deviation of the anode current during each angular sweep. For example, the upper bound on the beam efficiency is estimated by adding 1.1 mA to the beam current (1.6 mA/m^2 integrated from 0 to 66°) and dividing by the anode current depreciated by its own standard deviation. This is different from the standard method of uncertainty propagation through Taylor expansion, but is rather an estimate of a worst-case uncertainty and is considered to better reflect our confidence in the reduced data.

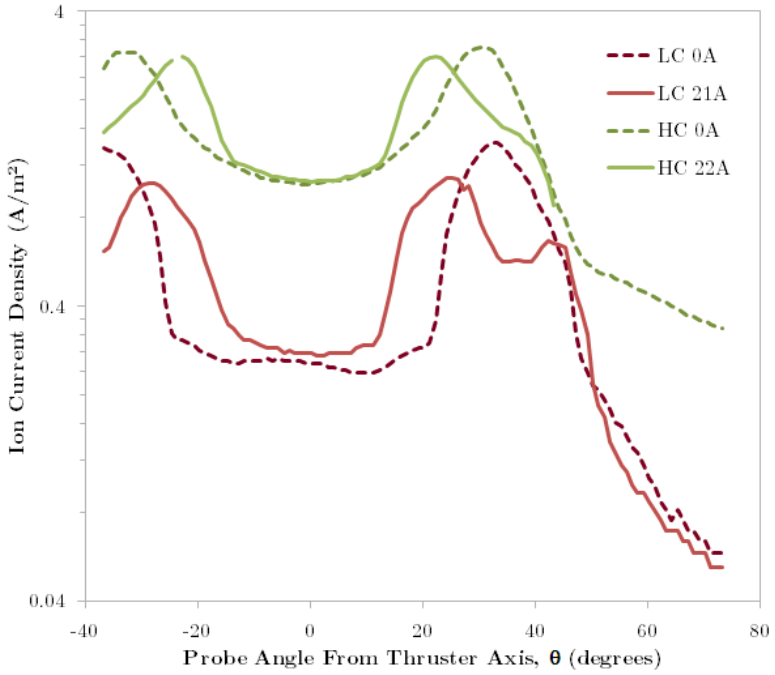

Figure 3-15: Faraday probe measured ion current density versus angle from thruster axis at R=38 cm shown for both LC and HC modes with either no EM current or a large EM current. DCFT operated at 300 V with 0.2 mg/s flow through the cathode. HC obtained with 0.69 mg/s on the anode and a 0.57 A keeper current. LC mode obtained with 0.59 mg/s on the anode and a 1 A keeper current.

A positive EM current is found to have the same effect, a turning of the main ion beam to lower divergence angles, in HC mode as well. A comparison of Faraday probe measurements in both modes, for both an unenergized EM and a high EM current, is given in Fig. 3-15. In HC mode, the peak ion current density is found at 22.5° at 22 A through the EM compared to 31° when the EM is unenergized. The anode current is choked off from 574 mA unenergized to 468 mA with 22 A on the electromagnet,

while a nearly identical anode current depreciation, from 243 mA to 208 mA for an EM current change from 0 A to 21 A, occurs in LC mode at the thruster conditions described in Fig. 3-15.

Measuring the angular dependence of the ion current density at a reasonably large distance from the origin (e.g. R=38 cm) can provide a snapshot of the fully developed plume (aside from the unwanted effects of vacuum chamber neutrals), but does not provide much information on how the plume evolves with distance from the thruster exit. Faraday probe measurements from at least three different radial distances from our measurement origin are necessary to trace the ion current peaks in the plume back upstream towards the exit of the thruster, and verify the linearity of the expansion.

Faraday probe measurements are shown at R=20, 25 and 30 cm for both positive and negative polarity EM currents as well as the unenergized state in Fig. 3-16. Lines fit through the two main ion current density peaks are overlaid on probe current contours in Fig. 3-16 and summarized in Table 3.1, in which the peak intercept refers to the radial location where the line intersects the exit plane. The R^2 value of all fits are greater than 0.9995, except for the inner peak at 0 A which is still well fit with R^2=0.996. A picture of the thruster firing with 20 A applied to the EM is shown in Fig. 3-16d with lines overlaid to highlight the splitting of the beam. The bright red spot, central to the picture, is the hollow cathode, which is mounted at 3 o'clock (looking at the anode from downstream) here, though it is at 12 o'clock during the Faraday probe measurements.

Table 3.1: Properties of linear fits to peak locations for Faraday probe measurements. DCFT operated in LC mode at 300 V with 0.49 mg/s on the anode, 0.15 mg/s flow through the cathode and a 1.25 A keeper current.

EM Current	-10 A	0 A	20 A
Anode Current (mA)	270	238	214
Inner Peak Intercept (mm)	-	34.4	17.0
Inner Peak Angle	-	23.0°	21.5°
Outer Peak Intercept (mm)	0	0	6.3
Outer Peak Angle	35°	35°	37.5°

Thruster efficiency metrics are calculated for the measurements of Fig. 3-16 using

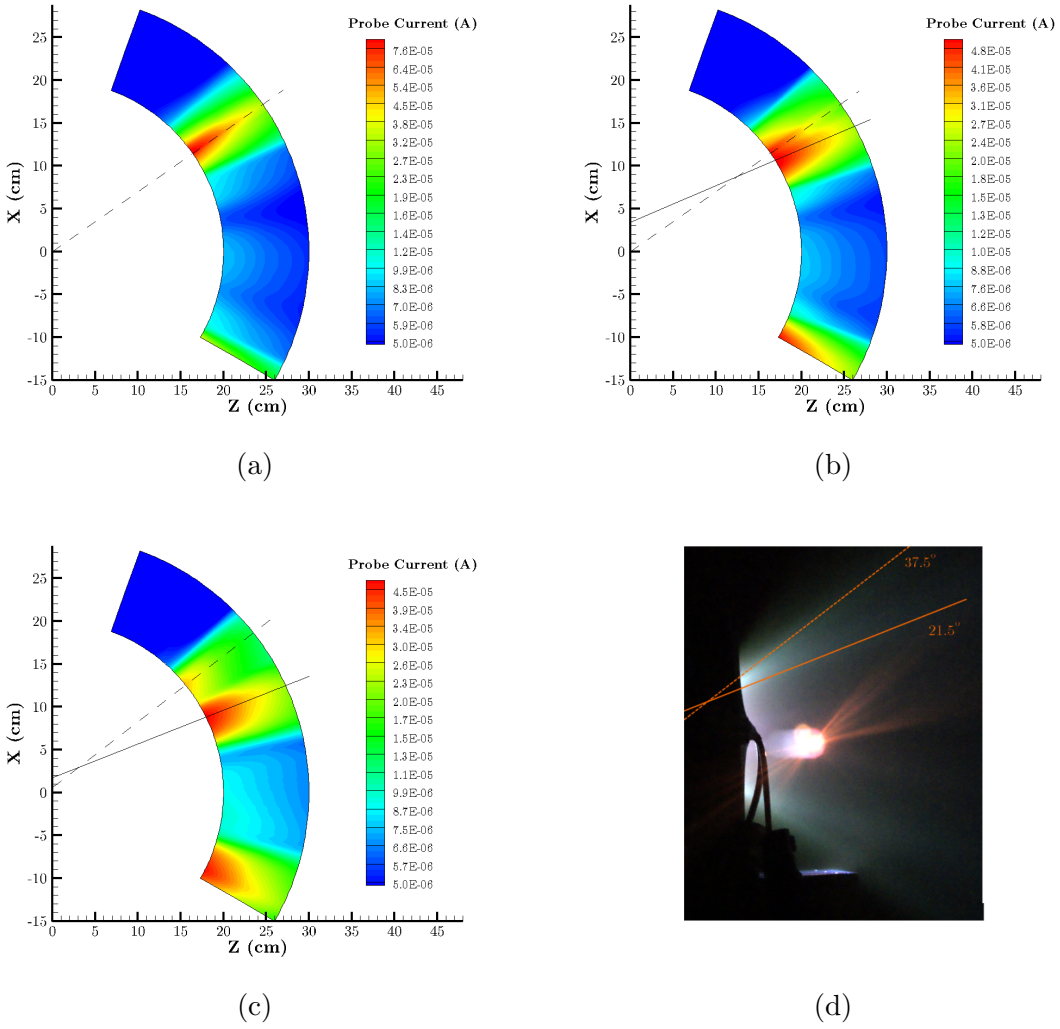

Figure 3-16: Faraday probe measurement contours with exponential scale at (a) -10 A (b) 0 A and (c) 20 A applied EM currents (d) picture of DCFT plume with 20 A EM current. Solid black line indicates linear fit to inner peak location, dashed line for outer peak. DCFT operating in LC mode at 300 V and 0.49 mg/s on the anode with 0.15 mg/s on the cathode and a 1.25 A keeper current.

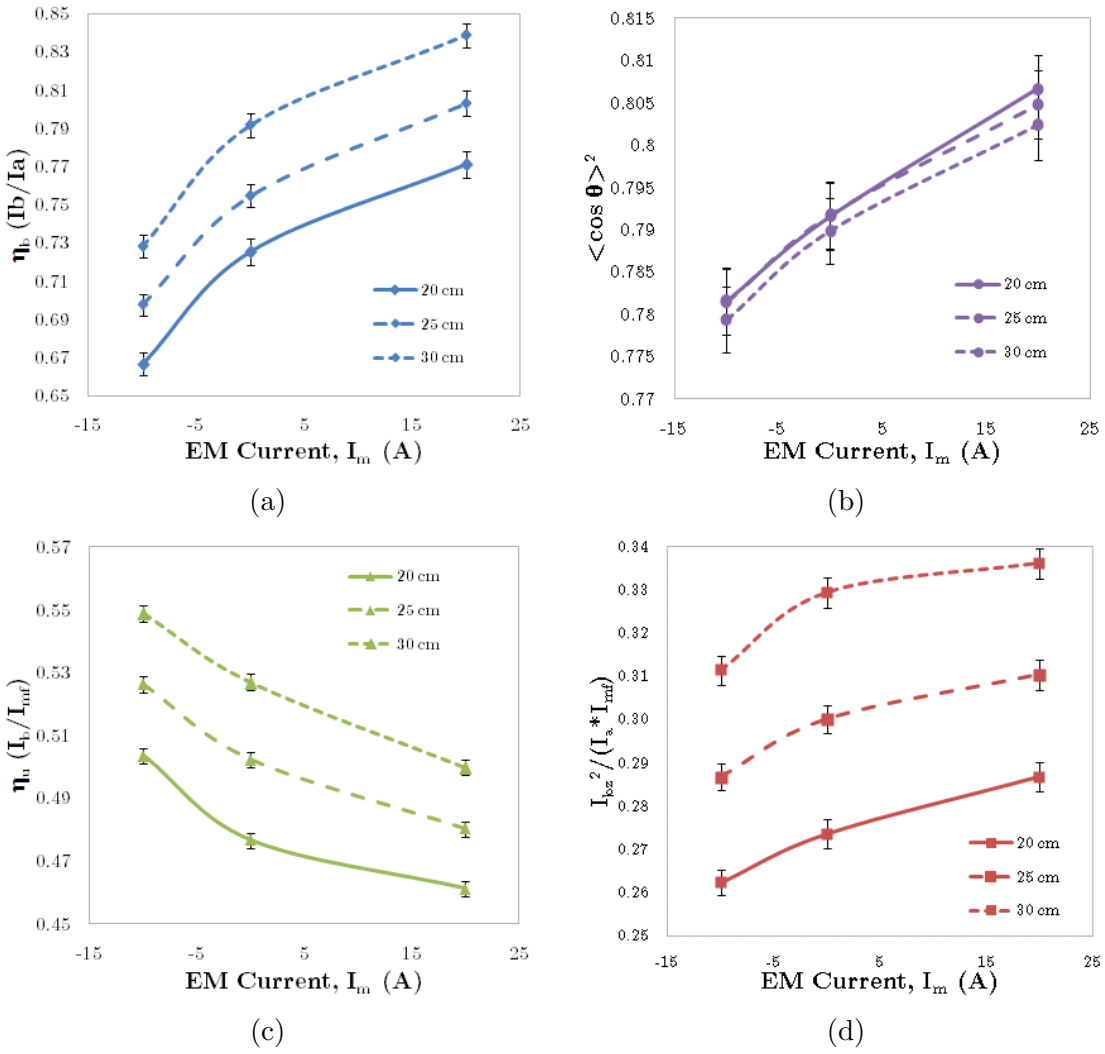

Figure 3-17: Integrated Faraday probe measurements of ion current density at several probe radii versus applied EM currents to estimate (a) beam efficiency (b) cosine-squared efficiency (c) utilization efficiency (d) product of (a), (b) and (c). DCFT operating in LC mode at 300 V and 0.49 mg/s on the anode with 0.15 mg/s on the cathode and a 1.25 A keeper current.

Eqns. 3.6 & 3.7 and presented in Fig. 3-17. The general trends in efficiency versus magnet current are the same regardless of distance of the measurement from the origin, however both the utilization and beam efficiencies are attributed enhanced values (as much as 7% higher) when the probe is further from the exit. The origin of the measured increase in beam current with distance from the exit may be attributable to charge exchange collisions with both unionized propellant and background chamber neutrals. Another, less likely, cause could be the unaccounted for beam current at angles $>70°$ being a larger portion of the total current for smaller measurement distances, though the opposite case is expected.

The contribution of charge exchange collisions to the measured beam current can be estimated using Eqn. 3.8, based on Eqn. 5.18 from [24], where I_m is the beam current estimated from probe measurements, I_b is the beam current with no charge exchange contributions, R is the distance of the probe from the measurement origin and $1/(\sigma_{cex} n_n)$ is the mean free path for charge exchange collisions in the vacuum chamber. Taking $\sigma_{cex} = 5.4 \times 10^{-19}$ m^2 ([81])and $n_n = 9.07 \times 10^{17}$ m^{-3} (based on a 35 μTorr chamber pressure and assumed 100°C neutral temperature) yields a mean free path of 2.74 m, and results in values of η_u using I_b calculated with Eqn. 3.8 being at most 2.5% higher at 30 cm compared to 20 cm, rather than 5% higher. If the neutral density is 2.2 times higher than the given estimate, the efficiencies calculated using the I_b of Eqn. 3.8 are identical at all values of R within the assumed uncertainty.

$$I_m \sim I_b \left(1 + \frac{R}{\sigma_{cex} n_n}\right) \tag{3.8}$$

Perhaps instead the problem stems from the coordinate system used to reduce the plume data to beam current, which has its origin (somewhat arbitrarily) at the intersection of the exit plane with the thruster axis. Choosing an origin which is displaced 3 cm upstream from the normal one results in the predicted η_u (without accounting for current projection on the new pointing angle) being no more than 0.7% more efficient at 30 cm compared to 20 cm, which is within the stated uncertainty. An upstream offset for the measurement origin appears natural, since the main beam

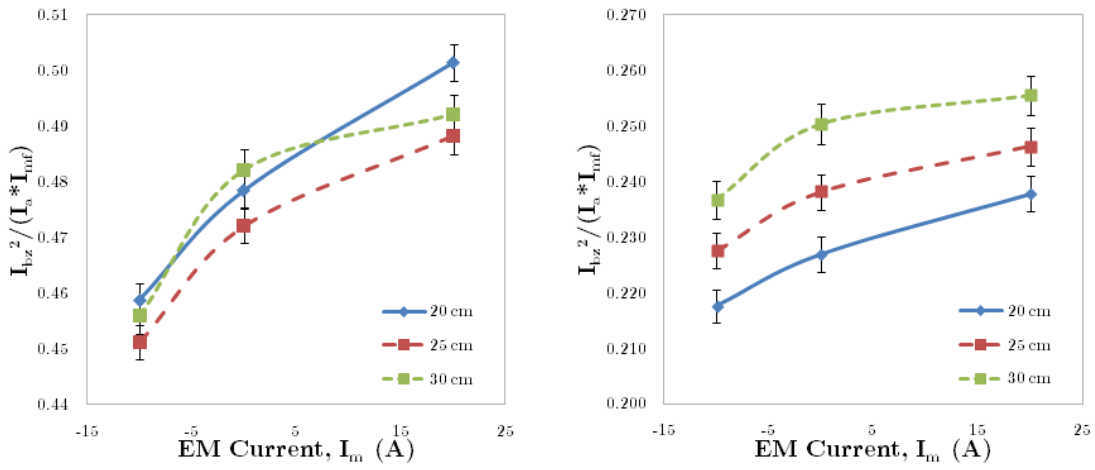

(a) (b)

Figure 3-18: Integrated Faraday probe measurements of ion current density at several probe radii versus applied EM currents to estimate net efficiency using (a) a measurement origin shifted 3 cm upstream or (b) a subtracted charge exchange current. DCFT operating in LC mode at 300 V and 0.49 mg/s on the anode with 0.15 mg/s on the cathode and a 1.25 A keeper current.

at 0 A and 20 A of EM current is linearly extrapolated to intercept the thruster axis between 8 and 4 cm upstream of the exit.

The change in the estimated efficiency is much easier to quantify for a shifted measurement origin than for an accumulated charge exchange current. This is due in part to the crudeness of Eqn. 3.8 and the lack of spatially resolved neutral density data making estimates of charge exchange contributions to the measured current highly uncertain. It is also due to the ability to estimate the location of a more appropriate measurement origin based on the Faraday probe data alone.

No effect on the cosine-squared efficiency is predicted by either the change in origin or the charge exchange current estimate, which is supported by the measurements shown in Fig. 3-17b. Using the charge exchange estimate from above (with $n_n = 9.07 \times 10^{17}$ m^{-3}) results in a roughly 6% decrease in the estimated net efficiency, while the fix based on an upstream measurement origin predicts an approximately 17% increase, with updated estimates in both cases given in Fig. 3-18. Ideally, both effects would be accounted for and some intermediate efficiency obtained.

Lateral scans, with 1 cm step sizes, were performed closer to the thruster exit with

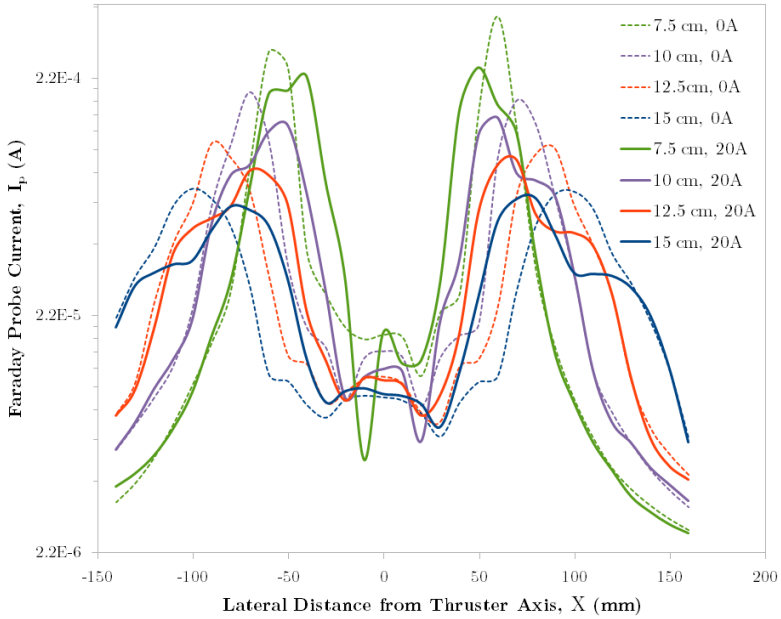

Figure 3-19: Axially pointing Faraday probe current versus lateral distance from thruster axis at various distances from thruster exit with either 0 or 20 A applied EM current. DCFT operated at 300 V with 0.49 mg/s on the anode, 0.15 mg/s flow through the cathode and a 1.3 A keeper current.

the Faraday probe pointed axially in an attempt to measure changes in the electron backstreaming current with applied EM current. The resulting profiles can be seen at axial distances from 75 to 150 mm from the exit for both an unenergized magnet and a 20 A EM current in Fig. 3-19. The axial component of the ion current has its peak density location shifted towards the thruster axis as the EM current is increased, though a hump in current density remains at higher radial positions.

Unlike the data obtained with the probe pointed towards the origin, the axially facing probe data often lacks an outer maximum, though the outer shell remains apparent. In a rough attempt to segregate inner from outer shells in the axially pointed probe data the peak current was fit with the sum of two, laterally separated Gaussian curves, as demonstrated in Fig. 3-20a and summarized in Table 3.2. The fitting was done visually and is only intended to 'guide-the-eye' rather than represent a physically accurate representation of nested beams. A laterally distributed Gaussian is expected to be a poor representation of beams which expand more closely as conical shells.

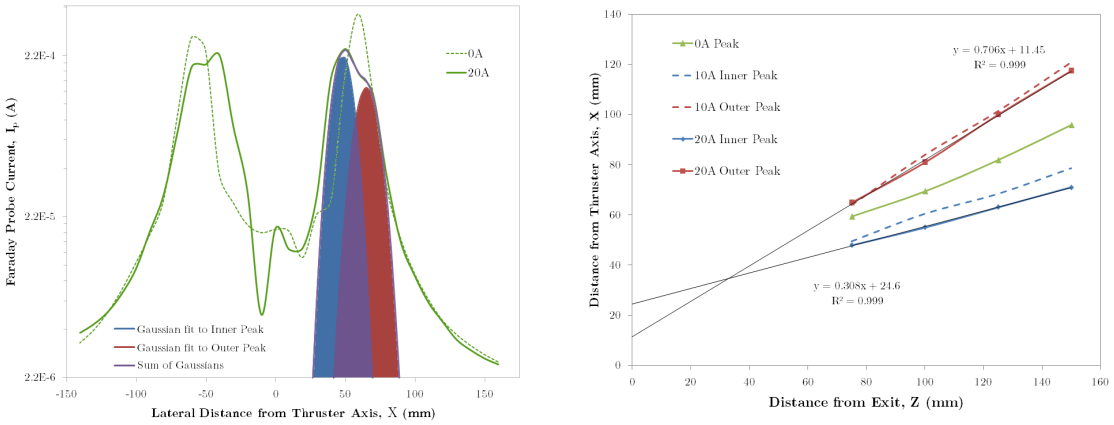

(a) (b)

Figure 3-20: DCFT operated in LC mode at 300 V with 0.49 mg/s on the anode, 0.15 mg/s flow through the cathode and a 1.3 A keeper current. (a) Axially pointed Faraday probe measurements at Z=75 mm for 0 and 20 A applied EM currents demonstrating use of Gaussian fits to inner and outer maxima in probe current. (b) Location of fitted Gaussian peaks versus axial location for inner and outer peaks at 10 A and 20 A on EM and for single peak at 0 A on EM. Solid black line shows linear fit.

The results described in Table 3.2 differ in some respects to those of Table 3.1 found with the thruster operating at the same conditions, however the main trends are unchanged. The inner peak appears to emanate from a location off-axis (extrapolated to the exit plane) at an angle which can be incrementally decreased by positive EM currents. The outer peak is relatively unaffected by the electromagnet, on the other hand, and can be linearly extrapolated to intersect the exit plane close to the origin.

The beam current through a plane perpendicular to the thruster axis is estimated using Eqn. 3.9, where x_{max} is the lateral limit of the measurement, which is 16 cm for the present case. The anode efficiency (where voltage and charge efficiencies are assumed as unity for convenience) is estimated directly with the axial beam current measurement and presented in Fig. 3-21a, which suggests the efficiency reaches its maximum value when the EM current is somewhere between 0 A and 20 A, likely close to 10 A. The data also suggest the measured efficiency decreases with axial distance from the thruster, though this is presumed to be due to the limited value of x_{max}, which results in an under-predicted value of the beam current by a fraction

EM Current	0 A	10 A	20 A
Anode Current (mA)	237	221	217
Inner Peak Intercept (mm)	21.9	21.2	24.6
Inner Peak Angle	26°	21°	17°
Outer Peak Intercept (mm)	-	7.8	11.5
Outer Peak Angle	-	37°	35°

Table 3.2: Properties of linear fits to Gaussian peak locations for axially pointed Faraday probe measurements. DCFT operated in LC mode at 300 V with 0.49 mg/s on the anode, 0.15 mg/s flow through the cathode and a 1.3 A keeper current.

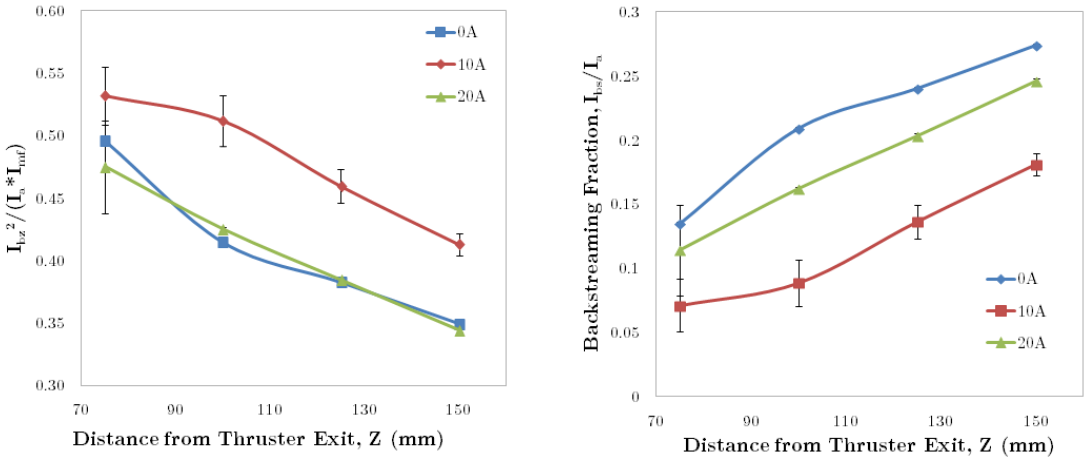

(a) (b)

Figure 3-21: Axial ion beam current integrated from 0 to +16 cm to estimate (a) product of beam, utilization and cosine-squared efficiencies and (b) ratio of backstreaming electron current to anode current versus distance from thruster exit. DCFT operated at 300 V with 0.49 mg/s on the anode, 0.15 mg/s flow through the cathode and a 1.3 A keeper current.

which increases as the plume expands.

$$I_{bz} = 2\pi \int_0^{x_{max}} J_{iz}(x) x dx \tag{3.9}$$

The error bars in Fig. 3-21 reflect the standard deviation in the 10 measurements averaged by the Keithley 2410 at each probe position. The standard deviation remained less than 0.65% of the mean with 0 A on the EM, but was as high as 19% for a 10 A EM current. The anode current normalization, in this case, is done point by point by matching thruster telemetry timestamps with timestamps taken at each

position in the Faraday scan, to account for anode current deviations *in situ*.

The backstreaming electron current fraction (I_{bs}/I_a) is estimated as $1 - \eta_{bz}$, using the axial beam efficiency, $\eta_{bz} = I_{bz}/I_a$, and is plotted in Fig. 3-21b. The backstreaming current obtained from these estimates appears to decrease as the EM is energized from 0 A to 10 A, but then increases slightly when the EM current is raised from 10 A to 20 A. At 10 cm, the backstreaming current is estimated at 50, 20 and 35 mA for EM currents of 0, 10 and 20 A respectively, hinting at a complex interplay between magnetic field and cathode-to-anode coupling. The cathode is less than 10 cm from the thruster exit, so the presented profiles should not be interpreted as a measurement of the true *in situ* electron current. Unfortunately, measurements closer to the axis (e.g. 7.5 cm) resulted in fairly large swings in the anode current during the course of a lateral scan, and we are left without an accurate gauge of the electron current profile in the cathode-to-exit.

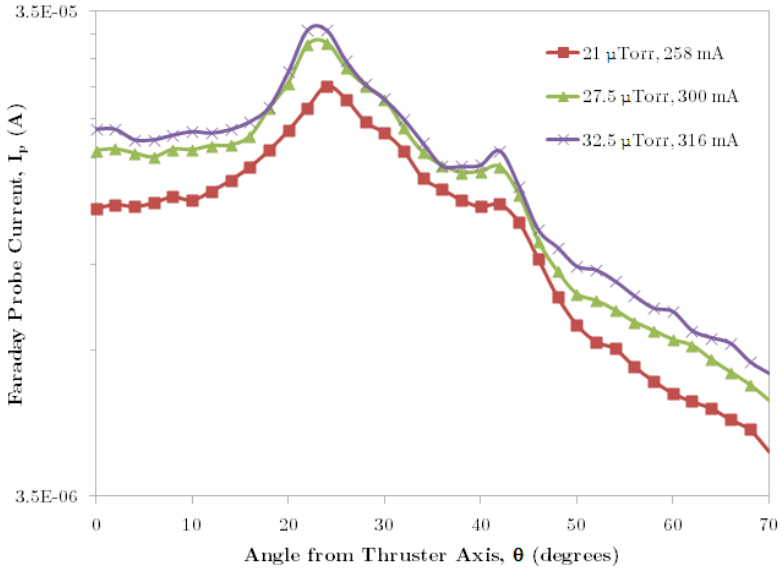

Figure 3-22: Faraday probe current versus angle from thruster axis at R=38 cm shown at three values of background pressure and corresponding anode currents. DCFT operated in HC mode at 400 V and 0.54 mg/s on the anode, 0.2 mg/s flow through the cathode and a 0.75 A keeper current.

An auxiliary flow of xenon was introduced to the vacuum chamber, from a tube placed roughly 30 cm below the thruster, to measure the effect of increased background pressure on the Faraday probe measurements. A comparison of probe cur-

rents versus angle from thruster axis is given in Fig. 3-22 with 0, 2.5 and 5 sccm of auxiliary xenon flow, which reveals a fairly complicated change in the plume structure with background pressure. When 2.5 sccm of auxiliary xenon is introduced (a 33% increase in total mass flow rate and 31% increase in background pressure) the anode current jumps up a full 16% and the ion current density peak shifts inward by 1°. The addition of an extra 2.5 sccm of auxiliary xenon (a 25% increase in total flow and 18% increase in pressure) results in a further increase in anode current of only 5% with no apparent changes in the plume shape.

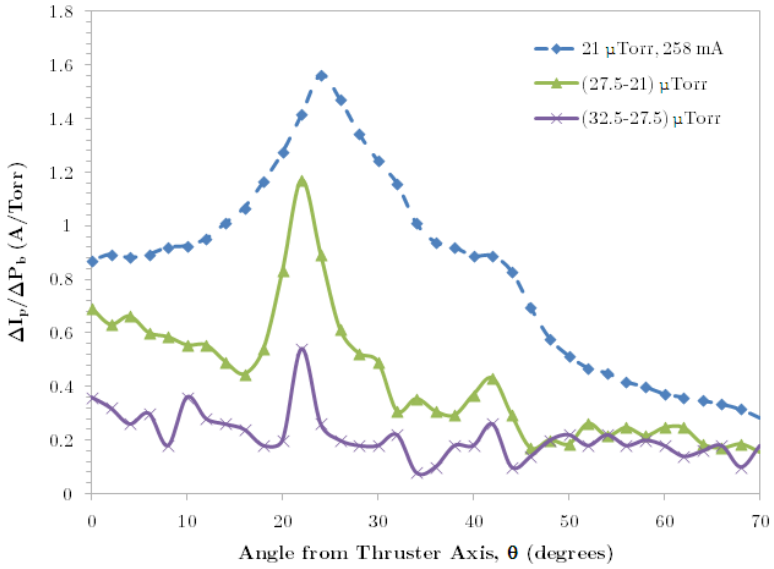

Figure 3-23: Change in Faraday probe current over change in background pressure versus angle from thruster axis at R=38 cm shown for two increments of background pressure. The ion current density (A/m^2) profile at the baseline pressure is shown with a dashed line. DCFT operated in HC mode at 400 V and 0.54 mg/s on the anode, 0.2 mg/s flow through the cathode and a 0.75 A keeper current.

The difference in the angular profiles of ion current density obtained at incrementally higher background pressures are shown in Fig. 3-23, where they are normalized by the change in pressure. The ion current density appears to increase with near angular independence when the pressure changes from 27.5 to 32.5 μTorr, but is clearly favorably enhanced at small angles when the pressure changes from 21 to 27.5 μTorr, especially at the angle just inside of that containing the peak current density. The current density appears to increase roughly linearly with background pressure for

angles ≥46°.

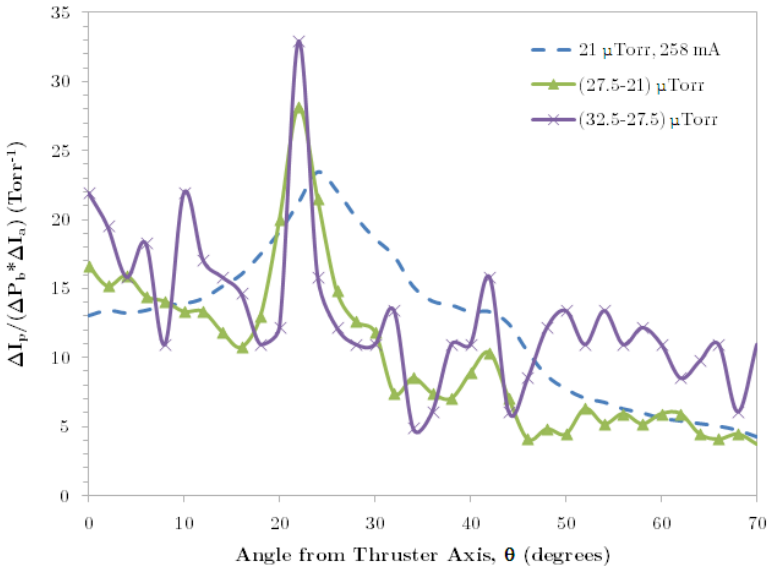

Figure 3-24: Change in Faraday probe current over product of change in background pressure with change in anode current versus angle from thruster axis at R=38 cm shown for two increments of background pressure. The ion current density profile at the baseline pressure is shown with a dashed line. DCFT operated in HC mode at 400 V and 0.54 mg/s on the anode, 0.2 mg/s flow through the cathode and a 0.75 A keeper current.

Further normalizing the differences in angular ion current distributions of Fig. 3-23 by the changes in anode current results in the profiles shown in Fig. 3-24. The normalized profiles now roughly overlap at angles <46° suggesting the enhanced ion beam close to the axis at higher pressures is tied to the amplified anode current. The complex structure of the change in angular ion current density distributions is likely related to the intricate plasma potential structure in the DCFT plume [8]. Charge exchange ions created in a Hall thruster plume are almost universally accelerated outward by electric fields pointing away from the thruster axis [24], while in the DCFT plume the θ-directed electric field changes directions more than once for θ between 0° and 90° from the thruster axis.

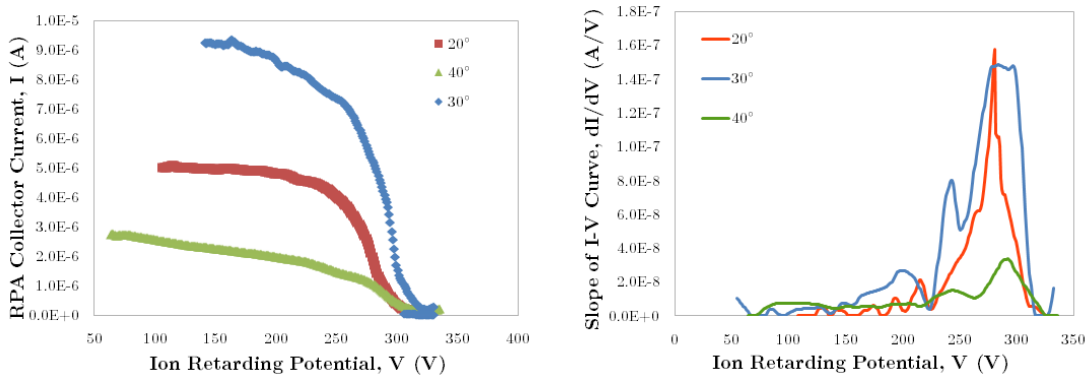

(a) (b)

Figure 3-25: RPA measurements, with 0 A applied to EM, at three angles with respect to the thruster axis given as (a) raw data and (b) the slope of spline fits to the data. Thruster operated at 300 V, 0.59 mg/s on the anode for a 320±1 mA current, with 0.098 mg/s on cathode and a 1.25 A keeper current. Probe is 38 cm from intersection of exit plane and thruster axis.

3.3.4 RPA Results

Though the Faraday probe measurements show an unambiguous shift in the location of peak ion current density to smaller angles as the exit separatrix is made less convex, there is no assurance that the energy content of the ion beam is left unchanged. RPA measurements are made in 10° increments from the thruster axis for the case of an unenergized EM (Fig. 3-25) and a 10 A EM current (Fig. 3-26) in order to ensure the ions which are vectored inward by the electromagnet are not born downstream of the main potential drop.

A comparison of Fig. 3-26b with Fig. 3-25b shows the most probable energy per unit charge for ions is 10-20 V below the applied anode potential from 20°-40° off-axis regardless of the applied EM current. Measurements outside of this range of angles resulted in very low signals which suggested the ion voltage distribution was broadly distributed between 50 and 250 V, but are not reproduced here. The low signal-to-noise encountered at these angles necessitates the acquisition of more sets of data at the same conditions before much confidence can be put in the results.

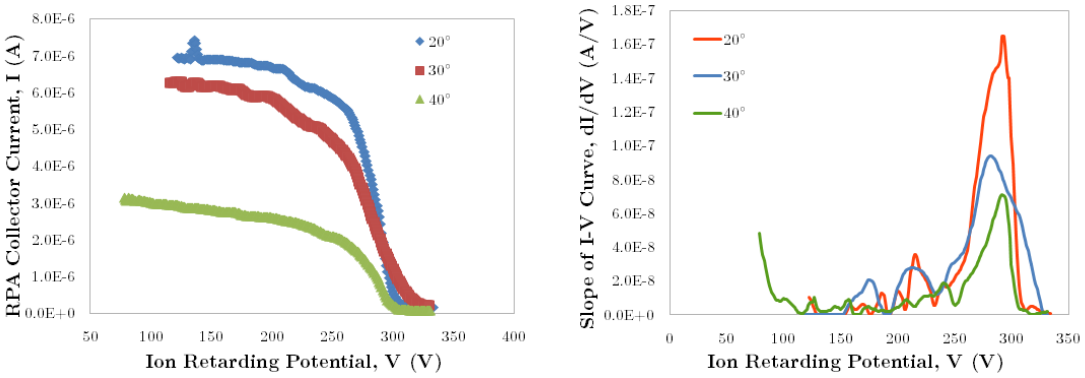

(a) (b)

Figure 3-26: RPA measurements, with 10 A applied to EM, at three angles with respect to the thruster axis given as (a) raw data and (b) the slope of spline fits to the data. Thruster operated at 300 V, 0.59 mg/s on the anode for a 313±1 mA current, with 0.098 mg/s on cathode and a 1.25 A keeper current. Probe is 38 cm from intersection of exit plane and thruster axis.

3.3.5 Emissive Probe Results

Emissive probes are set to high enough heater currents that the measured floating potential saturates and scanned along the thruster axis to allow for estimates of the plasma potential changes introduced by the external electromagnet. The floating potential measurement technique is chosen for its easy implementation, quick scan times and minimal plasma perturbation, but is noted to predict potentials at least 1-2T_e below the actual value, with T_e an unknown quantity. The on-axis spatial scan does not necessarily correspond to the location of greatest interest, however it is found to have far less impact on thruster operation than scans performed near the location of peak ion current density while still being able to show where the main potential drop occurs.

The on-axis scans were found to have a repeatable effect on the anode current, an example of which is given in Fig. 3-27. The anode current increases slightly as the probe is brought towards the exit from 10 cm away until reaching about 3 cm, at which point it begins to drop, eventually passing below its original value. When the probe is around 1.9-1.2 cm away the anode current rises again. Even at its peak, however, the anode current is less than 3% above its mean value, with a repeatable

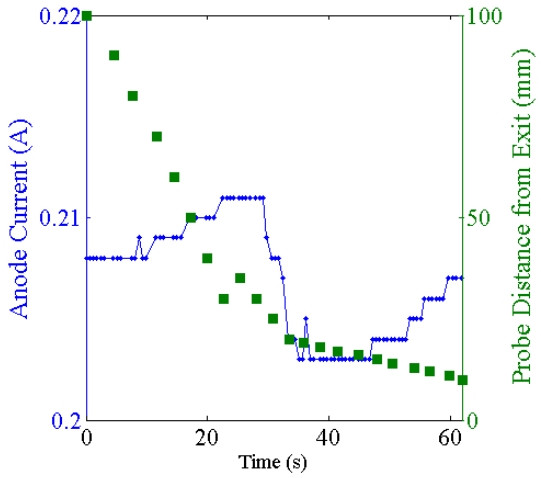

Figure 3-27: Anode current and emissive probe distance from exit versus time during an on-axis potential scan. DCFT operated in LC mode with 5 A EM current at 250 V and 0.49 mg/s on the anode, 0.1 mg/s flow through the cathode and a 1.25 A keeper current.

trend of less anode current deviation at higher positive EM current. The anode current alteration may be due to the small electron current emitted by the probe, and its variable polarity related to the location of the probe relative to the external point cusp roughly 2 cm downstream of the exit.

A floating potential of 110 V is measured on the emissive probe 10 mm downstream of the exit, with a 250 V potential and 5 sccm flow of xenon applied to the anode, when the EM is unenergized. The potential drops nearly linearly with distance down to 14.6 V at 30 mm from the exit, then reaches a secondary maximum of 15.8 V at 40 mm before decaying exponentially with distance to 11.4 V by 100 mm. As the EM is activated to progressively higher positive currents the potential at the secondary maximum rises (from 15.8 V at 0 A to 19.5 V at 15 A) and its location moves upstream along with the linear portion of the potential drop, as displayed in Fig. 3-28a.

The axial location of the magnetic null point (where the exit separatrix approaches the axis) moves upstream as the EM current is increased, so based on the simple electric field model espoused in the introduction of this chapter we would expect the electric field to move upstream as well. Maxwell simulations suggest the magnetic null point moves upstream approximately 2.2 mm every 10 A of positive EM current.

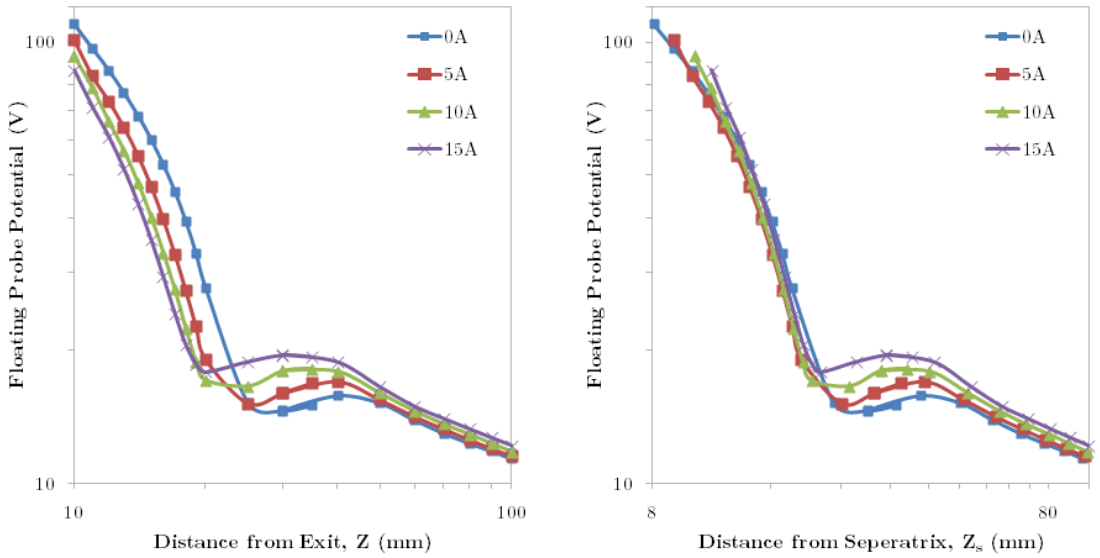

(a) (b)

Figure 3-28: Floating potential of emissive probe at various values of EM current versus (a) distance from thruster exit (b) distance from exit separatrix. DCFT operated in LC mode at 250 V and 0.49 mg/s on the anode, 0.1 mg/s flow through the cathode and a 1.25 A keeper current.

Plotting the floating potential profile with respect to the distance from the simulated magnetic null, as done in Fig. 3-28b, suggests that the potential structure is largely dragged upstream along with the separatrix when the EM current is increased. The axial electric field strength is estimated using forward differences and plotted versus distance from the null point in Fig. 3-29, which shows a steepening of the electric field between 8 and 16 mm from the separatrix as the EM current increases.

The same measurements are performed with the anode voltage increased to 300 V, however the range of EM currents which produce a stable LC mode is roughly halved at this condition. The results, plotted in Fig. 3-30, are very similar to those at 250 V, though the potential profiles essentially overlap at all EM currents (0 to 6 A) from around 8 to 20 mm downstream of the magnetic null point. The anode current for the conditions plotted in Figs. 3-28 & 3-30 is given in Fig. 3-31.

Similar measurements are obtained with the external magnet present but unenergized to examine how other thruster parameters affect the on-axis potential profile. The results of an anode mass flow rate scan are given in Fig. 3-32 which shows both

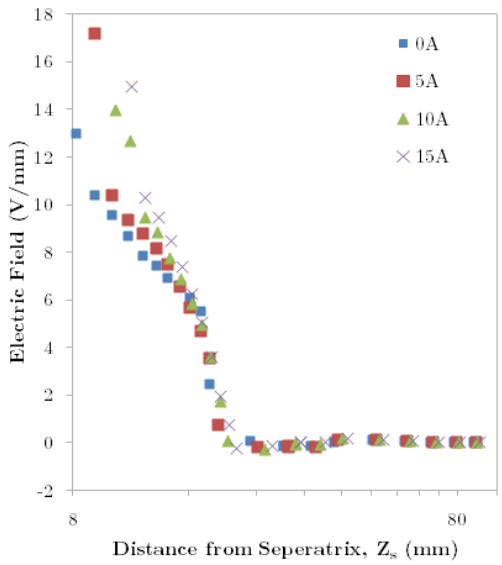

Figure 3-29: Axial electric field calculated from emissive probe measurements at various values of EM current versus distance from exit separatrix. DCFT operated in LC mode at 250 V and 0.49 mg/s on the anode, 0.1 mg/s flow through the cathode and a 1.25 A keeper current.

the floating potential profile and the calculated axial electric field. The anode current for this scan is presented in Fig. 3-33 which shows the current at 6.5 sccm of xenon (0.64 mg/s) both in LC mode, when the probe is less than 20 mm from the thruster exit, and HC mode, which is entered when the probe is further away.

Comparison of Fig. 3-32a with Fig. 3-30b suggests a similarity between raising the anode mass flow rate and raising the EM current, both of which eventually lead to a spontaneous switch to HC mode, in the region $\geq$23 mm downstream of the null point; the null point being about 2 mm downstream of exit with 0 A on the EM. The electric field shape is relatively unchanged in contrast to the electric field steepening seen with the EM current increase, though it appears to shift slightly upstream in the region within 12 mm of the null point as the flow rate is increased from 4.5 to 6 sccm of xenon. A large upstream shift occurrs when the flow is increased from 6 sccm of xenon to a conditionally stable point at 6.5 sccm.

The result of a scan in anode potential from 300 to 360 V at a constant 5 sccm flow of xenon to the anode is shown unprocessed in Fig. 3-34a and normalized by the anode potential in Fig. 3-34b. A decrease in anode potential, which usually leads to

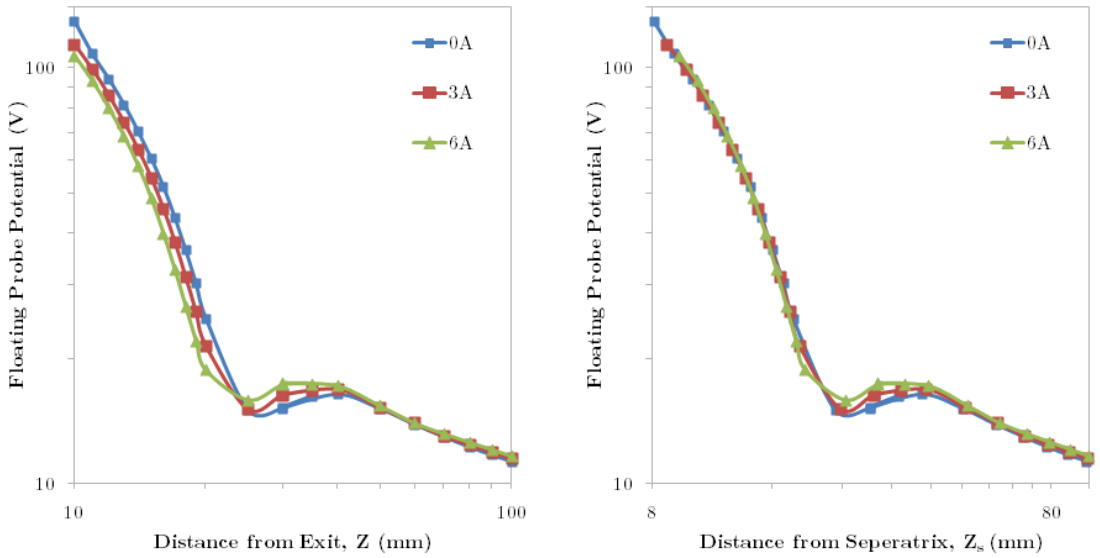

(a) (b)

Figure 3-30: Floating potential of emissive probe at various values of EM current versus (a) distance from thruster exit (b) distance from exit separatrix. DCFT operated in LC mode at 300 V and 0.49 mg/s on the anode, 0.1 mg/s flow through the cathode and a 1.25 A keeper current.

the eventual transition from LC to HC mode, is seen in Fig. 3-34b to monotonically increase the anode normalized potential of the secondary maximum, similar to Figs. 3-32a & 3-28b.

The normalized axial electric field, calculated from the anode potential normalized data of Fig. 3-34b, is shown in Fig. 3-35a to be independent of anode voltage at axial distances $\geq$1 cm downstream of the magnetic null. The normalized electric field is generally observed to steepen with anode voltage within 1 cm of the null point, resembling the trend observed in Fig. 3-29 when the EM current is raised.

It has also been noted that an unstable operating point can be made to favor LC over HC mode by increasing the keeper current, which leads to a hotter cathode insert and presumably easier extraction of electrons. The measured on-axis potential profiles for a scan in keeper currents from 0.6 to 0.9 A, shown in Fig. 3-36a, once again follow the trend of increased secondary maxima potentials as thruster conditions are brought closer to the transition point from LC to HC mode. The calculated axial electric field profile is minimally affected by changes in keeper current, as shown in

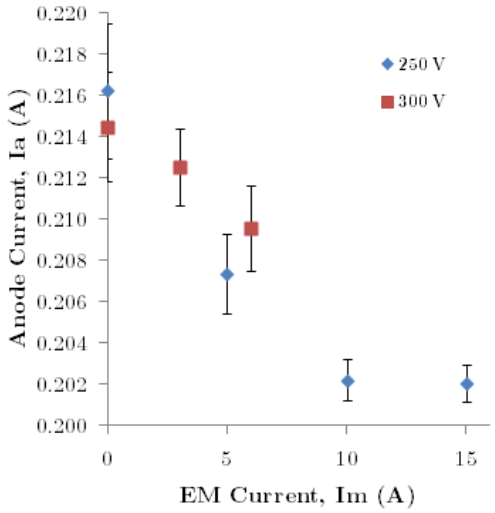

Figure 3-31: Anode current versus EM current at various values of anode potential. DCFT operated in LC mode at 0.49 mg/s on the anode, 0.1 mg/s flow through the cathode and a 1.25 A keeper current.

Fig. 3-36b.

The anode conditions for the keeper current scan are different from those used for the other parametric scans due to a malfunction of the CT10 cryopump which precluded the use of an anode flow rate higher than 4 sccm of xenon. A stable operating point, in the higher than normal background pressure, was found at 4 sccm of xenon with an anode potential of 200 V, a cathode flow of 1 sccm of xenon and a keeper current of 0.75 A, resulting in an anode current of 111±1 mA. The anode current varied by less than 2 mA during the keeper current scan.

The region near the thruster exit was also scanned in the X-Z plane with the floating emissive probe, in a small rectangle spanning from -2 to 2 cm in the X-direction and 1.5 to 3 cm in the Z-direction. Attempts to stretch the range of X positions scanned resulted in erratic thruster behavior, as the emissive probe entered the region of peak ion current density. The probe was also placed closer to the exit plane with similar results, specifically a flutter between HC and LC modes and, on at least one occasion, the destruction of the probe. The region scanned is small, but is used to contextualize the on-axis scans.

The 2-D potential contours for the lowest and highest EM currents of Fig. 3-

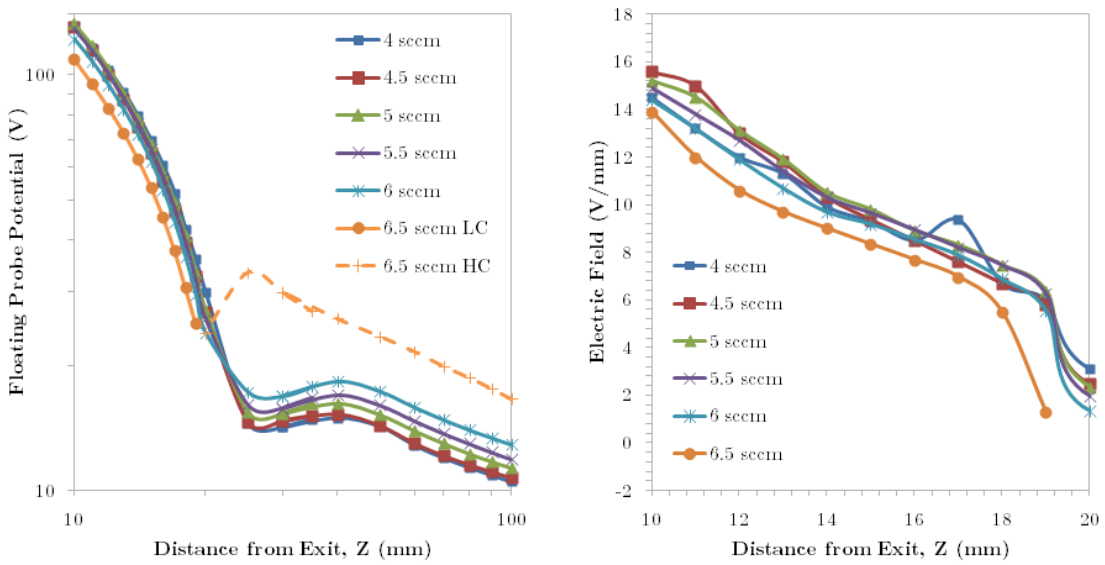

(a) (b)

Figure 3-32: (a) Floating potential of emissive probe and (b) axial electric field calculated from emissive probe measurements at various values of anode flow rate of xenon versus distance from thruster exit. DCFT operated in LC mode at 300 V, 0.1 mg/s flow through the cathode and a 1.25 A keeper current.

28b are shown in Fig. 3-37, on which the Maxwell simulated lines of magnetic flux are overlain. Arrows denote the relative strength and direction of the electric field calculated from the potential data while also demonstrating the locations of measurements. The extreme values of EM current from Fig. 3-30b are similarly displayed in 2-D contours in Fig. 3-38.

The trends of Figs. 3-28b & 3-30b are corroborated in Figs. 3-37 & 3-38 near the axis, where the main potential drop moves upstream with the separatrix (as the EM current is increased) and the potential outside of this drop rises globally. Large potentials at (X=±2 cm,Z=1.5 cm) are presumed to be due to the main beam of plasma emanating at an angle between 20 and 35° off-axis. Iso-potentials near these locations do not appear to move upstream with the separatrix, but instead correspond to higher anode-normalized potentials and seem to decrease in apparent angle with respect to the thruster axis.

The upper anode flow rate of Fig. 3-32 is also approached in an X-Z scan shown in Fig. 3-39 to compare the effects of the flow rate with those of the external EM. A

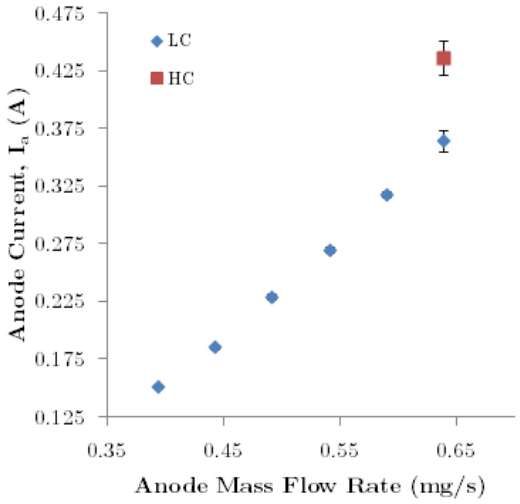

Figure 3-33: Anode current versus anode mass flow rate. DCFT operated in LC mode at 300 V, 0.1 mg/s flow through the cathode and a 1.25 A keeper current.

flow of 6.2 sccm xenon is used instead of 6.5 sccm to avoid the spontaneous change to HC mode. The main near-axis potential drop is shifted slightly upstream and the global potential outside this region increases, similar to Fig. 3-38b.

3.3.6 Conclusions

Faraday probe measurements show unambiguously that an external electromagnet can be used to turn the main ion beam in towards the axis. The reduced angle of the peak ion current density in the plume is expected to be due to the decreased convexity of the exit separatrix which is the theorized anchor of the main electric field. The strong correlation between exit separatrix and potential structure is corroborated by plasma potential estimates obtained with a floating emissive probe, which show the on-axis electric field being dragged back with the magnetic null point as the electromagnet current is increased. RPA data confirm that the less divergent, main beam is mostly comprised of ions with energy per charge near the applied anode voltage.

Unexpectedly, an outer shell of high energy ions is left behind around 35-40° from the thruster axis as the main beam is turned inward. RPA measurements suggest that this outer beam is also made up of ions born upstream of the main potential

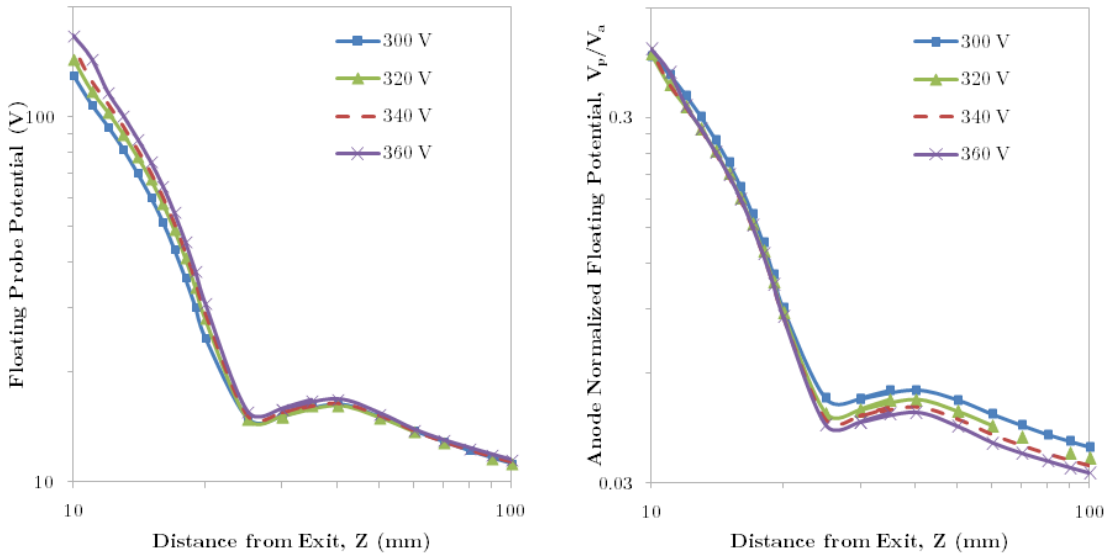

Figure 3-34: Floating potential of emissive probe (a) raw and (b) anode voltage normalized at various values of anode voltage versus distance from thruster exit. DCFT operated in LC mode at 0.49 mg/s anode mass flow, 0.1 mg/s flow through the cathode and a 1.25 A keeper current.

drop. Linear extrapolation of Faraday probe measurements made at a variety of distances from the thruster exit are used to show that the so-called outer shell appears to originate from a location closer to the thruster axis than where the inner beam originates.

One possible explanation for the stratification of the conical plume is that the ions which comprise the outer shell are born upstream of the exit separatrix and travel near the thruster axis, being accelerated by the wedge shaped potential profile observed in this region just downstream of the exit. The shape of the potential wedge is relatively independent of EM current and so the outer shell angle is roughly constant. The inner beam is posited to be made up of ions which are born near (or perhaps funneled into) the exit cusp which are then largely accelerated perpendicular to the separatrix.

Another possibility is that the outer shell is an artifact of the inability of the external magnet to affect the shape of the separatrix near the wall where the magnetic field is strongest. Since this region of the separatrix retains its original convexity, the ions born near the wall may still be accelerated to a highly divergent angle. The

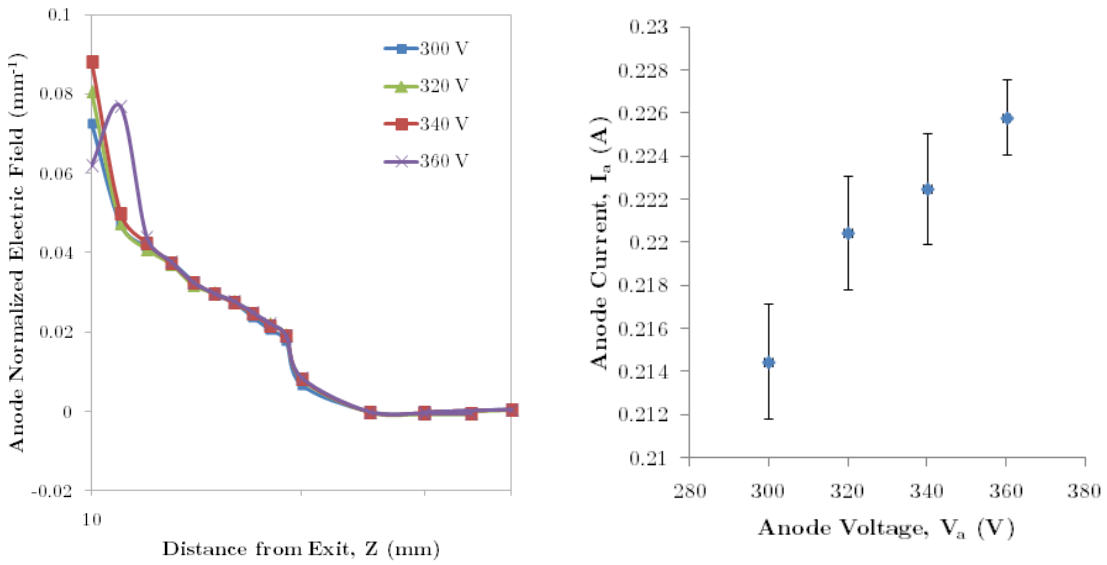

(a) (b)

Figure 3-35: (a) Axial electric field calculated from emissive probe measurements and normalized by anode potential versus distance from thruster exit and (b) anode current versus anode potential. DCFT operated in LC mode at 0.49 mg/s anode mass flow, 0.1 mg/s flow through the cathode and a 1.25 A keeper current.

measurements of ion flux in the near plume tend to refute this hypothesis in a purely geometric sense. The outer shell location traces back linearly to a point very near the origin (see Fig. 3-16 or Fig. 3-20b for example), which in consideration of the heurestic picture of ions moving ballistically perpendicular to the separatrix would not support the idea of the outer shelling having come from a divergent electric field near the wall. Considering the smooth curvature of the separatrix it is also unclear how the convexity of the field near the wall would create a discrete plume at high angles and not a continuous spread in beam angles, however it is possible that some potential structure in the near field provides such a splitting effect.

On-axis measurements using a floating emissive probe are used to monitor trends in the electric field just downstream of the thruster exit with changes in thruster parameters. The main potential drop, normalized by the anode voltage and measured with respect to the magnetic null point, does not appear to change much as EM current, anode potential, flow rate or keeper current are varied, however the normalized potential downstream of this drop is found to globally increase as any one of these

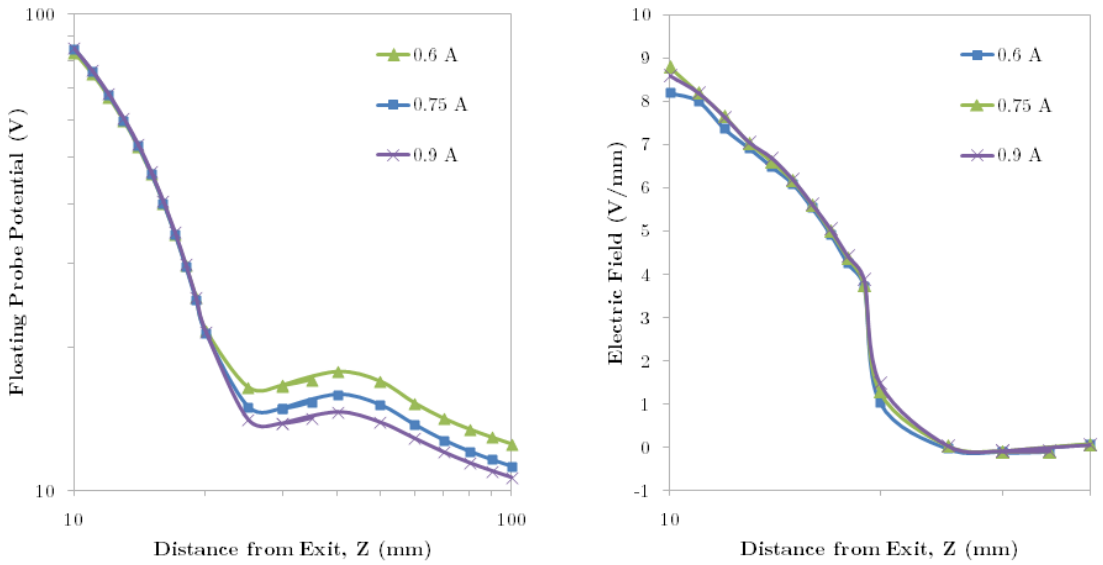

(a) (b)

Figure 3-36: (a) Floating potential of emissive probe and (b) axial electric field calculated from emissive probe measurements at various values of keeper current versus distance from thruster exit. DCFT operated in LC mode at 200 V and 0.39 mg/s on the anode, with 0.1 mg/s flow through the cathode.

parameters is used to approach the point of transition from LC to HC mode.

Some uncertainties remain due to the experimental setup. The structure of the external electromagnet is likely to have a non-negligible effect on thruster operation as it increases the local neutral density near the exit, both through entrainment and through recombination of ions at its inner surface. The EM structure also introduces an additional potential boundary in the near-field, constraining the local plasma to sit several T_e above the floating potential on the new surface. The sum of these effects is presently unknown, and it is left to tests using clever internal permanent magnet circuits which can create similar field topologies to extricate magnetic field effects from those caused by EM impingement.

The potential measurements are also limited due to the lack of reliable electron temperature data for all the parametric scans presented. Trends in the floating potential of the emissive probe should not be interpreted as solely due to trends in the plasma potential but as a sum of plasma potential and electron temperature changes. For example, the rise in the floating probe potential from 25 to 100 mm downstream of

the exit which accompanies an increase in mass flow rate may be due to a decreasing electron temperature in this region coupled with an unaffected plasma potential.

Unfortunately, reliable electron temperature measurements are fairly difficult to obtain in strong magnetic fields (of variable strength in this study). Preliminary data taken with a double Langmuir probe suggest the electron temperature is around 1-4 eV at axial distances of 25 mm and beyond, but can reach into the tens of eV at 1 cm from the thruster exit. Such temperatures may easily wash out the potential trends described above, however little variation has been found in on-axis temperature profiles between a 0 A and 20 A EM current case. LIF measurements remain a preferred alternative to the floating probe measurements described here in discerning the location of ion acceleration.

3.4 Chapter Summary

This chapter details a study of hollow conical plumes, a feature that has been measured on a variety of grid-less plasma thrusters utilizing permanents magnets to create at least one ring cusp. Noting that the main region of ion acceleration in such devices occurs near the exit of the discharge channel, it is hypothesized that the high divergence angle of the ion beam in these configurations is due to the shape of the field line which runs through the center of the cusp. This is expected to occur as a byproduct of the difficult cross-field path electrons emitted from an external cathode must traverse before reaching the closest separatrix and the comparative ease of electron travel from just upstream of this flux line to either an anode or to just downstream of the next internal separatrix. A high impedance between the cathode and the first separatrix met by cathode-emitted electrons (or secondaries created by them) would lead to the main potential drop occurring in this region, with its upstream edge demarcated by the separatrix.

The magnetic field topographies created by sets of axially magnetized ring magnets is discussed and compared to fields created by electromagnets. A convex downstream separatrix is shown to be a natural feature of these types of permanent magnet cir-

cuits in the absence of a concerted effort to mitigate such an effect through the use of ferromagnetic materials. Several circuits are discussed which redirect the exit separatrix, one from the literature which downgrades its importance by shielding out the strong exit magnetic field, and a new one which guides it to a downstream location where it can connect nearly radially the the axis of symmetry. Another method is presented which uses an external electromagnet to actively reshape the field without adding an additional separatrix and this method is chosen for an experimental study of field effects on the plume structure.

A test campaign is described which uses an external electromagnet to reduce (or increase) the convexity of the ultimate downstream separatrix on the DCFT. An active control of the most probable angle of ion flux density in the plume is demonstrated, in-line with the overall prediction. Unexpectedly, a portion of the ion beam remains at high angles, apparently unaffected by the change in magnetic topography. Several ideas are forwarded in the conclusions section as possible explanations for the stratification of the plume.

Strengthening the external magnetic field with the electromagnet is also measured to decrease the propellant utilization, it is thought by restriction of the electron current which streams from the cathode towards the anode. Near-field measurements did not show a monotonic decrease in axial electron current near the exit

Floating emissive probe measurements are detailed which suggest a tantalizing trend in the floating probe potential in the near field of the thruster with operating conditions. A slew of parametric scans are discussed which all result in an increase in the floating probe potential downstream of the main potential drop as the thruster is brought towards its transition point from LC to HC mode. The floating probe scans also suggest that the near-exit electric field moves upstream as the separatrix is pushed in the same direction by the external electromagnet field, with both moving an essentially equivalent distance. This further bolsters the hypothesis that the main accelerating field in the DCFT is tied to the exit separatrix.

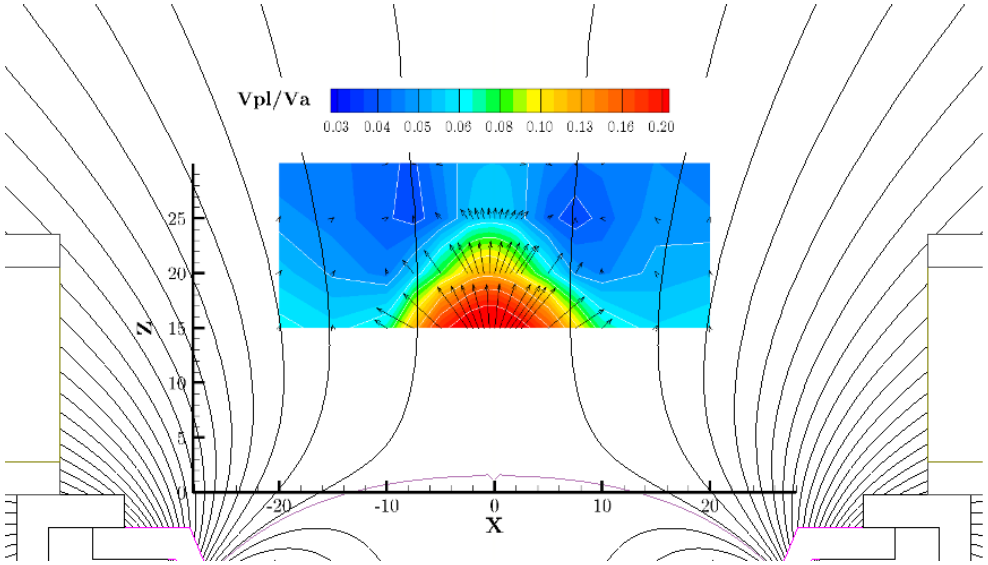

(a)

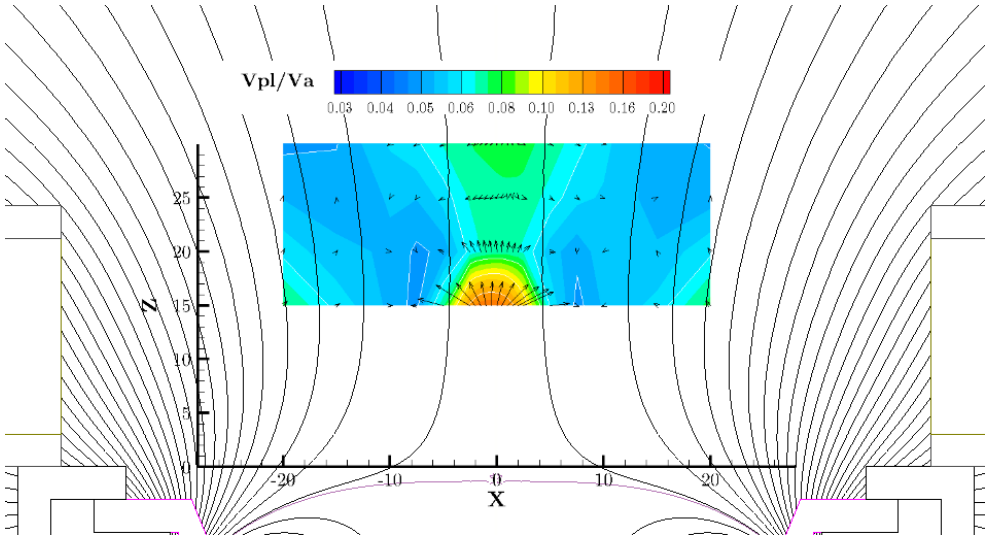

(b)

Figure 3-37: Emissive probe floating potential contours normalized by anode voltage for an EM current of (a) 0 A (b) 15 A, with relative electric field vectors and magnetic flux contours overlaid. DCFT operated in LC mode at 250 V and 0.49 mg/s on the anode, with 0.1 mg/s flow through the cathode and 1.25 A keeper current. Purple flux line denotes exit separatrix, all spatial dimensions in mm.

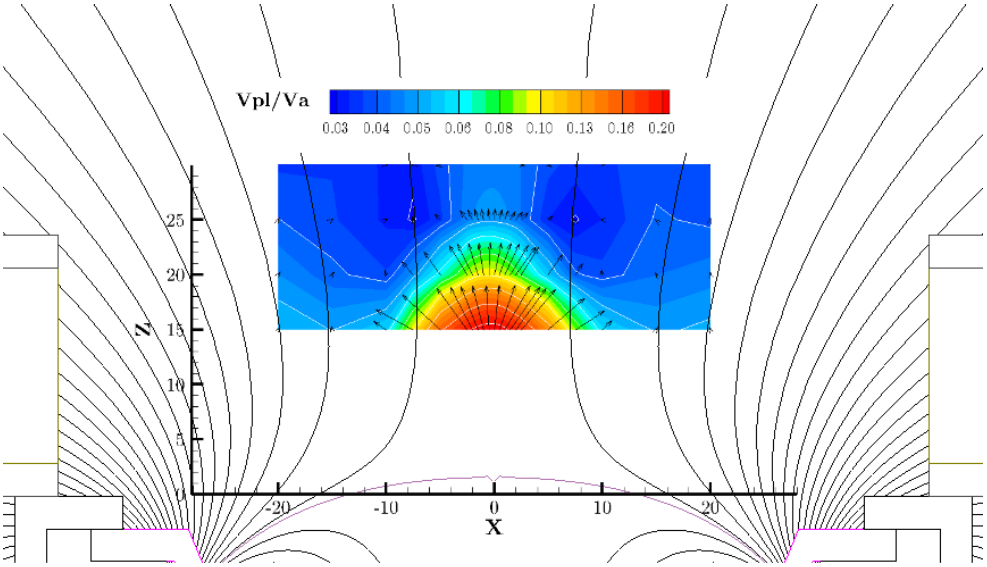

(a)

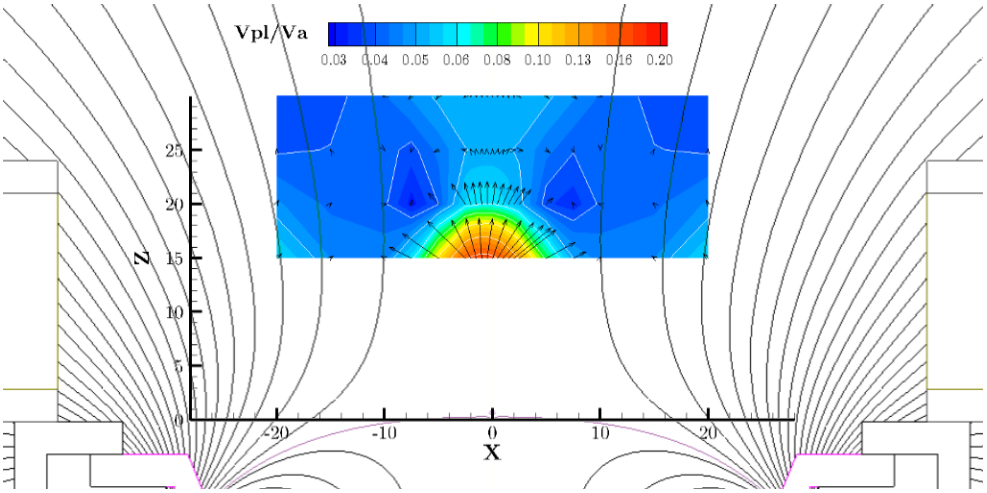

(b)

Figure 3-38: Emissive probe floating potential contours normalized by anode voltage for an EM current of (a) 0 A (b) 6 A, with relative electric field vectors and magnetic flux contours overlaid. DCFT operated in LC mode at 300 V and 0.49 mg/s on the anode, with 0.1 mg/s flow through the cathode and 1.25 A keeper current. Purple flux line denotes exit separatrix, all spatial dimensions in mm.

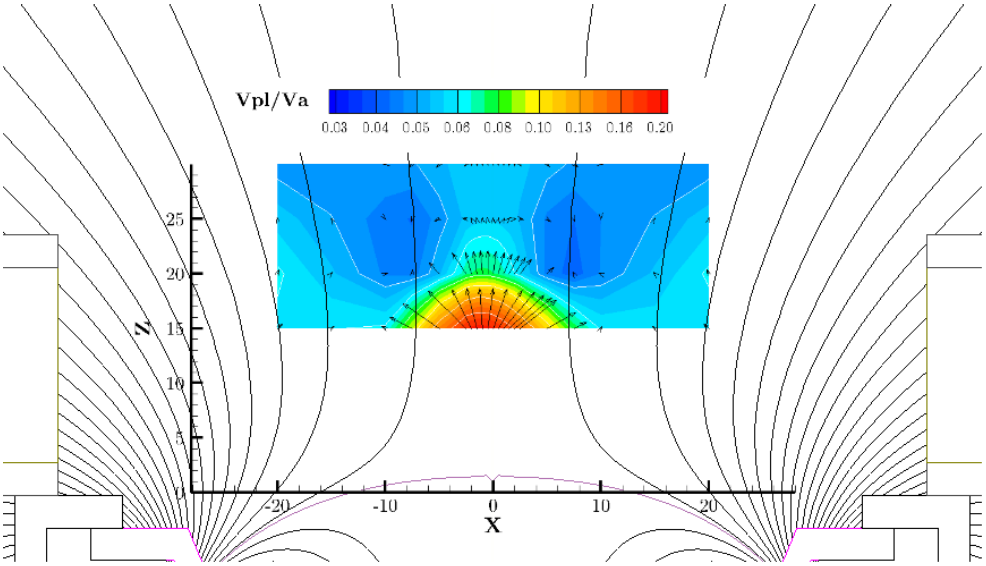

Figure 3-39: Emissive probe floating potential contours normalized by anode voltage for an EM current of 0 A, with relative electric field vectors and magnetic flux contours overlaid.DCFT operated in LC mode at 300 V and 0.61 mg/s on the anode, with 0.1 mg/s flow through the cathode and 1.25 A keeper current. Purple flux line denotes exit separatrix, all spatial dimensions in mm.

Chapter 4

Bi-Modal Operation of the DCFT

The DCFT has two main modes[a] of operation which are separated by a sharp transition as the anode voltage is increased, for a given flow rate. At high anode voltages the thruster runs in a low anode current mode with small scale, largely incoherent current fluctuations, and a plume which visibly appears to be concentrated in thin jets around 30° from the thrust axis. When operated at lower voltages (usually around 300 V) the thruster anode current jumps up substantially in its DC value (in some cases over 100%) and begins to exhibit high amplitude oscillations at a fundamental frequency around 2-5 kHz. The visual appearance of the plume in the high current mode is of a more diffuse, 'filled in', conical stream (see Fig. 4-1).

(a) (b) (c)

Figure 4-1: Pictures of the DCFT firing in (a) LC mode (b) HC mode (c) UHC mode

Original observations of the two modes by Courtney [16] in the MIT Space Propul-

[a]There is a third (UHC) mode, however this mode has only been observed with high vacuum vessel background pressures, suggesting it may be a facility effect rather than a natural mode

sion Laboratory's ASTROVAC chamber showed that the transition was fairly inconsistent but tended to occur a voltages from 300 to 400 V for flow rates from 0.68 to 0.98 mg/s of xenon. The transition voltage was highest at the highest flow rate but an intermediate flow of 0.78 mg/s remained in the low current mode at all anode voltages. These initial tests also showed that the keeper voltage dropped drastically along with the anode current, from 60-80 V down to around 20 V, for a keeper current of 0.25 A and cathode flow rate of 98 μg/s.

Confoundingly, when the thruster was run in a larger chamber with a nearly identical working background pressure ($\sim 4 \times 10^{-5}$ Torr) the high current (HC) mode was not obtained at any voltages for 0.68 and 0.98 mg/s flow rates, but occurred at voltages below 400 V at a flow rate of 0.83 mg/s. Thrust measurements show a clear drop in thrust and specific impulse when the thruster transitioned into low current (LC) mode between 400 and 450 V, but the thruster efficiency showed a slight increase, from 40% to around 42%, possibly within the unstated uncertainty of the measurement.

Subsequent testing by Courtney [17], after changing the anode material from 316 stainless steel to AXF-5Q Poco graphite, used a Faraday probe to measure the ion current in the plume and a Retarding Potential Analyzer (RPA) to measure the distribution of ion energy per charge at a representative operating condition in each of the two modes. The measurements show the peak ion current density in the plume is around 30 to 34° from the thrust axis, irrespective of operational mode, with the main difference being a roughly 30% increase in the fraction of current found at lower angles in the HC mode. The RPA data show both modes have a peak in ion energy about 50 V below the applied anode potential, but the peak appears somewhat wider in the oscillatory mode. In this paper the LC mode was obtained at an anode voltage of 450 V for a 0.52 A current while the HC mode had the anode at 300 V and 0.71 A. Both modes were obtained with a Xenon flow rate of 0.83 mg/s and a keeper current of 0.25A, with all potentials applied and measured relative to the chamber and facility ground.

Higher resolution measurements, also using an RPA and a Faraday probe mounted

on a rotating arm, of DCFT plume properties were made by Gildea [18] in a larger volume, lower backpressure ($< 4 \times 10^{-6}$ Torr) vacuum chamber. The LC mode in this chamber was only obtainable when using a keeper current of at least 1.5 A, compared to the nominal value (used for HC mode) of 0.25 A, and anode flow rates below 0.49 mg/s. The results show once again that the ion current density in both modes peaks at 30 to 35° from the axis, but the peak current density compared to the centerline density is roughly 5 times higher in the LC mode. RPA measurements, at angular positions near the peak current density, reveal peak ion energies at about 40 V below the applied potential (450 V for both modes in RPA data) with a FWHM of about 20 V in the HC mode. Peak ion energies of only around 10 V below the anode potential and a FWHM of 10 V were found in the LC mode case. A broad peak of ions with energies from 20 to 150 V appears, in addition to the peak near the applied potential, in the HC mode case measured on the centerline, while sharp peaks at 10 and 20 V show up, along with the main 440 V peak, in the LC mode case.

The keeper voltage is far lower during these experiments than in the initial results of Courtney [16], at around 17 V, with the transition from HC to LC mode resulting in a slight increase in keeper voltage of only around 1 V. The precise reason behind the large difference in cathode-keeper operation between the two examinations is unknown, but different cathodes of the same model were used and were possibly in much different stages of life. Integration of the current densities obtained by the Faraday probe suggest the HC mode exhibits much higher propellant utilization efficiencies ($I_b m_i/(e\dot{m}_i) \sim 75\%$ vs. $\sim 32\%$) but much lower beam efficiencies ($I_b/I_a \sim 75\%$ vs. $\sim 94\%$) than LC mode, though the effect of the elevated keeper current on the LC profiles is unclear. The half-angle of the cone containing 90% of the beam current is around 70° in HC mode and only 60° in LC mode.

The main breakthrough of Gildea's measurements was in time resolved monitoring of the anode current which revealed a sharp contrast in the signal spectra of the two operating modes. In HC mode the anode current is seen to oscillate regularly at a fundamental frequency of 3.5 to 4 kHz with peaks nearly 5 times the time-averaged value and minima near zero. Plots of the anode current power spectral density show

strong harmonics of the fundamental mode up to frequencies of almost 100 kHz. In LC mode, current oscillations were less than 10% of the time-averaged value and far more chaotic.

A more thorough examination of the nature of the anode current oscillations was later performed [19] using a high speed camera and AC coupled anode current probe to examine trends in the fluctuations with different operating conditions. The anode mass flow rate was scanned from 0.44 mg/s to 0.98 mg/s with a constant anode voltage of 250 V (to maintain the oscillatory HC mode) and a keeper current of 0.5 A. The anode voltage was varied from 250 V to 350 V for an anode flow of 0.84 mg/s and from 300 V to 450 V at a flow of 0.64 mg/s. The chamber pressure was also varied from about 1.9×10^{-5} Torr to 4×10^{-5} Torr using an auxiliary flow of xenon input far from the thruster at two different anode operating points: 200 V and 0.48 mg/s as well as 250 V and 0.38 mg/s to see what effect neutral ingestion might have on discharge oscillations.

Ultimately, a discernible, monotonic effect on the character of anode oscillations was only found for the anode flow rate scan. The fundamental oscillation frequency was shown to vary nearly linearly from 2.4 kHz to 3.8 kHz as the flow rate was raised from 0.44 mg/s to 0.98 mg/s, while the peak-to-peak amplitude nearly doubled. Interestingly, the character of the anode current waveform changed with the anode mass flow rate as well, with sample AC current measurements (i.e. time-varying component only) from this study shown in Fig. 4-2. The figure reports the anode flow rate in sccm[b] of xenon, where 1 sccm Xe = .0983 mg/s.

At low enough flow (0.34 mg/s) the LC mode is obtained which exhibits very little fluctuation, as the flow is increased (0.54 mg/s) a small amplitude ripple of several kHz in the AC coupled current develops which grows in amplitude with time before peaking and extinguishing in a semi-regular pattern of 2-5 ms period. At even higher flow rates (0.68 mg/s) a doubly peaked current waveform arises with the first peak,

[b]Standard cubic centimeters per minute (sccm) is generally more convenient in this report since all flow rates fall between 1 and 10 sccm and only one working gas is used. The volumetric flow rate at standard conditions, sccm in this case, is also the unit input and output to most mass flow controllers, making it more natural for reporting, despite the flow rate sensor integrated in the controller typically measuring mass flow.

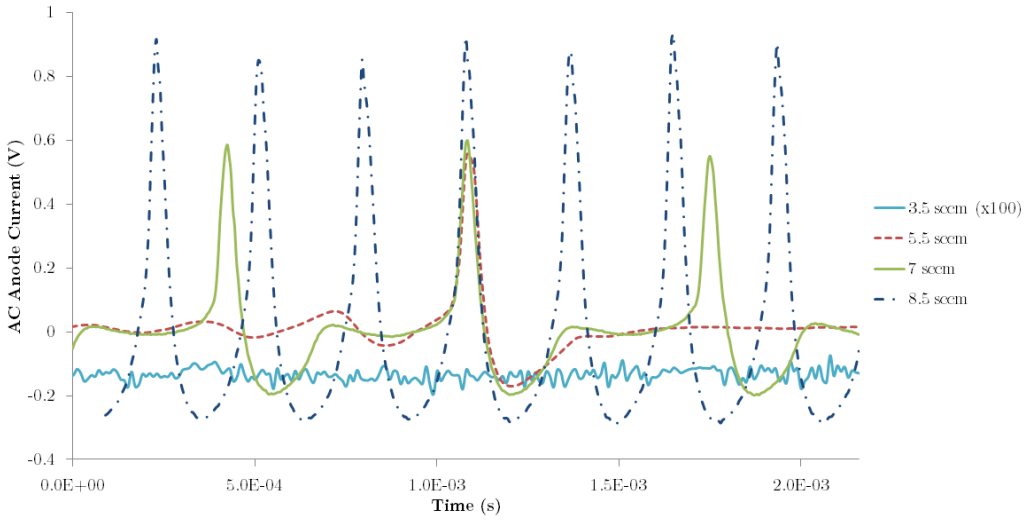

Figure 4-2: Sample AC anode current measurements at various anode mass flow rates of xenon with the DCFT operated at 250 V and a 0.5 A keeper current. The AC sensor measurement is amplified by a factor of 100 for the 3.5 sccm case (which is the only condition in LC mode) to allow its comparison to HC mode measurements.

occurring about 0.18 ms into the cycle (i.e. time since minimum current), barely overshooting the DC current value before subsiding slightly then rising to a peak of several Amperes, 0.55 ms into the oscillation, and quickly dropping to near extinction 0.12 ms later. The fundamental frequency of this cycle, based on the power spectral density, is twice the trough-to-trough frequency. At higher currents (>0.84 mg/s) the cycle converges to a regular pattern of large, sharp current peaks, with no more stunted local maxima and roughly 0.3 ms between minima.

These current oscillations are believed to be breathing modes in which an ionization avalanche occurs–as the plasma density increases through ionization there are now more electrons to ionize even more propellant–until the neutral propellant is almost fully depleted and ionization abates, allowing the plasma to be evacuated from the device faster than it is replenished. This is followed by a slow refilling of neutral particles before a new cycle of ionization begins. All three HC mode conditions plotted in Fig. 4-2 exhibit a constant 120 μs time difference between anode current maxima and the adjacent minima–this makes sense if the plasma is being flushed from the device at the ion speed (set to some degree by the anode voltage which is kept constant here) during the portion of the cycle when ionization is negligible. The time

between a current minimum and the subsequent current spike (as in the 0.84 mg/s case), stunted peak (0.68 mg/s) or attainment of the DC current value (0.54 mg/s) is also quite similar between cases, lasting 165, 175 and 220 μs for the respective (decreasing) flow rates. The neutral refill portion of the cycle commences some time before the current reaches a minimum and ends some time before it reaches its first local maximum, so it is expected to be some time between 0.15 and 0.3 ms for the conditions above. For a nuetral flow speed of 100 m/s the refill distance is about 1.5 to 3 cm, where 2 cm is roughly the distance between point cusps (or roughly equivalently separatrices) and 5 cm the distance from anode to exit.

At anode inputs of 200 V and 0.48 mg/s the addition of auxiliary xenon was seen to at first to have no perceptible impact on oscillation frequency, but at background pressures between 2.5×10^{-5} Torr and 4×10^{-5} Torr the frequency rose, non-monotonically from 2.7 kHz to 3.3 kHz. Throughout the pressure scan an observable, but relatively small increase in the DC anode current was noted as more auxiliary flow was added, suggesting a non-negligible effect on thruster operation due to background neutrals. At 250 V and 0.38 mg/s to the anode the effect on frequency was unclear, but at pressures above 2.5×10^{-5} Torr the thruster was seen to operate in a third mode, with almost no oscillations and a higher than normal anode current. The plume in this mode is visibly reddish, with a seemingly uniform conical jet diverging at the normal angle (see Fig. 4-1), and was first noted in a spectroscopic study of the DCFT by Matlock *et al* [20] where it is referred to as the 'diffuse' mode. We refer to this mode here as the ultra-high current (UHC) mode since current levels are significantly higher than found in HC mode.

The sharp jump in anode power and oscillation level seen in the DCFT is comparable to bifurcations noted in the literature for some similar plasma thrusters. Some examples of these dual modes are given in the following sections with particular attention to Hall thrusters. Of course, steep mode transitions are observed in many other plasma devices, such as Helicon thrusters when the RF power coupling mode changes and even Tokamaks where transition from low-confinement (L-mode) to high-confinement (H-mode) is observed accompanied by transient bursts in plasma flux to

walls. However, the general nature of the DCFT dual-mode is at first blush more comparable to the different oscillatory modes of Hall thrusters and their constituent hollow cathodes.

4.1 Dual Modes in Hall Thrusters

In typical Stationary Plasma Thrusters it has long been known that the level of the applied magnetic field, the anode mass flow rate, and applied voltage all have a strong effect on both the discharge current and the nature of the observed current oscillations [168, 169]. While these differing parametric regimes do not often result in a sharp transition in thruster power, they can effect discrete changes in the nature of discharge current oscillation modes and are thus important for contextualizing the bifurcated modes presented in the following section.

4.1.1 Oscillation Based Regimes of Operation

An early review of the oscillation characteristics over a range of magnetic field strengths is given by Tilinin [168], which examines the high-frequency components of the oscillation along with the usual high amplitude, low-frequency fluctuations which define the different magnetic regimes. An SPT fitted with flush mounted wall probes for detecting plasma density fluctuations is run at 200 V and a constant flow of 4 mg/s of xenon. When the maximum magnetic field in the channel is less than 60 G the thruster is in the so-called 'classical conductivity' regime where oscillation levels are low and Coulomb collisions are sufficient to explain the high discharge currents measured. The anode current monotonically decreases as the field is increased past 60 G and a fairly low amplitude drift wave becomes detectable along the length of the channel which is characterized as an azimuthal 'spoke' connecting anode to the exit of the thruster.

At field strengths above around 80 G the thruster enters a third regime (called the transition regime by Tilinin) where breathing, or 'loop', mode oscillations become prevalent at frequencies around 3 to 15 kHz, and other instabilities are relatively

weak. Tilinin describes this regime as one of low conductivity along the channel due to a lack of turbulence induced transport, though the current is still higher than classically predicted. A subsection of this regime, at fields between 100 and 140 G, the high frequency spectrum rises in amplitude and 70-500 kHz transit-time waves, characterized by the time for ions to leave the ionization region, become apparent along with a slight rise in the drift wave amplitude.

At higher magnetic fields an optimal regime is reached where the discharge current reaches a minimum. The loop oscillations become stable and are of a lower amplitude than in the previous regime (by about 1/3) and a higher frequency (10-20 kHz), while the drift wave is substantially diminished. The transit time oscillation is seen to coincide with a small spatial region just upstream of the peak magnetic field, which is expected to be the only location where the stability criterion,

$$\frac{d}{dz}(ln\frac{B}{n_e}) \leq 0 \tag{4.1}$$

is violated. The axial (i.e. longitudinal) coordinate is denoted z in Eqn. 4.1.

Past this optimal regime, at fields greater than 175 G, there is in fact mention of an abrupt jump in discharge current and breathing mode amplitude, accompanied by a strong increase in transit-time and higher frequency components of the spectrum as well. Operation in this regime was highly unstable and often resulted in self-extinguishing of the thruster. Beyond 230 G the discharge was once again stable and dominated by transit-time oscillations, with drift waves no longer being measured. Operation here was labeled the 'magnetic saturation' regime, due to the constancy of the discharge current and spectral characteristics as the magnetic field was raised up to 400 G. A more extensive review of oscillations in magnetic regimes, based on this architecture, is given by Choueiri [169].

The stability criterion noted by Eqtn. 4.1 is derived by Morozov et al [171] based on the dispersion relation for a linearized set of 2-D fluid equations for the ions and electrons. The continuity and momentum equations are given in axial and azimuthal coordinates without consideration of pressure gradient forces or collisions of any kind.

The steady state case is given as one with constant ion velocity in the axial direction and electrons drifting azimuthally with the ExB speed.

A similar classification of Hall thruster operation into regimes based on oscillations is presented by Gascon, Dudeck and Barral [4] which instead delineates regimes based on anode voltage, a scheme much more applicable to the relatively fixed field DCFT. The first regime is at low voltages (<100 V), where the anode current increases with applied voltage, and it exhibits moderate fluctuations at 5-15 kHz attributed to a rotating 'spoke' instability, with the main frequency shown to increase with voltage. In the second regime, centered around an inflection point in the anode I-V curve, the spoke instability lessens and more broadband noise occurs in the 20-80 kHz range. The third regime occurs between 120 and 160 V where the anode current actually decreases with voltage. In this regime, larger amplitude regular oscillations appear with a fundamental frequency around 5 kHz and up to 5 strong harmonics, which are associated with the loop oscillations of Tilinin and seen to grow in frequency with anode voltage. The waveform shown for this regime somewhat resembles that of the DCFT at 250 V and 0.68 mg/s of xenon [19].

The fourth regime occurs in a saturated regime of the anode I-V curve where current no longer changes with voltage. Here the fluctuations are fairly small but occur at a main frequency which increases with voltage from about 10 kHz to 20 kHz as the voltage rises from around 160 V to 340 V. The fluctuations are noted to be largely diminished at this point by an RLC low-pass filter applied to the anode power supply. In the fifth regime, spanning from 340-520 V, the anode current remains saturated but large amplitude, sinusoid-like oscillations arise with a fundamental frequency of 20-25 kHz and up to four harmonics. As the anode voltage is increased in this range the oscillation amplitude grows to nearly 100% of the DC current and the peaks become sharper. The RLC filter is not effective in diminishing these oscillations, which are identified as a breathing instability and are very similar in appearance to the waveforms of the DCFT at 250 V and a 0.84 mg/s anode mass flow rate [19]. They are seen to grow in amplitude, and to some extent frequency, slowly with voltage.

In a sixth regime (>540 V) the anode current exhibits a small jump upwards as

does the amplitude of oscillations, which are now comprised of a mixture of irregular small peaks and large sharp peaks over three times the time-averaged value. The main frequency here is around 15 kHz and is seen to trend downward as the anode voltage increases, though the oscillations are still thought to be of the breathing type. A seventh regime exists above 600 V, but only when the flow rate is decreased from the nominal value (from 5 mg/s to 2 mg/s in the example provided) and is marked by a sharp decrease in oscillation amplitude. The DC current, however, is higher than in the sixth regime. In a companion paper, a 1-D transient fluid model developed by Barral et al [170] reproduces the jump upwards in discharge current and drop in oscillation frequency at high voltages and shows that the discontinuity coincides with the space charge saturation of the wall sheath in the acceleration region.

4.1.2 Discrete Mode Transitions

The classification of Hall thruster operation into different regimes of low-frequency oscillation characteristics is a useful tool for organizing the effects of various operational parameters on the plasma response. Access of the various regimes appears to be dependent on both input conditions and particular thruster design features. The following section will describe various Hall thrusters which, under certain small parametric changes, exhibit large jumps in operational behavior.

Brown and Gallimore find a discrete change in Hall thruster operational mode at low anode voltage which results in a sharp jump in anode current and visible plume appearance[3]. They perform a systematic study of the mode change providing the best known baseline for comparison to our bifurcating operation. The thruster is a 6 kW laboratory model similar to the P5, with a centrally mounted neutralizing cathode and an RLC circuit attached to the anode power supply for low-pass filtering. The chamber pressures obtained during thruster operation never breached 1.5×10^{-5} torr with Xe mass flow rates of up to 20 mg/s.

The low current mode was found to be the normal mode of operation for the thruster at anode voltages above 115 V, while the high current mode could be obtained either by lowering the fraction of propellant flow rate going through the cath-

ode compared to the anode or changing the current through the electromagnets to settings off-optimal. Alternatively, at constant cathode flow fraction and magnetic field, the low current mode is obtainable by increasing the anode voltage, similar to the DCFT. It was also demonstrated that the low current mode could be maintained while lowering the cathode flow fraction if an auxiliary flow of Xenon surrounding the cathode tube was used to keep the cumulative flow through the central bore constant.

The high current to low current transition is marked by a $\sim$ 10% drop in the anode current, an extension of the plume visible emission intensity downstream and a suppression in anode current oscillation amplitude from near 50% of the mean current to $<$ 10%. Plume measurements indicate that the beam efficiency (I_b/I_a) also jumps upwards by 4 to 10% and the beam divergence ($cos^{-1}(I_{axial}/I_b)$) half-angle decreases by 1 to 5°. Another interesting feature of high current mode is the large dispersion in ion energy per charge as measured by an ExB probe in the plume, which the authors suggest could be due to an oscillation in the location of the ionization region at the same rate as the fundamental anode current mode.

Brown and Gallimore find that the cathode flow fraction necessary for mode transition decreases as the anode flow rate is increased for the 100 V case, but is a roughly constant 8% at 110 V. We can take an alternative view of this and see that at 100 V and about 2 mg/s of xenon to the cathode, the transition occurs regardless of anode mass flow rate (between 10 and 20 mg/s), while at higher anode voltages the cathode flow rate must be increased roughly proportionally with the anode flow for transition to occur. So, for example, at 110 V and a cathode flow of 1 mg/s, the thruster transitions from high to low current mode as the anode flow increases from 10 mg/s to 15 mg/s, which is the opposite of the anode mass flow effect seen in the DCFT.

The measured anode current oscillations have a fundamental frequency around 6 kHz, matching the frequency of measured cathode-to-ground voltage oscillations, with distinct harmonics appearing in the high current mode. The harmonics, which are not apparent in low current mode, appear to be reduced when the chamber pressure is increased. Increasing the chamber pressure further eventually led to a transition into low current mode during operation at 120 V, 10 mg/s of anode flow and a cathode

flow fraction of 7%. The fundamental frequency change, from 5 kHz at 105 V and 20 mg/s of anode flow to 6 kHz at 120 V and a 10 mg/s anode flow, follows a trend opposite that normally observed in the DCFT.

Ultimately, the authors suggest the mode change and concurrent oscillations are due to either an ionization instability, such as the common Hall thruster breathing mode (estimated at 7 kHz for their conditions), or an azimuthal spoke mode normally associated with low voltage operation, or a cathode instability, noting the jump in cathode oscillations found elsewhere accompanying a switch from spot to plume mode [144]. The evidence seems to support their hypothesis that the high current mode arises from a lack of neutrals near the exit. The authors suggest the dearth of neutrals may exacerbate a breathing instability, with the concurrent oscillations in plasma potential being fractionally more important at lower anode voltages. The relationship between this instability and the measured increase in backstreaming electron current is not examined.

Azziz describes a discrete visual change in the BHT-1500 plume occurring due to changes in magnetic field, accompanied by a transition in anode current oscillation amplitude[138]. A so-called 'jet' mode is obtained by adjusting the electromagnets to minimize the discharge current, which is characterized by a bright central jet and a breathing type oscillation in the anode current at 25 to 30 kHz and an amplitude of around 50% of the mean discharge current. An alternative mode, labelled 'collimated', is produced by lowering the magnet current to minimize anode current oscillations and is characterized visually by the disappearance of the central jet and emergence of a bright cylindrical region near the thruster exit.

Measurements of the plume structure by Azziz using both Faraday and RPA probes revealed a majority of the ion beam in the collimated mode is confined to within about 20° of the thruster axis, while the jet mode ion current is spread out to higher angles. The collimated ion energy distribution is peaked within 50 V of the applied potential within 20°, but at higher angles a second peak (distinct from the characteristic CEX peaks near the wings) at around half the applied voltage overtakes the high energy one and decreases in peak energy with increasing angle

from the thruster centerline. In contrast, the jet mode exhibits a continuous, low amplitude spread to lower energies at angles greater than 20°, without coalescence at any particular energy.

The author posits that the collimated mode is due to changes in the magnetic field allowing the main ionization region to move upstream into the insulated channel. Ions born in the channel and accelerated to high divergence angles are then lost to the walls instead of becoming part of the plume, explaining the collimated shape of the plume. The lost ions lead to wall heating and a recirculation of neutrals which can then be re-ionized at lower potentials or become involved in charge exchange collisions, resulting in the moderate energy ions found at high angles in the collimated mode. The hypothesis of collimation leading to higher wall losses was tested using thermocouples to monitor the channel wall temperature during mode changes. A clear rise in temperature was found when entering the collimated mode and taken as an indication of higher ion losses to the walls.

A cathode emission correlated mode change has been investigated by Raitses et al [153] using both a Cylindrical Hall Thruster and normal annular one, which also results in plume collimation and discharge oscillation suppression. The transition is not characterized by a steep jump in anode current, like the kind observed by Brown and Gallimore, but is instead a change from allowing the neutralizing hollow cathode to run in a self-heating mode with no applied power, to driving an auxiliary current through the emitter by applying a potential between it and the surrounding keeper structure. The authors claim that the anode current is not limited by the magnetic field when the cathode is in the self-sustained mode, but instead by the supplied electron current. Only when a high keeper current, of around 3 to 5 times the anode current in the cases presented, is supplied (or alternatively high heating to a thermionic filament cathode) can the discharge current saturate and become magnetically limited.

Measurements of the ion current density in the plumes of both thrusters demonstrate a much higher concentration to small angles (from thruster centerline) when a high keeper current is applied. The authors invoke the measured movement of the

acceleration region upstream within the channel, where the magnetic field topology is more favorable, as a probable explanation for the focusing of the beam. The CHT plume divergence (defined by the angle containing 90% of the beam current) half-angle drops from around 70° to 55° when the keeper current is increased from 0 A to 3 A. Meanwhile, the mean ion energy at low angles is seen to increase in both hall thruster types on the order of 10-30 eV.

When the polarity of the outer CHT electromagnet is reversed a cusp region forms on the outer channel wall and the thruster responds differently to the increased keeper current. In the normal configuration the anode current increases from about 0.57 A to 0.66 A with the increased keeper current, while in the cusped configuration the discharge current drops from 0.72 A to 0.65 A. While the propellant utilization increased with the applied keeper current in the normal configuration, it appeared to slightly drop during cusped operation, suggesting the drop in anode current in this mode is mainly due to a decrease in the beam current. The plasma potential and electron temperature at the exit plane are measured to drop when keeper current is applied regardless of the polarity of the outer magnet.

Low frequency anode current oscillations at around 20 kHz for the annular thruster and 10 kHz for the CHT were entirely quenched by the application of keeper current. The authors suggest that a local negative differential resistivity is suppressed by the additional electron current, though the precise nature of this mechanism is unclear. The sinusoid-like oscillations in the self-sustained mode appear to be somewhere near 60% of the mean current in mean-to-peak amplitude, while the sinusoid is essentially gone during operation with high keeper currents. The authors bring up several theories for low frequency Hall thruster current oscillations including an ionization front wave ($\omega \sim v_n/L$), a predator-prey cycle ($\omega \sim \sqrt{v_i v_n}/L$) and a Buneman type instability caused by the coupling of electric field with ion current as explanations for the self-sustained mode oscillations.

The authors also report increase in the fraction of multiply-charged ion flux going from self-sustained mode to a keeper current mode, from 10% and 2% for double and triply charged ions respectively to 30% and 20%, measured 40° off the thruster

centerline. This is suggested to be due to long residence times of ions born near the bottom of the potential hill, which moves upstream with increased keeper current.

The plasma potential (with respect to the cathode) measured at the exit of the annular thruster dropped from 75 V to 40 V as the keeper current was raised from 1 A to 3 A, while the anode current rose from 0.51 A to 0.58 A. An increase in backstreaming electron current with keeper current was given as the reason for the observed trend in anode current. The plasma potential in the CHT also dropped going from self sustained mode to keeper driven operation, from 165 V to 90 V just past the exit, while the electron temperature dropped from 25 eV to 15 eV.

The authors use a simplified Ohm's law, with Bohm-type diffusion to estimate an increase in the electron cross-field mobility by two times when changing from magnetically limited to self-sustained mode. The calculation essentially assumes that only the backstreaming electron current and electric field change, with the latter being the main driver for the factor of two obtained.

A follow-on study by Granstedt et al [154] was aimed at detangling the effects of enhanced electron emission from other hollow cathode phenomena by using a thoriated tungsten filament cathode instead. The results showed far less dramatic effects on the plume collimation with enhanced electron emission, although the 90% beam current half-angle did drop from 62° to 57° as the anode current rose (due to increased filament current only) from 210 mA to 230 mA. RPA measurements showed a shift in the mean ion energy in the plume from about 179 eV to to 193 eV over the same span of discharge currents with an applied voltage of 250 V, while the cathode-to-ground potential only increased around 2 V (from -3 V to -1 V). The beam efficiency (I_b/I_a) actually appeared to drop slightly using the higher filament current, which was attributed to increased backstreaming electrons, though the effect is within the given uncertainty of the measurement.

The authors also find a dependence of the measured plume characteristics on the position of the filament, which is generally strung in a wide arc across the face of the thruster. They also note a steady increase in electron backstreaming current over the course of several days for the same operating conditions, which is considered to be due

to the accumulation of sputtered tungsten from the filament onto the ceramic channel walls resulting in a conductive layer. Overall, the study indicates that some of the plume effects found in the non self-sustained hollow cathode mode can be attributed to higher levels of electron emission. No mention of current oscillations is made.

A further follow-up by Parker et al finds that not only does enhanced electron emission suppress low frequency anode current oscillations, it can also extinguish a rotating spoke instability. The spoke was seen visually with a high speed camera and measured with azimuthally separated, flush mounted Langmuir probes inside the discharge chamber to rotate at a frequency of 15-35 kHz. As the keeper current was raised past a threshold value of around 2-3 A the beam efficiency jumped up from 48 to 63% (due mainly to a drop in discharge current), the spoke disappeared, and an increase in anode current oscillations in the megahertz range was measured. A tungsten filament was used as an alternative cathode, as done by Granstedt et al, with results bearing out the trends observed with the hollow cathode. The spoke is only observed when the outer electromagnet is of the opposite polarity as the inner one, resulting in the so-called 'cusp' configuration. A permanent magnet version of the CHT, which displayed a hollow plume structure similar to the DCFT, also exhibited the spoke type oscillation at 3.3 kHz, simultaneously with a breathing oscillation in the discharge current at 14 kHz [21].

An investigation of facility effects on Hall thruster performance measurements undertaken by Walker [147] reveal a dependency of discharge current oscillation amplitude of 1 kW class thrusters on the background pressure in the chamber. Oscillations of frequencies of around 1 to 10 kHz were observed in a P5 thruster, consistent with normal Hall thruster breathing modes, which rose in amplitude as the background pressure (P_b) was increased from 5×10^{-6} Torr to 9×10^{-6} Torr for a flow rate of 5.25 mg/s of xenon. The oscillations recorded at high pressure were around 100% of the discharge current, with one case shown exhibiting current extinction at the low point of the fluctuation. No clear change in oscillation amplitude was seen for a flow rate of 10.46 mg/s, which the author attributes to a lower fractional entrainment of background neutrals.

Book and Walker examine the effects of cooling a Hall thruster anode, which in their case also serves as the propellant injector, on efficiency [148]. The experiment is based on the observation that cooler propellant leads to longer residence times in the chamber which may improve the propellant utilization efficiency of the device. The effect is predicted and shown to be proportionally greatest at low discharge voltages, since lower electron temperatures then require higher neutral residence times to proffer similar levels of ionization. They also find that cooling the anode led to a discernible, though not drastic, increase in the amplitude of anode current oscillations at breathing mode frequencies around 15 to 20 kHz. This was attributed to higher interaction rates between electrons and neutrals at lower neutral flow speeds allowing larger swings in electron flux to the anode. No discernible change in breathing mode frequency was found as the anode was cooled, which was not expected based on simple models of the oscillation, though the length of the ionization region is unquantified and may be changing with thruster conditions.

The accumulation of water on the Boron Nitride insulator of a 200-W Hall thruster was also found to cause a mode change by Hargus and Pote [149]. The first ten minutes of operation after exposure to atmosphere resulted in a diffuse plume and much stronger than normal discharge current oscillations at 18 kHz. After the hydrated layer burned off normal operation, with low amplitude 25 kHz current oscillations, was observed and remained through multiple re-starts until the next exposure to atmosphere. The diffuse start-up mode also exhibited a much larger than normal anode current which gradually decayed to the nominal level. The authors note that the change in the secondary electron yield, responsible for near wall conductivity, affected by hydration is a candidate for the observed change in anode current.

A recent study of a bi-modal operation in an annular Hall thruster shows perhaps the greatest similarity to the DCFT bifurcation [150], with a jump to a high anode current mode as the anode mass flow rate is increased. The high current mode is also marked by a large jump upwards in anode current oscillations, dominated by a 20 kHz breathing mode (which is far less prevalent in the lower current operation). The mode change is demonstrated to be due to the particular configuration of the

thruster (dissimilar to any of the thrusters listed above) in which the electromagnets which provide the radial magnetic field are placed in series with the discharge power supply, so that an increase in discharge current leads to an increase in the magnetic field strength. This particular mechanism is not directly available to the DCFT where the magnetic field is static, but a variation in the cross-field impedance of electrons with anode current may provide an analogous effect.

The occurrence of a bifurcation in the discharge current of a plasma device with a largely axial magnetic field [151] must also be noted here due to its strong resemblance to the DCFT mode change. The plasma of a cylindrical discharge column is noted to undergo a sharp, hysteretic jump from a low to high density state as the discharge voltage or magnetic field strength is increased, with a lower transition voltage at higher neutral pressures. The low density state (which is obtained through the same parametric changes which cause the transition to HC mode in the DCFT) also exhibits high amplitude plasma density oscillations with a peak frequency normally between 30-40 kHz (though at certain conditions a sharp peak at 10 kHz is seen with at least 3 strong harmonics) while the fluctuations in the high density state are broadband and less intense. The fluctuations are measured to propagate azimuthally with a phase velocity on the order of the ion acoustic speed.

Table 4.1: Bifurcations in Hall thrusters compared to DCFT

	Direction of parameter change which leads to highly oscillatory mode							
Thruster	$\dot{m}_a$	$\dot{m}_c$	P_b	V_a	I_k	I_{mag}	I_a	Notes
DCFT[19]	up	-	down$^{\mp}$	down	down	up*	up	
H6[3]	down	down	down	down	-	down	up	
BHT 1500[138]	-	-	-	-	-	up	down	(1)
BHT 200[149]	-	-	-	-	-	-	up	(2)
CHT[153, 155]	-	-	-	-	down	-	up$^{\pm}$	(3)
P5[147]	-	-	up	-	-	-	-	(4)

(1) Ionization shifts out (2) Hydrogenated BN (3) I_k kills spoke (4) Only low $\dot{m}_a$ $^{\mp}P_b$ causes 3^{rd} mode *Only when very high[156] $^{\pm}$In cusp mode

4.2 Dual Modes in Hollow Cathodes

The hollow cathodes used to sustain the discharges of both ion engines and Hall thrusters also exhibit a prominent bifurcation, marked by discrete changes in visual appearance and plasma oscillations. It is generally found that at low cathode propellant flow rates the cathode runs in 'plume' mode with an extended luminous region appearing past the keeper electrode. Alternatively, at high mass flow rates the cathode plume appears as a compact region of luminosity near the keeper orifice, corresponding to the so-called 'spot' mode.

An early characterization of the two modes by Csiky [139] was conducted with a Mercury vapor-fed hollow cathode coupled to a circular disk anode placed at varying distances from the cathode orifice. When the discharge current was set high the cathode operated in spot mode with low voltages (13.5 V at 2 A) between anode and cathode. When the discharge current was lowered past a certain point the plume mode was obtained and the discharge voltage required to maintain the current (60 V at 0.3 A) increased substantially. The plume mode is noted to exhibit oscillations ranging from 1 kHz to 1 MHz (unclear whether measured in plasma or on power supply) while the spot mode is noise-free.

Csiky was also able to obtain a smooth transition from spot to plume mode by increasing the distance between the cathode and anode, for a given mass flow rate, or by decreasing the mass flow rate, at a given anode distance. In both cases there is some region of parametric overlap where the cathode is observed to operate in either mode. Langmuir probe measurements indicate a much higher density in the inter-electrode region in the spot mode case, which Csiky uses as an indicator that the mode transition could be due to the internal wall sheath size approaching that of the cathode orifice. A cathode keeper was used to initiate the plasma and was kept on, except during the anode position experiments, at around 10 V and 0.1 A.

Fearn and Philip [140] also use a Mercury fed cathode and axially separated disc anode to examine the spot-to-plume mode transition, interestingly by changing the geometry of their Molybdenum cathode orifice. A stair-stepped, cylindrical orifice

consisting of one section with a large inner diameter upstream of a regular sized section at the exit resulted in two mode transitions, similar to the plume-to-spot transition in that a continuous increase in discharge current lead to discontinuous drops in the required discharge voltage. A bell curve shaped cathode orifice with a smoothly decreasing inner diameter resulted in no transitions to plume mode at much lower flow rates. The authors suggest that the change in transition point with geometry stems from the electron emission current density being constant during operation, while the active area of emission must rise to meet increasing discharge current demands. The emission area eventually includes the cathode orifice, which they suppose is emitting largely due to impact by excited metastable Mercury ions, which when activated leads to a large jump in available emission current and thus a decrease in requisite voltage.

In a 1990 paper, Fearn et al [141] extend their work on Mercury vapor fed cathodes to the use of noble gas propellants. Through the use of xenon, krypton, argon and neon they find a general trend in the need for higher mass flow rates to obtain spot mode as the atomic mass of the propellant decreases. For the same mass flow rate of Noble gas a lower atomic mass means a higher neutral particle density, flow speed and ionization potential. A stronger dependence of the mode transition on keeper current is also found when using noble gases instead of Mercury. At lower discharge currents a substantially higher keeper current is required to enter spot mode. Fearn et al also find the oscillations in discharge and keeper voltage to be much higher in amplitude for rare gases. For fixed currents an increase in cathode mass flow rate led to a gradual drop in keeper and discharge voltages while the amplitude of voltage oscillations rose. As the cathode transitioned to spot mode the discharge voltage exhibited its usual sharp drop (about 26 V to 15 V) and the voltage oscillations on both electrodes diminished by more than twenty fold (2-4 V peak-to-peak to < 70 mV). The DC keeper voltage, meanwhile, is not effected by the change in mode. The voltage oscillations were of a quasi-sinusoidal shape at a frequency of 1.2 MHz.

Studies by Jack et al [142] demonstrated the effect of cathode-to-keeper distance on spot mode accessibility, using a Xenon fed cathode and rectangular plate anode. As

the keeper spacing was increased the amplitude of voltage oscillations on both anode and keeper were drastically reduced, however, past a certain separation the keeper voltage noise began to rise again, signifying some optimal distance could be found. The experiments also revealed a strong dependence of voltage oscillation amplitude with keeper current, as the anode noise rose quickly with keeper current, especially for small keeper spacings. The authors also found a general enhancement of discharge stability when using a keeper which enclosed the entire cathode assembly, as opposed to earlier experiments where the keeper was essentially a simple tantalum washer.

In a 1994 paper by Mandell and Katz [143] the transition between the two modes is theorized to be due to a change in sheath polarity at the keeper. In their model, the spot mode corresponds to operation with sufficient ionization to more than support the discharge current, resulting in the normal electron-repelling sheath forming at the keeper electrode, which itself collects a current greater than or equal to the discharge current. When the mass flow rate becomes too low to allow sufficient ionization to match the discharge current the sheath becomes electron-attracting at the keeper and the cathode is in plume mode. The attracting sheath adds energy to electrons in that area resulting in enhanced radiation and ionization in the keeper orifice region. It is not immediately clear why the keeper should try to match the discharge current, as it is classically purposed for cathode plasma ignition after which it is turned off, though in some cases it remains on to maintain enough ion bombardment heating of the insert for sufficient field enhanced thermionic emission.

Thorough investigations of the oscillations in the cathode, keeper and anode region plasmas, were conducted by Goebel et al [144, 145] on several xenon-fed hollow cathodes set 1 cm upstream of a simulated, 30-cm diameter NSTAR ion thruster chamber with a ring-cusp magnetic field, but without ion optics. A solenoid encapsulating the keeper was used to simulate the largely axial magnetic field found near the cathode in the typical NSTAR configuration. In this arrangement they do not find a sharp transition in discharge voltage or current, but instead a continuous increase in the relative amplitude of discharge current oscillations as the mass flow rate is lowered or the DC level of the discharge current is increased. Increasing discharge current also

led to an increase in the fundamental frequency of oscillations. The large amplitude current oscillations measured at low flow rates are at relatively low frequencies (50-250 kHz) and appear similar in character to the ionization instabilities seen at low frequency in Hall thrusters, while at high mass flow rates the measured oscillations are incoherent with frequencies on the order of 2 MHz.

The low frequency discharge oscillations are also shown to be obtained or quenched with parametric adjustments other than the normal flow rate and discharge current. Plasma potential fluctuations, measured at the edge of the cathode 'plasma ball', turn from incoherent noise less than 30% of the mean potential to over 100% oscillations with a regular frequency of around 80 kHz when the axial magnetic field at the cathode is dropped from 78 G to 10 G [145]. Langmuir probe measurements of the ion saturation current reveal similar trends with the onset of high amplitude, periodic fluctuations occurring at low magnetic field, where discharge current oscillations are seen to nearly extinguish the plasma each cycle. Radial RPA measurements just downstream of the keeper exit and 7.5 cm off-axis revealed a large fraction of ions have energies greater than the discharge voltage when the magnetic field is turned down, corresponding to some extent with the large swings measured in the plasma potential.

The introduction of an auxiliary flow of neutral gas near the cathode plume is shown to effectively quench the high amplitude oscillations and the corollary existence of high energy ions [144]. The suppression of oscillations using an external flow allows large reductions in the internal cathode flow while maintaining a spot mode type operation. In fact the total flow, auxiliary plus internal, is found to be half of what is ordinarily needed to obtain a quiescent mode of operation. Alternatively, the addition of auxiliary flow through the region between keeper and cathode is found to be far less effective at quenching oscillations, obtaining the same discharge voltage with 2.5 times the flow needed with the external port. The high energy ion content is higher with the keeper flow than the external port as well, and the discharge voltage is observed to fluctuate on cathode heating timescales. The authors conclude that the difference in the efficacy of the two auxiliary flow systems is due to the much

higher temperatures expected for flow input inside the keeper enclosure, leading to lower neutral densities as the gas reaches the plume. High densities of neutrals in the plume can increase ionization and collisionality, both of which are suggested as mechanisms for reducing oscillations. This was also the explanation used by Brown and Gallimore to explain their low voltage Hall thruster bifurcation.

The strong correlation between Langmuir probe measured density oscillations and discharge current fluctuations leads the authors to believe the periodic mode is an ionization instability. They estimate the instability frequency as the ionization rate normalized by the ion density and find it in close agreement with the measured frequency [145]. Oscillations in the ion saturation current were not found in the cathode insert region, suggesting the instability begins in the region of cathode to keeper coupling or the region of keeper to anode coupling.

In summary, the hollow cathode mode transition appears to exhibit different tendencies depending on configuration, for example, whether the anode used is an axially displaced plate or a cone-to-cylinder enclosure, whether the keeper fully encloses the cathode or not, and what type of propellant is used. Throughout the different configurations a few persistent features appear. The keeper electrode and anode electrode coupling with the cathode are important in shaping the stable region of operation. The neutral density near the cathode exit appears to be the main factor in determining the nature of the discharge oscillations, for a given discharge current, leading to the conclusion that the plume mode is most likely due to the excitation of an ionization instability.

Though the characteristics of the mode change is very similar to that of the DCFT the operating condition dependencies trend in opposite directions. The visually diffuse, highly oscillatory mode is obtained in hollow cathodes by lowering the flow rate or increasing the discharge voltage, while for the DCFT this is the recipe for obtaining the quiescent, visually collimated regime. Experience has shown, however, that an increase in the keeper current can be useful in aiding the transition from oscillatory to quiet operation in the DCFT [18], hinting at the importance of cathode to anode coupling in exciting the different operational modes. The precise correlation has yet

to be adequately characterized.

4.3 Discharge Current Oscillations

There is a preponderance of evidence linking the existence of bifurcating operational modes in numerous plasma devices with the onset of large amplitude oscillations [4, 3, 138, 153, 139, 141, 145, 151]. In many cases these appear to be due to ionization related instabilities, among which either an azimuthal spoke mode or an axial breathing mode are often cited [4, 3, 153, 145]. High frequency imaging of the DCFT has revealed no signs of any azimuthal modes affecting luminosity, but does indicate a standing pattern of brightening and dimming occurs in the discharge chamber accompanied by an axially traveling ball of luminosity past the exit plane [19]. For this reason, the following section focuses primarily on breathing mode type oscillations prevalent in Hall thrusters.

Breathing oscillations refer to a regular fluctuation, clearly manifested in the discharge current, on a time scale near the neutral flow filling time (i.e. v_n/L) which is azimuthally uniform. One of the first models of the breathing mode was put forth by Fife et al in a 1997 paper as a simple physical justification for the regular current oscillations seen in their Hybrid-PIC (electrons treated as a fluid, ions treated kinetically by particle-in-cell method) simulations of an SPT [157]. They consider a 0-dimensional situation in which neutrals enter a volume at a constant velocity, v_n, and are ionized at a rate proportional to the plasma and neutral densities. The produced ions exit the volume at a constant velocity, v_i. The continuity equations for the two species follow as,

$$\frac{\partial n_n}{\partial t} = -\beta n_n n_i + v_n n_n \frac{1}{L} \tag{4.2}$$

$$\frac{\partial n_i}{\partial t} = \beta n_n n_i - v_i n_i \frac{1}{L} \tag{4.3}$$

where L is the length of the ionization volume and β is the ionization reaction rate in m^3/s and is only dependent on electron energies. Linearization of the equa-

tions, assuming constant electron temperature, results in a characteristic frequency of $\omega = \beta\sqrt{\overline{n}_i\overline{n}_n}$ where the overbar refers to unperturbed, or equivalently time-averaged, quantities. The equilibrium solution of the equations allows the frequency to be re-expressed as $\omega = \sqrt{\overline{v}_i\overline{v}_n}/L$. This system describes a 'predator-prey' type oscillation where cycles of strong ionization deplete the neutral density leading to a lull in ionization until the propellant flow replenishes the neutral density, allowing the cycle to start over. The authors note that numerical solutions to the non-linear equations yielded similar trends, though the results are not presented. Also of note is that the linearization scheme used keeps the incoming neutral velocity constant but allows a neutral density fluctuation, tantamount to a dependency of the input neutral flow rate on the downstream neutral density that is physically incorrect (though it may not be a bad model as discussed in the following section).

At the same time optical measurements by Darnon et al found evidence of an azimuthally independent oscillation in the intensity of visible light emitted from the discharge channel of an SPT in phase with discharge current fluctuations [158]. The thruster was run at 300 V and 4.5 A on an anode flow of 5 mg/s of xenon and a cathode flow of 0.4 mg/s and exhibited a regular fluctuation at 33 kHz (and 3 harmonics), with an amplitude (referenced in this paper as half the peak-to-peak value) of nearly 100% of the time averaged value and peaks in phase with negative peaks of the cathode-to-ground potential. The visible emission was collected by translatable optics set up outside the vacuum chamber at a 45° with respect to the thruster axis. A phase change in the 33 kHz intensity fluctuation between measurements intersecting the discharge channel and those intersecting the plume were used to infer an axially travelling wave at 20 km/s, which corresponds roughly to the velocity of ions in the plume. No phase change was found between measurements which intersected the discharge channel at different positions.

Fast camera imaging of the thruster is also performed at a viewing angle which captures a portion internal to the channel. The authors identify several stages of the oscillation from these images, beginning with a ~ 15 μs growth in the intensity in the channel while the plume remains dim. At some threshold the growth in channel

intensity becomes more rapid and is joined by what is presumed to be the visible luminosity equivalent of ion ejection. During this roughly 6 μs long stage the cathode is at its brightest and the discharge current begins to peak. A 4 μs stage of channel emptying follows with the plume intensity and discharge current reaching a maximum before rapidly diminishing.

Optical and electrostatic methods were used by Meezan et al to characterize two low power SPT's with the results showing the predominance of a roughly 10 kHz, azimuthally independent mode when the thrusters are operated at high voltages [159]. They also find that the peak oscillation frequency increases non-linearly with anode voltage (a reasonable fit is obtained with $V_a^{1/4}$) and nearly linearly with peak magnetic flux density, citing the model of Fife et al as an explanation for the observed trends. Magnetic field data are obtained at peak fields of 120, 160 and 200 G.

More recent and extensive measurements of the breathing oscillation effects in the near and far-field plume have been made by Lobbia and Gallimore [167] for a 600-W Hall thruster. The thruster is operated at voltages between 200 and 500 V with discharge currents ranging from 1.5 A to 4 A, with the magnetic field set to maximize thrust and efficiency at the nominal 600 W operation (therefore the B-field is not optimal for lower power operation). The power spectral density of the anode current at each setting revealed the prevalence of multiple strong harmonics of the breathing mode at low voltages (150 and 200 V) which appear to be suppressed at higher currents in the 200 V case. A general trend of increasing fundamental frequency with applied voltage is shown, which somewhat tracks estimates based on the Fife et al model of the breathing mode.

More interesting is the strong correlation between electron density in the plume and discharge current traces versus time which exhibit a phase difference used to estimate an ion transit time of 24.7 μs (corresponding to propagation on the order of 10 km/s). The plasma potential and electron temperature in the plume are much more chaotic, and are said to have a component in-phase with current oscillations (due to high speeds of electrons) and a component in-phase with the density fluctuation (carried by the ejected ion wave). Tabulation of the oscillation parameters

over a range of operating conditions reveals an approximate expression for relative fluctuation amplitudes for the different plasma properties. The density fluctuation amplitude normalized by the mean is roughly equal to that of the current fluctuation, while the normalized amplitudes of electron temperature and plasma potential oscillations are about half that value.

Numerical and analytical models of varying fidelity have also been utilized to predict and describe both the breathing and spoke mode instabilities. The models range from 0-D, highly generalized theories to detailed 2-D PIC codes and are all capable of reproducing the basic nature of the fluctuation. All models discussed only consider electron impact ionization of xenon to a singly charged state.

An early quasineutral 1-D model by Boeuf and Garrigues [160] tracks ions using the Vlasov equation and treats electrons as a Maxwellian fluid. The magnetic field effect on the ions and ion losses to the wall are neglected with all ions born at the neutral flow speed, which is assumed constant along the thruster channel. Neutral atoms are modeled with the continuity equation with a constant input flux at the upstream boundary. The electron fluid equations are simplified by neglecting electron inertia, diffusion due to pressure gradients, heat conduction, and Coulomb collisions as well as all time derivatives, since the fluctuations of interest are much slower than typical electron time scales. The electron mobility is given the classical form but an effective collision frequency term is used which is the sum of the electron-neutral collision frequency and either an adjustable wall collision frequency term or Bohm-like fluctuation frequency. The mean energy of electrons entering the channel is set to 10 eV and the energy lost by electrons to the walls is estimated using a somewhat arbitrary, Boltzmann-like form.

Using a second-order upwind scheme for the ion equation and a fourth-order Runge-Kutta integration for the electrons the authors were able to reasonably reproduce the time averaged properties of an SPT-100. Discharge current oscillations were found to occur only at applied anode voltages between 200 and 350 V, which lies in the current saturation region of the discharge current vs. voltage curve. The oscillation amplitude grows with anode voltage up to 100% amplitude at 270 V and

then gradually decreases as the voltage approaches 350 V. The frequency of the simulated oscillation grows almost linearly with anode voltage from 15 kHz at 200 V to 22 kHz at 300 V.

Simulations of the magnetic field strength effect showed the onset of breathing oscillations at fields above 170 G, with the amplitude increasing to a peak value at 220 G before diminishing to extinction at 280 G. The frequency of the oscillation is seen to decrease as the magnetic field strength is raised and the magnetic field strength at fluctuation onset is shown to decrease at lower anode voltage. The resulting mode of simulated operation would seem to fit into the transition regime described by Tilinin, which for his thruster occurred at field strengths between 90 and 140 G, where breathing oscillations dominate the current spectrum and a gradual reduction in discharge current is seen with increasing field strength [168]. The authors claim to fit instead into the region of macroscopic instability occurring above optimal field strengths (170 G to 230 G) where the breathing mode is largest and visible instabilities were observed in experiments. The thruster simulated by Boeuf and Garrigues is a 100 mm channel outer diameter SPT at 240 V and 5 mg/s of xenon to the anode while the measurements of Tilinin are for a 90mm outer diameter SPT-type thruster 200 V with 4 mg/s of xenon, allowing for a reasonably close comparison. The main difference in the two thrusters are the magnetic field profiles, which peaks at the exit and has negligible strength at the anode in the simulations but for Tilinin peaks about 1 cm upstream of the exit and at the anode has a field strength around 10% of the maximum.

Simulations where the upstream magnetic field is increased resulted in a different character of oscillations. The original low frequency oscillations appear as a kind of sawtooth pattern in the neutral density front with time, due to rapid depletion of neutrals near the exit by ionization followed by a slow refilling after a dearth of neutrals leads to a drop in electron mobility towards the anode and ionization abates. The oscillations obtained with a higher upstream field appear at much higher frequencies (50-80 kHz) and are marked by periodic perturbations in the electric field in the region near the anode which propagate from anode to exhaust. In contrast to

the normal breathing mode, these oscillations were found to increase in frequency as the peak magnetic field strength was raised.

The authors also examine the effect of the artificial amount of electron wall-collisionality imposed in their model. They find a general trend of decreasing oscillation amplitude with increased wall collisions. This is explained by the increase in wall induced electron mobility and thus the weakening of the effect of neutral density on electron flux to the anode. The value of wall collisionality is set in their normal simulations to match experimental values of anode current under nominal operation. In a similar manner the term controlling electron energy loss to the walls is adjusted to maintain an ionization region localization near the peak magnetic field as seen in experiment. When using their Bohm-type collision frequency, which does not include any energy loss mechanism for the electrons, the authors find the electron front moves unimpeded deep into the channel resulting in unphysically high anode currents.

Chable and Rogier used a model nearly identical to Boeuf and Garrigues but find a different mechanism for the low frequency current oscillations [161]. In order to study the character of the oscillations they linearize the ion Vlasov, electron continuity and electron energy equations about steady state relations for the ion and neutral densities. The real eigenvalue components of the linearized rate equation (i.e. the linear growth rates) are then compared with oscillation amplitudes found through numerical solutions to the non-linear problem and found to trend similarly with anode voltage, magnetic field strength and neutral flow speed–this is somewhat surprising since the amplitude of such large oscillations ought to be determined by some non-linear saturation mechanism rather than the linear growth rate from a small-amplitude perturbation analysis. The authors then compare the eigenvalues of the linear equations when certain perturbation terms are turned off and find that unstable modes are only accessible if the plasma potential disturbances are included. They then conclude that the observed oscillations are driven solely by coupling between the ion current and electric field fluctuations.

The relative unimportance of the ionization terms allows them to construct a simplified model where the neutral density, magnetic field and electron energy are

held constant along the channel and the steady state ion speed is everywhere set to the exhaust velocity. The dispersion relationship results in a stability parameter which predicts oscillations to be damped when the cross field mobility approaches zero or infinity and when the neutral velocity is increased. The electric field fluctuation is identified as a Buneman-type instability and the authors state that it is responsible for the low frequency current fluctuations found in SPT's.

A similar approach is taken by Chesta, Meezan and Cappelli [162], but with a model extended to the azimuthal direction as well as the axial. Fluid equations are given for ions, neutrals and electrons which appear to neglect the pressure gradient (in the momentum formulations) and compression work (in the electron energy equation) along with the common assumption of zero heat conduction. Wall losses are considered as a sink for ions and electrons (they are oddly not considered a source of neutrals) with the loss rate determined semi-empirically through measurements of the axial distribution of plasma properties. Electron energy losses due to excitation of neutrals or wall collisions are not considered, but the electron inertia terms are kept through the initial linearization of the 2-D model. The model is then posed as an eigenvalue problem, at which point electron inertia is discarded, and the properties of the roots are examined numerically for a case of known time-averaged properties at low anode voltage. The results indicate an azimuthally tilted spoke instability is present at these conditions which is highly sensitive to the ionization rate.

Yamamato et al develop an essentially 0-D model of the dispersion relation beginning with the assumption that linear perturbations to the neutral density propagate with a phase velocity equal to the axial neutral velocity and evanesce with a wavenumber inversely proportional to the mean free path of ionization [163]. Perturbations to the plasma density are assumed to propagate instantly on the timescales under investigation and thus have no wavenumber. The continuity equations for electrons and neutrals, both neglecting ion recombination at the walls as a source of neutrals and sink of plasma, are then linearized about these assumptions. The authors maintain that electrons should be considered rather than the ions (as was done by Fife et al), due to the comparative slowness of electron cross field diffusion. This con-

sideration introduces the dependence of electron backstreaming velocity on neutral density when classical diffusion is considered. The resulting dispersion relation is far more complex than that of Fife, but is shown to agree reasonably well in its predicted oscillation frequency with measurements made on both TAL and SPT type thrusters. The dispersion of the SPT type device was derived assuming anomalous diffusion of electrons, which is independent of neutral density.

The model of Yamamoto et al also considers the non-equality of surface areas at the exit and anode sides of the thruster, which will likely be necessary for any rigorous derivations of the DCFT dispersion relation. After some simplification the derived dispersion relation shows that the range of stable operation is greater if the axial electron current normalized by the local plasma density is higher at the anode than the exit, assuming this condition has no effect on the volume ionization rate. The authors use this relation to suggest a divergent channel will have a smaller range of stable operation than a convergent channel, and then show experimentally that this bears out for some modified designs of both TAL and SPT type devices. If this same type of dispersion relation can be applied to the DCFT it may explain why the divergent chamber used in the MIT variant can operate in a highly oscillatory mode, while the use of cylindrical chambers in the Stanford variant and the HEMP-T results in the apparent extinction of this mode.

A more recent model of the breathing mode has been undertaken by Barral and Ahedo [12] which reviews the previous work on the topic and employs a more developed quasineutral 1-D fluid model. The model is 1-D in that it only considers axial gradients, however the plasma properties represent radially averaged values and the azimuthal electron velocity is considered in the electron momentum and energy formulations. The convective derivate of axial electron momentum is neglected, but not azimuthal and the applied voltage, electron temperature and azimuthal velocity at the exit and the ion velocity at the anode are held constant. The wall collision frequency is set by the channel width, Bohm velocity of ions and the secondary electron emission fraction from the walls, as opposed to the models discussed above where the wall collision term is adjusted to fit data or set semi-empirically. A quasi-steady

model is developed based on the equations in which $d(lnI)/dt$ and n_e/I reach a steady state.

The fully time-dependent model and the quasi-steady model are evaluated numerically and found to be in close comparison, especially in their rendering of the high amplitude, low frequency current oscillations. Noting this consistency, the authors then linearize the simpler quasi-steady model to analyze the oscillations. The frequency of the unstable oscillation, for $\epsilon = \overline{n_e}/\overline{n_n} \rightarrow 0$, is approximated as $\omega = \sqrt{\int_0^L \gamma(z)\Psi(z)dz}$ where γ is the steady-state ionization frequency and Ψ is a weighting function for the relative effect of neutral density perturbations on current growth. In a more physically relevant form the main frequency is found to scale as $\omega = (v_n/L)\mathcal{O}(\epsilon^{-1/2})$ which is nearly equivalent to the predator-prey model solution. The authors note that the instability appears as a stable limit cycle, thus the non-linear system is not well described by the linear analysis. Solutions for the non-linear mode frequencies are given as a function of discharge voltage (of which they are relatively independent).

A more in-depth analysis of the non-linear modes is presented by Barral and Peradzyski [164]. The equations are analyzed by separating the breathing cycles into two constituent phases. For the majority of the cycle the neutral flow is convective and ionization is negligible until the onset of a second phase where an impulsive ionization event occurs during which convection becomes negligible. Ultimately, the frequency of the non-linear modes is found to be proportional almost exclusively to the neutral fill time, v_n/L.

This non-linear breathing mode analysis appears to bear the most similarity to DCFT observations. The fundamental frequency of current oscillations has been measured to be largely independent of the anode voltage, but increases steadily with mass flow rate [19]. While increasing the mass flow rate does not necessarily mean higher neutral velocities it does increase the anode current. It is possible that increased current leads to higher temperatures of the porous diffuser through which propellant is input to the chamber, causing in turn faster neutral flow. Further support of the non-linear type scaling of Barral and Peradzyski was found when the DCFT anode was moved axially downstream roughly half the length of the chamber, resulting in an ap-

proximate doubling of the breathing frequency concurrent with the naive hypothesis of a doubled neutral fill rate.

4.3.1 Non-Linear vs. Linear Analysis

Though much of the Hall thruster literature cites the model of Fife *et al* [157] as a theoretical backing for observed oscillations due to its simplicity, it has some inherent problems. The model presented is a form of the Lotka-Volterra predator-prey equations which describe natural cycles of predation based on the relative populations of prey and predator. The birth rate of neutrals being proportional to neutral density in the ionization zone is not strictly physical in this case, since neutral information propagates downstream only, instead it is mainly set by a constant mass flow rate at the chamber entrance. Also, the linearized Lotka-Volterra equations cannot predict the stability of the system (as demonstrated below), and since the oscillations observed in the DCFT (in HC mode) have amplitudes which are typically larger than the steady-state current, they cannot be expected to describe the characteristics of these clearly non-linear features.

The equilibrium points for Eqns.4.2 & 4.3 can be found by setting the time derivatives to zero which results in two solutions, represented in the form $P_i = (\overline{n_n}, \overline{n_i})$ as $P_1 = (0, 0)$ and $P_2 = (v_i/(L\beta), v_n/(L\beta))$. Linear variational equations (Eqn.4.4 and Eqn.4.5) are constructed from the non-trivial equilibrium point, P_2, by defining a shifted coordinate system with P_2 at the origin, namely $\eta = n_n - v_i/(L\beta)$ and $\xi = n_i - v_n/(L\beta)$. Taylor expansion about the new origin leads to,

$$\frac{\partial \eta}{\partial t} \simeq \frac{\partial}{\partial n_n}\left(\frac{\partial n_n}{\partial t}\right)_{P_2}\eta + \frac{\partial}{\partial n_i}\left(\frac{\partial n_n}{\partial t}\right)_{P_2}\xi = -(v_i/L)\xi \tag{4.4}$$

$$\frac{\partial \xi}{\partial t} \simeq \frac{\partial}{\partial n_n}\left(\frac{\partial n_i}{\partial t}\right)_{P_2}\eta + \frac{\partial}{\partial n_i}\left(\frac{\partial n_i}{\partial t}\right)_{P_2}\xi = (v_n/L)\eta \tag{4.5}$$

which becomes a straightforward eigenvalue problem assuming perturbations of the form $\eta = Ae^{\lambda t}$ and $\xi = Be^{\lambda t}$. In this case the eigenvalues are purely imaginary, $\lambda = \pm i/L\sqrt{v_n v_i}$, which would make P_2 a center-type critical point, meaning the

linearized solutions in (n_n, n_i) phase-space correspond to circles around P_2. Generally, if the critical point is a positive (or negative) attractor, meaning solutions approach it as time increases, in the linear analysis then it is also a positive (or negative) attractor for the non-linear equations (given the non-linear term is continuously differentiable in the neighborhood of the critical point), however no such condition can be applied to a center [165]. This is to say that though a small perturbation from the equilibrium solution of Eqns. 4.2 & 4.3 is found by linear analysis to always lead to a stable, periodic solution, full consideration of the non-linear terms may result in an unstable solution or a solution which spirals (in phase space) towards P_2 as well as the possible center-type solution predicted by the linearization. The linearized equations of a system do not necessarily describe the behavior of the non-linear system, even very near to an equilibrium point.

If the neutral birth rate is set constant, to $n_{n0}v_n/L$ for example, then the non-trivial critical point becomes $(n_{n0}v_n/v_i, v_i/(L\beta))$. The eigenvalues about this point are $\lambda = -\nu(1 \pm i\sqrt{1 - 2v_i/(\nu L)})$, where $\nu = 0.5\beta n_{n0}v_n/v_i$, and the linearized solutions either approach the equilibrium point parabolically in phase-space or in a spiral. The linear behavior of this critical point is then applicable to the non-linear system by the property described above, however this solution, which always returns to equilibrium, does little to describe the breathing cycles actually observed. This type of simple analysis was also presented by Barral and Peradzyski [180].

It is interesting that the Lotka-Volterra equations have done a fairly good job predicting the oscillation frequencies for low amplitude breathing modes in Hall thrusters, while the frequency derived assuming the more intuitively pleasing constant neutral birth rate does not. Perhaps the neutral refill rate link to neutral density in the ionization region is through the depletion, though much smaller, of neutrals which occurs even upstream of the main ionization, causing the neutral flow rate at the ionization region inlet to be decreased during neutral depletion events in the breathing cycle.

4.4 Oscillation Measurements in the DCFT

Measurements of the breathing mode characteristics of the DCFT are made over a range of operating parameters. All tests were performed inside the ASTROVAC chamber described in Sec. 3.3.1, on either the original DCFT [16] or a thruster of similar design, outfitted with a boron nitride cone machined with ports for flush mounted Langmuir probing of the internal plasma [104]. The latter thruster variant shall be referred to as the instrumented DCFT. The background pressure in the vacuum chamber is 45 μTorr on average when 9 sccm of total (anode plus cathode) xenon flow is in use.

The DC current value is output by the Agilent N5772A Programmable Power Supply connected to the anode and logged at a rate of about 1 Hz. The AC component of the anode current is monitored by a Tektronix P6016 AC current probe which encircles the anode wire at a point between the chamber feedthrough and power supply. The AC probe is connected to an Agilent Infinivision oscilloscope, from which a 1000 point waveform is sampled once every 20 seconds (typically) by a LabView program used for all thruster command and telemetry.

The AC anode current waveforms are processed using the Fast Fourier Transform function in Matlab which takes the Discrete Fourier Transform (DFT) of the signal using the Cooley-Tukey algorithm. The signals were padded with zeros to make the length a multiple of 2 (in this case 1024) for more efficient processing of the thousands of waveforms. The DFT of each waveform is used to calculate the power spectral density (PSD) of the AC anode current signal, which is then shown as a function of time of operation for various conditions in the sections to follow. Several PSDs show the effects of zero-padding, equivalent to using a rectangular window, manifest as lobe-like features at high frequencies, though the main features of the spectra remain clear.

The mode change from LC to HC which occurs when the voltage is lowered is displayed in PSD versus time format in Fig. 4-3 from data taken on the original DCFT. The individual spectra at each anode voltage tried in the attempt to reach

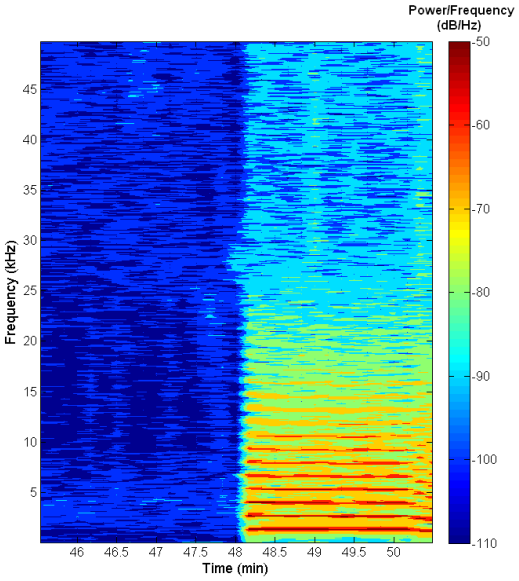

Figure 4-3: PSD versus time during mode change from LC to HC as anode potential is lowered from 410 V to 320 V with a constant anode flow rate of 7 sccm xenon, cathode flow of 1 sccm and keeper current of 0.5 A.

HC mode are shown in Fig. 4-4, with an upward shift of 30 dB used to segregate spectra taken at progressively later times. Thruster data taken during the mode change are displayed in Fig. 4-5.

The anode flow rate is kept at a constant 7 sccm during the mode change. A stable LC mode has been running for about 35 minutes at an anode potential of 410 V before the voltage is lowered incrementally until the highly oscillatory mode is obtained at 320 V. The low level broadband noise characteristic of LC mode is shown to starkly give way to the pronounced low frequency anode current oscillations with strong harmonics (more than 15 are visible in this case) which delineate the HC mode in both Fig. 4-3 and Fig. 4-4.

A slight peak in the power spectral density of the LC mode anode current waveforms occurs around 4 kHz at all anode voltages. Interestingly, a larger peak develops near 28 kHz at an anode voltage of 320 V just before this condition transitions from LC to HC mode, at a power density roughly equivalent to that found in the same frequency range in the far noisier HC mode, which can be seen clearly in Fig. 4-4. There is also an apparent peak at 6.8 kHz at this condition which matches the 5th

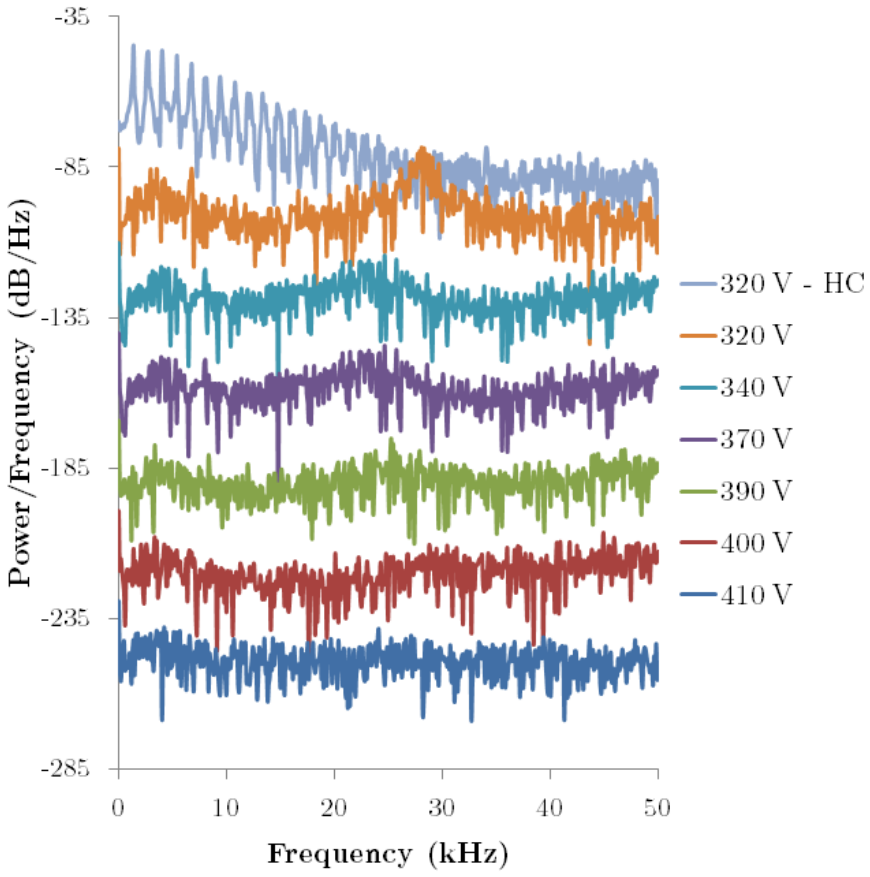

Figure 4-4: PSD at each voltage during mode change from LC to HC as anode potential is lowered from 410 V to 320 V with a constant anode flow rate of 7 sccm xenon, cathode flow of 1 sccm and keeper current of 0.5 A. Spectra are shifted 30 dB at each voltage change. The PSD is shown at 320 V in LC mode right before that condition leads to an HC mode-type spectrum.

harmonic of the fundamental breathing frequency measured in HC mode at the same anode potential. The development of a similarly broad peak near 90 kHz was found by Gildea *et al* in an LC mode at 450 V and 8.5 sccm xenon to the anode which gradually gave way to an HC mode as the thruster heated up [18].

The reverse mode change, from HC to LC, is shown in Figs. 4-6, 4-7 & 4-8 where the anode potential is incrementally increased from 320 to 390 V while all other thruster inputs are kept constant. The often hysteretic nature of the mode change, mentioned earlier, is exemplified by these scans in which anode potentials which led to a stable LC modes just 40 minutes earlier are now stuck in HC mode. Breathing oscillations are of the plateau-type, meaning much of the cycle is spent with an anode

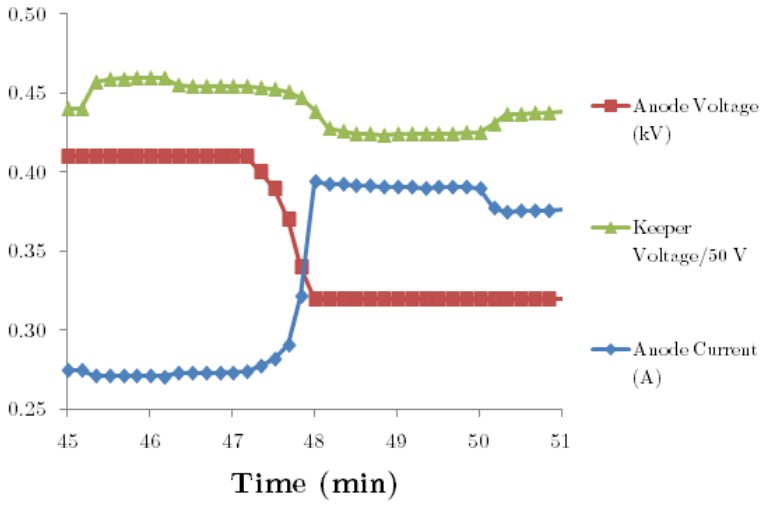

Figure 4-5: Thruster data versus time during mode change from LC to HC as anode potential is lowered from 410 V to 320 V with a constant anode flow rate of 7 sccm xenon, cathode flow of 1 sccm and keeper current of 0.5 A

current fluctuating near the LC value until a spontaneous burst of current occurs, followed by its near extinction, with fundamental frequencies between 1.2-1.4 kHz.

An anode of voltage of 380 V leads initially to an LC mode with a peak in the anode current power spectral density near 26 kHz, similar to the short-lived LC mode at 320 V in Fig. 4-4, with a secondary peak at 3.2 kHz. The 380 V LC mode spontaneously switches to HC, with a fundamental breathing mode frequency around 700 Hz, though the waveform is unfortunately cutoff in amplitude due to a failure to change the range of our oscilloscope during measurements, leading to the lobe pattern in the PSD. An LC mode is reobtained with an anode potential of 390 V which exhibits an anode current waveform very similar to that found for the 380 V LC case. This operating point is still observed to occasionally flicker into HC mode, as can be seen in Fig. 4-6 as thin vertical lines in the PSD, and the peak frequency of the 20-30 kHz oscillation noted to drift over time.

4.4.1 Flow Rate Scan

Thruster data are plotted in Fig.4-9 during a stepwise increase in mass flow rate on the instrumented DCFT with a constant anode potential of 300 V, cathode flow rate

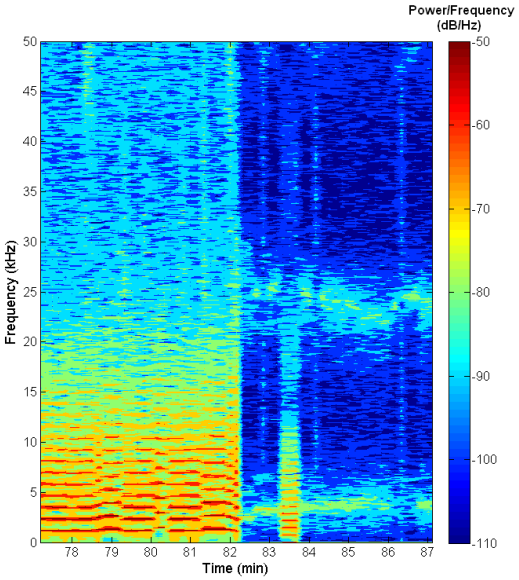

Figure 4-6: PSD versus time during mode change from HC to LC as anode potential is raised from 320 V to 390 V with a constant anode flow rate of 7 sccm xenon, cathode flow of 1 sccm and keeper current of 0.5 A.

of 1 sccm and keeper current of 0.5 A. Vertical dashed lines in Fig. 4-9 indicate the time at which the flow rate is incremented, for example, from 5 to 6 sccm at 25 minutes into the scan, and from 6 to 7 sccm roughly 38 minutes in.

Figure 4-9a shows the frequency at which the highest power spectral density is found from the anode current waveform as a function of time, which alternates between a frequency in the 3-6 kHz range and a much faster fluctuation in the 63-71 kHz range when the anode flow rate is 5 sccm. At a flow rate of 7 sccm, with the thruster in HC mode, the peak frequency also oscillates, but in a much lower range, between about 1.8 kHz and 3.7 kHz, with 3.7 kHz being the peak frequency of the anode waveform in LC mode at 6 sccm. Though the peak frequencies are sometimes the same between these two modes the amplitude of the oscillations, shown in Fig. 4-9b, differ by more than one order of magnitude. The amplitudes plotted in Fig. 4-9b are of the range of voltages measured in each waveform by the passive Tektronix probe which has a nominal 2 A/V conversion, though this conversion ratio was found to be imprecise, so the uncalibrated peak-to-peak amplitudes are given in their raw form to show that they are merely conveying relative information.

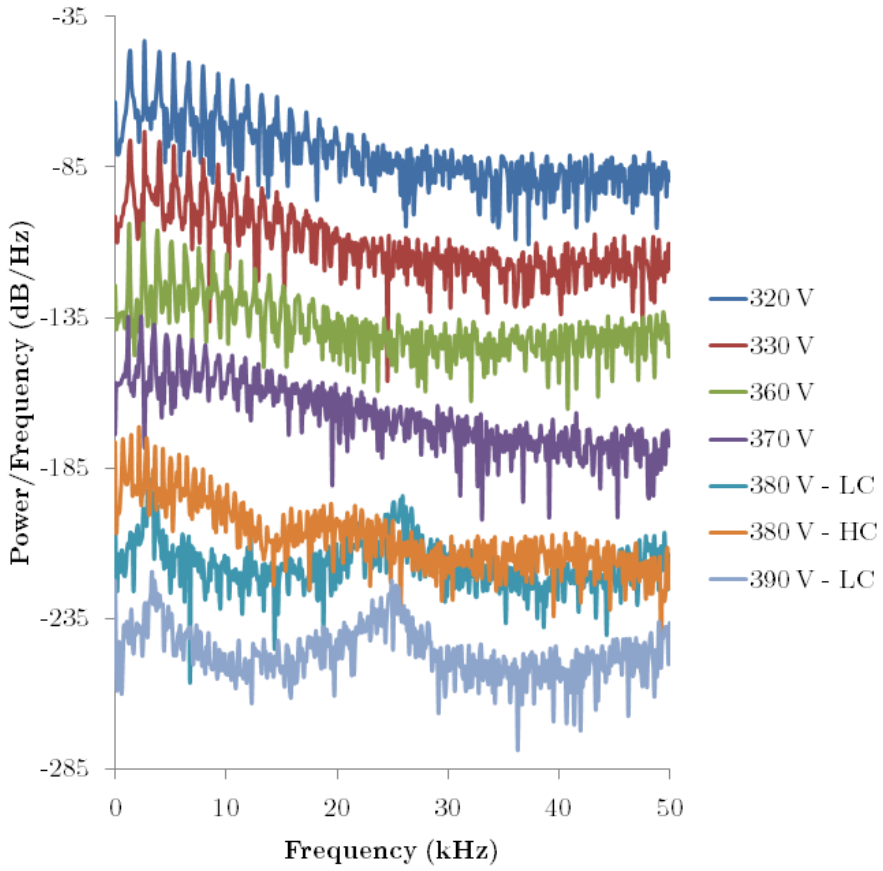

Figure 4-7: PSD at each voltage during mode change from HC to LC as anode potential is raised from 320 V to 390 V with a constant anode flow rate of 7 sccm xenon, cathode flow of 1 sccm and keeper current of 0.5 A. Spectra are shifted 30 dB at each voltage change. An LC mode is initially obtained with 380 V before that condition switches back to HC mode spontaneously.

The DC anode current and keeper voltage, shown in Figs. 4-9c & 4-9d, are nearly mirror images of one another after an initial transient in the keeper potential. The keeper potential relates to the coupling between the hollow cathode system and the thruster anode and may be most directly seen as a metric for the amount of power spent ensuring the cathode provides the necessary current to sustain the discharge.

The thruster operates in LC mode for anode flow rates of 5 and 6 sccm of xenon, with low amplitude quasi-sinusoidal oscillations in anode current shown in Fig. 4-10. Anode flow rates from 7 to 9 sccm resulted in HC mode operation with anode current waveforms, shown in Fig. 4-11, which transition gradually towards a higher frequency oscillation which is more nearly sinusoidal as the flow rate is increased. Note that

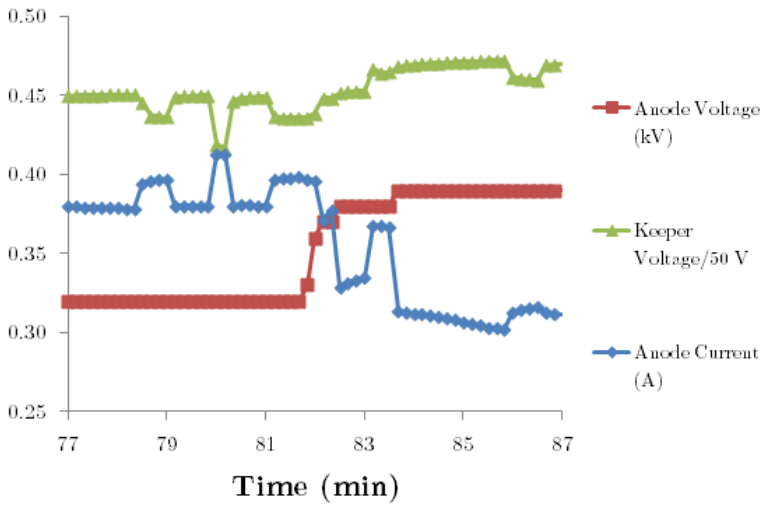

Figure 4-8: Thruster data versus time during mode change from HC to LC as anode potential is raised from 320 V to 390 V with a constant anode flow rate of 7 sccm xenon, cathode flow of 1 sccm and keeper current of 0.5 A

Figs. 4-10 and 4-11 exhibit negative currents between peaks because it is only the time varying (i.e. AC) component of the current that is being plotted. The most negative portions in AC current traces shown in Fig. 4-11, for example, are typically just over zero when added to the DC current [18], meaning the thruster is nearly self-extinguishing promptly after each spike in anode current. The anode current is at its time-averaged (i.e. DC) value when the AC component is zero.

The PSD at each flow rate is averaged over the last 15 traces at that condition, with the result shown in Fig. 4-12. The averaging procedure clarifies the high frequency peaks in the LC mode spectra, around 70 kHz and 60 kHz for flow rates of 5 and 6 sccm respectively. A closer inspection of the PSD at low frequencies is taken in Fig. 4-12b which shows the gradual increase in the fundamental frequency of the breathing mode accompanying the increase in flow rate, from 1.8 to 2 to 2.2 kHz at 7, 8 and 9 sccm respectively, which is also displayed in Fig. 4-9a. The LC mode flow rates exhibit low frequency peaks near 3.8 and 4.4 kHz for 5 and 6 sccm of xenon respectively.

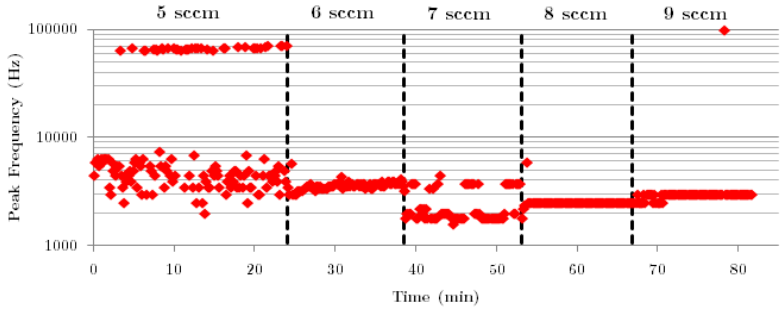

(a)

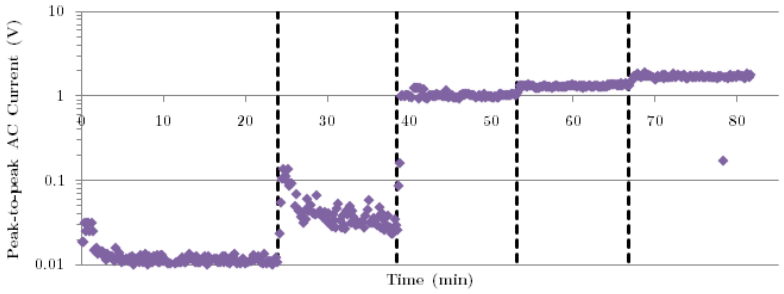

(b)

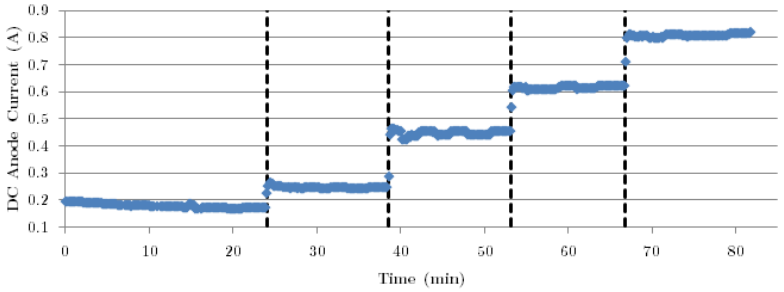

(c)

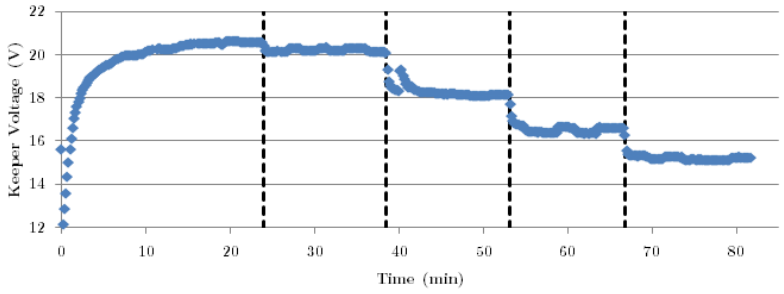

(d)

Figure 4-9: Thruster data for stepwise increase in mass flow rate over time from 5 to 9 sccm xenon in 1 sccm increments. Dashed lines indicate time of flow increase. Constant anode potential of 300 V, cathode flow rate of 1 sccm and keeper current of 0.5 A.

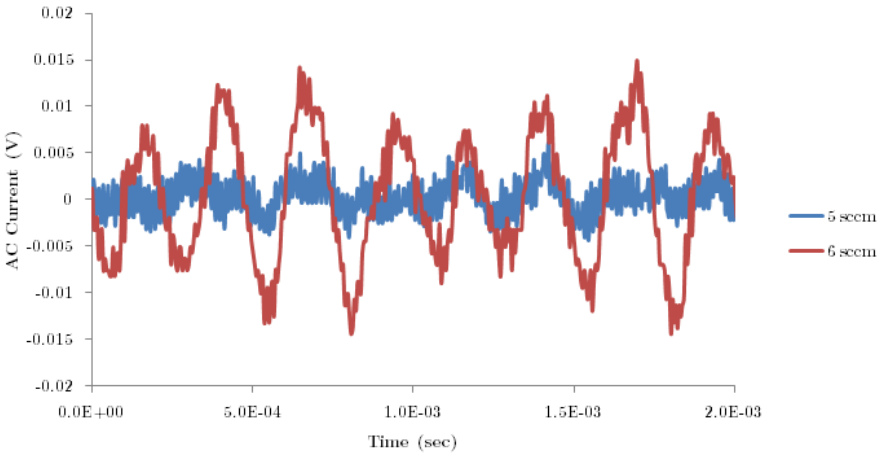

Figure 4-10: Sample AC anode current component waveforms for mass flow rates in LC mode. Constant anode potential of 300 V.

4.4.2 Voltage Scan

Thruster data is shown in Fig. 4-13 for the upward portion of the anode voltage scan taken with the original DCFT for IR camera tests. The voltage is incremented from 200 to 450 V in 50 V steps with the thruster operating in HC mode. Figure 4-13a shows that the peak frequency of the breathing mode does not increase with voltage, as in the predator-prey model, but instead appears to decrease slightly from around 2900 Hz at 200 V to 2250 Hz at 450 V.

Anode current oscillation amplitudes are shown in Fig. 4-13b to increase fairly steadily with voltage between 250 and 350 V. A steeper jump in amplitude is observed in the transition from 200 to 250 V and from 350 to 400 V. The DC anode current, meanwhile, is observed to follow a strongly non-monotonic trend, plotted in Fig. 4-13c, with the current increasing upon transition from 200 to 250 V and from 300 to 350 V, but decreasing during the other voltage transitions. Stratifications in the current at a single voltage set point are mainly due to the thruster alternating between being pointed down the axis of the vacuum chamber and being pointed at an angle to allow viewing of the thruster channel by an infrared camera which is pointed diametrically across the chamber. Lower currents are observed when the thruster fires down the length of the vacuum chamber.

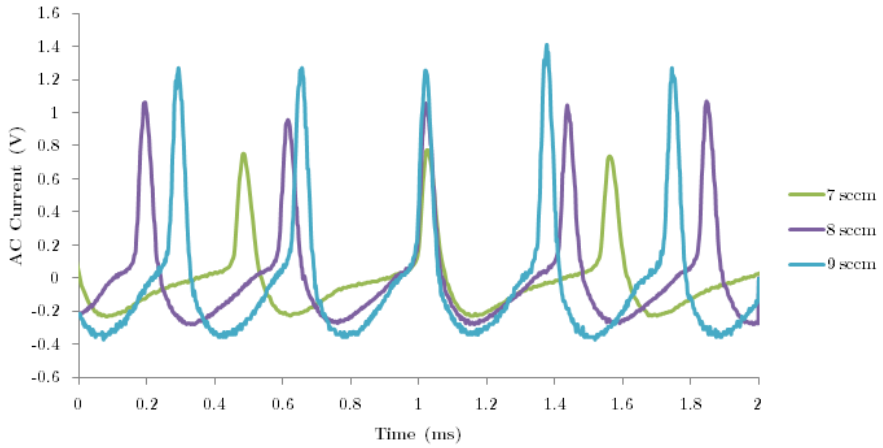

Figure 4-11: Sample AC anode current component waveforms for mass flow rates in HC mode. Constant anode potential of 300 V.

Thruster data from the upward portion of an anode voltage scan taken on the instrumented DCFT are shown in Fig. 4-14, where the anode potential is incremented from 250 to 450 V in 50 V steps. The results are similar in character to those obtained on the original DCFT, in Fig. 4-13. The thruster operates mostly in HC mode, though an occasional flicker into UHC mode is observed at 250 V, which is clearly identified by the 20% increase in DC current accompanied by an order of magnitude drop in AC current amplitude. A few brief forays into LC mode can be seen in the telemtry at 400 and 450 V, when both the DC and AC anode current experience pronounced dips.

Samples of the AC anode current measurements at each voltage are shown in Fig. 4-15 which again give the current component in terms of the passive probe voltage. At low anode voltage the oscillation approaches a sinusoidal shape, shown in Fig. 4-15a, with the fundamental frequency (which is also the frequency between anode current bursts) matching the peak frequency plotted in Fig. 4-14a because none of its harmonics have a higher power density. This is not the case at 350 V, where the AC current waveform shown in Fig. 4-15c exhibits a stunted peak preceding each full current burst by a half cycle. The fundamental frequency is 1100 Hz for the wave in Fig. 4-15c, but the peak frequency from the PSD is roughly 2200 Hz due to the stunted peak.

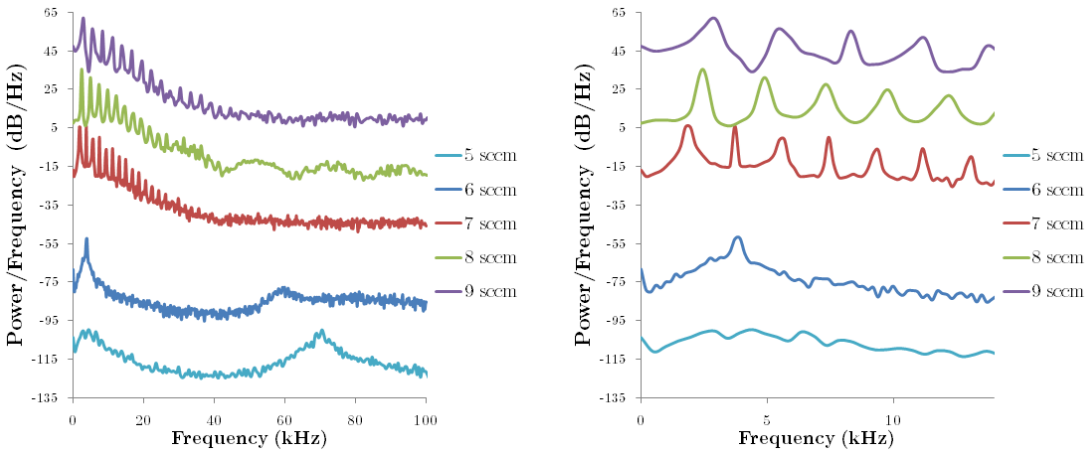

Figure 4-12: Averaged Power Spectral Densities at various anode mass flow rates showing (a) full bandwidth (b) low frequency only. Constant anode potential of 300 V. Upward 26 dB shift as flow rate increases added for clarity.

The intermediate waveform at a 300 V anode potential shows a progression towards the double peak, though the fundamental frequency is still the location of the maximum in the PSD. The anode current reaches its steady state value roughly 60% of the way through the cycle, which is too slow to add power to the second harmonic, and essentially levels off before the current burst. At 400 V the anode current approaches its time-averaged value shortly after each minimum and oscillates there for a time before eventually leading to a burst in current, as shown in Fig. 4-15d. The PSD at this potential is cluttered and varied, as can be surmised from Fig. 4-14b, due to the current bursts occuring more irregularly than found at lower anode potentials.

4.4.3 External EM Scan

The purpose of the external electromagnet (EM) study described in Section 3.3.1.1 was to determine how the shape of the near-exit magnetic field affected the shape of the plume, however an interesting auxiliary result was the demonstration of magnetic field initiated mode changes. While no anode current waveforms were captured during an EM-caused mode transition, the effects of the EM on the anode current spectra are presented in both LC and HC modes separately.

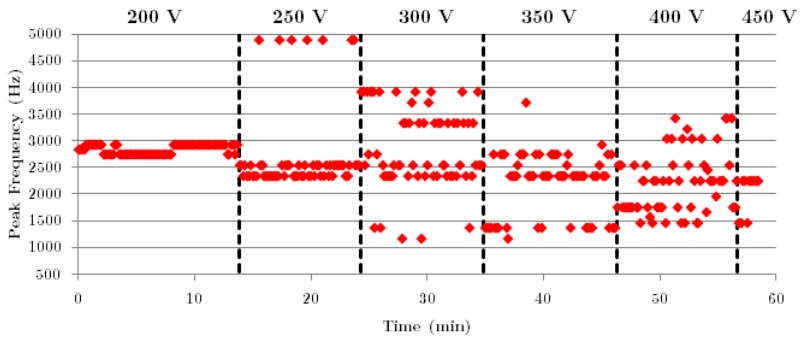

(a)

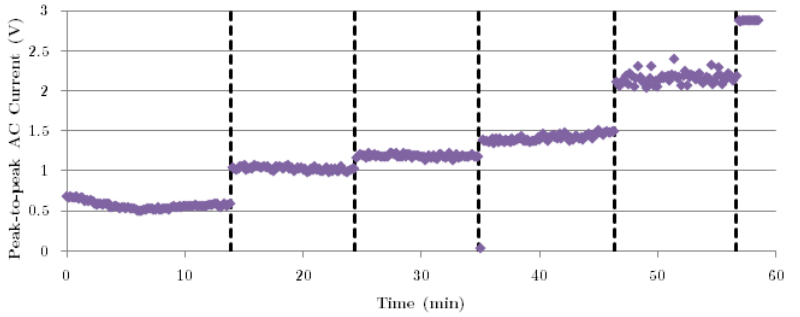

(b)

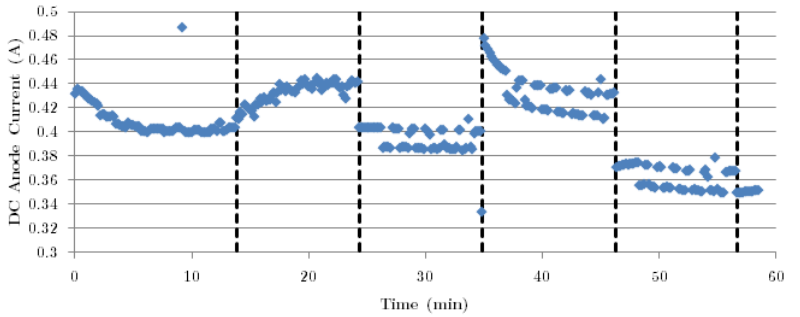

(c)

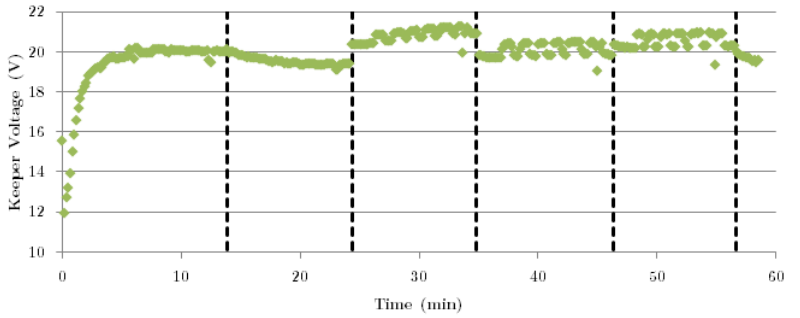

(d)

Figure 4-13: Thruster data for stepwise increase in voltage over time from 200 to 450 V in 50V increments. Dashed lines indicate time of voltage increase. Constant anode mass flow rate of 7 sccm xenon, 2 sccm cathode flow and 0.5 A keeper current.

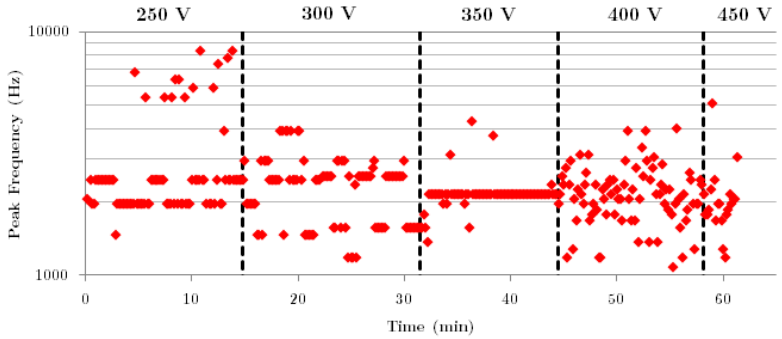

(a)

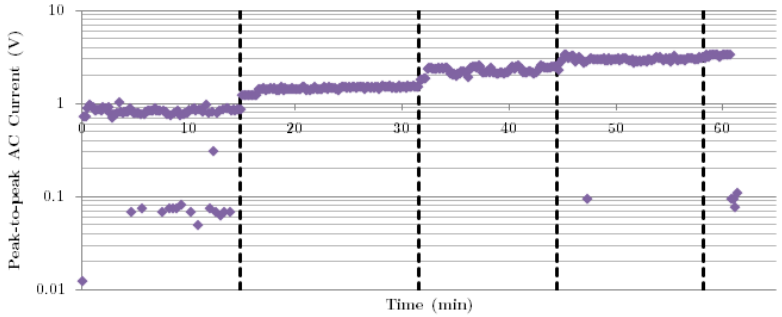

(b)

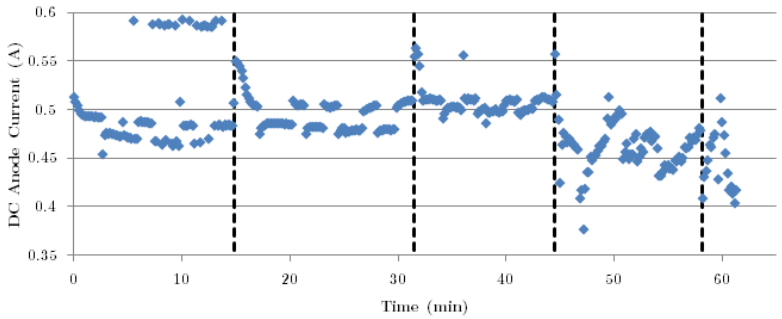

(c)

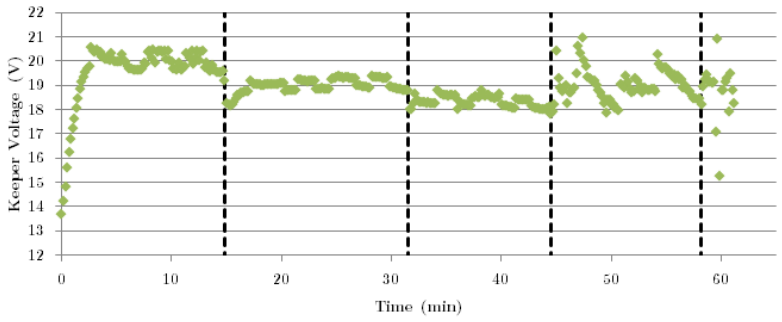

(d)

Figure 4-14: Thruster data for stepwise increase in voltage over time from 250 to 450 V in 50V increments. Dashed lines indicate time of voltage increase. Constant anode mass flow rate of 7 sccm xenon, 1 sccm cathode flow and 0.5 A keeper current.

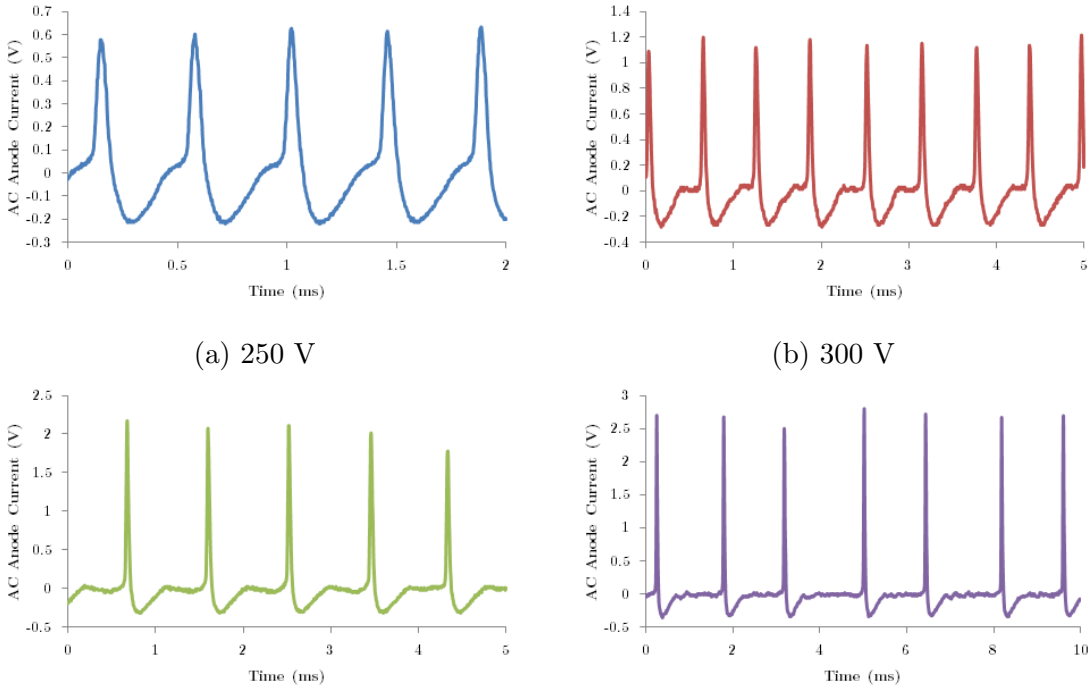

(a) 250 V

(b) 300 V

(c) 350 V

(d) 400 V

Figure 4-15: Sample AC anode current waveforms at different anode voltages. Constant anode mass flow rate of 7 sccm.

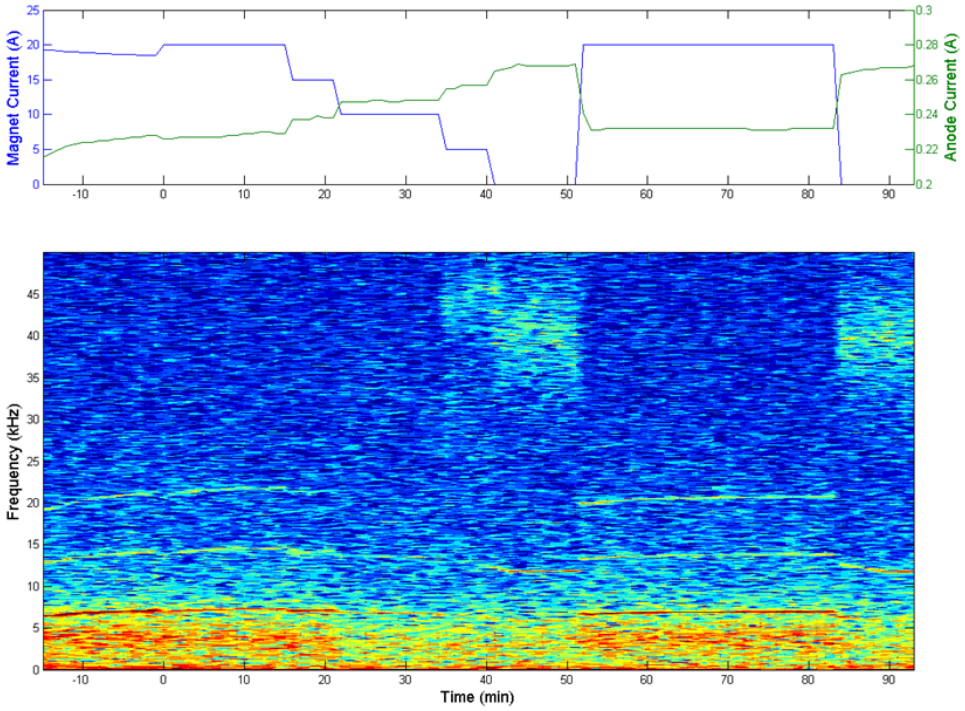

Figure 4-16: PSD versus time in main figure. Top subfigure shows the applied electromagnet current and resulting anode current versus time. DCFT in LC mode at 350 V with an anode mass flow rate of 5 sccm xenon, 2 sccm on the cathode and a 1.365 A keeper current.

An LC mode is obtained with an anode voltage of 350 V a mass flow rate of 5 sccm Xe and a keeper current of 1.365 A (lower keeper currents resulted in unstable modes). Figure 4-16 presents the evolution the anode current PSD over time as the EM current is toggled, demonstrating that a decrease in the EM current in this mode corresponds to an increase in anode current and with a gradual decrease in the peak frequency of anode current fluctuations. The PSDs in Fig. 4-16 exhibit sharp peaks in the 6-8 kHz range which have up to three visible harmonics, resembling the PSD found on an EM-less DCFT by Gildea during operation in LC mode at 476 V, 5.8 sccm xenon on the anode and 1.48 A on the keeper [18], which shows a 6 kHz mode with 3 apparent harmonics. Fluctuations at the fundamental frequency appear to become weaker at lower EM currents, with the 2nd harmonic actually dominating when no EM current is applied. There is also some broader noise in the 1-4 kHz region, and in 35-45 kHz when the EM current is below 10 A. The main frequency of

the fluctuations in the 35-45 kHz band appears to decrease when the EM current is dropped from 5 A to 0 A.

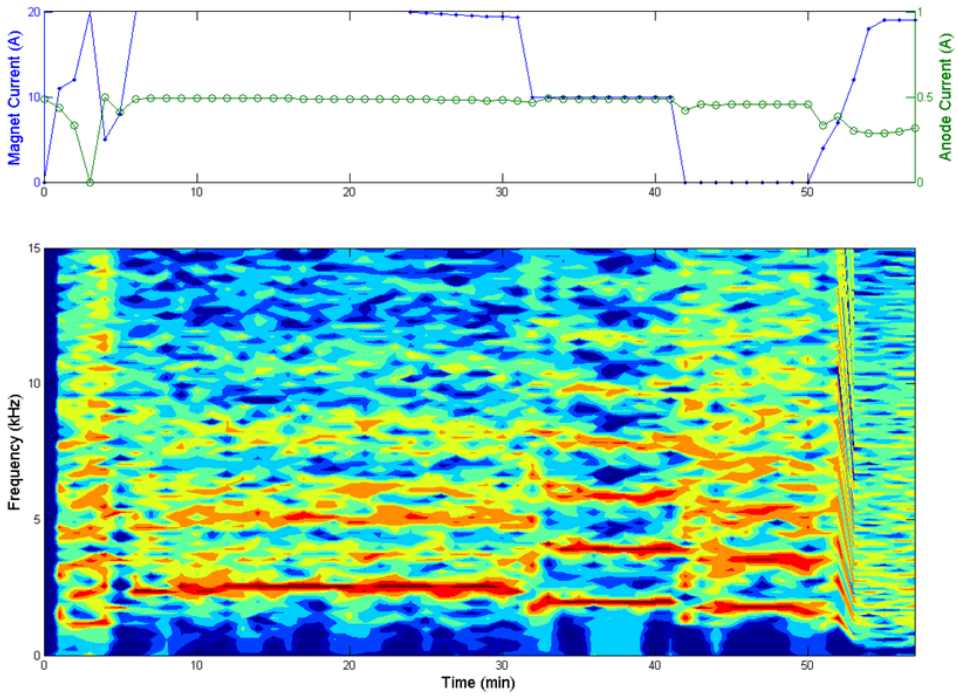

Figure 4-17: PSD versus time in main figure. Top subfigure shows the applied electromagnet current and resulting anode current versus time. DCFT in HC mode at 300 V with an anode mass flow rate of 6 sccm xenon, 1 sccm on the cathode and a 0.75 A keeper current.

A similar PSD evolution is shown in Fig. 4-17 with the thruster operating in HC mode at a constant anode potential of 300 V, anode flow of 6 sccm Xe and 0.75 A keeper current. The PSD exhibits a sharp peak at 2.5 kHz with 20 A applied to the EM, though the harmonics of this mode are more blurred out than typical HC mode spectra (see Fig. 4-3 for example). The fundamental frequency decreases as the EM current is dropped to 10 A (where it is 2.0 kHz) and then 0 A (where it is 1.8 kHz), with 4 or 5 clear harmonics visible in both cases.

Sample AC current waveforms are shown for each value of applied EM current examined in HC mode in Fig. 4-18. At 20 A of EM current the spacing between current bursts appears to be somewhat irregular, likely leading to the blurred PSD described above. As the EM current is lowered the waveform appears to be stretched out in time. One can also see the amplitude of the current oscillations generally

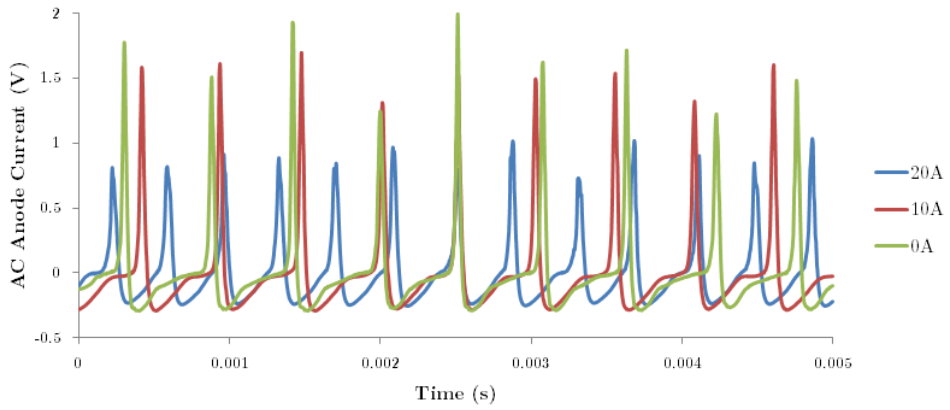

Figure 4-18: Sample AC anode current waveforms at various values of applied electromagnet current. DCFT in HC mode at 300 V with an anode mass flow rate of 6 sccm xenon, 1 sccm on the cathode and a 0.75 A keeper current.

increasing as the EM current is decreased.

A summary of the DC anode current and the peak AC oscillation frequency as a function of EM current is given in Fig. 4-19. Interestingly, the DC current trends in opposite directions when the EM current is raised depending on the mode, with the LC mode experiencing a significant decrease in current. The peak frequency of the AC spectra rises with the EM current regardless of mode though the curvature of the upward trends appear to differ. The frequency of the prominent fluctuation in LC mode is several times larger than that for HC mode, so the third harmonic of the fundamental HC mode frequency is plotted in Fig. 4-19b for easier comparison.

An increased EM current is known to result in an upstream motion of the exit separatrix and external electric field as well from Sec. 3.3.2 which would reduce the time for neutrals to refill the region spanning from propellant inlet to the edge of the acceleration region. This effect might lead to a linear increase in the breathing frequency with EM current, but is likely not enough to account for the observed frequency change in either mode.

4.4.4 Cathode Position Scan

A two-dimensional stage was constructed and installed to position the hollow cathode axially and vertically (i.e. radially) during tests with the external electromagnet.

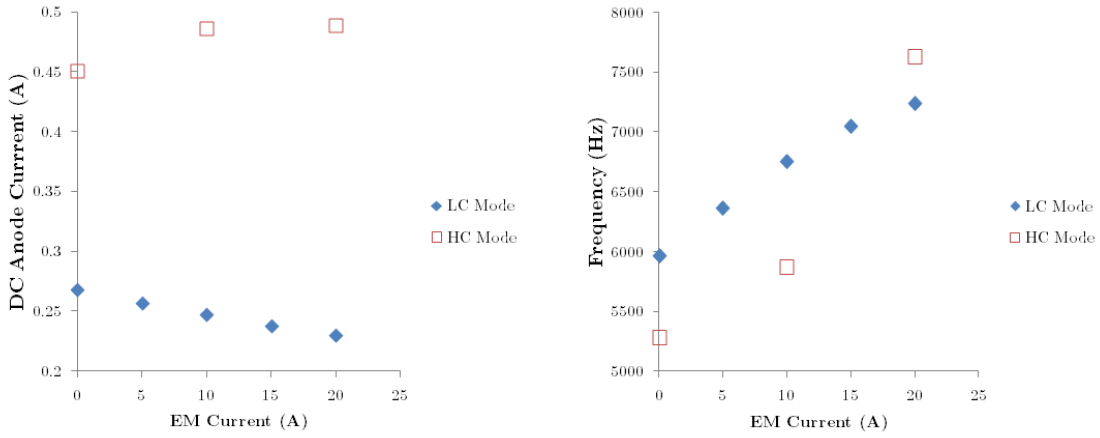

(a) (b)

Figure 4-19: LC mode is 350 V and 5 sccm Xe on the anode, while HC mode is 300 V and 6 sccm Xe. (a) DC anode current at various applied EM currents. (b) Anode current oscillation peak frequencies at various applied EM currents. The 3rd harmonic of the peak frequency is plotted for the HC mode to allow comparison on the same scale.

Impingement with the EM precluded use of the normal cathode position, so the stage allowed some rough optimization of the cathode position. Adjustment of the cathode position during EM testing revealed a highly repeatable set of mode changes based on the relative location of the cathode and the visual edge of the ion jet roughly 30° off-axis.

It was found that a stable LC mode could be obtained with the cathode placed just outside of the jet radially. When moved into the luminous region coinciding roughly with the peak ion flux the thruster would transition spontaneously into HC mode. A less sharp transition into HC mode was also obtained as the cathode was moved to large radial values outside of the jet. The same trend was observed when the cathode was moved axially. A radial position outside of the jet at low axial distances from the thruster exit with anode conditions resulting in LC mode would switch to HC mode as the cathode was moved axially further from the thruster. The point of the transition would always occur as the cathode passed the visual edge of the ion beam.

The DC anode current and power spectral density of the AC anode current are shown in Fig. 4-20 as a function of the cathode position. Due to a malfunction in

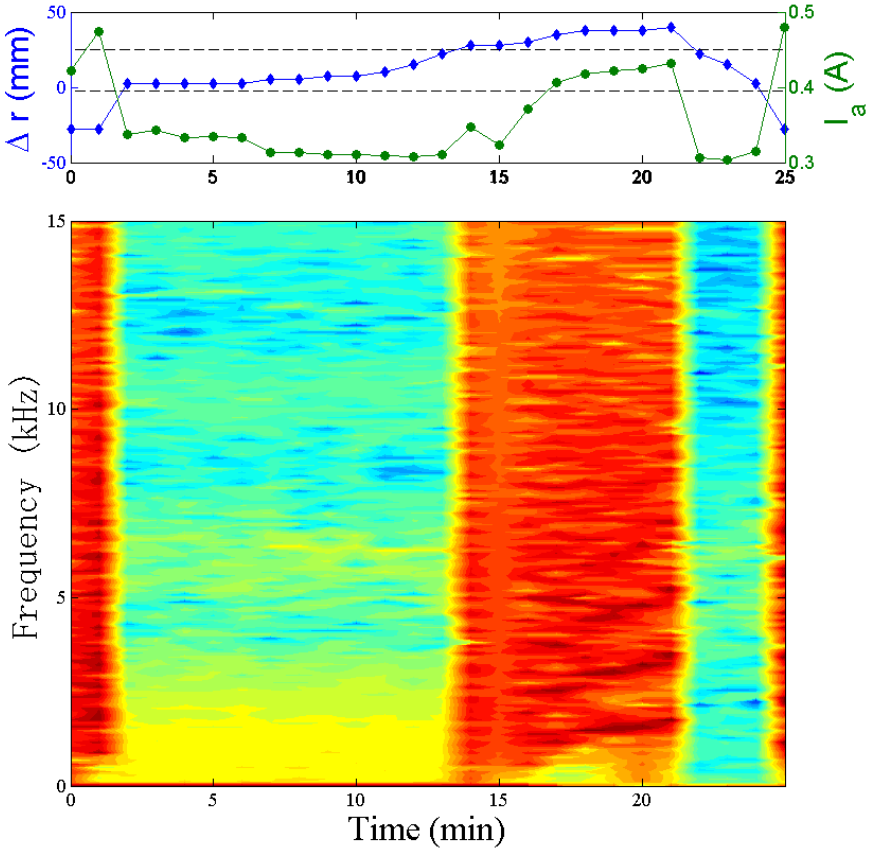

Figure 4-20: PSD versus time as cathode is moved radially with respect to the edge of the jet. Anode flow rate of 6 sccm Xe and 300 V applied potential. Dashed lines in the top subplot indicate radial locations where mode transitions occur

the cathode stage data, the true position of the cathode is not accurately known. The radial location at which the cathode orifice coincides with the visual beam edge was noted and the deviation from this point, Δr, is given based on commanded increments. The axial location of the cathode during the conditions of Fig. 4-20 is known to be 7.3 $\pm$ 0.1 cm from the exit face of the BN cone and the radial location corresponding to Δr=0 is estimated to be 4.9 cm from the thruster axis.

The power spectral density contours shown in Figure 4-20 illustrate the transition in spectral content of the anode current as the cathode moves out of a 2.5 cm wide range of radial positions just outside of the edge of the ion beam (i.e. the 'quiet' band $0 > \Delta r > 25$ mm). Within the 2.5 cm wide region the amount of power in the

AC component of the anode current is small, with the peak power spectral density occurring at frequencies below 2 kHz and in a small band near 6 kHz. When the cathode is outside of the near-edge region the DC anode current and the amplitude of the AC component increase dramatically for the same anode mass flow rate (6 sccm Xe) and anode potential (300 V). The AC current waveforms outside the near-edge region exhibit the normal breathing mode-type behavior which marks the HC mode, with peak spectral densities at around 1500 Hz. The fundamental frequency of the breathing oscillation is also seen to increase by around 25% as the cathode is moved from 3 cm to 4 cm from the edge of the jet.

4.5 Thermal Measurements

Thruster temperatures were monitored during the oscillation measurements using type K thermocouples on the thruster body and a modified MiKroScan TH5104 infrared camera viewing the BN cone and anode. The thermal camera, on loan from Michigan Tech University's Ion Space Propulsion Lab, operates outside of the vacuum chamber, viewing the thruster at alternating angles of 90 and 20 degrees off the thruster axis through a ZnSe viewport, on loan from the AFRL/RZSS Electric Propulsion Lab. Calibrations performed to match infrared camera output to thermocouple measurements of heated objects inside the vacuum chamber suggest a transmissivity of about 70% for the ZnSe viewport. Reported infrared camera measurements are corrected for the viewport transmissivity unless otherwise noted, while all emitters are assumed to be blackbodies for the purpose of transparent presention of the raw data.

The thruster is fired down the length of the vacuum chamber for the majority of testing, but is turned towards the infrared camera periodically on a Velmex B4872TS rotary table, with a pictorial representation of the change in angle given in Fig. 4-21. Aluminum foil coats the chamber walls and electrical cabling in the path of the plume when the thruster is pointed to allow anode viewing by the camera. The anode current is notably higher when the thruster is pointed for camera viewing, as is clear

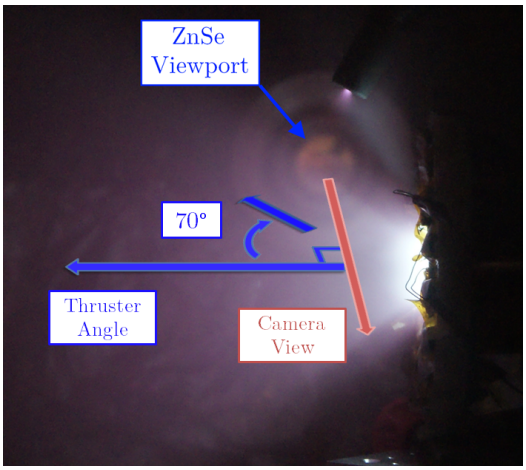

Figure 4-21: Picture of the instrumented thruster firing demonstrating the two firing angles used during thermal imaging experiments with respect to the IR camera line of sight.

in the anode current data of Fig. 4-13c in which there is a stratification of the current at anode potentials from 300 to 400 V. The higher anode current values in Fig. 4-13c for a given anode voltage correspond to times when the thruster points towards sides of the vacuum chamber.

Uncalibrated thruster temperatures are shown in Fig. 4-22 which correspond to the thruster conditions displayed in Fig. 4-9, where TC refers to a thermocouple (shown in Fig. 4-23) placed on the outer surface of the BN cone in the vicinity of C2, the second downstream wall cusp. The uncalibrated results are just the raw camera output which considers all radiators as blackbodies and all intermediate material as completely transmissive. The cathode temperature is taken as that which the camera measures at the cathode orifice, which is reasonably covered by the blackbody assumption due to internal reflections of radiation inside the keeper.

The diffuser temperature measured by the camera is also included, though it is not expected to accurately reflect the temperature of the porous steel disc, due to the typically low infrared emissivity of polished metal surfaces. If the emissivity of the diffuser is around 0.2, for example, then the thermal radiation leaving the diffuser is 20% of the blackbody emissive power of the diffuser plus 80% of the radiated power incident on the diffuser from adjacent surfaces (such as the BN cone and the BN anode guard). This is a simplified picture, but in any case the thermal radiation

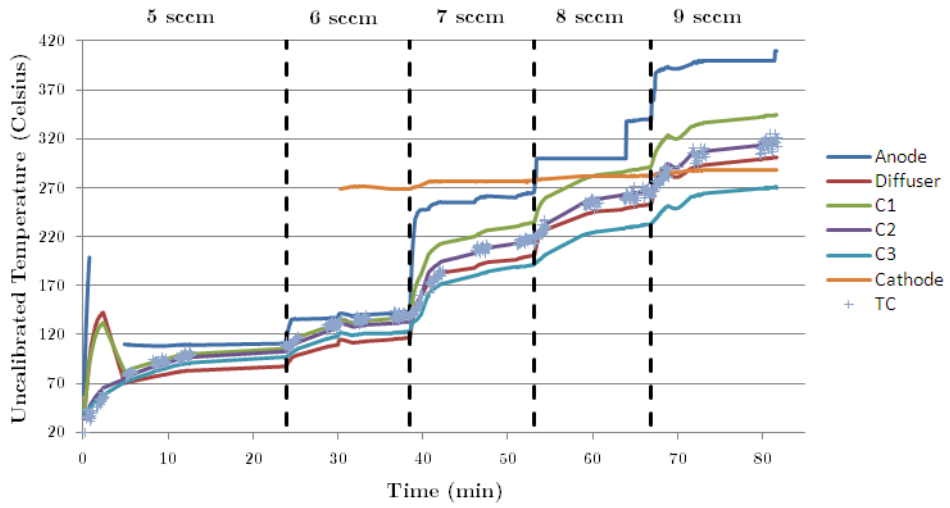

Figure 4-22: Thruster temperatures for stepwise increase in mass flow rate over time from 5 to 9 sccm xenon in 1 sccm increments. Dashed lines indicate time of flow increase. Constant anode potential of 300 V, cathode flow rate of 1 sccm and keeper current of 0.5 A.

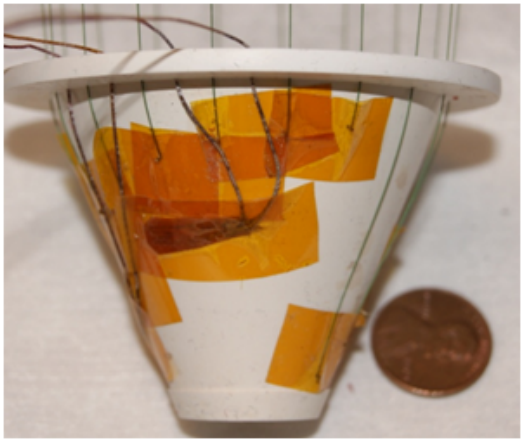

Figure 4-23: Picture of the instrumented boron nitride cone showing the 18 Langmuir probes and one thermocouple in the center affixed by Kapton tape to the outer surface.

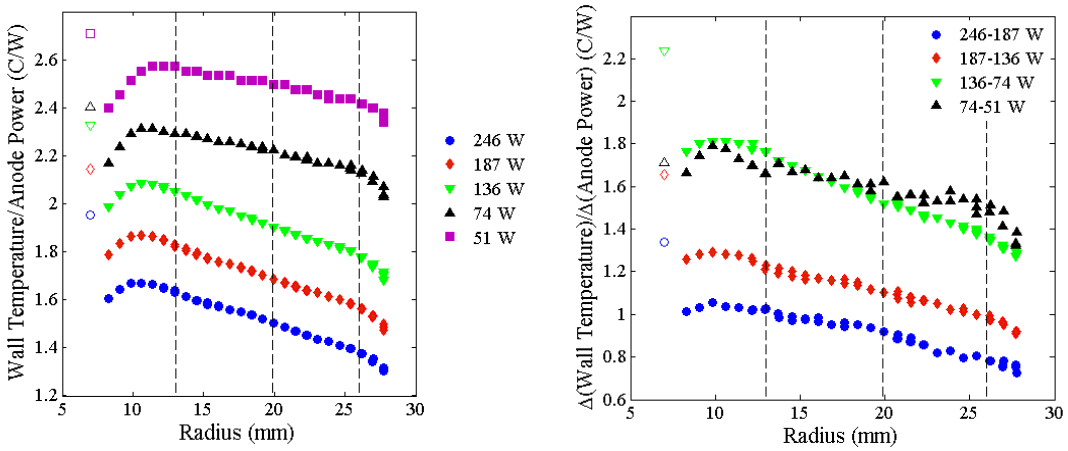

(a) (b)

Figure 4-24: (a) Transmissivity calibrated temperatures measured along BN wall during flow rate scan of Fig.4-9 normalized by anode power. (b) Calibrated temperature differences along wall normalized by change in anode power. Open symbols denote anode temperature (a) normalized by anode power (b) differences normalized by anode power change. Anode powers >100 W correspond to HC mode operation.

leaving a low emissivity material is not a reliable indicator of the temperature of the material.

Temperature profiles along the insulating wall are shown in Fig. 4-24a (plotted in degrees Celsius normalized by the anode power at each condition for visual clarity) and calibrated to account for the transmissivity of the viewport, where radius refers to the radius of the cone's inner wall at the point of measurement. The figure also shows the anode power normalized anode temperature. The difference in the temperature profile at each power level with the profile at the power level just below it is shown in Fig. 4-24b normalized by the change in anode power.

Figure 4-24a shows that the temperature along the wall is relatively flat in the low power LC modes at 51 and 74 W, but becomes more strongly peaked near the anode in HC mode. It also shows that the anode temperature increases with anode power differently in LC mode than HC mode, increasing from 139 to 178°C at LC mode anode currents of 171 and 248 mA, before jumping up to 318°C at 455 mA then linearly increasing to 480°C at 819 mA. The jump in anode temperature at the mode change likely indicates an increase in the fraction of anode power being lost by

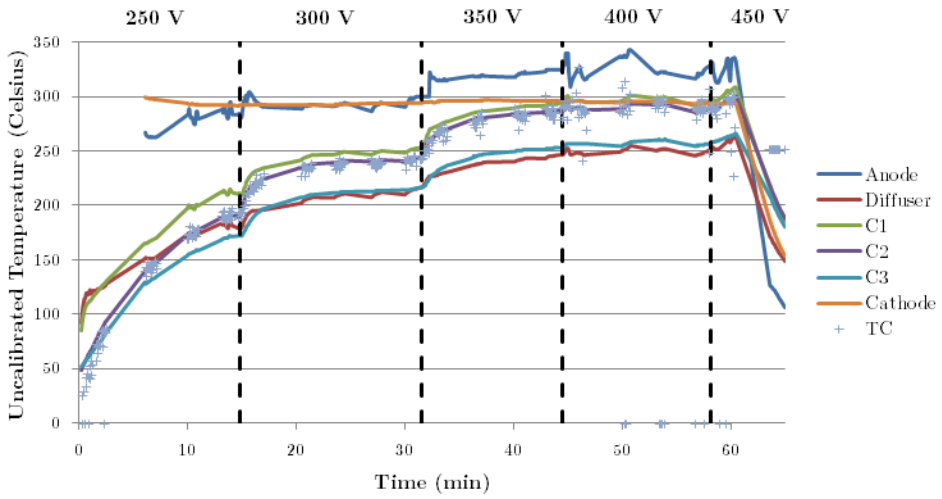

Figure 4-25: Thruster temperatures for stepwise increase in anode voltage over time from 250 to 450 V in 50 V increments. Dashed lines indicate time of flow increase. Constant anode mass flow rate of 7 sccm xenon, cathode flow rate of 1 sccm and keeper current of 0.5 A.

plasma impingement on the anode, though in both cases this fraction is expected to be fairly small.

Figure 4-24b reveals a surprising similarity in the incremental change in wall temperature per added watt of anode power when the anode flow is increased from 5 to 6 sccm (both in LC mode) and when the flow is increased from 6 to 7 scmm (with the higher flow rate corresponding to HC mode operation). The power increase when both conditions are LC mode, however, leads to a larger proportional change in temperature near C3. Once in HC mode (i.e. for the $\Delta T/\Delta P_a$ profiles from 7 to 8 and 8 to 9 sccm), the temperature change has a fairly constant shape, and is seen to decrease in proportion to the change in anode current as the flow rate is increased.

Temperatures measured during the voltage scan are presented in Fig. 4-25, with the corresponding data in Fig. 4-14. The wall temperature profiles obtained prior to each voltage increment are shown in Fig. 4-26a, which are essentially the same shape for voltages from 300 to 450 V. The temperature changes between power levels normalized by the anode power increment are shown in Fig. 4-26b, where it appears that the wall is heated strongly in C2 and (slightly less strongly) in C3 as the anode potential is increased from 250 to 300 V and from 300 to 350 V. The wall temperature

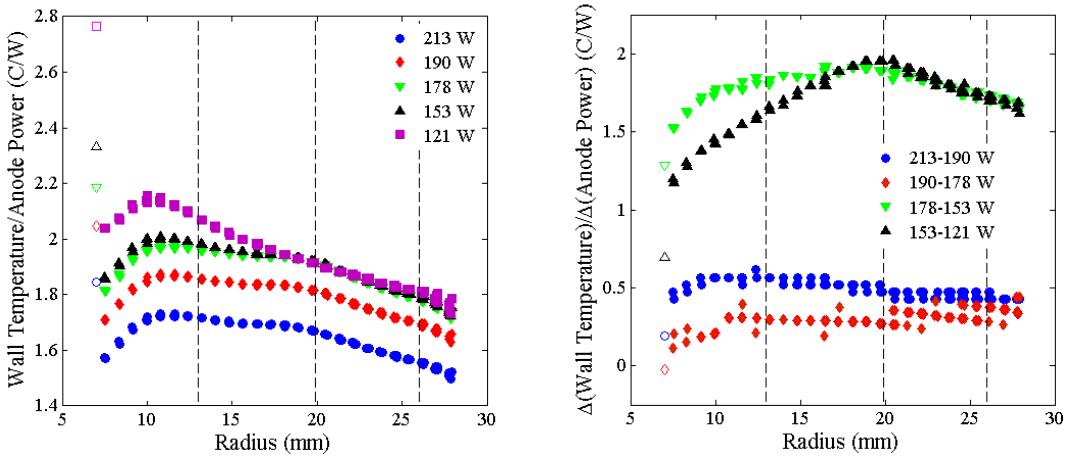

(a) (b)

Figure 4-26: (a) Transmissivity calibrated temperatures measured along BN wall during anode voltage scan of Fig.4-14 normalized by anode power. (b) Calibrated temperature differences along wall normalized by change in anode power. Open symbols denote anode temperature (a) normalized by anode power (b) differences normalized by anode power change.

increase is fairly evenly distributed upon anode potential increase from 350 to 400 V and from 400 to 450 V.

The anode current increases fairly steadily from 335°C at 250 V to 357°C at 300 V then levels off near 390°C for anode potentials of 350-450 V. The anode current decreases by 34 mA as the anode potential is increased from 350 to 400 V, though the anode temperatures in the two cases are identical (there is also little change in the wall temperature profiles with only 12 W added to anode power). The saturation of the anode temperature near 350 V indicates a pronounced change in the dependence of the plasma energy content near the anode on the anode potential or perhaps a change in the anode voltage dependence of the proportional ion-to-electron current reaching the anode.

Figures 4-24a and 4-26a both indicate that a more evenly distributed wall temperature profile corresponds to a lower anode-to-wall temperature ratio, while higher anode-to-wall temperature ratios result in profiles more strongly peaked upstream. The increased wall temperatures measured near the anode in the latter case may be in some part due to the increased radiation from the anode (and BN anode guard)

incident on the nearby cone, possibly being reflected and contributing non-negligibly to the total radiosity from the cone surface.

4.5.0.1 Thermal Modeling

A simple analysis of the thermal camera data requires some tenuous assumptions in order to estimate the power lost to the thruster surfaces from the plasma. An alternative method to estimate power losses from temperature data, which requires an entirely different set of assumptions, is to use commercial finite element analysis software to model the thermal system and finding the required power input to plasma-exposed surfaces to match temperature profiles. A thermal model of the instrumented DCFT was constructed using SolidWorks Simulation software, utilizing its iterative finite element solver, in order to employ this method for comparison with estimates based on a simplistic analysis.

The thruster, cathode, PTFE Langmuir probe terminal and required supports are all modeled along with the thin PTFE pad used to electrically insulate the thruster body from the grounded thruster mount. The bottom of the PTFE pad is set as a room temperature thermostat, due to its low thermal conductivity coupled with its connection to the vacuum chamber (which is never far from room temperature during testing) through a large metal structure. A room temperature boundary condition is also applied to the end of the long copper wire connected to the anode stem which eventually connects to an (unmodeled) electrical feedthrough. The length of the wire is seen in simulations to affect anode heating and cooling rates, but has little impact elsewhere.

Radiative transfer between surfaces and from external surfaces to the room temperature vaccum chamber is considered with lumped emissivities of 0.2 for all conductors (except for the anode which is given a value of 0.7 based on calibration with the thermal camera) and 0.85 for all non-conductors. All radiators are considered diffuse greybodies. These are broad assumptions which will certainly affect the overall uncertainty of the model, but are expected to be reasonable enough for the estimates ultimately obtainable.

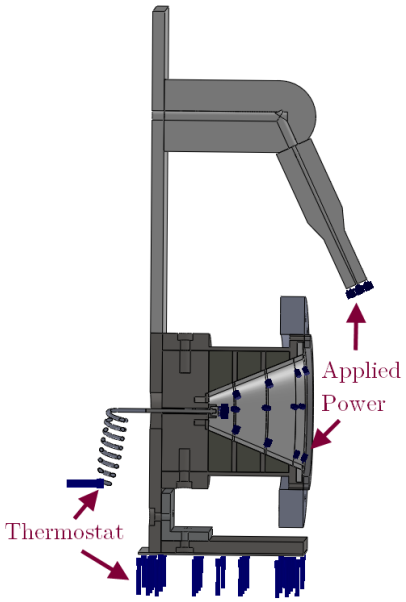

Figure 4-27: SolidWorks model of instrumented DCFT in cross section showing location of constant temperature boundary conditions and constant heat power inputs.

Evenly distributed power sources, shown in Fig. 4-27, were applied to the cathode orifice plate (3 W for all simulations presented), the anode and to sections of the cone which were artificially separated by the three wall cusps in order to allow a spatial dependence of the power input to the BN cone. Plasma loss is primarily through the wall cusps, so a proper matching of thermal model to temperature profiles on the cone is expected to require some segregation of the amount of power reaching each cusp separately from the intermediate spaces.

Perhaps the most difficult boundary conditions to prescribe are the thermal contact resistances between thruster materials which occur due to some mismatching at the surfaces. Some values of thermal contact resistance for common materials under different loading conditions can be found in the literature, but the measurements often prescribe resistances which vary by one or more orders of magnitude as conditions are changed [172, 173]. The dependence of the thermal contact resistance on unmeasured properties, such as surface roughness characteristics for all the different materials in use and contact pressure, makes it difficult to make a confident estimate for use in our model.

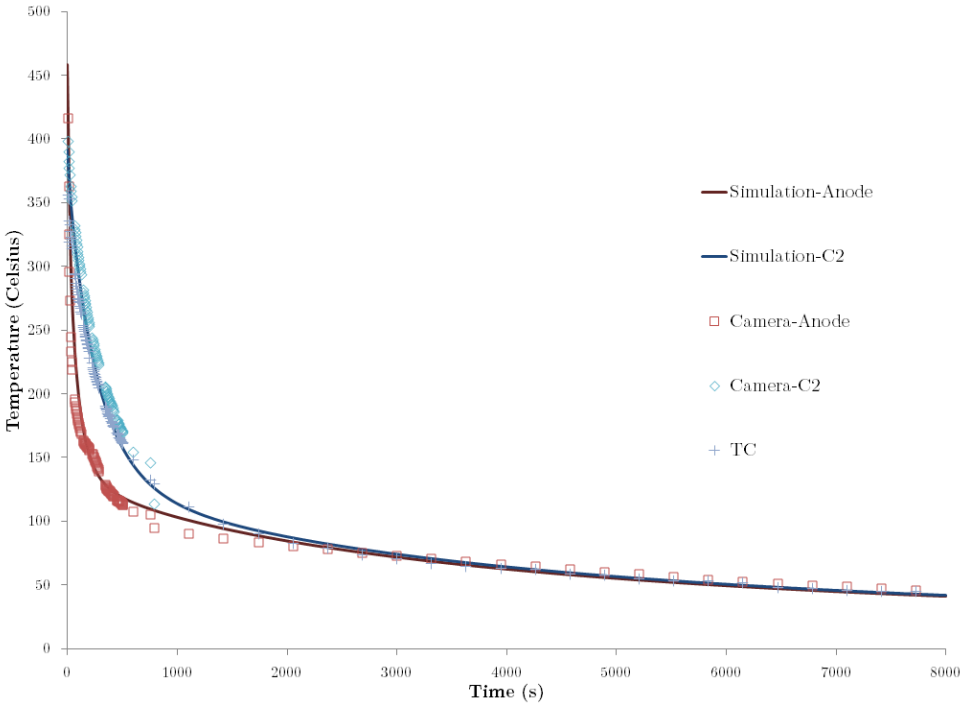

Figure 4-28: Thruster temperatures during cool-down after operation at 450 V and 0.56 A from SolidWorks simulations, transmissivity calibrated thermal camera and thermocouple measurements.

Instead, relative values were prescribed based on general classes of materials and the absolute value changed until unsteady simulations of the thruster cooling matched camera measurements. Matching a cooling transient is a far better gauge of the validity of the thermal model than the matching of a heating transient as the applied power knobs can be tuned to match measurements essentially regardless of the other boundary conditions.

Conductive materials in contact with other conductive materials were given contact resistance ten times less than contacts between non-conductive materials and any surface. The outer wall of the boron nitride cone is not given a conductive path to the surrounding magnets, since the instrumented cone has a slot between the two surfaces to allow probe leads to fit. The bottom of the cone is given a contact resistance five times higher than normal to the base core and diffuser due to the generally loose fit observed between the two. The best match with cooling data is found with conductor-conductor contact resistances of 0.00125 K-m^2/W (which is on the same

order as values in the literature [173]), with results plotted in Fig. 4-28.

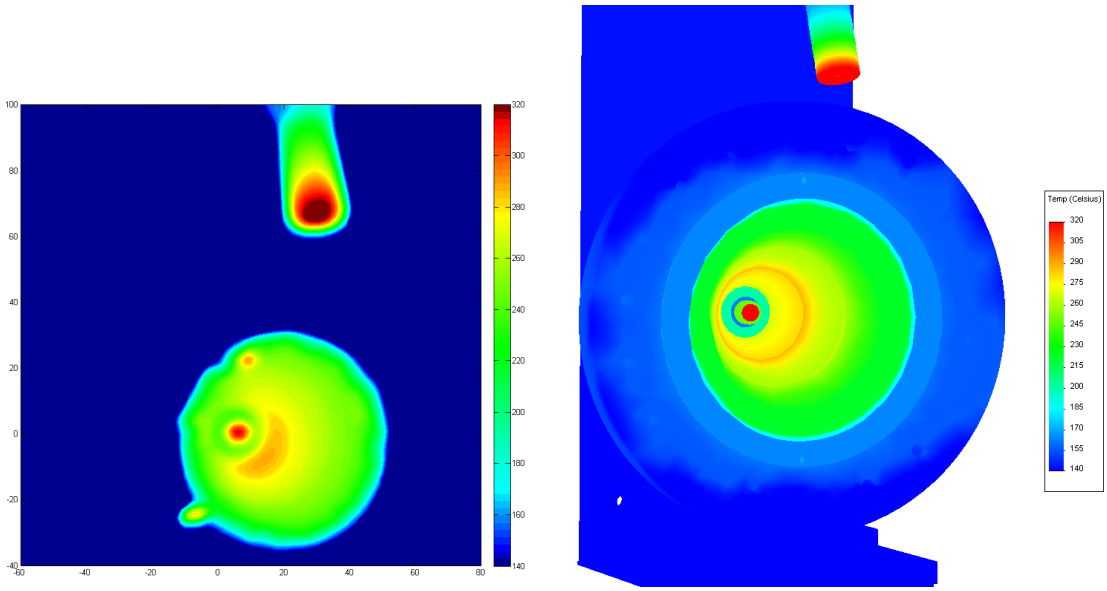

(a) (b)

Figure 4-29: (a) Transmissivity calibrated temperatures measured by the thermal camera (b) Output temperatures from SolidWorks model

The model is then used to find which power inputs to the cone and anode result in predicted temperatures matching IR camera data, with an example of matched temperature outputs shown in Fig. 4-29. Examples of matched cone wall temperature profiles are shown in Fig. 4-30, which also demonstrate two different profile shapes. The power distributed to the cone in Fig. 4-30a is roughly the same for the upstream, middle and downstream thirds of the insulator, while over half the total power to the cone is concentrated in C3 to match the profile of Fig. 4-30b.

Total power input to the wall is plotted versus anode power in Fig. 4-31 for the flow rate scan, showing results obtained by the finite element model and by a simple energy equation analysis of the wall temperature profiles detailed in Appendix C. The two estimation methods provide very similar ranges for the power lost to the walls, which is nearly constant at 20-30% of the input power. Trends in power loss with input power are generally opposed in the two methods, however large uncertainties in both cases, which arise primarily from the underlying assumptions, limit the utility of analysing such small changes.

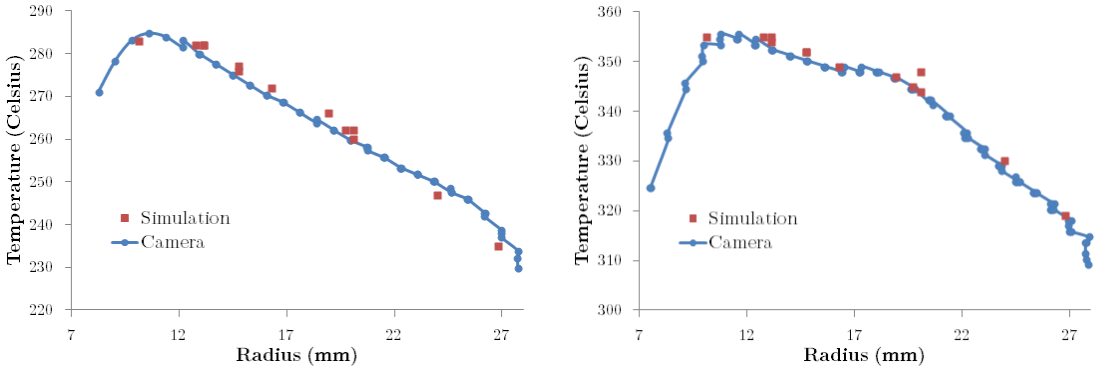

(a) (b)

Figure 4-30: Comparison of simulated and thermal camera measured temperatures along the BN cone wall for the (a) 7 sccm case from the flow rate scan of Fig.4-9 and (b) the 400 V case from the voltage scan of Fig.4-14.

A similar exposition of the results of the two methods is given in Fig. 4-32 for the anode voltage scan. The estimated power losses are again in the 20-30% range for all voltages tested at a 7 sccm xenon flow rate, with little dependence on voltage. Thrust measurements on similar DCFT prototypes are reported by Courtney [1] and Daspit [2] to yield anode efficiencies in the 20-30% range. The anode efficiency of Eqn. 2.6 can be re-expressed as the product of the utilization efficiency, η_u, the cosine-squared efficiency, $< \cos\theta >^2$, and the ratio of ion beam power to input anode power. Assuming the anode power is spent on wall losses and inelastic collisions (ionization and excitation, with no reabsorbtion of radiated energy) with the remainder being expelled in the ion beam, and further that η_u and $< \cos\theta >^2$ are 65% and 80% respectively (based on data in Fig. 3-17, correcting for measurement origin), the wall loss estimates above suggest that 15-35% of the input power is lost through inelastic processes.

The wall power estimated by the simulations is found by matching steady-state solutions to the thermal model with camera-obtained temperature profiles which have not necessarily reached a steady state (as can be gleaned from the non-zero temperature slopes in Fig. 4-22). During the flow rate scan the thruster has only been operating for 24 minutes before the flow is increased from 5 to 6 scccm of xenon, with subsequent flow rate changes occurring every 15 minutes or so. Initial tests with the

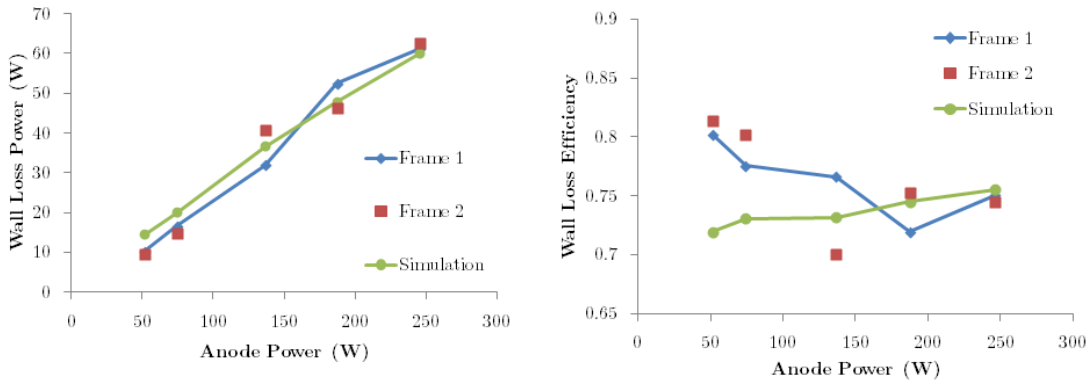

(a) (b)

Figure 4-31: Comparison of output of thermal model and simple analysis of cone temperatures for (a) total power lost to the wall and (b) unity minus power loss over anode power (1-P_w/P_a) versus anode power for the flow rate scan of Fig.4-9 with estimates made using the method of Appendix C and either the first IR camera image obtained after an anode power change (Frame 1) or the second image (Frame 2).

infrared camera suggest the BN cone reaches a steady temperature after roughly 45 minutes, with the temperature change after 15 minutes reaching over 75% of the total temperature increase from start-up to steady. By matching steady-state simulations to temperature profiles below their steady values we are underestimating the power lost to the walls, likely by less as the total time of the parameter scan increases.

Unsteady simulations can be obtained using SolidWorks to match the under-developed temperature profile measurements, however this is a time consuming process. A typical steady-state simulation takes roughly 10 minutes, allowing a simple guess-and-check method to be applied to find a matching input power condition, while each unsteady simulation takes several hours.

Measurements made with the internal Langmuir probes which run from 0.5 cm upstream of C1 to 0,5 cm downstream of C2 can also be used to estimate plasma deposited power to the walls. The details of a study using the internal probes are given in a separate paper [104], with one of the major results being an abnormally high ion current collected by probes near C1 and C2. The power to the wall can be estimated using the measured ion saturation current and the equation,

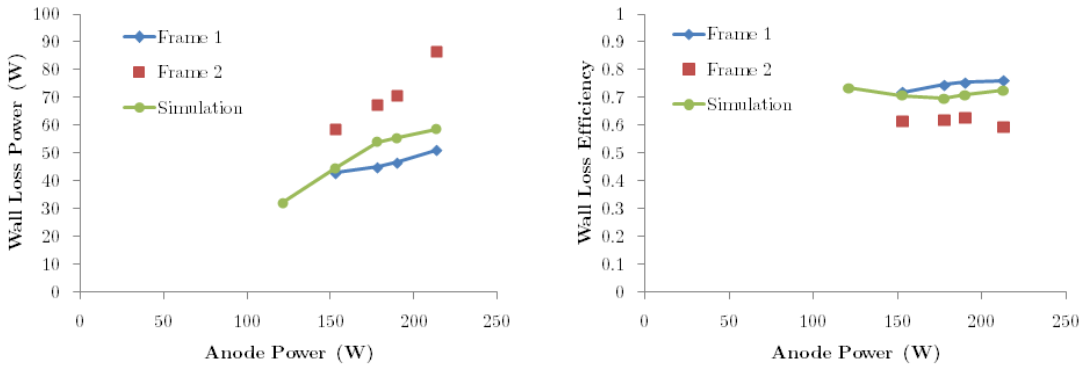

(a) (b)

Figure 4-32: Comparison of output of thermal model and simple analysis of cone temperatures for (a) total power lost to the wall and (b) efficiency of thruster minus power loss versus anode power for the anode voltage scan of Fig.4-14.

$$P_w \approx \frac{I_{i,sat}}{A_p}(2\pi R_w \Delta h) T_e \left\{ \frac{1}{2} + \ln\left[(1-\Gamma)\sqrt{\frac{m_i}{2\pi m_e}} \right] + \frac{2}{1-\Gamma} \right\} \tag{4.6}$$

where A_p is the area of the probe, R_w is the cone radius at the probe location and Δh is the axial length of the cell whose incident power is being estimated. The first two terms in the brackets correspond to the energy brought to the wall by ions accelerated by the presheath and sheath potential drops, while the third term accounts for the average energy of wall impinging electrons of $2T_e$.

A spline was fit to the ion current and electron temperature profiles measured by the wall probes with a resultant Δh of 1 mm. Raw ion saturation current measurements lead to an estimated wall power of 3.3 kW for an applied anode power of 135 W, demonstrating the extent to which the wall probes draw an anomalously high ion current. The aforementioned paper presents the resulting plasma densities obtained by using data reduction methods which rely on the electron current, as opposed to the ion current, collected by the probe and uses the ratio of the ion current-predicted plasma density with the new density measurements to prescribe an effective probe area 10-100 times larger than the physical one [104].

Using the effective probe areas presented in the paper to estimate the wall losses results in the profile given in Fig. 4-33 which show strongly peaked power losses in

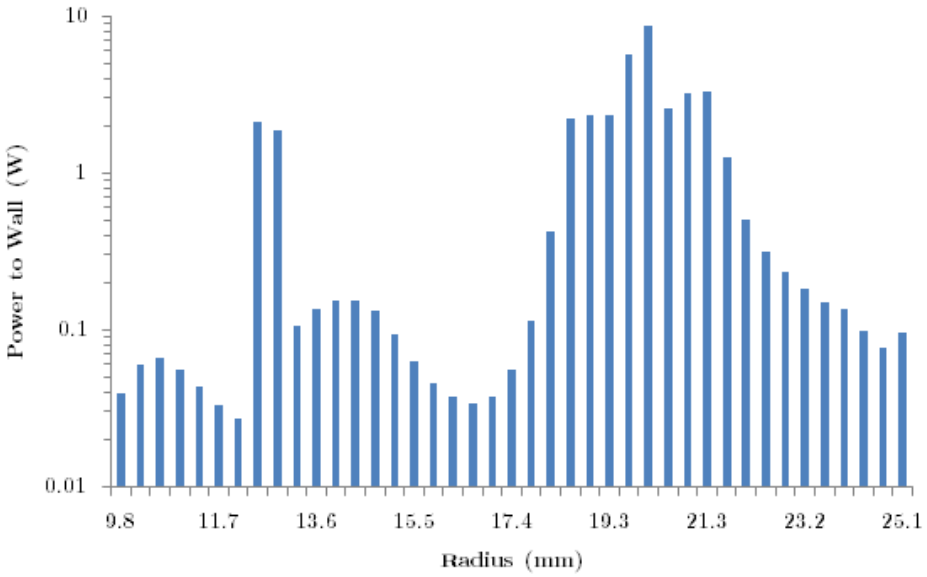

Figure 4-33: Estimates of plasma deposited power on the insulating cone wall in 1 mm axial increments versus wall radius. DCFT operating in LC mode at 410 V and 330 mA on the anode using 7 sccm xenon anode flow rate.

C1 (at a 13 mm radius) and C2 (at a 20 mm radius). The total power to the wall calculated this way is 39.2 W, or 29% of the anode power, falling in line nicely with the estimates presented using the thermal model and thermal imaging data. This technique also underestimates the total power deposited on the walls seeing as no data is obtained for C3, which may reasonably increase the total power by a third or so.

4.6 Chapter Summary

In this chapter a review is made of prior literature describing first the bifurcation observed in the DCFT followed by various types of bifurcations found in Hall thrusters and hollow cathodes. Low frequency anode current oscillations in Hall thrusters are also reviewed, both through measurement and simulation, before experimental results of anode current oscillation monitoring on the DCFT through parametric scans of anode flow rate, voltage, external EM current, and cathode position are presented.

The DCFT transitions from a quiescent low-current mode to a high current mode

marked by large amplitude breathing-type oscillations under anode conditions which correspond, in the absence of a plasma, to a lowering of the reduced electric field, E/n_n. The reduced field is a measure used widely in Townsend discharges due to its strong correlation with the average electron energy. Anode current oscillation measurements show a distinct trend as the anode conditions are brought to lower values of the (plasma-free) reduced electric field, by either raising the anode mass flow rate or lowering the anode voltage.

In LC mode the anode current oscillations are a small fraction of the DC current, with a peak power spectral density in the 4-8 kHz range, which under some conditions exhibits several harmonics. As the reduced field is lowered a coherent peak becomes measurable in the 25-100 kHz range, which is noted in one case to decrease in frequency as the anode flow rate is further increased, while the lower frequency peak moves to a slightly higher frequency. The occurrence of the 25-100 kHz oscillation seems to appear (at least within the bandwidth of the AC current measurements) only at conditions close to mode transition.

Near the transition point the thruster is typically highly unstable, sometimes visibly flickering between modes. The anode current waveforms in this region exhibit intermittent spikes in anode current which reach several times the DC current value, with multiple periods worth of quasi-sinusoidal oscillations about the DC current in between. As the reduced field is further lowered the thruster enters a more stable HC mode, typically exhibiting a stunted current peak roughly one third to one half of the period between current minima, with a sharp (tens of μs long) high amplitude current peak occurring just before the near-extinction of anode current. Lowering the reduced field even more appears to shift the main anode current spike closer in phase to the stunted peak until it is eventually incorporated into a singly peaked structure. The power spectral density in HC mode is marked by sharp high amplitude peaks around 1-4 kHz with many clear harmonics of the fundamental frequency.

An increase in the current to an external electromagnet, which increases the field strength near the axis just downstream of the exit separatrix but decreases it just upstream, is shown to increase the frequency of the breathing mode in HC modes as

well as the frequency of both the 6-8 kHz oscillations and the 35-45 kHz fluctuations (which are only in the range of measurements at low EM currents). The increase in breathing frequency with EM current appears similar in nature to the increased frequency found by increasing the anode flow rate, in that a stunted peak is reached a fairly consistent interval after anode current minima, but the main current spike occurs increasingly close (in time) to this point.

Similarly a scan of cathode position relative to the edge of the main ion beam in the plume shows an increase in breathing mode frequency as the thruster is brought further from conditions which lead to the LC mode. In this case, the LC mode occurs when the cathode is just outside of the beam edge, while HC mode is obtained when the cathode is either far outside of the plume or at radial positions inside that of the main ion beam.

Some similarities can be drawn to the DCFT from the literature presented in this chapter. The transition from a high current mode marked by high amplitude, low frequency oscillations to a quiescent low current mode at high voltages found by Brown and Gallimore [3] on the H6 bears a striking resemblance to the DCFT bifurcation, except for its opposite dependence on anode mass flow rate. The authors show that an increase in the neutral density near the centrally-mounted cathode can quench the oscillations and lead to the recovery of a low current mode, similar to studies done on hollow cathodes for use in ion engine discharge chambers by Goebel et al [145]. A recent study by MacDonald and Gallimore on the H6 suggests that the transition to low current mode is tied to an increase in the coherence of a rotating spoke mode [174] with an m=1 frequency of 5 kHz.

High speed camera imaging of the DCFT has yet to reveal any azimuthal fluctuations [19], even using the same types of normalization techniques discussed by MacDonald and Gallimore. It is also a bit mind-bending to try to imagine how a spoke mode might propagate in the complicated electric and magnetic fields internal to a device like the DCFT. If the axial motion of the electrons in the spoke is due to an $E_\theta \times B_r$ drift, then the azimuthal electric field must change direction upon crossing each point cusp, where the radial magnetic field changes sign, in order to lead

to a continuous flow towards the anode. The rotational direction of the spoke must also change directions at each separatrix assuming the electric field in the plasma is pointing towards the ring cusp (which it generally does to keep ions bound to the well-confined electrons). Although a spoke mode may not exist in the DCFT in the same sense as it does in Hall thrusters, it is acknowledged that an oscillation exists in LC mode in the same general frequency range which is as yet unidentified and may or may not have an impact on electron transport.

Another similarity from the literature is in the use of high keeper currents in the CHT in order to dampen a dominant low frequency oscillation, which in cusp mode led to a decrease in anode current as well [153], with the high keeper current mode estimated to lead to a halving in the anomalous transport frequency. In the DCFT an increase in keeper current has been shown to aide in obtaining a stable LC mode, but also, as demonstrated in this chapter, the proximity of the cathode to the edge of the ion beam plays a strong role in determining the mode of operation. These two effects, higher keeper current and plume adjacent cathode position, may be sides of the same coin, as both can be expected to lead to better coupling of the hollow cathode system with the anode. The increased keeper current was shown by Raitses et al to lead to an upstream motion of the electric field, while in the DCFT it is shown in Ch. 3 to lead only to a decrease in the overall potential in plume (which is accomplished alternatively by increasing the plasma-free reduced electric field). Parker demonstrates that a high enough keeper current can also cause an observed rotating spoke mode to extinguish in the CHT [155].

The high speed camera imaging of the DCFT bears a strong resemblance to the optical measurements of Darnon et al [158] who find a stationary cycle of brightening and dimming inside the chamber which corresponds with the breathing oscillations measured on the anode. Darnon et al also find an ejection of luminosity past the exit estimated to travel around 20 km/s, similar to the ejected blob seen in the DCFT [19] and in time-resolved Hall thruster plume measurements by Lobbia and Gallimore [167]. There is not much doubt that the low frequency oscillations in HC mode are of the breathing mode type, however the 25-100 kHz fluctuations measured in the LC

mode anode current signal are still quite mysterious.

Thermal measurements show no evidence of enhanced wall losses during operation in HC mode, with the main difference in modes manifest as a jump in anode temperature, and a larger gradient in temperature along the wall, pointing towards the upstream end. The lack of a clear jump in power lost to the wall does not necessarily rule out a change in the erosion rates between modes as the sputtering process is highly ion energy dependent. One could imagine a steady stream of low energy ions resulting in the same time-averaged wall deposited power as intermittent, short bursts of high energy ion impingement, though the latter case can result in much higher erosion rates.

Perhaps the main result from the thermal experiments is the lack of clear evidence for any increase in proportional power loss to the second and third ring cusp regions of the wall when the thruster transitions from LC to HC mode. There is no evidence to discredit a jump in the power deposited upstream of the first wall cusp upon transition to HC mode, however it is possible that at least some of the heating observed by infrared camera measurements in this region is an artifact of the non-ideal emission characteristics of the wall material–the conical boron nitride surface is not a diffuse blackbody radiator, as assumed for convenience, and its radiosity may in fact have a large contribution from the anode and anode guard. Once in HC mode, an increase in voltage (and thus anode power) appears to increase the power deposited near C3 and C2 (especially) without much effect upstream.

Several methods for estimating the power deposited by the plasma to the discharge chamber walls were presented with results all suggesting a wall loss of roughly 30% of the anode power, which is not a high percentage. Such a low wall loss would suggest a large percentage of the anode power was being lost to inelastic collisions, which generally only dominate the power balance at low ($<$10 eV) electron temperatures. The estimations presented, however, are all expected to underpredict the power deposited on the walls.

Chapter 5

Unsteady Model of Cross-Field Plasma Flows

The dominant oscillation in the DCFT bears many similarities to the breathing mode found in Hall thrusters and though the magnetic field structures and chamber geometries are quite different in the two devices, the fundamental interaction of ionization zone with neutral front is expected to remain as the driving factor. With this in mind, an unsteady, one-dimensional model of a Hall thruster discharge is adapted from the work of Barral and Ahedo [12] in order to investigate trends in the self-excitation (or damping) of breathing modes with respect to model inputs. Simulations varying the input mass flow rate show that the high amplitude oscillations are strongly damped at low flow rates. This result matches qualitatively what is seen experimentally in the DCFT, suggesting a similar mechanism may be in place.

The model relies on at least a few simplifying assumptions which may, at first glance, appear to preclude its use from describing dynamics in the DCFT, however the main focus of this exercise is to determine how a breathing-type oscillation can be initiated by increasing the mass flow rate, or alternatively lowering the applied voltage, past some threshold value. A quantitatively accurate result is not sought, instead some insight into qualitative effects of magnetic field strength, anode voltage and mass flow rate on the instability in question is desired.

In the following section the 1-D model equations are derived starting from the

normal fluid equations using a procedure of radial averaging. The equations are then cast into a form amenable to simple numerical schemes, and the implementation of those schemes is discussed. The general procedure largely mirrors that described by Barral and Ahedo [12] in order to compare our initial results to some from the recent literature on Hall thruster breathing modes, before departing towards a model intended to capture some of the effects of the DCFT's distinct geometry.

5.1 Derivation of 1-D Fluid Equations

While a complete description of Hall thruster dynamics is likely to require three spatial dimensions, due to the essential contribution azimuthal fluctuations are expected to have on electron transport, it is possible to relax this constraint, at the cost of self-consistency, by summing up all azimuthal inhomogeneities into a phenomenological Bohm diffusion-type term. The problem is then only spatially dependent on the axial and radial directions, the second of which can be removed from the fluid equations by averaging all macroscopic properties over the radial extent of the discharge channel. This procedure is demonstrated below where the ion continuity equation, Eqn. 5.3, is transformed into a 1-D equation expressed in terms of radially averaged quantities. The radial average (denoted by an overbar) of quantity g is defined as,

$$\overline{g} = \frac{1}{A}\int_{r_0}^{r_1} 2\pi r g dr \tag{5.1}$$

where r_0 is the inner radius of the channel, r_1 is the outer radius, and A is the cross-sectional area. Much use is made of Reynold's transport theorem in the form,

$$\frac{\partial}{\partial x}\int_a^b g dr = \int_a^b \frac{\partial g}{\partial x} dr + \frac{\partial b}{\partial x} g(b) - \frac{\partial a}{\partial x} g(a) \tag{5.2}$$

Starting with the differential form of the continuity equation, where quasineutrality is imposed through $n_i = n_e$,

$$\frac{\partial n_e}{\partial t} + \nabla \cdot (n_e \mathbf{v}_i) = n_e \nu_{ion} \tag{5.3}$$

and averaging over the radial direction,

$$\frac{2\pi}{A}\int_{r_0}^{r_1} r\frac{\partial n_e}{\partial t}dr + \frac{2\pi}{A}\int_{r_0}^{r_1}[\frac{\partial}{\partial x}(n_e v_{ix}) + \frac{1}{r}\frac{\partial}{\partial r}(r n_e v_{ir})]rdr = \frac{2\pi}{A}\int_{r_0}^{r_1} r n_e \nu_{ion} dr \quad (5.4)$$

we can apply Eqns. 5.1 and 5.2 to obtain,

$$\frac{\partial \overline{n_e}}{\partial t} + \frac{1}{A}\frac{\partial}{\partial x}(\overline{n_e v_{ix}}A) = \overline{n_e \nu_{ion}} - \overline{n_e \nu_{iw}} \quad (5.5)$$

where the average wall collision frequency, ν_{iw}, is defined through Eqn. 5.6 below. The only assumption made between Eqn. 5.3 and Eqn. 5.5 is one of azimuthal symmetry.

$$\overline{n_e \nu_{iw}} = \frac{2\pi}{A}\left[r n_e v_{ir}|_{r_1} - r n_e v_{ir}|_{r_0} + r n_e v_{ix}|_{r_0}\frac{\partial r_0}{\partial x} - r n_e v_{ix}|_{r_1}\frac{\partial r_1}{\partial x}\right] \quad (5.6)$$

The representation of the radially averaged wall collision frequency in Eqn. 5.6 may not be immediately clear, however by introducing a divergence in the wall channel at an angle of $+\alpha$ at r_1 and $-\alpha$ at r_0, so that $\partial r_1/\partial x = \tan\alpha$ and $\partial r_0/\partial x = -\tan\alpha$, Eqn. 5.6 becomes,

$$\overline{n_e \nu_{iw}} = \frac{2\pi}{A}\left[(r n_e(v_{ir} - v_{ix}\tan\alpha))|_{r_1} + (r n_e(-v_{ir} - v_{ix}\tan\alpha))|_{r_0}\right] \quad (5.7)$$

The velocity component along the outward normal to the chamber walls, v_{iw}, can be expressed at r_1 as $v_{iw} = v_{ir}\cos\alpha - v_{ix}\sin\alpha$ and at at r_0 as $v_{iw} = -v_{ir}\cos\alpha - v_{ix}\sin\alpha$. Rewriting Eqn. 5.7 in terms of v_{iw} and noting that $\cos\alpha$ is equal to the ratio of a differential distance in the x-direction, Δx, with a differential distance measured along the wall, Δw, we obtain,

$$\overline{n_e \nu_{iw}} = \frac{2\pi r_1 \Delta w}{A\Delta x}(n_e v_{iw})|_{r_1} + \frac{2\pi r_0 \Delta w}{A\Delta x}(n_e v_{iw})|_{r_0} \quad (5.8)$$

which is clearly the number of particles hitting a differential area along both walls each second divided by the differential volume of the chamber in that region.

Since the ion gyroradius is large compared to the size of a typical Hall thruster channel, the Lorentz force effect on ion motion can be neglected and only the axial component of the ion momentum equation need be considered. Another assumption, typical to Hall thrusters, is the smallness of the ion pressure gradient term in comparison to the electric field and drag force terms. Since the ions are not magnetically confined, the electric field tends to mainly increase the ion kinetic energy, rather than thermal, and ions do not thermalize much with the far hotter electrons due to the large mass disparity between ions and electrons and the infrequency of collisions between the two species compared to collisions with the dense neutral background. All this generally leads to ion temperatures which are low in comparison to electrons.

The axial ion momentum equation is given below in cylindrical coordinates, where the last term on the left-hand-side is due to the influx of momentum in the considered volume due to ions being born at the neutral speed. The total ion collision frequency, ν_i, is the sum of hard-sphere-type ion-neutral collisions, ν_{in}, and resonant charge exchange processes, ν_{cx}, with a 0.5 factor due to the reduced mass, so that $\nu_i = 0.5(\nu_{in} + \nu_{cx})$.

$$\frac{\partial n_e m_i v_{ix}}{\partial t} + \frac{\partial n_e m_i v_{ix}^2}{\partial x} + \frac{1}{r}\frac{\partial r n_e m_i v_{ir} v_{ix}}{\partial r} - m_i n_e \nu_{ion} v_n = e n_e E_x - n_e \nu_i m_i (v_{ix} - v_n) \quad (5.9)$$

The radial averaging of the ion continuity equation proceeds similarly to derivation of Eqn. 5.5 and results in,

$$\frac{\partial \overline{n_e m_i v_{ix}}}{\partial t} + \frac{1}{A}\frac{\partial \overline{n_e m_i v_{ix}^2} A}{\partial x} = e\overline{n_e E_x} - m_i \overline{n_e v_{ix} \nu_{iw}} + m_i \overline{n_e \nu_{ion}} v_n \quad (5.10)$$

where we assume $\nu_i << \nu_{ion}, \nu_{iw}$, even though the cross section for charge-exchange is larger than for ionization in xenon, because ions generally move much slower than electrons, leading to relatively low reaction rates.

We continue, applying the same procedure to the electron momentum equation, shown below in cylindrical coordinates, where ν_e is total collision frequency for electrons, here comprised of electron-neutral collisions and effective turbulent scattering,

and where **E** and **B** represent the applied electric and magnetic fields. Azimuthal symmetry (i.e. $\partial/\partial\theta \to 0$) is once again assumed.

$$\frac{\partial n_e m_e v_{ex}}{\partial t} + \frac{\partial n_e m_e v_{ex} v_{ex}}{\partial x} + \frac{1}{r}\frac{\partial r n_e m_e v_{er} v_{ex}}{\partial r} = -\frac{\partial n_e T_e}{\partial x} - e n_e E_x - e n_e v_{e\theta} B_r - n_e \nu_e m_e v_{ex} \tag{5.11}$$

$$\frac{\partial n_e m_e v_{e\theta}}{\partial t} + \frac{\partial n_e m_e v_{ex} v_{e\theta}}{\partial x} + n_e m_e v_{er}\frac{1}{r}\frac{\partial r v_{e\theta}}{\partial r} + \frac{n_e m_e v_{e\theta}}{r}\frac{\partial r v_{er}}{\partial r} = e n_e (v_{ex} B_r - v_{er} B_x) - n_e \nu_e m_e v_{e\theta} \tag{5.12}$$

$$\frac{\partial n_e m_e v_{er}}{\partial t} + \frac{\partial n_e m_e v_{ex} v_{er}}{\partial x} + \frac{1}{r}\frac{\partial r n_e m_e v_{er} v_{er}}{\partial r} - \frac{m_e n_e v_{e\theta}^2}{r} = -\frac{\partial n_e T_e}{\partial r} - e n_e E_r + e n_e v_{e\theta} B_x - n_e \nu_e m_e v_{er} \tag{5.13}$$

The axial and radial momentum equations (Eqns. 5.11 & 5.13) have a simple radially averaged form, which can be obtained by inspection of Eqns. 5.4 & 5.5.

$$\frac{\partial \overline{n_e m_e v_{ex}}}{\partial t} + \frac{1}{A}\frac{\partial}{\partial x}(\overline{n_e v_{ex} m_e v_{ex}} A) + \overline{n_e \nu_{ew} m_e v_{ex}} = -e\overline{n_e E_x} - e\overline{n_e v_{e\theta} B_r} - \overline{\frac{\partial n_e T_e}{\partial x}} - \overline{n_e \nu_e m_e v_{ex}} \tag{5.14}$$

$$\frac{\partial \overline{n_e m_e v_{er}}}{\partial t} + \frac{1}{A}\frac{\partial}{\partial x}(\overline{n_e v_{ex} m_e v_{er}} A) + \overline{n_e \nu_{ew} m_e v_{er}} - \overline{\frac{n_e m_e v_{e\theta}^2}{r}} = -e\overline{n_e E_r} + e\overline{n_e v_{e\theta} B_x} - \overline{\frac{\partial n_e T_e}{\partial r}} - \overline{n_e \nu_e m_e v_{er}} \tag{5.15}$$

The radial derivatives in Eqn. 5.12 can be regrouped to resemble the radial deriva-

tive in Eqn. 5.4 plus an additional term yielding,

$$\begin{aligned}\frac{\partial\overline{n_e m_e v_{e\theta}}}{\partial t} &+ \frac{1}{A}\frac{\partial}{\partial x}(\overline{n_e v_{ex} m_e v_{e\theta}}A) + \overline{n_e \nu_{ew} m_e v_{e\theta}} + \frac{\overline{n_e m_e v_{er} v_{e\theta}}}{r} \\ &= e\overline{n_e v_{ex} B_r} - e\overline{n_e v_{er} B_x} - \overline{n_e \nu_e m_e v_{e\theta}} \end{aligned} \tag{5.16}$$

where the final term on the left-hand-side can be neglected due to the assumed symmetry of the radial velocity (electrons flow towards the wall on either side of the mid-channel radius). The wall collision terms can be incorporated into the total electron collision frequency by defining $\nu_{em} = \nu_e + \nu_{ew} = \nu_{en} + \alpha_B\omega_{ce} + \nu_{ew}$. The axial magnetic field can typically be neglected in a Hall thruster, as can the axial electron inertia. The relevant equations then simplify to,

$$e\overline{n_e E_x} = -m_e\overline{n_e v_{e\theta}\omega_{ce}} - \frac{\overline{\partial n_e T_e}}{\partial x} - m_e\overline{n_e \nu_{em} v_{ex}} \tag{5.17}$$

$$\frac{\partial\overline{n_e m_e v_{e\theta}}}{\partial t} + \frac{1}{A}\frac{\partial}{\partial x}(\overline{n_e v_{ex} m_e v_{e\theta}}A) = m_e\overline{n_e v_{ex}\omega_{ce}} - \overline{n_e \nu_{em} m_e v_{e\theta}} \tag{5.18}$$

Lastly, we consider the electron energy equation, given below, which includes the heat flux vector, $\mathbf{q_e}$, and a term for energy lost through inelastic collisions, $\alpha_i E_i$, where α_i is a factor (a local ion production cost) accounting for both ionization and excitation, and E_i is the ionization potential of the working gas.

$$\begin{aligned}\frac{\partial}{\partial t}(\frac{3}{2}n_e T_e + \frac{1}{2}m_e n_e v_e^2) + \nabla\cdot(n_e\mathbf{v_e}\frac{5}{2}T_e + \frac{1}{2}m_e n_e v_e^2\mathbf{v_e} + \mathbf{q}_e) \\ = -en_e\mathbf{v_e}\cdot\mathbf{E} - n_e\nu_{ion}\alpha_i E_i \end{aligned} \tag{5.19}$$

In Eqn. 5.19 the electron pressure is assumed to be isotropic, i.e. $\vec{\vec{P}}_e = n_e T_e \vec{\vec{I}}$, and the interspecies temperature equilibration term resulting from elastic collisions is neglected due to the large disparity in masses between electrons and ions. In further versions of the energy equation we will also neglect the contributions from

the heat flux vector, which is zero for an isotropic electron distribution function. The presence of strong electric and magnetic fields and of the channel walls will certainly lead to anisotropies in the electron distribution [183], but such effects are beyond the scope of the present model. Neglecting the heat conduction term reduces the order of the equation by one and, it is hoped, still retains the main mechanisms behind the sought-after instability.

Care must be taken when radially averaging the divergence term in Eqn. 5.19 due to the presence of the sheath, which changes the net average energy of the electron flux across the sheath edge. Recalling the derivation of the electron energy equation from the Boltzmann equation we can see that the divergence term is really $\nabla \cdot (< 1/2 m_e w^2 \mathbf{w} >_e)$. We return to this definition and take the average energy of the radial component having enough velocity to reach the wall in Eqn. 5.20, assuming a drifting Maxwellian distribution function.

$$< \frac{1}{2} m_e w^2 w_z >_e = n_{e\infty} (\frac{m_e}{2\pi T_e})^{3/2} \int_{-\infty}^{\infty} \int_{-\infty}^{\infty} \int_{\sqrt{\frac{2e\phi_{sh}}{m_e}}}^{\infty} w_z \frac{1}{2} m w^2 e^{\frac{-m w_z^2}{2T_e}} dw_z e^{\frac{-m(w_x - v_x)^2}{2T_e}} dw_x e^{-\frac{-m(w_y - v_y)^2}{2T_e}} dw_y \tag{5.20}$$

A slab model is used in Eqn. 5.20 for simplicity with z pointing towards the wall, y pointing azimuthally, and x remaining as the axial coordinate. The plasma density away from the wall is denoted $n_{e\infty}$ and the potential difference between the $n_{e\infty}$ location and the wall is expressed as ϕ_{sh}. Electrons with w_z less than that required to reach the wall can still pass the sheath edge, which is our limit of integration when taking radial averages, but they will be reflected and return to the sheath edge with the same energy they brought across. Carrying out the integration in Eqn. 5.20 results in,

$$< \frac{1}{2} m_e w^2 w_z >_e = n_{e\infty} \sqrt{\frac{T_e}{2\pi m_e}} e^{\frac{-e\phi_{sh}}{T_e}} [2T_e + \frac{1}{2} m_e (v_x^2 + v_y^2) + e\phi_{sh}] \tag{5.21}$$

where the term to the left of the square brackets is the flux of electrons to the wall, which leaves the bracketed term as the average energy of an electron leaving the plasma. Now that we have evaluated the average flux of energy at the entrance to each of the wall sheaths, the remainder of the radial averaging of Eqn. 5.19 is trivial, leading simply to,

$$\begin{aligned} \frac{\partial}{\partial t}(\frac{3}{2}\overline{n_e T_e} + \frac{1}{2}\overline{n_e m_e(v_{ex}^2 + v_{e\theta}^2)}) &+ \frac{1}{A}\frac{\partial}{\partial x}(\overline{n_e v_{ex}\frac{5}{2}T_e}A + \overline{n_e v_{ex}\frac{1}{2}m_e(v_{ex}^2 + v_{e\theta}^2)}A) \\ &= -e\overline{n_e v_{ex} E_x} - \overline{n_e \nu_{ion}\alpha_i}E_i - \overline{n_e \nu_{ew}\epsilon_w} \end{aligned} \quad (5.22)$$

where $\epsilon_w = 2T_e + 0.5m_e(v_{ex}^2 + v_{e\theta}^2) + e\phi_{sh}$ is the average energy lost from the plasma at the walls.

Neglected in the above derivations is the reflux of electrons from the channel walls, where the impact of high energy electrons on the channel surface leads to the emission of secondary electrons, while low energy electrons may be elastically reflected in a process known as backscattering. These effects are loosely accounted for by a lumped secondary electron yield, Γ, which is just the ratio of electron flux leaving the surface to re-enter the plasma with the flux of (primary) electrons leaving the plasma which are incident on the surface. When the channel surface is a dielectric, no current is collected and the secondary electron yield can be used to equate ion and electron wall fluxes through,

$$\nu_{iw} = \nu_{ew}(1 - \Gamma) \quad (5.23)$$

where it is assumed that particle fluxes are conserved across the plasma sheath (i.e. no ionization occurs in this thin region). As derived in section 2.3.2, the presence of secondaries alters the sheath potential, which for a dielectric is given by,

$$e\phi_{sh} = T_e \ln[(1 - \Gamma)\sqrt{\frac{m_i}{2\pi m_e}}] \quad (5.24)$$

The secondaries are emitted from the wall with little energy compared to the

primaries (except in the case of elastic backscattering, which is neglected here for convenience, due to lack of well-established empirical data) and therefore enter the plasma with roughly the sheath energy. Considering the reintroduction of energy to the plasma by secondaries we can now express the net average energy of an electron leaving the plasma as $\epsilon_w = 2T_e + 0.5m_e(v_{ex}^2 + v_{e\theta}^2) + (1-\Gamma)e\phi_{sh}$.

The reflux of electrons at the walls due to secondaries must be accounted for in the electron continuity and momentum equations as well. The inflow of electron momentum is only in the direction of the inward normal to the channel walls, which for a channel with little-to-no divergence is largely radial and therefore has no net contribution. The inflow of secondaries can be accounted for in in the continuity equation straightforwardly as,

$$\frac{\partial \overline{n_e}}{\partial t} + \frac{1}{A}\frac{\partial}{\partial x}(\overline{n_e v_{ex}} A) = n_e \nu_{ion} - (1-\Gamma)\overline{n_e \nu_{ew}} \tag{5.25}$$

so that the radially averaged equation results in current continuity, $d(n_e v_{ix} - n_e v_{ex})/dx = 0$, when added to Eqn. 5.5, using the identity in Eqn. 5.23. The net current through any r-θ plane does not change with x, and is equal to the instantaneous anode current, defined as,

$$I_a(t) = e n_e(x,t) A(x)(v_{ix}(x,t) - v_{ex}(x,t)) \tag{5.26}$$

where, for now, we allow the cross-sectional area to vary with the axial position, but not with time. A more complete model might allow for the change in the area containing the plasma plume with time, but this added complication is not expected to qualitatively affect our results.

Another wall process which must be accounted for is the recombination of ions with electrons near the surface of the wall material leading to the reintroduction of a neutral particle into the chamber, at a rate of roughly one neutral out per incoming ion. This leads to the form of the neutral conservation equation to be used the remainder of this study,

$$\frac{\partial \overline{n_n}}{\partial t} + \frac{v_n}{A}\frac{\partial \overline{n_n} A}{\partial x} = \overline{n_e \nu_{iw}} - \overline{n_e \nu_{ion}} \tag{5.27}$$

where the neutral flow speed is assumed constant for convenience, although it will accelerate axially due to preferential depletion of slower neutrals by ionization as well as by rarefaction past the channel exit. A more precise accounting of the neutral flow speed has been included in other 1-D Hall thruster models, without much apparent effect on the nature (as opposed to accurate recreation) of the sought-after current oscillations [175, 61].

5.2 Solution Method for the 1-D Fluid Equations

The set of equations above (namely 5.5, 5.10, 5.18, 5.22 & 5.27) contain n_n, n_e, v_{ix}, v_{ex}, $v_{e\theta}$, and T_e, as the only unknowns when the frequencies ν_{ion}, ν_{ew} and ν_{iw} can be expressed as functions of these variables. The set is closed with the condition that the potential difference between the cathode plane and anode remains constant in time. This condition is represented by Eqn. 5.28, where V_a is the applied anode potential, and the anode sheath (likely on the order of 10 V) is neglected. Some sophisticated models have included a more thorough treatment of the anode power supply as it couples to the plasma oscillations [184], however an ideal voltage source approximation ought to be sufficient for our purposes.

$$V_a = \int_0^L E_x dx \tag{5.28}$$

The system of non-linear, first-order, partial differential equations can be solved numerically using well-established numerical techniques. In particular, Eqns. 5.5, 5.10 and 5.18 can be cast as conservation equations, lending themselves to solution by finite volume methods. We once again follow Barral and Ahedo [12] in using the Harten-Lax-van Leer (HLL) method [176] to solve the conservative equations. First, we will introduce the HLL method and discuss its merits and drawbacks before discussing its implementation in our code.

5.2.1 The Harten-Lax-van Leer Method for Conservation Equations

The HLL scheme is a first order Godunov method which seeks to solve the initial value problem of Eqn. 5.29 at nodes representing cells of finite volume. Here u is a vector of functions of x and t, subscripts denote partial derivatives with respect to the subscripted variable and $f(u)$ is the flux of u.

$$u_t + f(u)_x = 0 \tag{5.29}$$

Numerical solution of the problem requires discretization onto grids in x and t, as demonstrated pictorially in Fig. 5-1 where u has a value at each x node and time t, designated $u(x_j, t^n) = u_j^n$. The Godunov scheme considers an approximate numerical solution of u, here called v, which is a piecewise constant function of x at each time step. The value v_j^n is the average value of the exact solution, u_j^n, evaluated from $x_{j-1/2}$ to $x_{j+1/2}$, and is also constant over this interval, so that a discontinuity exists in v halfway between each x node. A Riemann problem must be solved at each cell interface (i.e. at $x_{j-1/2}$ and $x_{j+1/2}$) in order to evaluate the fluxes there and calculate v_j at the next time step through Eqn. 5.30, where $f_{j+1/2}(v_j, v_{j+1})$ is the numerical flux at the interface based on the state on either side.

$$v_j^{n+1} = v_j^n - \frac{\Delta t}{\Delta x}(f_{j+1/2}^n(v_j^n, v_{j+1}^n) - f_{j-1/2}^n(v_{j-1}^n, v_j^n)) \tag{5.30}$$

Using a cell-interface referenced spatial coordinate, $x^* = x - x_{j+1/2}$, and a similar shift in the time, $t^* = t - t^n$, the Riemann problem is given as,

$$u_{t^*} + f(u(x^*, t^*))_{x^*} = 0, u(x^*, 0) = \begin{cases} u_L & \text{if } x^* < 0 \\ u_R & \text{if } x^* > 0 \end{cases} \tag{5.31}$$

and is represented pictorially in Fig. 5-1 for the case of a u vector with three components, in which signals propagate at speeds $\lambda_{1,2,3}$ and where $u_L = u_0$ is the value of u_j at $t = 0$ and $u_R = u_3$ is the value of u_{j+1} at $t = 0$. Harten, Lax, and

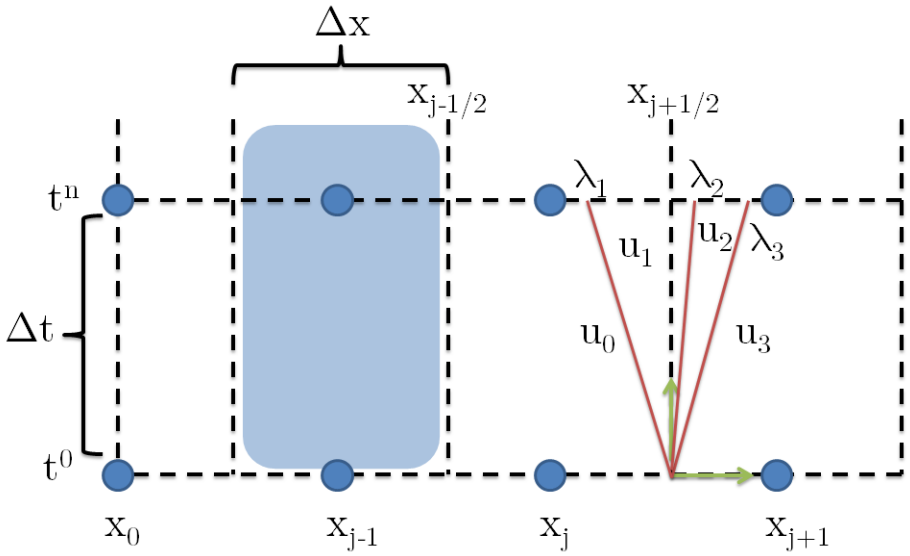

Figure 5-1: Nodal Representation of Finite Volume Method and Riemann Problem for a 3 Component u. Here u_i (i=0,1,2,3) refer to the different states of u separated by red lines denoting characteristics propagating at speeds λ_j (j=1,2,3).

van Leer note that the full Riemann solution is not necessary, as only the value at the interface (e.g. u_1 in Fig. 5-1) is used in the Godunov scheme. They propose a simple scheme which considers only one intermediate value between u_L and u_R which depends on the lower and upper bounds of the signal velocity, a_L and a_R respectively. If a_R is negative the solution is exactly u_R, while if a_L is positive the solution is exactly u_L. In the third case, $a_L < 0 < a_R$, the average value of the exact solution from $x^* = a_L \Delta t$ to $a_R \Delta t$ is used, and designated u_{LR}. The flux evaluated for this intermediate case is given as,

$$f(u_{LR}) = \frac{-a_L}{a_R - a_L} f(u_R) + \frac{a_R}{a_R - a_L} f(u_L) + \frac{a_L a_R}{a_R - a_L}(u_R - u_L) \tag{5.32}$$

This scheme is simple and is demonstrated to be entropy-satisfying, however the algorithm for calculating the upper and lower signal velocity bounds is left for the reader to determine. Several possibilities for the signal velocity bounds are presented by Davis [177] and demonstrated on a popular test case attributed to Sod.

Considering again the states u_k, $k = 0, 1, ..., m$, for a u vector with m components, which are separated by waves determined by the eigenvalues, λ_j, $j = 1, 2, ..., m$, of the

matrix $A = f(u)_u$, there exist several distinct cases which prescribe certain bounds of signal propagation speed. If $\lambda_k(u_{k-1}) = \lambda_k(u_k)$ the kth wave is a contact discontinuity propagating with velocity $a_k = \lambda_k$, while if $\lambda_k(u_{k-1}) < \lambda_k(u_k)$ the kth wave is a rarefaction wave with lower and upper velocity bounds which are $(a_k)_{min} \leq \lambda_k(u_{k-1})$ and $(a_k)_{max} \geq \lambda_k(u_k)$. The third case of $\lambda_k(u_{k-1}) > \lambda_k(u_k)$ corresponds to a shock wave propagating at a speed between the two valuations of λ_k. Here, as in Fig. 5-1, the eigenvalues have the property $\lambda_j \leq \lambda_i$ for $i > j$.

For a first-order Godunov method, Davis suggests an algorithm for choosing signal velocity bounds without the need for information from any states intermediate to u_L and u_R,

$$a_L = min(\lambda_1(u_L), \lambda_1(u_R)) \tag{5.33}$$

$$a_R = max(\lambda_m(u_L), \lambda_m(u_R)) \tag{5.34}$$

which satisfies the velocity bounds for any rarefaction waves, though not necessarily for shocks. If the 1-wave is a shock and $\lambda_1(u_1) < \lambda_1(u_R)$ or if the m-wave is a shock and $\lambda_m(u_L) < \lambda_m(u_{m-1})$ then the proposed bounds are inaccurate. However, the author argues that an incorrect shock velocity should not violate entropy as it might for the case of an expansion wave, and it is therefore less essential to the solution to produce an accurate shock speed.

5.2.2 Application of the HLL scheme to the 1-D Plasma Equations

The utility of using a Godunov-type scheme is in its exactness for conservative problems, where the rate change of an unknown function in time averaged over a finite volume is equal to the product of the incoming flux at the volume boundaries and the surface area of the boundary. Our system of conservative plasma equations are re-created here, without overbars, as Eqns. 5.35, 5.36 and 5.37, using Eqn. 5.17 to cancel out the electric field in Eqn. 5.10. The neutral continuity equation is not

included, since we take the limit where the neutral speed is constant over x, turning the conservative equation into an advection equation which is more simply solved using a first order upwind scheme. The electron energy equation is left out of the conservative system since it cannot be manipulated into a conservative form without a spatial derivative term appearing in the right-hand-side, which complicates its implementation. The solution methods for these two equations are further described in the following section.

$$\frac{\partial n_e}{\partial t} + \frac{\partial}{\partial x}(n_e v_{ix}) = n_e(\nu_{ion} - \nu_{iw}) - n_e v_{ix}\frac{\partial \ln A}{\partial x} \tag{5.35}$$

$$\begin{aligned} \frac{\partial n_e m_i v_{ix}}{\partial t} &+ \frac{\partial}{\partial x}(n_e m_i v_{ix}^2 + n_e T_e) = -n_e m_e(\omega_{ce} v_{e\theta} + \nu_{em} v_{ex}) \\ &- n_e m_i(\nu_{iw} v_{ix} - \nu_{ion} v_n) - n_e m_i v_{ix}^2 \frac{\partial \ln A}{\partial x} \end{aligned} \tag{5.36}$$

$$\frac{\partial n_e m_e v_{e\theta}}{\partial t} + \frac{\partial}{\partial x}(n_e v_{ex} m_e v_{e\theta}) = n_e m_e(\omega_{ce} v_{ex} - \nu_{em} v_{e\theta}) - n_e m_e v_{ex} v_{e\theta}\frac{\partial \ln A}{\partial x} \tag{5.37}$$

Since only the x component of the ion velocity is tracked, it's designation is dropped in the remaining expressions presented in this chapter. For now we will neglect the final term in each of these equations, due to an axially changing area, for the sake of notational economy, however we will discuss their reintroduction (maintaining the conservative form to allow continued implementation of the Godunov method) at the end of the derivation. We begin by expressing the system of equations in the same form as Eqn. 5.38,

$$u_t + f(u)_x = g \tag{5.38}$$

where the vector u of unknowns is,

$$u = \begin{pmatrix} n_e \\ n_e m_i v_i \\ n_e v_{e\theta} \end{pmatrix} = \begin{pmatrix} u_1 \\ u_2 \\ u_3 \end{pmatrix} \tag{5.39}$$

the flux function $f(u)$ is,

$$f = \begin{pmatrix} n_e v_i \\ n_e m_i v_i^2 + n_e T_e \\ n_e v_{e\theta}(v_i - \frac{I_a}{e n_e A}) \end{pmatrix} = \begin{pmatrix} u_2/m_i \\ u_2^2/(m_i u_1) + u_1 T_e \\ u_3(u_2/(m_i u_1) - I_a/(e u_1 A)) \end{pmatrix} \tag{5.40}$$

and the source term g is,

$$g = \begin{pmatrix} n_e(\nu_{ion} - \nu_{iw}) \\ -n_e m_i(\nu_{iw} v_i - \nu_{ion} v_n) - n_e m_e(\omega_{ce} v_{e\theta} + \nu_{em} v_{ex}) \\ n_e(\omega_{ce} v_{ex} - \nu_{em} v_{e\theta}) \end{pmatrix} \tag{5.41}$$

which does not include any convective terms, as it would if the electron energy equation were included.

The next step in applying the HLL scheme described above is finding the characteristics of the system, starting with the definition of the matrix $F = \partial f/\partial u$. The matrix F is given by Eqn. 5.43, which is found using Eqn. 5.42.

$$F = \frac{\partial f}{\partial u} = \begin{pmatrix} \frac{\partial f_1}{\partial u_1} & \frac{\partial f_1}{\partial u_2} & \frac{\partial f_1}{\partial u_3} \\ \frac{\partial f_2}{\partial u_1} & \frac{\partial f_2}{\partial u_2} & \frac{\partial f_2}{\partial u_3} \\ \frac{\partial f_3}{\partial u_1} & \frac{\partial f_3}{\partial u_2} & \frac{\partial f_3}{\partial u_3} \end{pmatrix} \tag{5.42}$$

$$F = \begin{pmatrix} 0 & \frac{1}{m_i} & 0 \\ T_e - \frac{u_2^2}{m_i u_1^2} & \frac{2u_2}{m_i u_1} & 0 \\ u_3(\frac{I_a}{e u_1^2} - \frac{u_2}{m_i u_1^2}) & \frac{u_3}{m_i u_1} & \frac{u_2}{m_i u_1} - \frac{I_a}{e u_1} \end{pmatrix} \tag{5.43}$$

The eigenvalues are found by solving the characteristic equation of F, $det(\lambda I - F) = 0$, where I is the identity matrix. It should be noted that any manipulation of radially averaged equations, other than direct addition or subtraction, requires some assumption on the nature of the radial profiles, which for simplicity we take as

relatively flat. The characteristic polynomial is given in Eqn. 5.44, which is regrouped and expressed in terms of plasma parameters in Eqn 5.45, where $c_s^2 = T_e/m_i$ is the ion acoustic speed. From Eqn. 5.45 the three eigenvalues are simply $\lambda = v_{ex}, v_i \pm c_s$.

$$\lambda(\lambda - \frac{2u_2}{m_i u_1})(\lambda - [\frac{u_2}{m_i u_1} - \frac{I_a}{eu_1}]) + (\lambda - [\frac{u_2}{m_i u_1} - \frac{I_a}{eu_1}])(\left(\frac{u_2}{m_i u_1}\right)^2 - \frac{T_e}{m_i}) = 0 \quad (5.44)$$

$$(\lambda - v_{ex})\left[(\lambda - v_i)^2 - c_s^2\right] = 0 \quad (5.45)$$

Through most of the domain the ion velocity is positive while the axial electron velocity is negative, however, there is no guarantee that one eigenvalue will remain the minimum. In order to apply the velocity bounds of Davis in Eqns. 5.33 & 5.34 we must make an additional evaluation, given explicitly as,

$$(a_L)_{j+1/2} = min(min(v_{ex}, v_i - c_s)_j, min(v_{ex}, v_i - c_s)_{j+1}) \quad (5.46)$$

$$(a_R)_{j+1/2} = max((v_i + c_s)_j, (v_i + c_s)_{j+1}) \quad (5.47)$$

where the velocity bounds are evaluated for the $x_{j+1/2}$ cell interface as an example.

Once the velocity bounds are calculated, the fluxes are evaluated at the cell interfaces on either side of a given node using,

$$f = \begin{cases} f(u_L) & \text{if } a_L > 0 \\ f(u_{LR}) & \text{if } a_L < 0 < a_R \\ f(u_R) & \text{if } a_R < 0 \end{cases} \quad (5.48)$$

where $f(u_{LR})$ is given by Eqn. 5.32. The calculated fluxes are then used to update the vector u explicitly through,

$$u_j^{n+1} = u_j^n - \frac{\Delta t}{\Delta x}(f_{j+1/2}^n - f_{j-1/2}^n) + \Delta t g_j^n \quad (5.49)$$

If the cross-sectional area, A, is allowed to vary with x, but not with t, the

analysis is identical, but the vectors given above are replaced by $u' = Au$, $f' = Af$ and $g' = Ag$. In this manner, the areas used to calculate u_t and g are the values at the given node, while the areas used in the flux calculation are of an intermediate nature. If the area is unsteady, one could similarly use u' and f', but add a term so that $g' = Ag - uA_t$, assuming the rate of area change can be calculated explicitly.

The implementation of the first-order HLL scheme is very simple, and this is the main reason for its adoption in solving the fairly crude model described herein. Several problems with its application are evident from the formulation. First, in the case of a Hall thruster the propagation velocity bounds are almost universally of opposite sign, so that we are perpetually computing the value of $f(u_{LR})$, which is spatially averaged to the furthest extent in the HLL scheme. Second, the source term, as given here, is evaluated using the cell-averaged u, which approaches the cell-averaged value of the source term only for small Δx. Other methods for handling the source term include upwinding the source term, so that its solution depends on the Riemann solutions at the interfaces, as well as splitting methods which solve a combination of the homogeneous conservation equations and an ODE for the source term.

Though not essential to the method, we treat the anode boundary as a half cell, as shown for x_0 in Fig. 5-1, setting $u_{-1/2} = 0$ so that the only incoming flux is from $f(u_{1/2})$. The ions are constrained to the Bohm condition at the anode, $v_i(x = 0) = -c_s$, as is necessary for the formation of a stable sheath. No fixed values of n_e or $v_{e\theta}$ need be imposed at the anode since both are almost entirely determined by the incoming flux of values from downstream. At the far boundary, $x = L$, which represents the cathode plane, the ion velocity is positive and so once again the plasma density does not require a constraint, however the electron flux is typically in the negative x direction and a boundary condition is needed for the azimuthal momentum. We neglect electron inertia (i.e. $m_e \partial v_{e\theta}/\partial t + m_e(\mathbf{v_e} \cdot \nabla) v_{e\theta} << \sum F_\theta$) in the azimuthal momentum equation at the cathode plane, resulting in,

$$v_{e\theta}|_L = \frac{v_{ex}\omega_{ce}}{\nu_e + \nu_{ion} - \nu_{iw}}|_L \tag{5.50}$$

which is expected to be a good approximation due to the dominance of the source term in determining the local vale of the azimuthal momentum. Typical electron gyrofrequencies are still on the order of 0.1-1 GHz several centimeters downstream of the thruster exit. The $..|_N$ notation in Eqn. 5.50 is used to express that the term to the left of the bar is evaluated at $j = N$.

A ghost cell is used downstream of $x = L$, which has the same value of u as in the boundary cell, in order to compute the flux at $x = L + \Delta x/2$ for u_1 and u_2. This is equivalent to setting the axial derivative of the ion beam current to zero past the cathode, which is well justified. We also specify that no further ion acceleration occurs, which is less accurate, but is acceptable in this context. An accurate description of ion acceleration in the plume is well beyond the purview of a 1-D fluid model, and is not considered critical in capturing the interaction of the ionization zone with the neutral flow front.

5.2.3 Neutral Density and Electron Temperature Solvers

The neutral continuity equation is solved using a simple upwind method, given in Eqn. 5.51. The upwind method is used for its stability, simplicity and its clear applicability to the physical situation. A boundary condition is needed for the neutral density at the anode, since information on the neutral population propagates downstream, which we set based on the input propellant mass flow rate, $\dot{m}_n$, using Eqn. 5.52, which neglects ion recombination at the anode as a source of neutrals.

$$\begin{aligned}(n_n)_j^{n+1} = (n_n)_j^n - \frac{\Delta t}{\Delta x} v_n[(n_n)_j^n - (n_n)_{j-1}^n] \quad &- \quad \Delta t (n_e)_j^n [(\nu_{ion})_j^n - (\nu_{iw})_j^n] \\ &- \quad \Delta t v_n (n_n \frac{\partial \ln A}{\partial x})_j^n \end{aligned} \tag{5.51}$$

$$(n_n)_0 = \frac{\dot{m}_n}{m_n v_n A} \tag{5.52}$$

The electron temperature is solved at each time step using an entropy-like version

of Eqn. 5.22. This formulation is derived by first chain rule expanding the left-hand-side of Eqn. 5.22 to obtain,

$$\frac{3}{2}T_e\frac{\partial n_e}{\partial t}+\frac{3}{2}n_e\frac{\partial T_e}{\partial t}+\frac{1}{2}m_e v_e^2\frac{\partial n_e}{\partial t}+n_e\frac{\partial \frac{1}{2}m_e v_e^2}{\partial t}+\frac{3}{2}T_e\frac{\partial n_e v_{ex}}{\partial x}+\frac{3}{2}n_e v_{ex}\frac{\partial T_e}{\partial x}$$
$$+\frac{1}{2}m_e v_e^2\frac{\partial n_e v_{ex}}{\partial x}+n_e v_{ex}\frac{\partial \frac{1}{2}m_e v_e^2}{\partial x}+v_{ex}\frac{\partial n_e T_e}{\partial x}+n_e T_e\frac{\partial v_{ex}}{\partial x} \quad (5.53)$$

which can be simplified using the electron continuity equation. We also regroup terms in Eqn. 5.53 to fit the form,

$$\frac{\partial}{\partial t}\frac{T_e^{3/2}}{n_e}=\frac{T_e^{1/2}}{n_e^2}(\frac{3}{2}n_e\frac{\partial T_e}{\partial t}-T_e\frac{\partial n_e}{\partial t}) \quad (5.54)$$

which results in,

$$\frac{3}{2}n_e\frac{\partial T_e}{\partial t}-T_e\frac{\partial n_e}{\partial t}+\frac{3}{2}n_e v_{ex}\frac{\partial T_e}{\partial x}-T_e v_{ex}\frac{\partial n_e}{\partial x}$$
$$+(\frac{5}{2}T_e+\frac{1}{2}m_e v_e^2)n_e(\nu_{ion}-\nu_{iw})+v_{ex}\frac{\partial n_e T_e}{\partial x}+m_e n_e(\frac{\partial}{\partial t}+v_{ex}\frac{\partial}{\partial x})\frac{v_e^2}{2} \quad (5.55)$$

The final term may be simplified by splitting the two velocity components, v_{ex}^2 and $v_{e\theta}^2$, and making use of the chain rule, $\frac{\partial}{\partial t}\frac{v_e^2}{2}=v_e\frac{\partial v_e}{\partial t}$. The resulting term containing the axial electron inertia may be neglected, while the term containing the azimuthal inertia may be replaced by Eqn. 5.18. The new form of the energy equation is given in Eqn. 5.56, in which the electric field has been replaced by Eqn. 5.17.

$$\frac{n_e^2}{T_e^{1/2}}\frac{d}{dt}\frac{T_e^{3/2}}{n_e}+(\frac{5}{2}T_e+\frac{1}{2}m_e v_e^2)n_e(\nu_{ion}-\nu_{iw})-m_e v_{e\theta}n_e(\nu_{em}+\nu_{ion}-\nu_{iw})$$
$$=m_e v_{ex}^2 n_e\nu_{em}-n_e(\nu_{ew}\epsilon_w+\nu_{ion}\alpha_i E_i) \quad (5.56)$$

The final form of the energy equation used is given in Eqn. 5.57. This equation is similar to the neutral continuity equation in form, except now the coefficient in

front of the spatial derivative is a function of x and t, making its solution slightly more complex. We continue to use a first order upwind scheme, and though v_{ex} is normally in the negative direction, we use an algorithm which allows for a change in the direction of advection.

$$\begin{aligned}(\frac{\partial}{\partial t} + v_{ex}\frac{\partial}{\partial x})\frac{T_e^{3/2}}{n_e} =& \frac{T_e^{3/2}}{n_e}[\frac{m_e v_e^2}{T_e}\nu_{em} - \frac{\epsilon_w}{T_e}\nu_{ew} - \frac{\alpha_i E_i}{T_e}\nu_{ion} \\ &+ \frac{\frac{5}{2}T_e + \frac{1}{2}m_e(v_{ex} - v_{e\theta})^2}{T_e}(\nu_{ew}(1-\Gamma) - \nu_{ion})] \end{aligned} \tag{5.57}$$

The area was assumed constant in the above derivation, but can easily be added back in to the right-hand-side of Eqn. 5.57 in a similar form as in Eqn. 5.51. Denoting the bracketed term on the right-hand-side of Eqn. 5.57 as S_E, the upwind scheme used to update the electron temperature can be expressed as,

$$a^- = \frac{1}{2}(v_{ex} - |v_{ex}|)_j^n \tag{5.58}$$

$$a^+ = \frac{1}{2}(v_{ex} + |v_{ex}|)_j^n \tag{5.59}$$

$$\begin{aligned}(\frac{T_e^{3/2}}{n_e})_j^{n+1} =& \left(1 - \frac{\Delta t}{\Delta x}|v_{ex}|_j^n\right)(\frac{T_e^{3/2}}{n_e})_j^n \\ &\frac{\Delta t}{\Delta x}\left(a^+(\frac{T_e^{3/2}}{n_e})_{j-1}^n - a^-(\frac{T_e^{3/2}}{n_e})_{j+1}^n\right) + \Delta t(\frac{T_e^{3/2}}{n_e})_j^n(S_E)_j^n \end{aligned} \tag{5.60}$$

The $T_e^{3/2}/n_e$ term is advected by the axial electron velocity, which is always negative at the anode, so we do not need to impose a boundary condition there. We do impose a constant electron temperature at the cathode plane, which is 5 eV unless otherwise noted. The temperature is largely determined locally in this region, so we do not expect the constant cathode temperature to have a large effect on the solution.

5.2.4 Collision Frequencies

Finally, some expressions for the ionization, wall collision and momentum exchange frequencies are needed in terms of the solved-for variables. We use the expressions for these frequencies found in the paper by Barral and Ahedo [12] unless otherwise noted. These expressions are given below in Eqns. 5.61,5.62, 5.63 and 5.64, where $\epsilon_e = \frac{3}{2}T_e + \frac{1}{2}m_e(v_{ex}^2 + v_{e\theta}^2)$.

$$\nu_{ion} = n_n 1.8 \times 10^{-13} \left(\frac{\epsilon_e}{E_i}\right)^{1/4} exp\left(-\frac{2E_i}{\epsilon_e}\right) \tag{5.61}$$

$$\nu_{en} = n_n 2.5 \times 10^{-13} \tag{5.62}$$

$$\nu_{em} = \nu_{en} + \nu_{iw}/(1-\Gamma) + \alpha_B \omega_{ce} \tag{5.63}$$

$$\nu_{iw} = \frac{4}{3}\frac{1}{r_1 - r_0}\sqrt{\frac{T_e}{m_i}} \tag{5.64}$$

Equations 5.61 and 5.62 represent rough fits to collision cross section data for xenon, which are ensemble averaged over the assumed drifting Maxwellian distribution function for electron energy. The electron-neutral collision frequency has a fairly weak dependence on electron temperature in the range of interest, changing from around 3×10^{-13} $m^3 s^{-1}$ to 2×10^{-13} $m^3 s^{-1}$ when the temperature changes from 5 eV to 25 eV for a stationary Maxwellian. An average value for ν_{en}/n_n, independent of electron energy, is used for convenience.

The $\alpha_B \omega_{ce}$ term in Eqn. 5.63 is incorporated to account for anomalous cross-field diffusion in a phenomenological manner. Following the original work of Bohm [113] would lead to an α_B value of 1/16, however Hall thruster simulations often require much less diffusion in order to match experiments and our case is no different in this regard [10, 185]. A value of $\alpha_B = 1/160$ is used in our simulations, unless otherwise noted.

The effective ion wall collision frequency, given in Eqn. 5.64, can be derived from

a simple planar presheath problem, which is reproduced here [178]. We start with the radial component of the ion momentum equation,

$$\frac{\partial n_e m_i v_{ir}}{\partial t} + \frac{\partial n_e m_i v_{ix} v_{ir}}{\partial x} + \frac{1}{r}\frac{\partial r n_e m_i v_{ir}^2}{\partial r} - m_i n_e \nu_{ion} v_{nr} = e n_e E_r - n_e \nu_i m_i (v_{ir} - v_{nr}) \tag{5.65}$$

where the ion pressure gradient is once again neglected, as is the azimuthal component of the ion drift velocity. The radial electric field can be replaced using $en_eE_r = -\partial(n_eT_e)/\partial r$, which arises from the application of the Boltzmann relation for the radially confined electrons. Under the planar approximation ($r_1 - r_0 << r$) the fictitious forces can be removed and Eqn. 5.65 is simplified, with use of the ion continuity equation (Eqn. 5.4), to the form,

$$\frac{\partial n_e m_i v_{ir}^2 + n_e T_e}{\partial r} = -m_i n_e v_{ir} \left[\nu_r - \nu_w\right] \tag{5.66}$$

$$\nu_r = \nu_{ion}(1 - \frac{v_{nr}}{v_{ir}}) + \frac{1}{v_{ir}}\frac{\partial v_{ir}}{\partial t} + \frac{v_{ix}}{v_{ir}}\frac{\partial v_{ir}}{\partial x} \tag{5.67}$$

$$\nu_w = \frac{1}{n_e}\frac{\partial n_e v_{ir}}{\partial r} = \nu_{ion} - \frac{1}{n_e}\frac{\partial n_e}{\partial t} - \frac{1}{n_e}\frac{\partial n_e v_{ix}}{\partial x} \tag{5.68}$$

The new frequencies, ν_r and ν_w, can be shown to be independent of r in the case where $v_{nr}/v_{ir} << 1$, n_n and T_e are nearly radially constant in the quasineutral plasma (as assumed in the above derivations), and when n_e and v_{ir} can be expressed in separable forms, such as $v_{ir}(x, r, t) = f(r)c_s(x, t)$.

Next, we re-express Eqn. 5.66 by expanding the derivative, using the identity in Eqn. 5.68 and introducing the Bohm speed, $c_s = \sqrt{T_e/m_i}$, to obtain,

$$(v_{ir} + \frac{c_s^2}{v_{ir}})n_e\nu_w + n_e v_{ir}(1 - \frac{c_s^2}{v_{ir}^2})\frac{\partial v_{ir}}{\partial r} = -n_e v_{ir}\nu_w\left(\alpha - 1\right) \tag{5.69}$$

where we define $\alpha = \nu_r/\nu_w$. This equation may be rewritten in terms of the radial ion Mach number, $M = v_{ir}/c_s$, and regrouped into an integrable equation,

$$\frac{1-M^2}{1+\alpha M^2}dM = \frac{\nu_w}{c_s}dr \tag{5.70}$$

which is solved in the planar case by integrating from the middle of the channel, where $M = 0$, to the sheath edge at the outer wall, where $M = 1$ to satisfy the Bohm condition. The general solution is given in Eqn. 5.71. In the case where $\alpha \to 0$, the integration is straightforward and leads to $1 - \frac{1}{3} = \frac{\nu_w(r_1 - r_0)}{2c_s}$, which is identical to Eqn. 5.64.

$$\frac{1+\alpha}{\alpha^{3/2}} \arctan\sqrt{\alpha} - \frac{1}{\alpha} = \frac{\nu_w(r_1 - r_0)}{2c_s} \tag{5.71}$$

5.2.5 Implicit Source Term

A difficulty with the implementation of the methods described above arises when integrating Eqn. 5.28 after evaluating u_j^{n+1}, $(T_e)_j^{n+1}$ and $(n_n)_j^{n+1}$ for all j in order to find the anode current, I_a^{n+1}, necessary to keep the total potential drop constant. The problem can be seen clearly when Eqn. 5.17 is substituted into Eqn. 5.28 to yield,

$$V_a = -\int_0^L \left(\frac{m_e}{e} v_{e\theta}\omega_{ce} + \frac{1}{en_e}\frac{\partial n_e T_e}{\partial x} + \frac{m_e}{e}\nu_{em}v_{ex} \right) dx \tag{5.72}$$

into which the anode current enters naturally through the v_{ex} term. The problem is that $v_{e\theta}\omega_{ce} >> v_{ex}\nu_{em}$ is met by a large degree, except at a root in $v_{e\theta}$, and so the constancy of V_a would require huge swings in I_a to compensate for a minuscule change in $v_{e\theta}$ in the present formulation. Any substantial change in anode current would also feedback into the azimuthal momentum equation through the dominant $\omega_{ce}v_{ex}$ source term, amplifying any small change in $v_{e\theta}$.

This problem can be overcome by treating the source term in the azimuthal momentum equation implicitly. Making the source term implicit adds a dependency on I_a^{n+1} into $v_{e\theta}^{n+1}$, the dominant term in Eqn. 5.72, so that the current necessary to maintain a constant anode voltage need not change drastically at any given time step. A simple implicit scheme, which can be derived by taking the Taylor series expansion of $(n_e v_{e\theta})$ to the second order in time, is the well-known Crank-Nicolson method. The

application of this method to the azimuthal momentum equation is shown in Eqn. 5.73 where the flux term is not made implicit, a simplification which is justified if the time derivative of the flux term is small compared to the time derivative of the source term.

$$(n_e v_{e\theta})_j^{n+1} = (n_e v_{e\theta})^n - \frac{\Delta t}{\Delta x}(f_{j+1/2}^n - f_{j-1/2}^n) + \frac{\Delta t}{2}\left((n_e\omega_{ce}v_{ex})_j^n - (n_e\nu_{em}v_{e\theta})_j^n\right) + \frac{\Delta t}{2}\left((n_e\omega_{ce}v_{ex})_j^{n+1} - (n_e\nu_{em}v_{e\theta})_j^{n+1}\right) \tag{5.73}$$

We denote the explicit portion of the solution to Eqn. 5.73 as $(n_e)_j^n(v_{e\theta})_j^*$, so that,

$$(n_e v_{e\theta})_j^{n+1} = (n_e)_j^n(v_{e\theta})_j^* + \frac{\Delta t}{2}\left((n_e\omega_{ce}v_{ex})_j^{n+1} - (n_e\nu_{em}v_{e\theta})_j^{n+1}\right) \tag{5.74}$$

and solve for this intermediate value of the azimuthal flux in the main loop through all j values. Solving for $(v_{e\theta})_j^{n+1}$ in Eqn. 5.74 yields,

$$(v_{e\theta})_j^{n+1} = \frac{\frac{(n_e)_j^n}{(n_e)_j^{n+1}}(v_{e\theta})_j^* + \frac{\Delta t}{2}\omega_{ce}(v_{ex})_j^{n+1}}{1 + \frac{\Delta t}{2}(\nu_{em})_j^{n+1}} \tag{5.75}$$

which is plugged back in to Eqn. 5.72,

$$V_a = -\int_0^L \left(\frac{m_e}{e}v_{e\theta}^* r_n \omega'_{ce} + \frac{1}{en_e}\frac{\partial n_e T_e}{\partial x} + (\frac{m_e}{e}\nu_{em} + \frac{\Delta t}{2}\omega'_{ce}B)v_{ex}\right)dx \tag{5.76}$$

where $r_n = (n_e^n)/(n_e^{n+1})$, $\omega'_{ce} = \omega_{ce}/(1 + \frac{\Delta t}{2}(\nu_{em})^{n+1})$, and all functions are evaluated at time $n+1$ unless otherwise noted. The numerical integration of Eqn. 5.76 is made simple by the nature of the finite volume method, wherein the value at each node corresponds to the exact value of the function averaged over x for the width of the cell. For an evenly distributed mesh, one needs only sum up the numerical values of a given function at each node and multiply by Δx in order to find the exact integral of that function over all x. The same method may be used to approximate the integral when products of two or more functions are integrated, as long as Δx is

small enough.

$$\frac{I_a}{eA} = \Bigg\{ \Delta x \sum_{j=2}^{N-1} \left[\frac{m_e}{e} v_{e\theta}^* r_n \omega'_{ce}|_j + \frac{n_e T_e|_{j+1} - n_e T_e|_{j-1}}{2\Delta x e n_e|_j} + (\frac{m_e}{e}\nu_{em}|_j + \frac{\Delta t}{2}\omega'_{ce} B|_j) v_i|_j \right]$$
$$+ \frac{\Delta x}{2} \left[\frac{m_e}{e} v_{e\theta}^* r_n \omega'_{ce}|_1 + 2\frac{n_e T_e|_2 - n_e T_e|_1}{\Delta x e n_e|_1} + (\frac{m_e}{e}\nu_{em}|_1 + \frac{\Delta t}{2}\omega'_{ce} B|_1) v_i|_1 \right]$$
$$+ \frac{\Delta x}{2} \left[B_N \frac{\omega_{ce}}{\nu_{em} + \nu_{ion} - \nu_{iw}}|_N + 2\frac{n_e T_e|_N - n_e T_e|_{N-1}}{\Delta x e n_e|_N} + \frac{m_e}{e}\nu_{em} v_i|_N \right] \Bigg\} /$$
$$\Bigg\{ \Delta x \sum_{j=2}^{N-1} \left[\frac{m_e}{e}\nu_{em}|_j + \frac{\Delta t}{2}\omega'_{ce} B|_j) \right] \frac{1}{n_e|_j} + \frac{\Delta x}{2n_e|_1} \left[\frac{m_e}{e}\nu_{em}|_1 + \frac{\Delta t}{2}\omega'_{ce} B|_1) \right]$$
$$+ \frac{\Delta x}{2n_e|_N} \left[B_N \frac{\omega_{ce}}{\nu_{em} + \nu_{ion} - \nu_{iw}}|_N + \frac{m_e}{e}\nu_{em} \right] \Bigg\} \tag{5.77}$$

The value of I_a necessary to maintain a constant potential drop is calculated using Eqn. 5.77. The summation is a straightforward integration of Eqn. 5.76, with a slight deviation at the boundaries, which have a width of $\Delta x/2$. The value of $v_{e\theta}|_N^{n+1}$ is given by the boundary condition shown in Eqn. 5.50 as opposed to the implicit form of Eqn. 5.75.

It is also important to identify the maximum allowable time step, Δt, for a given grid. For the Riemann problem discussed above to make sense the waves originating from the discontinuity at a given cell interface should not propagate past that half of the cell in a given Δt. We then take,

$$\Delta t = C \frac{\Delta x}{max(|(v_{ex})^{n+1}|, |(v_i)^{n+1} \pm c_s^{n+1}|)} \tag{5.78}$$

where C is some coefficient satisfying $C \leq 0.5$. The application of Eqn. 5.78 is clear for the system of equations solved by the HLL scheme, but this time step also satisfies the Courant condition for the energy equation which advects at the axial electron velocity. The neutral speed is much less than any of the speeds in Eqn. 5.78 and therefore the neutral continuity equation is very well resolved.

The order of operations in the unsteady solver described here is displayed schemat-

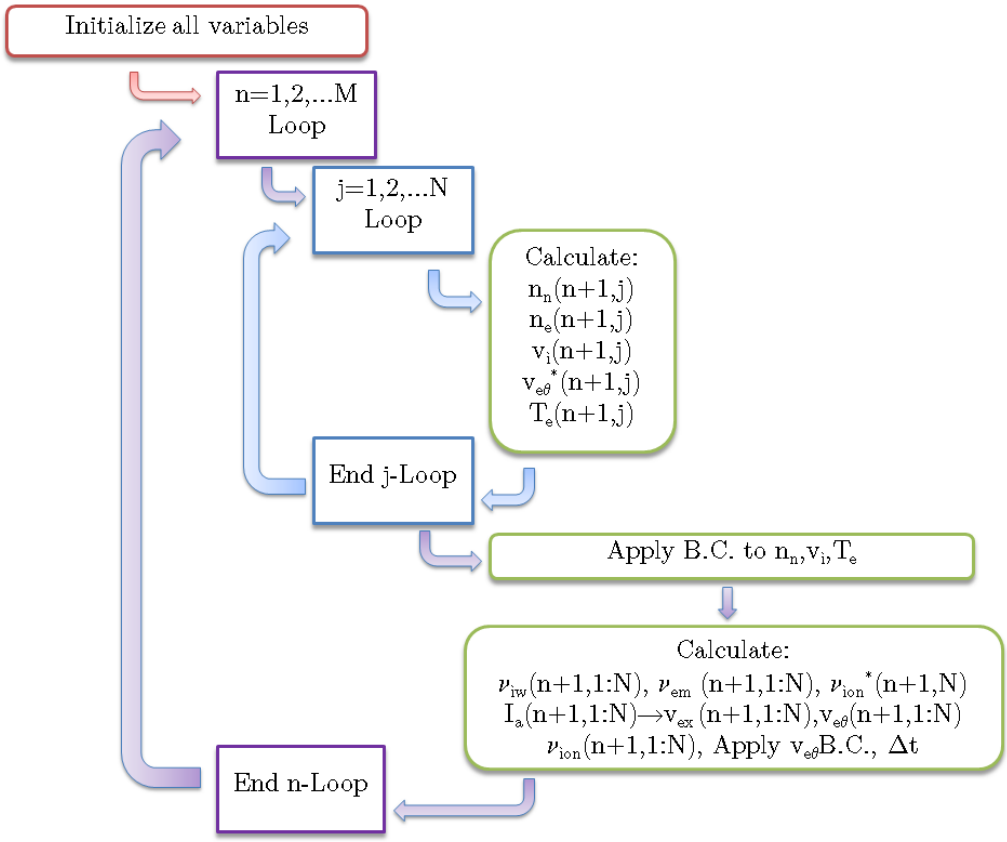

Figure 5-2: Flow Chart Representing the Order of Operations in the Unsteady 1-D Plasma Code

ically in Fig. 5-2. The resulting code is relatively simple and written entirely in Matlab. Typical run-times to simulate 0.5 milliseconds of thruster operation are on the order of 80 minutes.

5.3 Solutions for SPT-100 Type Conditions

Initial results are obtained with the nominal parameters mirroring those of Barral and Ahedo, which describe a Hall thruster similar to the well-characterized SPT-100. Namely, the magnetic field profile is approximated as a Gaussian, peaked at the channel exit, with different widths inside and outside the channel. The expression for the magnetic field can be found in Eqn. 5.79 where x_m =2.5 cm, B_{max} =22 mT and

l_B is 1.25 cm.

$$B(x) = B_{max} exp\left[-\left(\frac{x - x_m}{l_B}\right)^2\right] \tag{5.79}$$

The outer and inner radii of the channel are taken as 5 cm and 3 cm, and the channel length, L_{ch}, as 2.5 cm. The cathode plane is set 1 cm downstream of the exit, but the height of the plasma column is kept constant at that of the channel. This leads to unphysically high values for the neutral and plasma densities in the near-field plume while removing a potential source of cooling for the electrons and acceleration for the ions. The wall collision frequency is set to zero downstream of the exit, which removes the only other source of electron cooling in the model besides inelastic collisions with neutrals. Downstream of the channel exit, electrons are still magnetized and highly confined to the field lines which all eventually intersect some thruster surface, so that in reality energetic electrons are still colliding with some kind of wall. The thruster material outside of the channel may be conducting and may have a vastly different secondary electron yield than boron nitride, which adds some complication, but the main impediment to implementing external wall collisions is the difficulty in rigorously adapting the slab model used internally to the more complicated external field.

The nominal anode voltage and propellant mass flow rate used in the simulations are 180 V and 5 mg/s, respectively. The anode voltage is below the normal 300 V used in the SPT-100, but this offset is taken to make up for some deficiencies in the model. Typical 1-D fluid models, such as the one used here, are incapable of accurately describing the near-field plume region where a sometimes substantial portion of the potential drop is found in experiments [121, 186], however the stability of the breathing mode is not expected to depend strongly on any residual external potential drop not captured here. The loss of the full potential drop is only expected to effect the accurate representation of the flushing stage of a breathing cycle.

A simple linear model for the effective secondary electron yield is used, where $\Gamma = min(T_e/25, 0.986)$, which is a rough estimate for the emission from a boron nitride-

based wall. The upper bound of $\Gamma = 0.986$ corresponds to the space-charge saturated sheath discussed in Sec.2.3.2. We also take the ionization cost α_i =3, irrespective of electron temperature, unless otherwise noted. The model for α_i described by Dugan and Sovie [179] asymptotes to a minimum of 2.5 for xenon at temperatures above about 6eV.

The simulations are initialized by flat profiles of T_e, n_e, v_i and n_n, with $n_e = 2 \times 10^{17} m^{-3}$ while the other variables are set to their boundary values. The initial profile of $v_{e\theta}$ and the initial anode current are calculated in order to satisfy the anode voltage boundary condition. It should be noted that these initial conditions correspond to a state far from equilibrium, so in the baseline case we are not examining linear stability, but rather checking for periodic cycles. A condition may exist where operation is stable and non-periodic near a critical point but behaves as a limit cycle when far from equilibrium. Our initialization method might not catch the stable spiral solution in such a case.

5.3.1 Model Convergence

The model described above has so far closely followed that of Barral and Ahedo [12] in part so that it may be easily verified using the results presented in their article. Our implementation does indeed end up closely mirroring those results as will be shown in some of the following sections, however it is also important to establish independently that the code converges as the mesh is refined.

The effect of grid refinement on the solution can be seen in Fig. 5-3a for a case which results in a damped oscillation, and in Fig. 5-3b for a case with self-sustained current oscillations. In both cases the coarsest mesh predicts the lowest oscillation frequency. The damped solution appears to be very nearly converged when the spatial dimension is split into 121 nodes and not far off with just 81 nodes, while the sustained oscillation solution may need more than 200 nodes to converge. The differences in solutions of different grid fineness are not too large in either case, with only a 5% increase in predicted frequency when N is upped from 81 to 200 for the 7 mg/s solution. The stability of the anode current has not been altered in any way by the

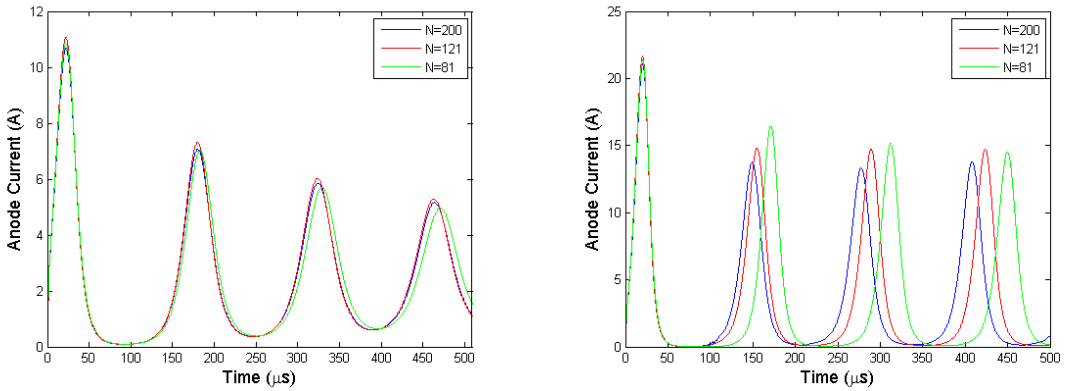

(a) 6 mg/s (b) 7 mg/s

Figure 5-3: Anode current versus time for several values of x-grid point number, N. Model inputs are 180 V and (a) 6 mg/s or (b) 7 mg/s.

changes in grid fineness, so the lower value of N should be suitable for our needs.

5.3.2 Structure of Oscillations

Before discussing the operational inputs which excite or damp large amplitude current oscillations, we will discuss the classification of solutions and present the different phases of a breathing cycle. In general, the anode current solutions are in one of two familiar forms: a sustained, self-excited oscillation (as in Fig. 5-4a) or a damped harmonic oscillator (as in Fig. 5-4b).

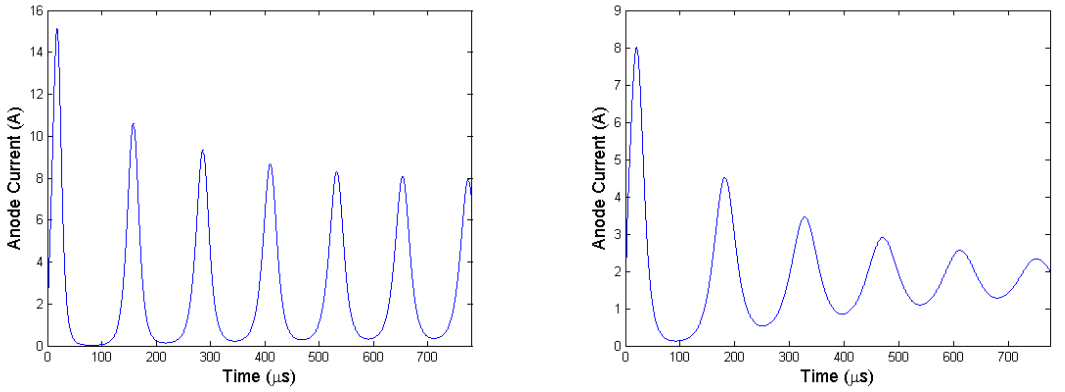

(a) (b)

Figure 5-4: Simulated anode current versus time at 5 mg/s flow rate, 180 V and a Bohm coefficient of (a) 1/120 and (b) 1/140

These two forms may also be easily distinguished by their representation in phase space, as in Fig. 5-5, where we have chosen the neutral density (averaged over all values of x) and the anode current as the representative dependent variables, as done by Barral and Peradzynski [180]. In these, and all the following figures of this section, the neutral density is normalized by its value at the anode/inlet, which is kept constant at $n_{nA} = \dot{m}_a/(m_i v_n A_{ch})$.

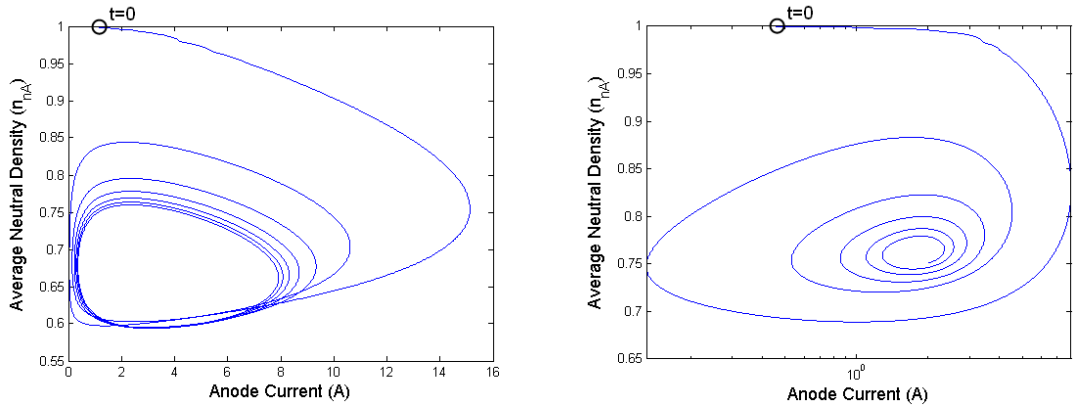

(a) (b)

Figure 5-5: Simulated spatially averaged neutral density versus anode current at 5 mg/s flow rate, 180 V and a Bohm coefficient of (a) 1/120 and (b) 1/140. Simulations are initialized with flat profile of $n_n(x) = n_{nA}$

The phase flow makes it clear that the anode current oscillations of Figs. 5-4a & 5-5a are in the form of a stable limit cycle, meaning the trajectory of the solution in phase space asymptotically approaches a closed orbit as time approaches $+\infty$. The phase flow of the oscillations in Figs. 5-4b & 5-5b represents a stable spiral (or focus), where the phase space trajectory asymptotically approaches a stationary solution as $t \to +\infty$. The trajectories of Figs. 5-5a & 5-5b would correspond to an unstable limit cycle and an unstable focus, respectively, if they were obtained as $t \to -\infty$.

The appearance of a stable spiral solution indicates that the model predicts the eventual damping out of the breathing mode and approach of an equilibrium solution. Stable limit cycle solutions, on the other hand, represent self-sustained breathing oscillations and the combined factors leading into or out of this mode are the primary focus of this investigation. We first dissect the properties of a representative limit

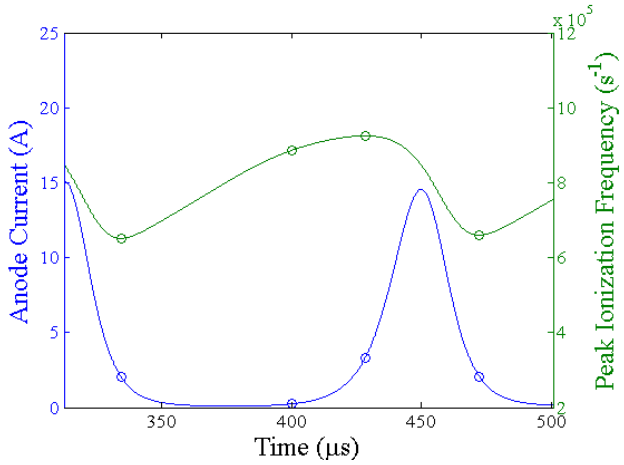

Figure 5-6: Anode current and ionization frequency versus time. Circles indicate sections of cycle in terms of ν_{ion}: from minimum to end of linear growth portion, then to peak and back to minimum.

cycle solution in order to better contrast its properties with those of a damped cycle.

A representative anode current and ionization frequency cycle, obtained for an input voltage of 180 V and flow rate of 7 mg/s, is shown in Fig. 5-6, where open circles denote the extrema of the different portions of the cycle. The first portion of the cycle we will consider begins when the peak ionization frequency in the channel, $max(\nu_{ion}(x))$, reaches a minimum and constitutes the majority of a phase of neutral refill, during which the peak ionization frequency increases in a largely linear fashion. The anode current is decreasing for most of this time, reaching its minimum value at some point in this phase. This is the longest phase of the cycle, lasting 66 μs in this example.

The time evolution of the main plasma parameter profiles during this portion are shown in Fig. 5-7, in which the ion speed is normalized by the speed of an ion accelerated by the full anode voltage, $\sqrt{2eV_a/m_i}$. Thin black lines trace the location of the peak plasma density, electron temperature, electric field and ionization frequency through time, indicating the appearance of a convective portion of the oscillations in each parameter. The only dependent variable known to have a truly convective behavior is the neutral density, which in Fig. 5-7d can be seen to refill the chamber with a slope that is essentially the neutral flow speed (here 200 m/s). The other

quantities are not truly convected in the sense that a fluid element with a large electron temperature, for example, is moving downstream at a rate of several hundred meters per second. Instead, the apparent motion is more nearly due to the spatial offset between dissipative and additive standing waves (though there is some feedback to the loss/gain terms which cause them to move a bit as well).

The plasma density drops by more than an order of magnitude for the first 40μs of this phase, during which time the location of the plasma density peak moves downstream at a rate just below the neutral flow speed (as is apparent in Fig. 5-7d). In this case, the motion of the peak plasma density appears to largely be due to the upstream location (relative to the density peak) of the peak frequency of convective loss (to the anode). Near the end of this phase the net ion generation frequency ($\nu_{ion} - \nu_{iw}$) becomes greater than loss frequency due to flow out ($n_e^{-1} d(n_e v_{ex})/dx$) and the downstream motion of the plasma peak abates.

The electron temperature and electric field follow a somewhat similar trend as the plasma density, though their values change by no more than 50%, with the peaks of both profiles moving downstream (for most of this phase) at rates near the neutral flow speed. The location of the peak electron temperature tends to sit between the peak electric field and peak plasma density but also to shift more rapidly downstream than either of the other two peaks due to the spatial differential in Joule heating (shifted downstream by the electric field) and inelastic collisional cooling (shifted upstream by the dearth of neutrals in the region of depletion). It is difficult to detangle cause and effect, but the downstream motion of the electric field peak is expected to be tied to the motion of the peak in plasma density and also the minimum in neutral density (where the local electron mobility is depressed), until the neutrals refill the chamber and anode current begins to rise again. Interestingly, LIF measurements of the ion velocity during a forced breathing cycle were found by Mazzoufre *et al* to suggest a periodic upstream motion of the electric field at roughly the neutral sound speed [181].

The second portion of the cycle, shown in Fig. 5-8 is also the shortest (28 μs in the present example) and is characterized by the exponential in-place growth of

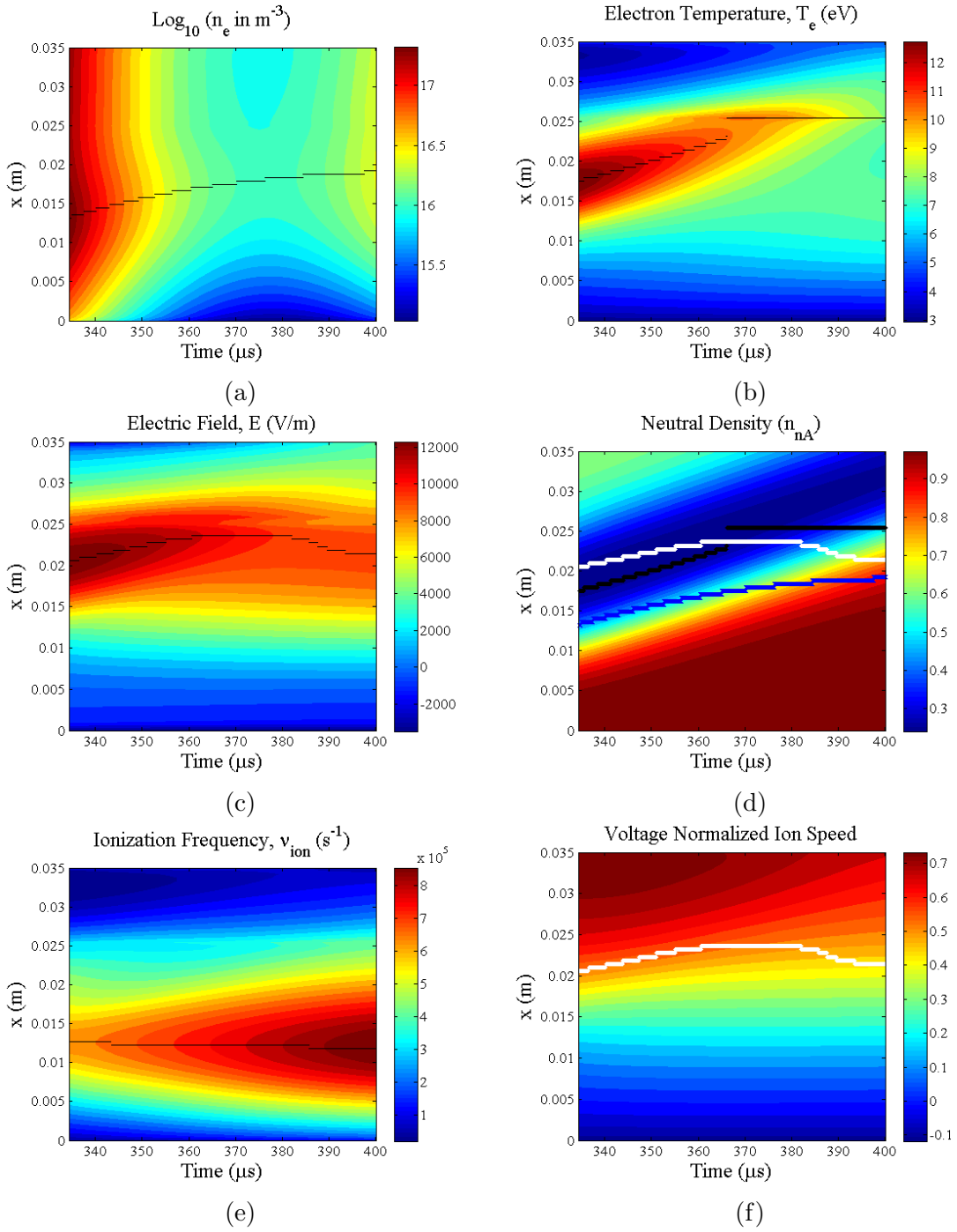

Figure 5-7: Model results for 180 V and 7 mg/s during linear growth of ionization frequency. (a) Log_{10} of plasma density profile (b) Electron temperature profile (c) Electric field profile (d) Neutral density profile (e) Ionization frequency profile (f) Ion speed normalized by anode voltage speed profile versus time. (a)-(c), (e) Thin black line traces location of peak of plotted variable. (d),(f) Blue line traces location of peak n_e, black line is peak T_e, white line is peak E.

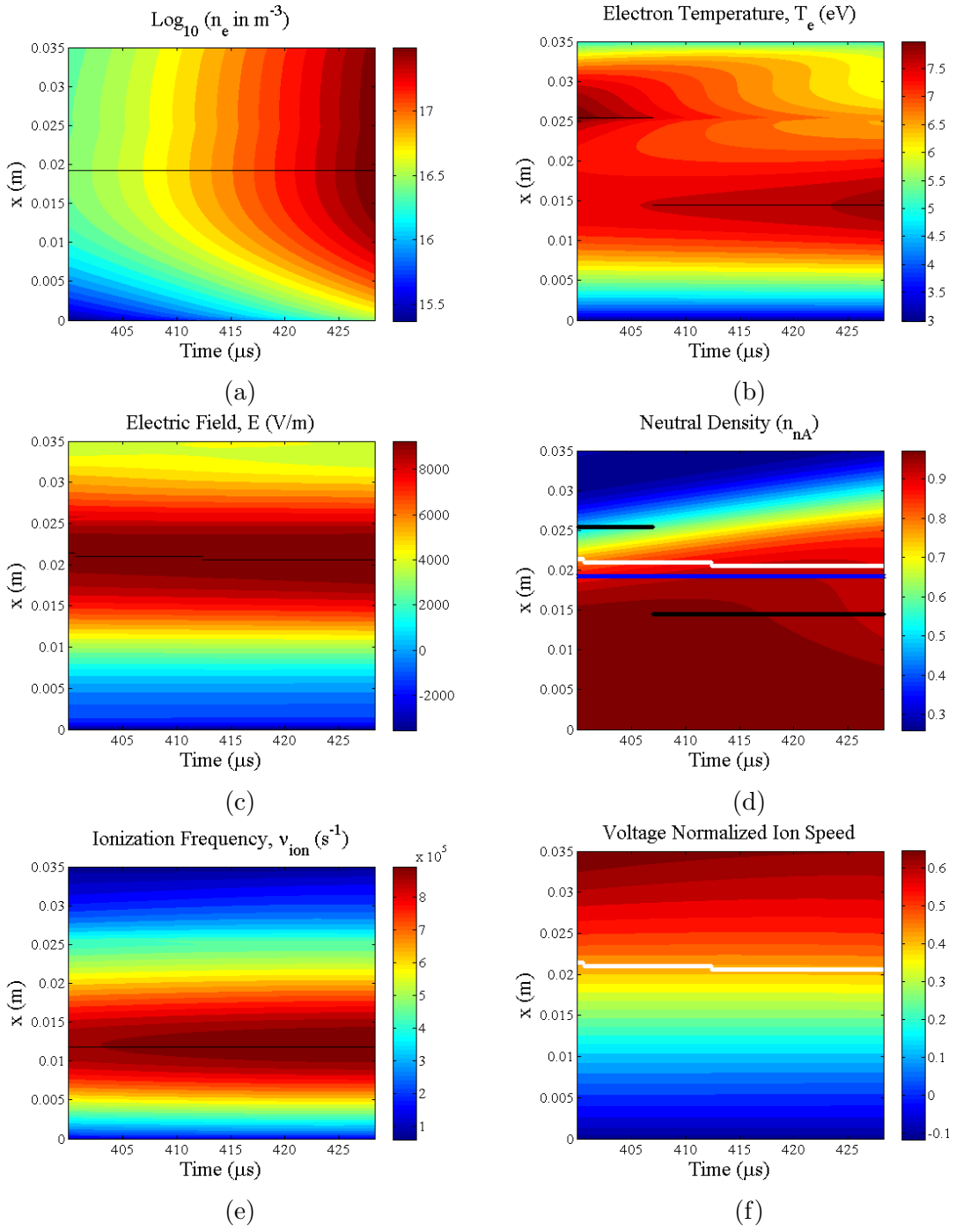

Figure 5-8: Model results for 180 V and 7 mg/s during exponential growth of plasma density. (a) Log_{10} of plasma density profile (b) Electron temperature profile (c) Electric field profile (d) Neutral density profile (e) Ionization frequency profile (f) Ion speed normalized by anode voltage speed profile versus time. (a)-(c), (e) Thin black line traces location of peak of plotted variable. (d),(f) Blue line traces location of peak n_e, black line is peak T_e, white line is peak E.

the plasma density (at an axial location of 19.3 mm in this case). The electron temperature also grows in-place, though to a far lesser extent. At the end of this phase, the ionization frequency reaches its peak value and the depletion of the now nearly fully refilled neutral population commences.

The final phase may readily be split into two sections: the rapid spike in anode current and depletion of neutrals, followed by the rapid decline in ionization frequency and expulsion of the plasma. Both sections are presented in Fig. 5-9, split by the vertical dashed line used to indicate the time of peak anode current. As the plasma density continues its rapid growth, the upstream location of the peak ionization frequency compared to the peak plasma density begins to drive the location of the latter towards the former, with the majority of the apparent motion occurring within a 20 μs span straddling the time of the current peak.

The net ion generation rate begins its rapid decline at the start of this phase, as neutrals are depleted from the main zone of ionization. The current peaks and begins its decay after the net generation rate drops below the loss rate. The location of peak plasma density begins to turn back downstream due to the preferential depletion near the anode described in the first phase of the cycle. Around the same time the electron temperature and electric field reach their peak values (a little over a 1/8th cycle delay past the current peak for this case) and continue their gradual apparent downstream motion as a new cycle begins.

The continued growth of the electric field amplitude after the current begins to decay may be associated with the time lag between plasma decay near the exit and plasma decay near the anode. If the plasma density is decaying downstream of the electric field, but not upstream, then the field strength ought to increase to accelerate the downstream plasma as current is conserved throughout the axial domain. A similar effect is likely occurring simultaneously due to the depletion of neutrals upstream of the peak electric field, which lowers the local electron mobility, requiring a stronger electric field (or some density redistribution) to maintain current continuity. The reduction in mobility is forwarded by Bareilles *et al* [194] to explain the continued increase in electric field (after the current peak) for roughly 1/8th of a cycle observed

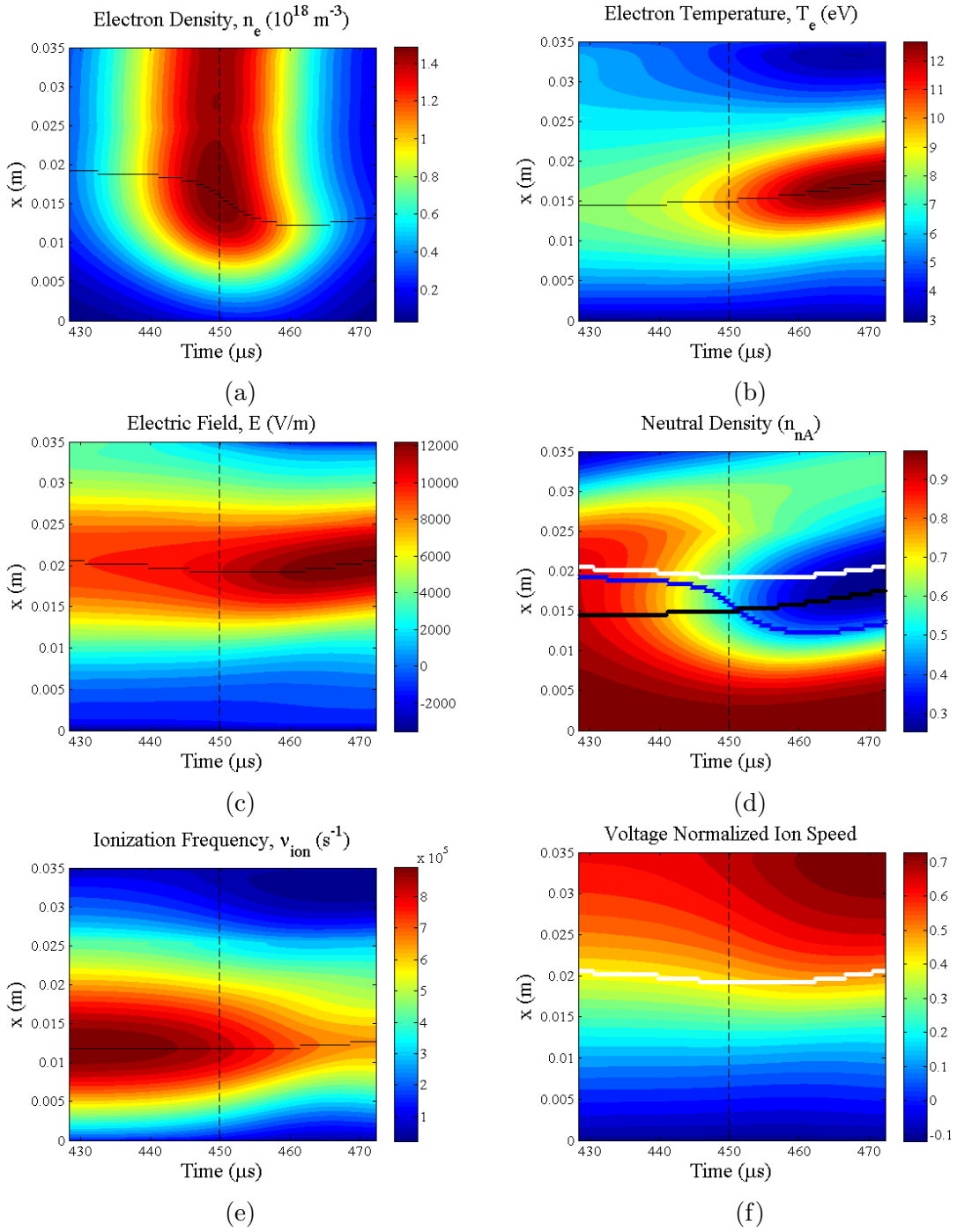

Figure 5-9: Model results for 180 V and 7 mg/s during current peak and decay. (a) plasma density profile (b) Electron temperature profile (c) Electric field profile (d) Neutral density profile (e) Ionization frequency profile (f) Ion speed normalized by anode voltage speed profile versus time. (a)-(c), (e) Thin black line traces location of peak of plotted variable. (d),(f) Blue line traces location of peak n_e, black line is peak T_e, white line is peak E.

in their 2D hybrid simulations of a Hall thruster. We note that removing ν_{en} from our model still results in limit cycle solutions with the same time lag in electric field peak, and apparent downstream motion of temperature, plasma density, and electric field.

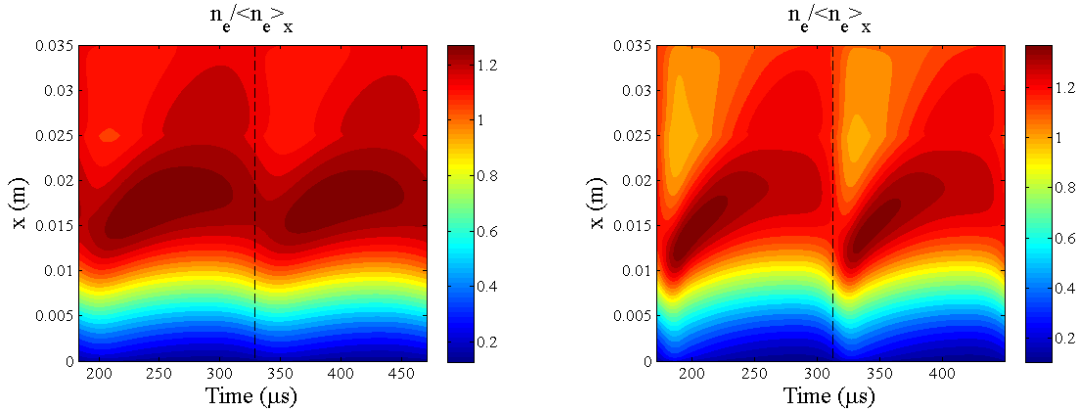

Figure 5-10: Simulated plasma density profile normalized by spatially averaged plasma density versus anode current at 180 V and a flow rate of (a) 6 mg/s (b) 7 mg/s. Condition (a) leads to a focus and (b) leads to a limit cycle type solution

The motion of the plasma density peak (along with the electric field peak in some sense) is a second order effect in a given breathing cycle, largely overshadowed by the first order standing wave in plasma density which is directly reflected in the highly peaked anode current. The convective part of the plasma density perturbation can be more clearly seen in Fig. 5-10, which shows the evolution of the plasma density profile normalized by the mean density along the axis at each instant.

The progression of model outputs for a damped breathing cycle is quite similar, as shown in Appendix D. The swings in plasma parameters and their peak positions are all diminished, however, and the end of each cycle results in a state closer to a stationary solution.

5.3.3 Flow Rate Scan

Model results show that for a constant anode voltage there is a range of low anode mass flow rates which produce damped solutions, where the breathing oscillations die

out after several low amplitude cycles. A summary of the results of flow rate scans at two different anode voltages is given in Fig. 5-11, which shows the time averaged anode current with the standard deviation of oscillations as well as the peak-to-peak frequency of the breathing cycle at each flow rate. Self-sustained oscillations become clear at a flow rate of 4 mg/s with a 220 V anode potential, while a similar solution is not obtained at 180 V until a flow of 7 mg/s. This trend is the opposite of what is generally observed in the DCFT, in which higher anode voltages require higher gas flow rates to switch in to the breathing oscillation dominated mode.

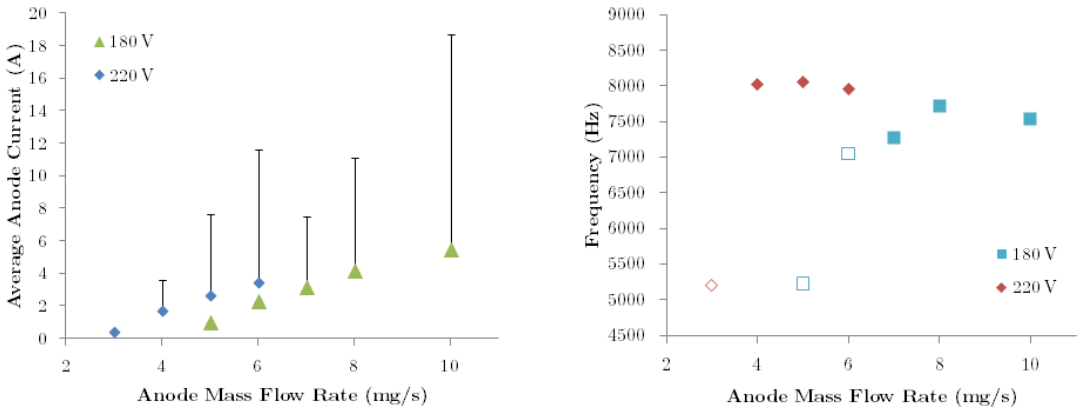

(a) (b)

Figure 5-11: Model results for 180 V and 220 V at various flow rates. (a) Time averaged anode current with error bar showing 1 standard deviation. (b) Anode current oscillation peak-to-peak frequencies. Empty markers represent conditions where oscillations are damped.

The progression from stable spiral type solutions to stable limit cycles is reflected in Figs. 5-12 through 5-18, which show the simulated plasma parameters over the span of two breathing cycles for four of the flow rates tested at 180 V. The anode current and plasma density are similarly shown to exhibit higher, narrower peaks as the flow rate is increased, though the time between peaks is not strongly affected by flow rate once the limit cycle is established, as evident in Fig. 5-11b.

Figure 5-14 demonstrates the progressively higher peak electron temperatures obtained as the mass flow rate is increased. This effect is somewhat counterintuitive since from a steady perspective an increase in neutral density might be expected to

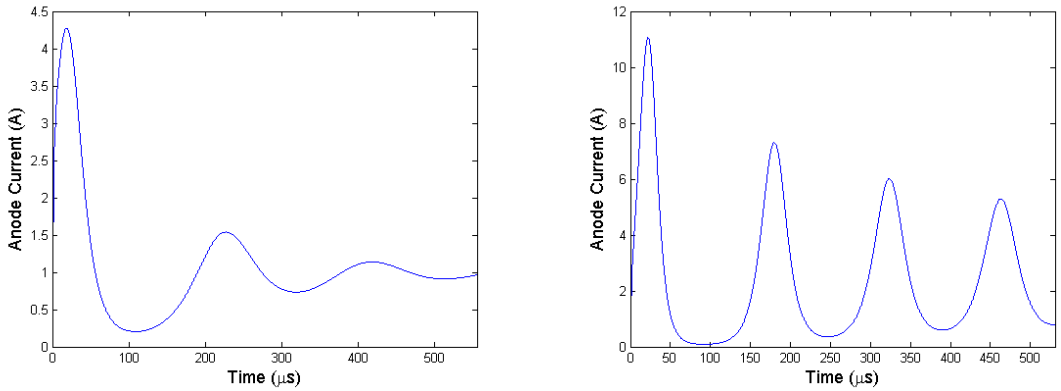

(a) 5 mg/s

(b) 6 mg/s

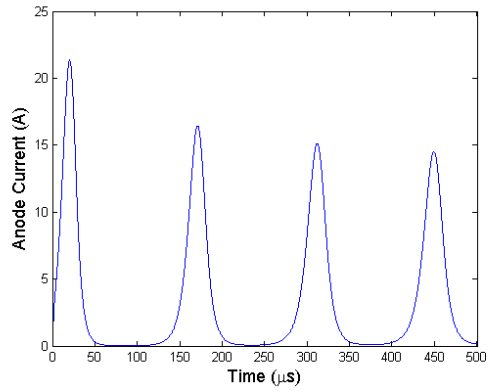

(c) 7 mg/s

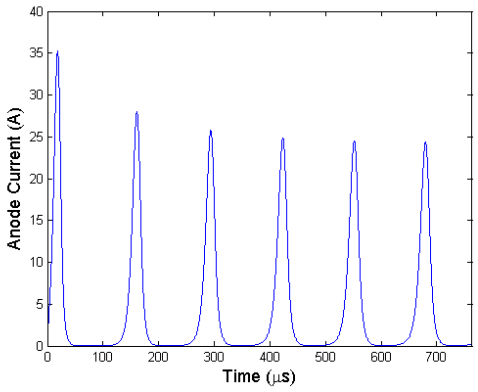

(d) 8 mg/s

Figure 5-12: Simulated anode current waveforms at different anode mass flow rates. Constant anode potential of 180 V.

further quench the electron temperature through enhanced collisions. In the unsteady solution, however, the higher flow rates lead to higher plasma density spikes (see Fig. 5-13) which lead to much higher instantaneous power input to the electrons through Joule heating.

Increasing the flow rate also increases the steepness and depth of the neutral depletion, shown in Fig. 5-15, as a corollary to the enhanced sharpness and height of the plasma density peaks. The locations of the peak plasma density, electron temperature and electric field are traced on top of the neutral density contours of Fig. 5-15 to demonstrate how the rate and range of their apparent motion diminishes with the extent of neutral depletion as the flow rate decreases.

An additional oscillation appears on top of the breathing mode at a flow rate of

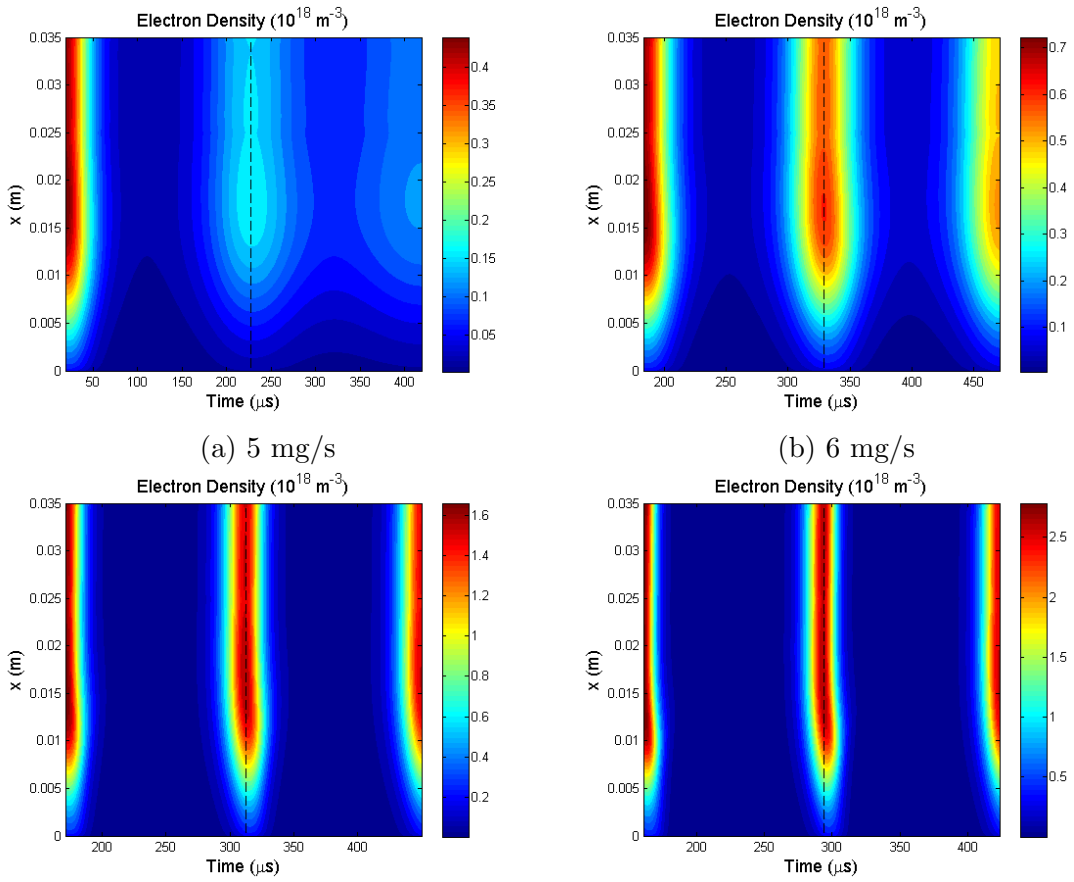

(a) 5 mg/s

(b) 6 mg/s

(c) 7 mg/s

(d) 8 mg/s

Figure 5-13: Simulated plasma density profiles versus time at different anode mass flow rates. Constant anode potential of 180 V.

8 mg/s, which is apparent in Figs. 5-14d, 5-16d, 5-17d & 5-18d during the neutral refill portion of the cycle. These oscillations begin roughly half a cycle after the current peak, abating just prior to the subsequent peak. These oscillations do not appear to have much effect on the anode current, despite involving large fluctuations in electron temperature and ion velocity. This is similar to the high frequency oscillation simulated by Barral and Ahedo [12] which was identified as the ion transit-time instability. This instability will be discussed in further detail near the end of this chapter.

The time averaged profiles of plasma density and electron temperature, shown in Fig. 5-19, exhibit some interesting trends. Profiles are averaged from the third to the fourth anode current peak, to avoid any spurious effects from including data near the

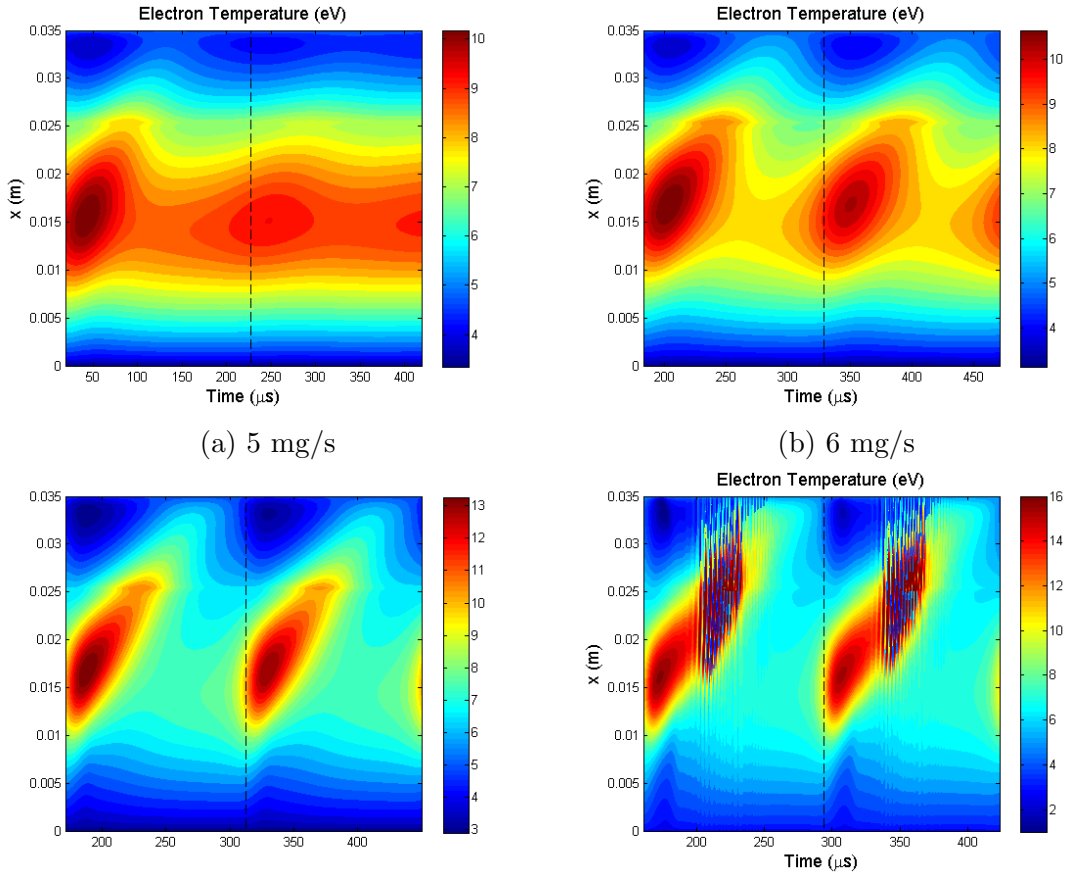

(a) 5 mg/s

(b) 6 mg/s

(c) 7 mg/s

(d) 8 mg/s

Figure 5-14: Simulated electron temperature profiles versus time at different anode mass flow rates. Constant anode potential of 180 V.

start-up transient which occurs due to the initial conditions being far from physically realistic. Figure 5-19a shows the time-averaged plasma density peak moves upstream as the flow rate is increased in these simulations, while Fig. 5-19b indicates the peak time-averaged electron temperature moves downstream.

Though the time-averaged plasma density profiles peak closer to the anode at higher flow rates, the peak density location during the in-place, exponential plasma growth portion of the breathing cycle is found further downstream when the flow rate is increased. In-place growth begins with the plasma density peak located 17.9 mm from the anode with a 5 mg/s flow rate, for example, at 19.3 mm for a 7 mg/s flow rate, and out to 20.1 mm for a 10 mg/s flow.

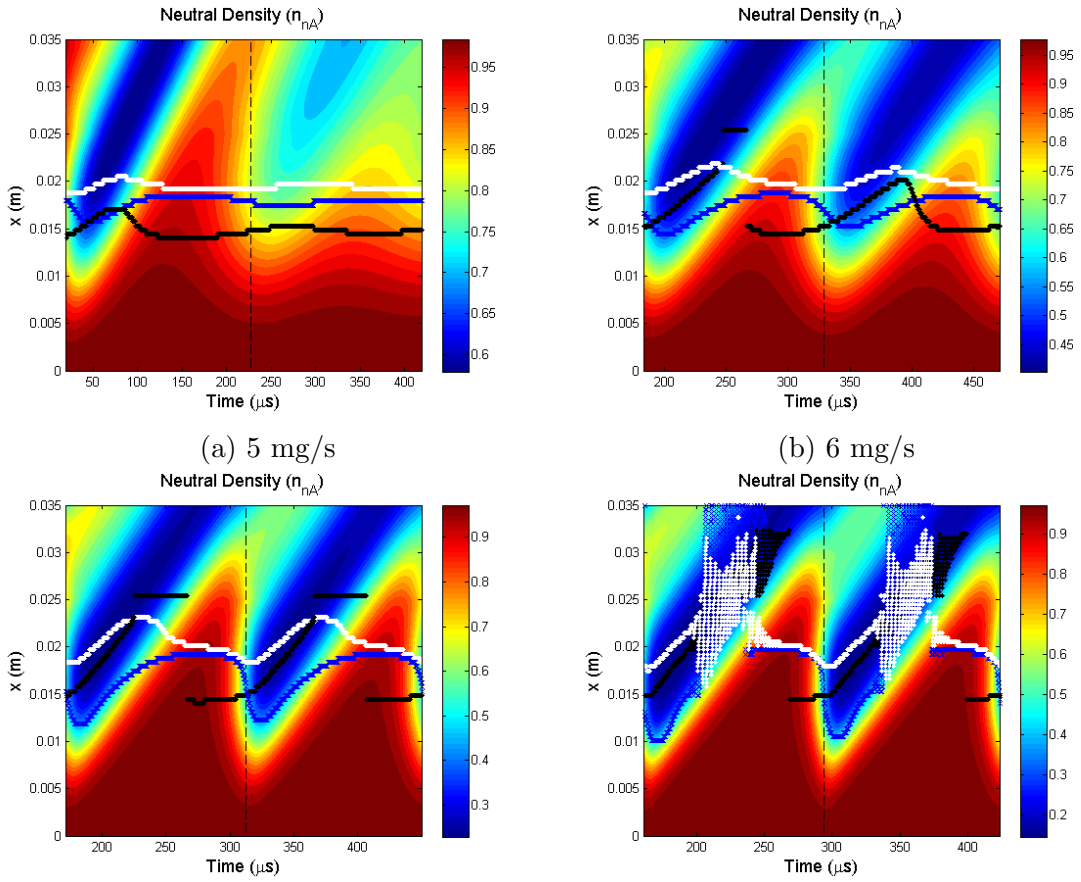

(a) 5 mg/s

(b) 6 mg/s

(c) 7 mg/s

(d) 8 mg/s

Figure 5-15: Simulated neutral density profiles versus time at different anode mass flow rates, normalized by the neutral density at the anode. Constant anode potential of 180 V. Blue x designates location of plasma density peak. Black diamond designates location of peak electron temperature. White diamond designates location of peak electric field.

5.3.4 Voltage Scan

A large range of input anode voltages were simulated with the anode flow rate kept constant at 5 mg/s. Stable spiral type solutions were found at applied potentials below 200 V, as illustrated in Fig. 5-20, and unexpectedly at potentials above 280 V. The anode potential was also found to have a fairly small effect on the frequency of the breathing oscillations, as shown in Fig. 5-20b.

The low voltage transition from a stationary solution to a limit cycle occurs between 190 V and 200 V. The change in the unsteady behavior of the model outputs as the voltage is brought through the transition point is nearly identical to the changes

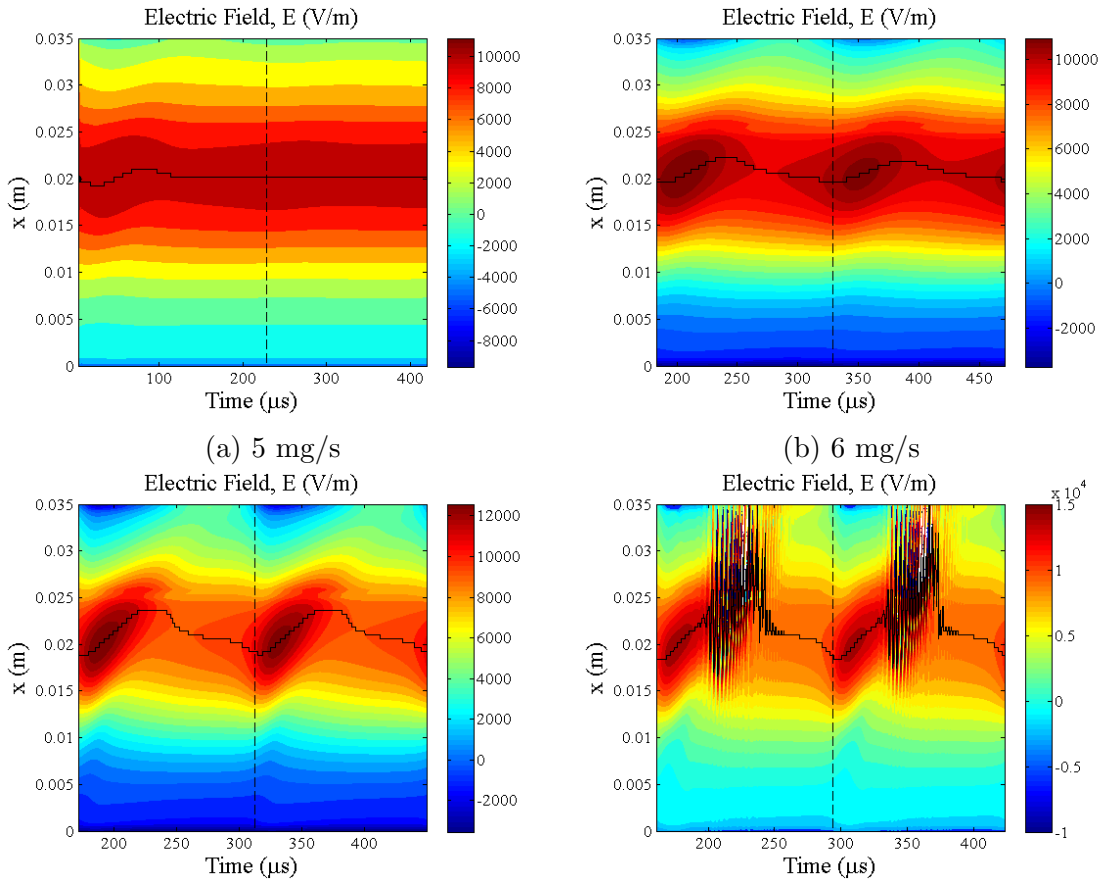

(a) 5 mg/s

(b) 6 mg/s

(c) 7 mg/s

(d) 8 mg/s

Figure 5-16: Simulated electric field profiles versus time at different anode mass flow rates. Constant anode potential of 180 V.

which occur as the flow rate is raised to cause a similar transition and which are displayed in Figs. 5-12 through 5-17. The density and current peaks become increasingly high and narrow as the voltage is raised. Once again, as the oscillations become larger, the axial location of the peak plasma density starts the phase of exponential current growth further from the anode (and from the axial location of the electron temperature peak) and moves closer to it as the current begins to decay. Transit-time oscillations appear at anode potentials of 220 V and higher.

Interestingly, at high enough voltages a stable focus solution is found. The anode current asymptotically approaches 4.1 A (3.65 A corresponds to a fully singly ionized flow of 5 mg/s) at an anode potential of 300 V, with only 0.8 A (standard deviation) transit-time fluctuations remaining. The eventual damping of the breathing mode is

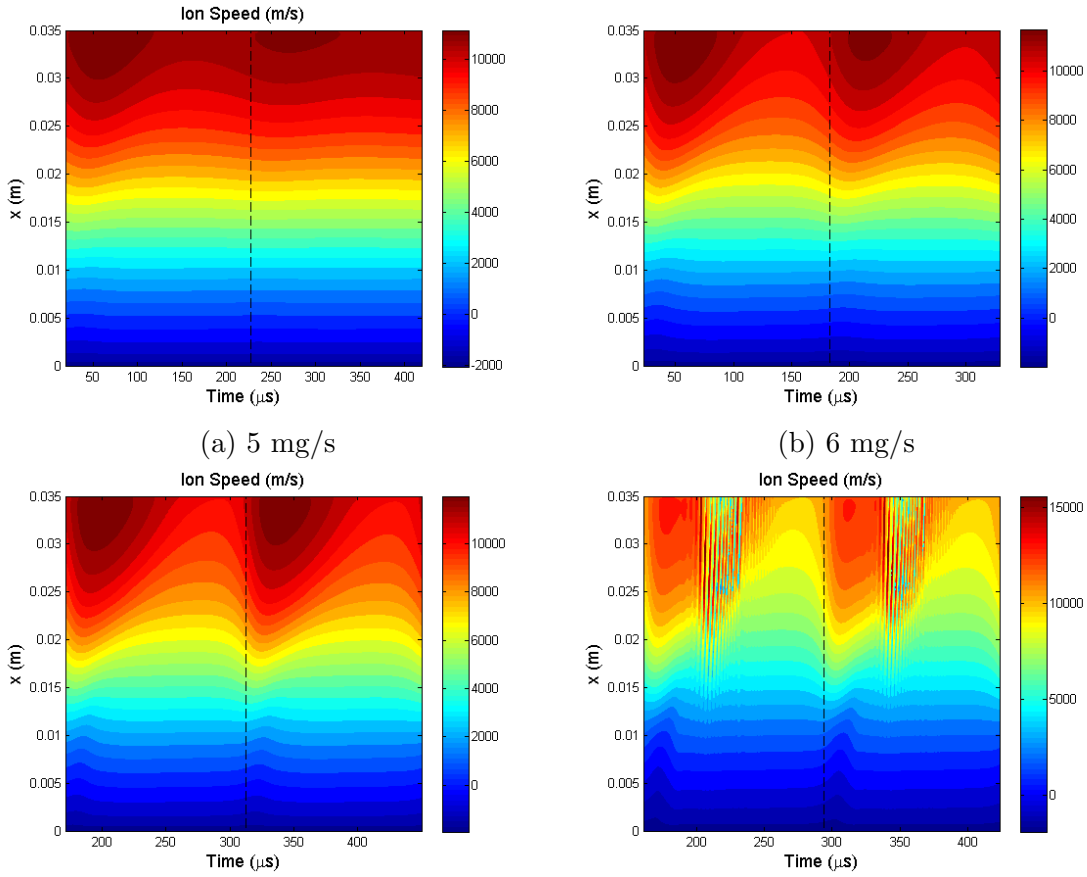

(a) 5 mg/s (b) 6 mg/s

(c) 7 mg/s (d) 8 mg/s

Figure 5-17: Simulated axial ion velocity profiles versus time at different anode mass flow rates. Constant anode potential of 180 V.

shown in Fig. 5-21 where the undamped anode current waveform at a lower voltage is also shown for comparison. As the breathing oscillations begin to die out, the transit-time oscillations (at 110 kHz) begin to dominate, even having visible effects on the neutral density profile. Any effect the transit-time fluctuations might have on the neutrals is otherwise washed out by the dominant breathing mode.

The evolution of the electron temperature profiles for the limit cycle at 280 V and the focus at 300 V are shown Fig. 5-22 from a quarter cycle before the current peak to a half cycle afterwards. Transit-time oscillations lead to very high temperatures external to the discharge chamber leading up to the current peak at both anode voltages, but the maximum external temperature is only around 40 eV when 280 V is applied and a whopping 80 eV at 300 V. This sudden hot spot is likely the source

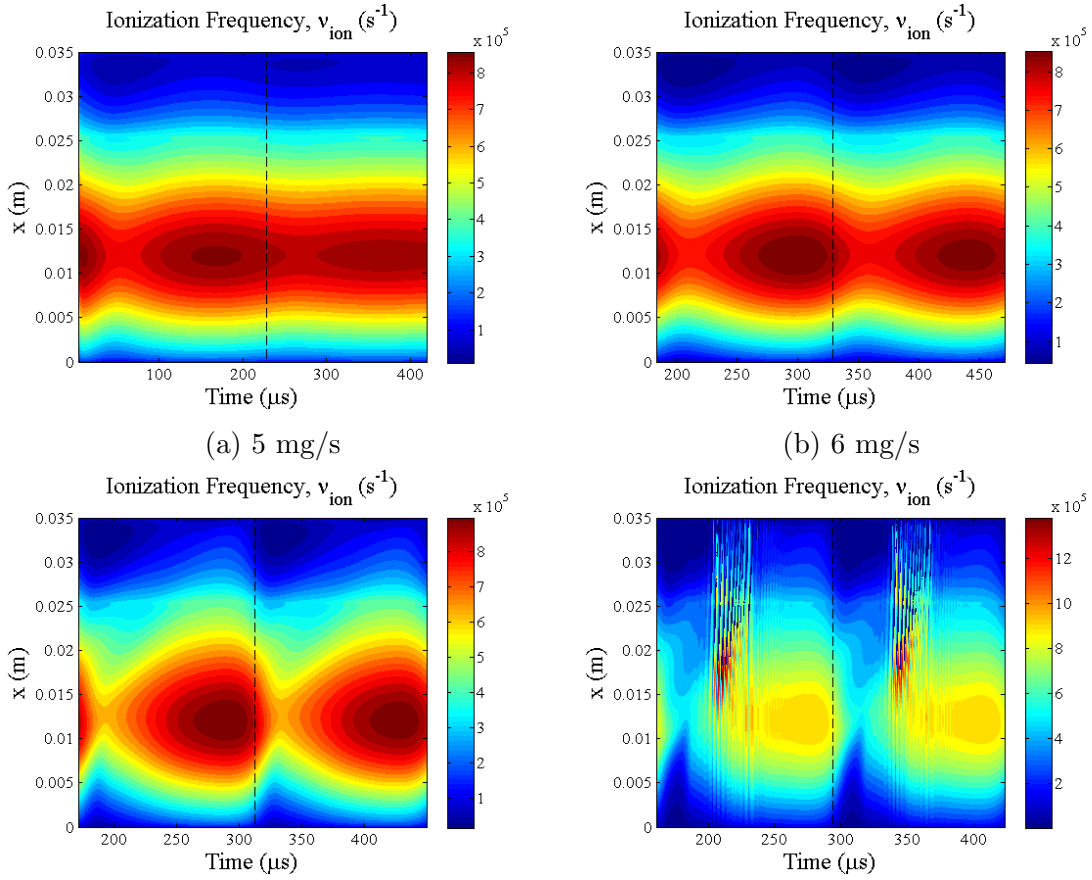

(a) 5 mg/s

(b) 6 mg/s

(c) 7 mg/s

(d) 8 mg/s

Figure 5-18: Simulated ionization frequency profiles versus time at different anode mass flow rates. Constant anode potential of 180 V.

of the dissipation which eventually extinguishes the breathing mode at 300 V.

The extreme external temperature elevates the electron temperature just upstream of the exit, leading to excessive power loss to the walls there. This effect is evidenced by plots of the different avenues of power loss and gain plotted as a function of time for the voltages on either side of the transition, given in Fig. 5-23. The plots show the instantaneous power being input to the electrons through Joule heating ($en_e v_{ex} E$), the power lost to inelastic collisions ($n_e \nu_{ion} \alpha_i E_i$) and the power lost to the walls ($n_e \nu_{ew} \epsilon_w$) summed over the axial domain at each time step.

The obvious difference in the evolution of the electron energy source/sink terms between the two anode voltages occurs in the wall loss term just after the current peaks, when, in the 300 V case, the energy dumped to the walls briefly exceeds the

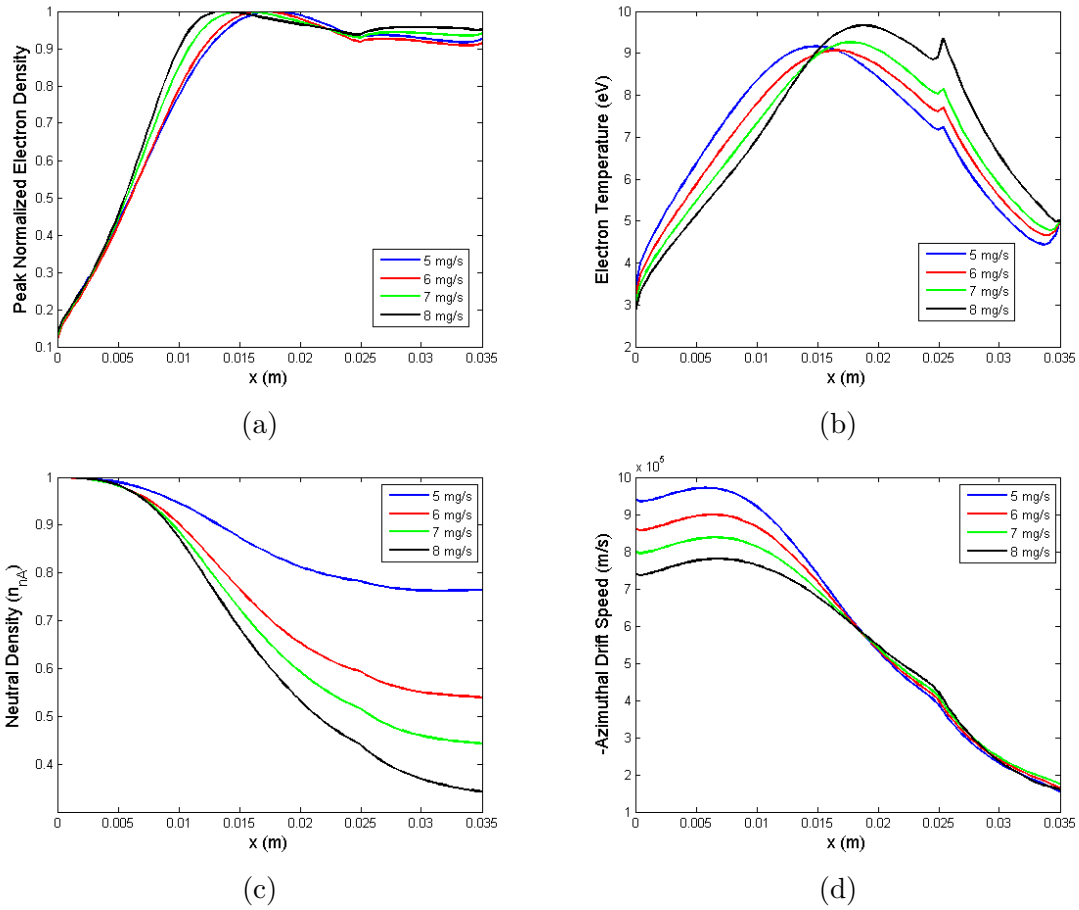

Figure 5-19: Model results for 180 V and various flow rates. (a) Time averaged plasma density normalized by the peak density at each flow rate (b) Time average electron temperature (c) Time averaged neutral density (d) Time averaged electron azimuthal drift speed

energy gained from the electric field. At 280 V, the wall losses, which peak just after the current does, are essentially the same as the inelastic losses just before the current peak, both of which are always a good margin below the Joule heating term. The dashed blue line in Fig. 5-23b shows what the wall losses would be at 300 V if the contributions from the 0.4 mm wide axial bin closest to the exit was removed from the sum. In this case, the wall loss term drops nearly an order of magnitude when the point affected by a large electron temperature discontinuity is neglected.

The strong temperature discontinuity which muddies the results at 300 V exposes a fundamental flaw of the present, drastically simplified model. By neglecting heat conduction, plume expansion and reducing wall collisions sharply to zero past the

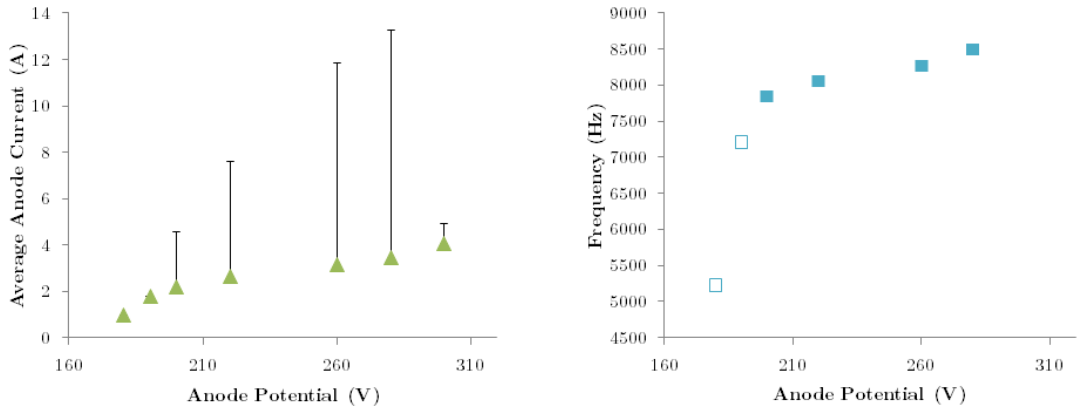

(a) (b)

Figure 5-20: Model results for 5 mg/s and various anode potentials. (a) Time averaged anode current with error bar showing 1 standard deviation. (b) Anode current oscillation peak-to-peak frequencies. Empty squares represent conditions where oscillations are damped.

exit, we no longer have a mechanism to cool electrons in this region. The self-imposed discontinuity in electron cooling becomes a major factor at high voltages, at which point ion-transit time oscillations are strong and the electrons can gain a substantial amount of energy in the short distance between cathode and channel exit. A more detailed model is necessary to validate the existence of excessive wall losses as a breathing mode damping mechanism at high voltages.

5.3.5 Magnetic Field Effects

A stable spiral can be reached at slightly lower anode voltages when the peak magnetic field strength is lowered as well, as found in similar 1-D models [160, 12]. When the peak field is 22 mT, a limit cycle is obtained at 280 V, but when lowered to 20 mT, the 280 V condition damps towards a stable value in a manner similar to that described for the 300 V, 22 mT case. The damped anode current waveform and electron power loss breakdown are shown in Fig. 5-24 for the 280 V simulation with a peak field strength of 20 mT.

The changes are generally subtle between the two magnetic field cases, however a roughly 70 eV hot spot forms just downstream of the exit in the low magnetic field

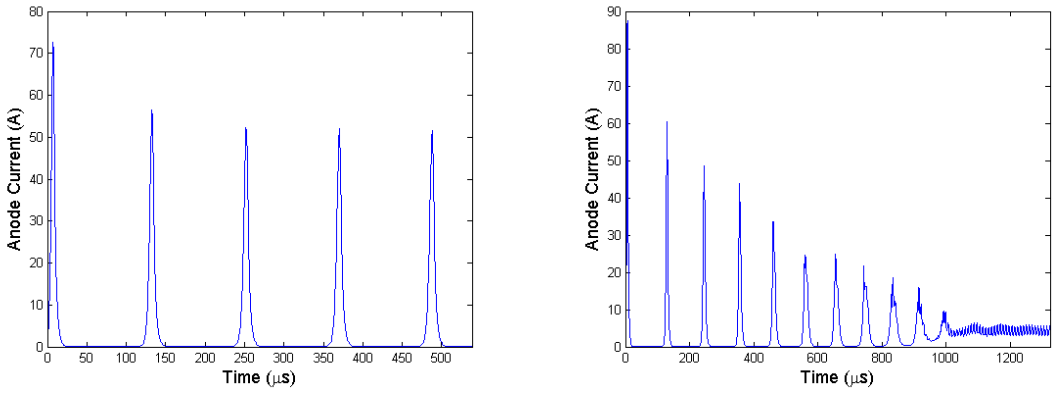

(a) (b)

Figure 5-21: Simulated anode current at 5 mg/s flow rate and an anode potential of (a) 280 V and (b) 300 V

case, similar to the high-field 300 V case. The hot spot can be seen in Fig. 5-25b and compared to the far cooler external temperatures in Fig. 5-22a for the 22 mT simulation. A highly localize high plasma density region forms just upstream of the hot spot as shown in Fig. 5-25a.

The anode voltage envelope with self-excited breathing oscillations (see Fig. 5-46) can alternatively be expanded by reducing the strength of the external magnetic field only. We model a weakened external field using a piecewise-Gaussian with the normal width of l_B=1.25 cm internally, and a width of l_{B2}=0.5 cm downstream of the exit. The stable focus at 300 V becomes a limit cycle with the weakened field, as shown in Fig. 5-26a, however a damped solution is regained at an anode potential of 340 V, shown in Fig. 5-26b.

Unexpectedly, the ion transit-time oscillations which dominate the current waveform at 300 V with the normal magnetic field are not present (after the first 0.7 ms of the simulation) in the damped 340 V case with the altered field. The discontinuity in temperature remains a major factor however, as can be seen in Fig. 5-27. Figure 5-28b demonstrates that, although the power lost to the walls is not substantial compared to Joule heating at 340 V, it does exceed the power spent on inelastic collision at all points of the cycle, unlike normal limit cycles, such as the one in Fig. 5-28b.

Moving the location of the magnetic field peak can also cause damping as illus-

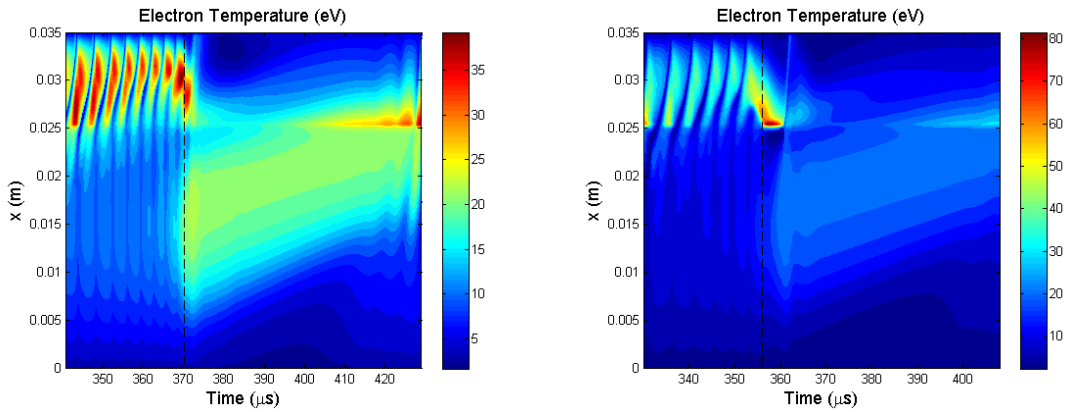

(a) (b)

Figure 5-22: Simulated electron temperature profile versus time at a 5 mg/s flow rate and an anode potential of (a) 280 V and (b) 300 V. Dashed line indicates location of anode current peak.

trated for the normally self-sustained breathing condition at 220 V and 5 mg/s. When the peak is moved 5 mm downstream of the exit, or alternatively 10 mm upstream, a stable spiral appears. The result of moving the location of the magnetic field peak in 5 mm increments off of the exit plane is summarized in Fig. 5-29a, from which it appears that this voltage and flow rate experiences its strongest breathing mode when the peak is near the exit.

The breathing frequency is seen in Fig. 5-29b to decrease by 13% when the peak field was moved upstream 5 mm from the exit, even though the plasma density and electron temperature peaks move upstream by roughly the same amount (Fig. 5-30a). The width of the ionization region, which is apparent in the neutral density contours of Fig. 5-31 as the area of strong depletion, does not increase when the magnetic field peak is moved upstream, making the reason for the frequency decrease unclear. Perhaps the neutral refill period is extended because the peak ionization occurs further upstream, causing an increase in the time for the region of depleted neutrals to be convected from the thruster.

When the peak magnetic field is moved to 15 mm from the anode the location of peak ionization frequency is forced to abut the anode. The plasma density is necessarily low adjacent to the anode so $\dot{n}_e = n_e \nu_{ion}$ is never high enough to create the

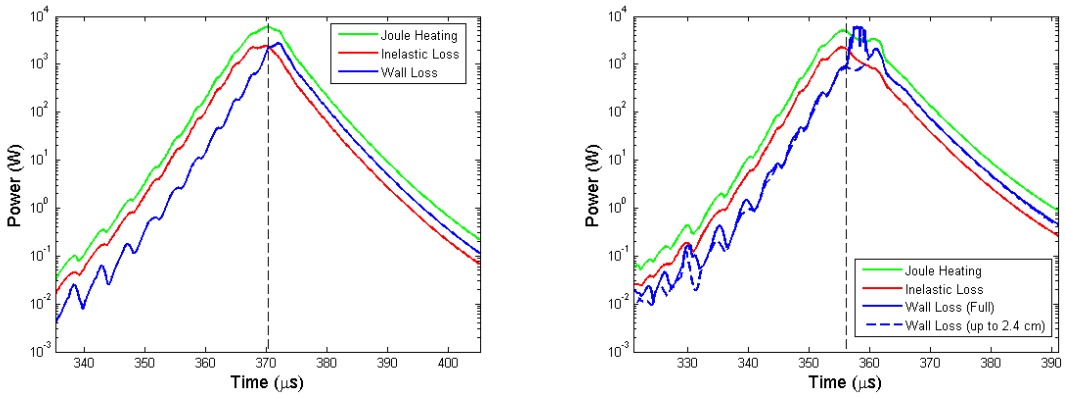

(a) (b)

Figure 5-23: Simulated electron power gain/loss versus time at a 5 mg/s flow rate and an anode potential of (a) 280 V and (b) 300 V. Dashed line indicates location of anode current peak.

large ionization transients necessary for a sustained breathing mode. The reason for the damping of the breathing mode when x_m=30 mm is likely related to the downstream shift in the electric field not being joined by a downstream shift in electron temperature or density, as seen in Fig. 5-30b.

5.3.6 Neutral Model Effects

At a neutral speed of 100 m/s strong self-sustained oscillations are observed, when at 200 m/s the anode current damped to a steady value (at the 180 V and 5 mg/s condition). The lower neutral speed doubles the density of neutrals at the inlet so the growth rate of the current may be expected to rise while the refill rate of neutrals is expected to decrease, combining to allow the excitation of the relaxation oscillation. During the in-place growth of plasma density the location of the peak density is further downstream than for the 200 m/s case at 20.1 mm compared to 17.9 mm, while the location of peak temperature stays the same at 14.9 mm.

Decreasing the neutral speed from 150 m/s to 100 m/s results in a nearly linear decrease in breathing mode frequency, as shown in Fig. 5-33b. The frequency at 150 m/s is expected to be slightly less than 3/2 the frequency at 100 m/s due to the decreased current growth time arising from the lower inlet neutral density. The

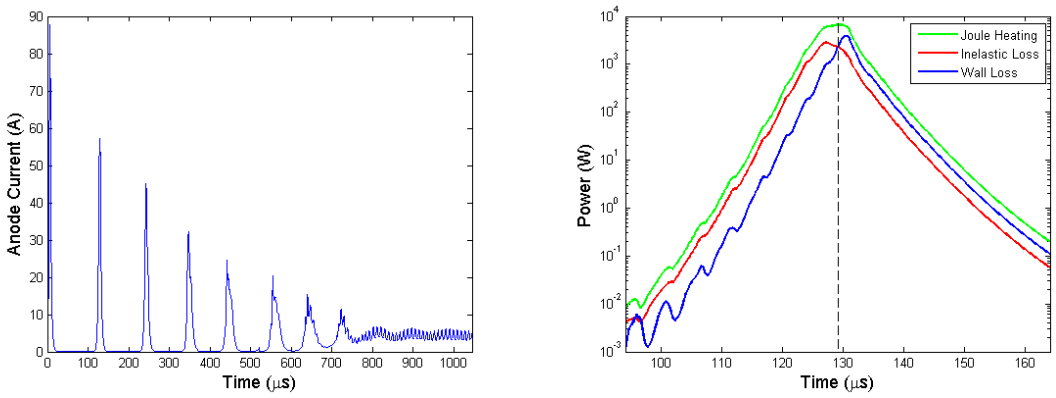

(a) (b)

Figure 5-24: Simulated (a) anode current (b) electron power gain/loss versus time at 5 mg/s at 280 V with a peak magnetic field of 20 mT. Dashed line indicates location of the second anode current peak.

location of the plasma density peak as the exponential current growth portion of each cycle begins moves downstream as the neutral speed decreases, while the peak electron temperature location remains relatively unchanged. The dependence of the axial position of the peak plasma density during its in-place growth on the neutral speed is similar to its dependence on the mass flow rate. Plotting the location of the initial plasma peak as a function of the inlet neutral density which results from either of these parametric changes, as done in Fig. 5-34, shows how the plasma peak sets up further downstream as the neutral density is raised.

A simulation was performed with a flow rate of 3.75 mg/s and a neutral speed of 150 m/s in order to match the neutral density at the anode of the baseline case of 200 m/s neutrals at 5 mg/s. The resulting anode current is similarly damped, and other than the plasma density decreasing by a factor of 3/4, the time averaged profiles are virtually the same as the baseline. Despite the lower neutral speed, the location of the plasma density peak as the current begins to rise is the same as it is in the baseline case, further suggesting this position is set by neutral density when the anode potential is constant.

Similarly, a flow rate of 6.67 mg/s with a neutral speed of 200 m/s was simulated to compare with the undamped 5 mg/s mass flow and 150 m/s neutral speed case.

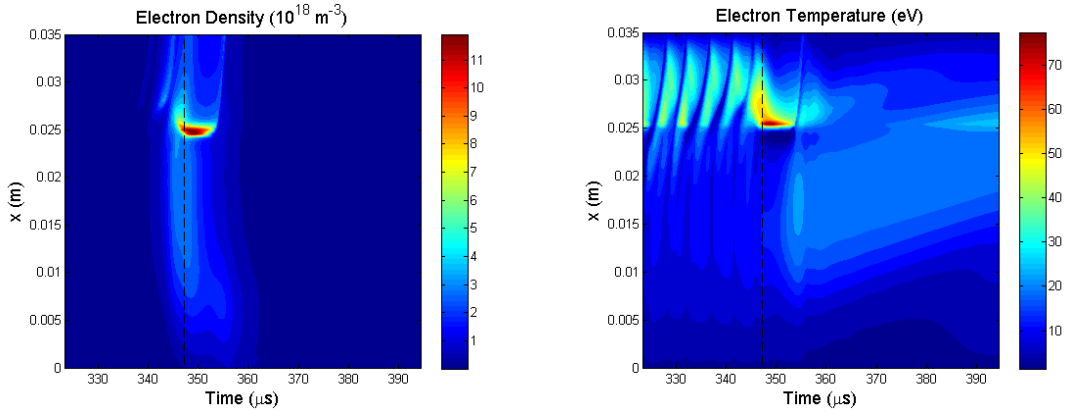

(a) (b)

Figure 5-25: Simulated (a) plasma density (b) electron temperature profiles versus time at 5 mg/s at 280 V with a peak magnetic field of 20 mT. Dashed line indicates location of anode current peak.

The self-excited breathing mode remained in the higher neutral speed case, though at a higher frequency by a factor of 4/3. The time averaged profiles are also very similar, with the electron density slightly higher than 4/3 times the density at the lower flow rate for axial locations further than 1 cm from the anode.

5.3.7 Wall-Interaction Model Effects

The wall-collision frequency model is very basic, utilizing the limits $h_c/r_0 << 1$ and $\nu_r \rightarrow 0$. Solution of Eqn. 5.71 shows that the normal coefficient of 4/3 used in Eqn. 5.64 to calculate the wall-collision frequency takes a lower value when $\nu_r > 0$ [178]. When the wall-collision frequency coefficient is low enough, a limit cycle can occur for conditions which are normally stable.

Relaxation oscillations are obtained, for example, when the coefficient in Eqn. 5.64 is changed from 4/3 to 2/3 for anode conditions (180 V, 5 mg/s) which normally lead to a stable focus. Trends in the effect of the decrease of the ν_{iw} coefficient on the anode current are summarized in Fig. 5-35, which shows very nearly linear increases in average anode current and breathing frequency as the coefficient is lowered. The model outputs for a coefficient of 1 are very similar, qualitatively, to those found in the flow rate scan at 6 mg/s, while the outputs at a coefficient of 2/3 resemble those

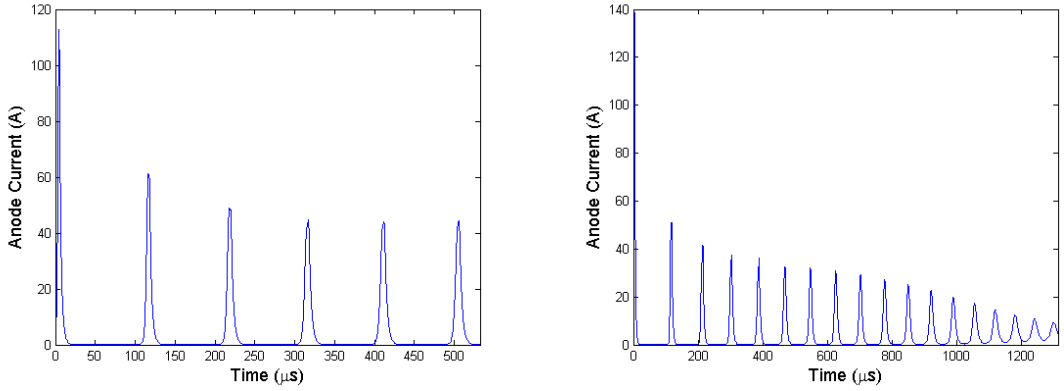

(a) (b)

Figure 5-26: Simulated anode current at 5 mg/s flow rate and an anode potential of (a) 300 V and (b) 340 V

found at 8 mg/s.

The decrease in wall collision coefficient can lead to the limit cycle type breathing oscillation by both increasing the net ion generation rate directly and by reducing the power loss avenue for electrons. These effects combined can lead to the large bursts of ionization necessary to sustain a breathing cycle.

The modeling of wall-interactions may also play a role in the transition to a stable focus at high voltages. There is not a large difference between the limit cycle at 280 V and the stable focus at 300 V, with no more than a 0.5 eV difference in the peak internal electron temperature at any time. The internal temperature begins to approach the limit where the wall sheaths become space charge saturated at both of these high voltages. As the temperature approaches the crossover energy the electron confining sheath potential drop shrinks non-linearly, leading to a rapid increase in electron power lost to the walls.

The secondary electron emission crossover energy was increased from 25 eV to 30 eV to see if an applied anode potential of 300 V would still lead to a stable focus prediction. Instead of reducing wall losses to allow a limit cycle, the peak internal electron temperature rose along with the crossover energy, continuing to lead to the eventual damping of the breathing mode. The rise in the peak temperature slightly lagged the crossover energy, as shown in Fig. 5-36a, with the temperature increasing

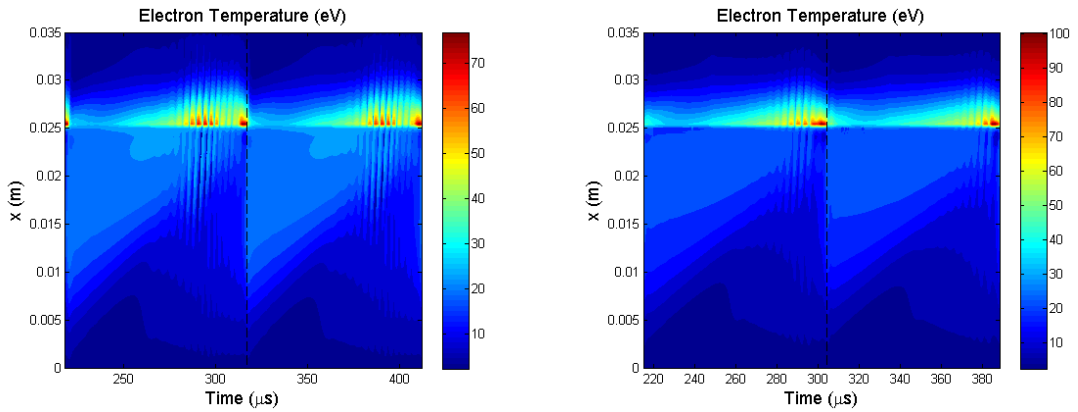

(a) (b)

Figure 5-27: Simulated electron temperature profile versus time at a 5 mg/s flow rate and an anode potential of (a) 300 V and (b) 340 V. Dashed line indicates location of anode current peak.

by about 13%, compared to a 20% increase in the crossover energy. In the same vein, the crossover energy was decreased from 25 eV to 20 eV at an anode potential of 280 V, but the limit cycle remained. The resulting cycles in peak electron temperature are dispalyed in Fig. 5-36b.

It appears that the amount of power being lost to the walls by electrons is too large to sustain breathing oscillations at 300 V and too little to extinguish them at 280 V, regardless of a 5 eV swing in the SEE crossover energy. The wall collision frequency coefficient was changed from 4/3 to 2/3 in an attempt to verify that increased wall losses were leading to the damped breathing mode at 300 V. Indeed a limit cycle is recovered when the wall collision frequency is reduced, however an oddly shaped current waveform results, as shown in Fig. 5-37a. Nevertheless, the tell-tale depletion and refill of neutrals, seen in Fig. 5-37b, suggests the anode current waveform is still dominated by the breathing mode.

5.3.8 Channel Divergence Effects

A small degree of channel divergence can be added without violating the model assumptions, using the simple method described in Sec. 5.2.2. We use the 1-D model to test the hypothesis that a diverging Hall thruster channel increases the range of con-

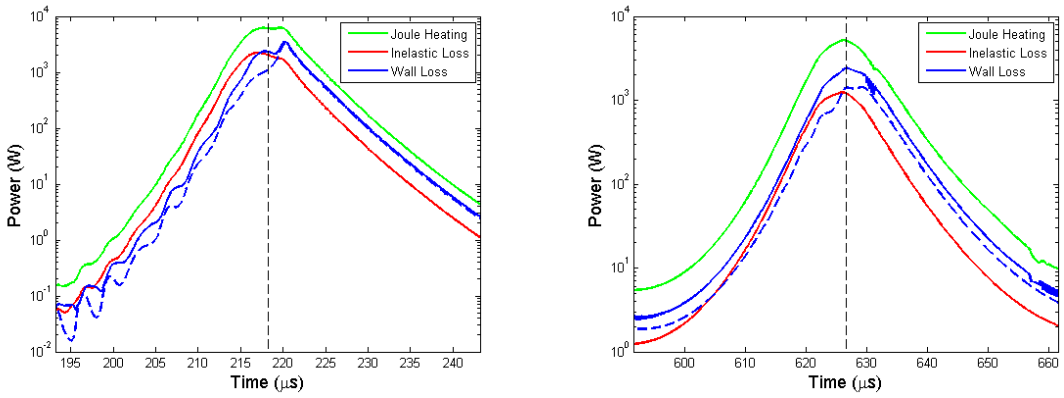

(a) (b)

Figure 5-28: Simulated electron power gain/loss versus time at a 5 mg/s flow rate and an anode potential of (a) 300 V and (b) 340 V. Black dashed line indicates location of anode current peak. Blue dashed line shows what wall losses are excluding the point closest to the exit.

ditions which result in breathing mode oscillations, as predicted by the 0-D dispersion relation of Yamamoto et al [163]. An exhaustive study has not been undertaken, but adding either a 15 or 30 degree angle of divergence to both inner and outer walls does not change the stability of the breathing mode at 180 V with either a 5, 6 or 7 mg/s anode flow rate.

The divergence angle, α, is added to both the channel walls and the area in the plume, so the rarefaction of neutrals is continuous. The channel height is kept as 2 cm at the anode, so if $\alpha = 30°$ and the cathode plane is at x=3.5 cm the inner radius of the plume is at 1 cm and the outer radius is at 7 cm. The planar assumption no longer holds as the height of the simulation is now larger than the mean radius (by a factor of 3/2). At $\alpha = 15°$ the planar assumption may be marginal at the cathode, but is still reasonable within the channel (i.e. x$\leq$2.5 cm).

The main effect on the current waveform of adding divergence to the simulation is a stronger start transient which reaches a substantially higher current peak and lower current trough before settling out to an anode current similar to that for the straight channel. The region where the electron temperature is highest remains seated just upstream of the peak magnetic field, but the peak plasma density tends to be located much closer to the anode than in the divergence-free case, as can be seen in Fig. 5-38.

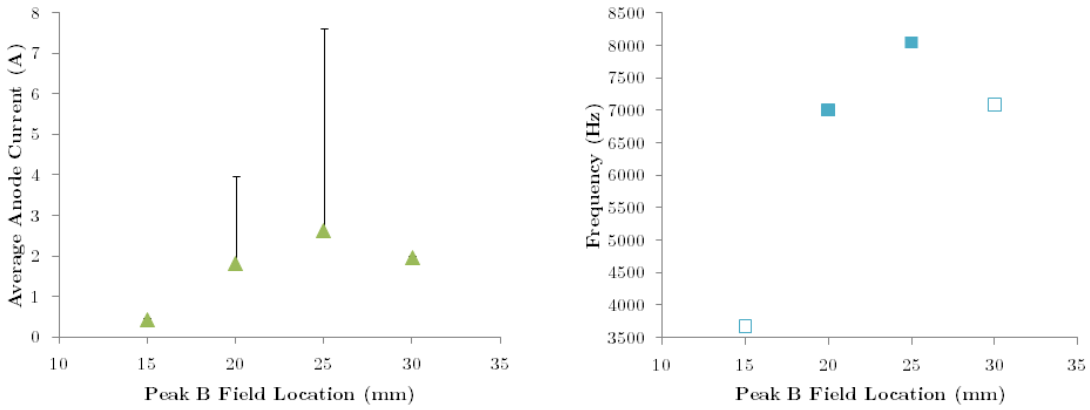

(a) (b)

Figure 5-29: Model results for 220 V, 5 mg/s and various locations of the peak magnetic field. (a) Time averaged anode current with error bar showing 1 standard deviation. (b) Anode current oscillation peak-to-peak frequencies. Empty squares represent conditions where oscillations are damped.

The average anode current changes by less than 4% between the three angles shown in Fig. 5-38 and the damped breathing frequency changes by even less. The lack of any change in stability may come about from a balance of the opposing effects of lower wall collisionality downstream enabling further current growth with lower neutral densities there due to rarefaction inhibiting growth.

5.3.9 Anomalous Diffusion Effects

Increasing the anomalous diffusion coefficient from 1/160 to 1/120 leads to another limit cycle for conditions which are normally damped. Anode current properties for a range of Bohm coefficients at a constant anode potential of 180 V and flow rate of 5 mg/s are presented in Fig. 5-39, showing that impedance reductions can excite the non-linear breathing mode. The small increase in the breathing frequency when the coefficient is changed from 1/120 to 1/80 may be due to the same mechanism which causes the observed decrease in frequency when the Gaussian magnetic field was shifted upstream. Transit-time oscillations are absent at all values of Bohm coefficient presented, except 1/80.

The peak density during in-place growth is somewhat counter-intuitively further

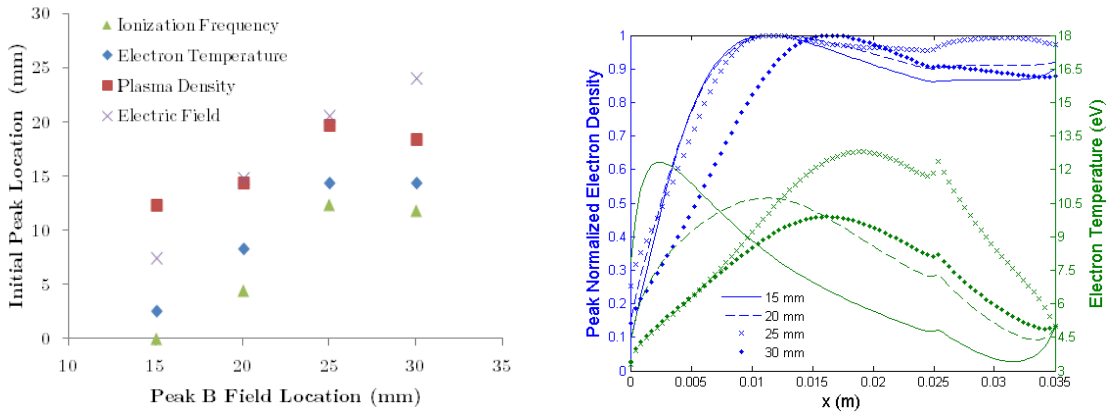

(a) (b)

Figure 5-30: Model results for 220 V, 5 mg/s and various locations of the peak magnetic field. (a) Location of variable peaks at start of current rise. (b) Time averaged plasma density and electron temperature profiles.

downstream at 19.7 mm rather than 17.9 mm, when the Bohm coefficient is increased from 1/160 to 1/120, though the temperature still peaks at 14.9 mm downstream of the anode, as shown in Fig. 5-40. The observed trend of the initial peak plasma density location moving downstream as the anomalous diffusion is increased is similar in effect to the trends seen when the inlet neutral density or the anode voltage (to a point) is increased. It is clear how each one of these inputs can increase the current growth rate, but less obvious why, after the plasma is evacuated from the simulation volume, the plasma density profile sets up for the next cycle the way it does.

5.3.9.1 Turbulent Shear Modeling

Noting that a decrease in the amount of anomalous diffusion introduced into the simulation can extinguish the breathing mode led to the conjecture that somehow the high voltage transition observed in the DCFT is due to a turning off of the anomalous diffusion mechanism. One such mechanism, known to the plasma fusion community since the late 1980's, is a shearing of the turbulent eddies believed to be responsible for anomalous diffusion [13, 14].

The idea, applied to the geometry of a Hall thruster, is that a fluctuating azimuthal electric field (or pressure gradient) and electron density will lead to a net axial electron

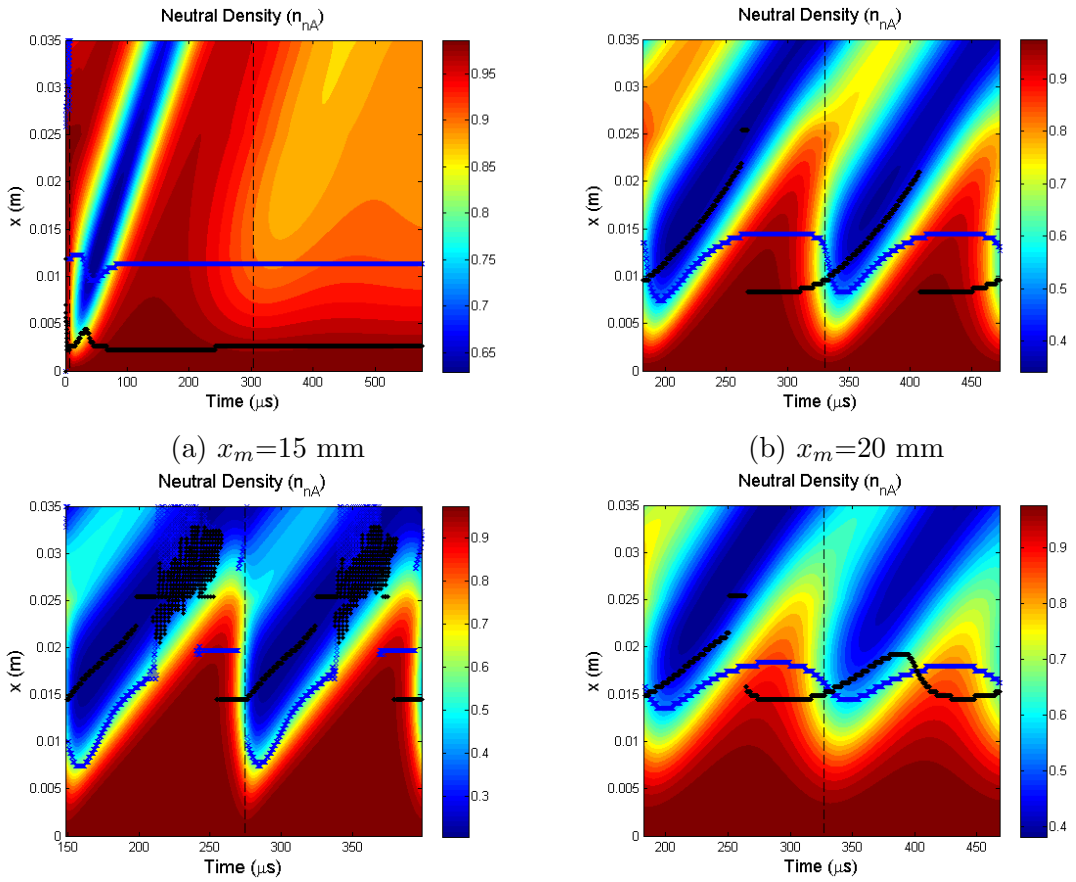

(a) x_m=15 mm (b) x_m=20 mm

(c) x_m=25 mm (d) x_m=30 mm

Figure 5-31: Simulated neutral density profiles versus time at different locations of the peak magnetic field, normalized by the neutral density at the anode. Constant anode potential of 220 V and flow rate of 5 mg/s. Blue x designates location of plasma density peak. Black diamond designates location of peak electron temperature

current if properly correlated. The correlation of the fluctuations can be described by the correlation time, with a longer correlation time equating to a larger net current. If the fluctuations are turbulent, as is often assumed, the correlation time is essentially the eddy turnover time, the convective time-scale for one eddy to transfer its energy to another.

In the presence of a shear in the flow which advects the turbulent eddies (which in this case is the azimuthal electron current), the eddy turnover time may effectively be reduced as the eddy is stretched to its coherence length quicker in the flow-wise direction by the differential advective speeds [188]. The decrease in the correlation time leads to decreased turbulence-induced diffusion, however the mechanism requires

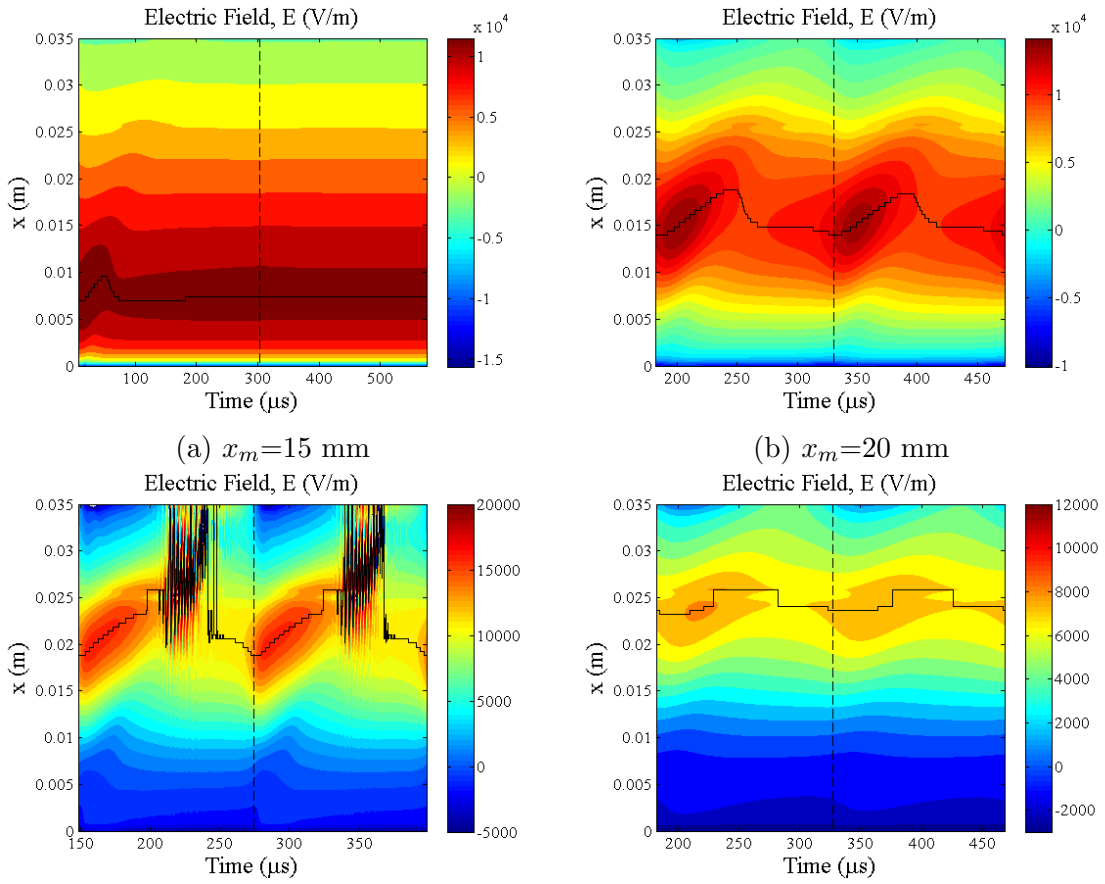

(a) x_m=15 mm (b) x_m=20 mm

(c) x_m=25 mm (d) x_m=30 mm

Figure 5-32: Simulated electric field profiles versus time at different locations of the peak magnetic field. Constant anode potential of 220 V and flow rate of 5 mg/s. Black line designates location of peak electric field

that the shear rate ($dv_{e\theta}/dx$) be greater than the eddy turnover rate.

Both theoretical and empirical models exist for predicting the anomalous diffusivity reduction in the presence of shear flow, with a review of its effects on magnetic confinement experiments given by Burrell [187] and an expansive review of the broad application of turbulence suppression theory given by Terry [188]. The various models have been applied to numerical simulations in both the fusion and Hall thruster communities [15, 189, 190]. Here we apply the model used by Scharfe et al[189] in a 2-D hybrid-PIC model of a Hall thruster, the general form of which is given in Eqn. 5.80, where α_{B0} is the Bohm coefficient in the absence of shear, γ_s is the shear rate, γ_t the eddy turnover rate and b is a fit parameter (generally around 1-2 [191]) which

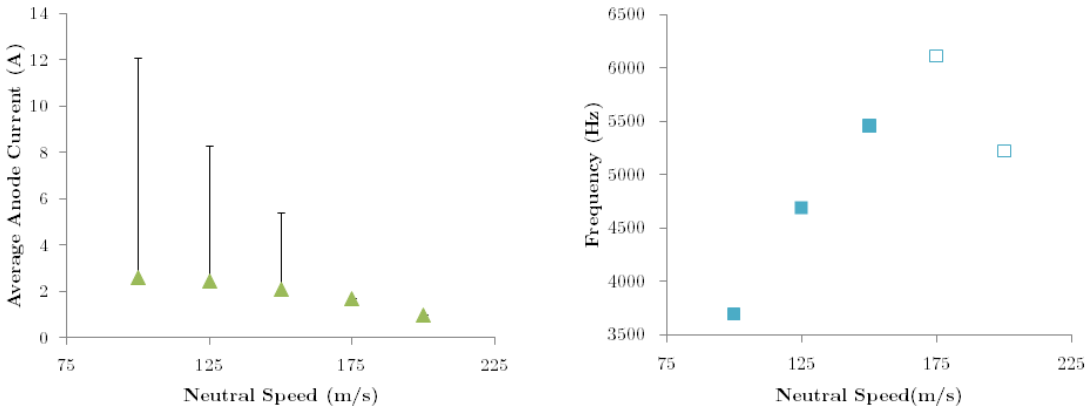

(a) (b)

Figure 5-33: Model results for 180 V, 5 mg/s and various neutral flow speeds. (a) Time averaged anode current with error bar showing 1 standard deviation. (b) Anode current oscillation peak-to-peak frequencies. Empty squares represent conditions where oscillations are damped.

determines the sharpness of suppression.

$$\alpha_B = \frac{\alpha_{B0}}{1 + \left(\frac{\gamma_s}{\gamma_t}\right)^b} \tag{5.80}$$

The above equation applies for a steady state, where the shear rate and anomalous diffusivity are established self-consistently. Applying Eqn. 5.80 to find an instantaneous Bohm coefficient for an instantaneous shear rate does not fit in with the physical picture just described, as the sheared flow must exist long enough to effectively decorrelate the eddies in order for the turbulent diffusion to be reduced. An analytical estimate by Hahm et al suggests that a shear rate which itself fluctuates faster than the eddy turnover rate will effectively decorrelate the tranport-driving turbulence less than a stable shear rate would at half the time-averaged value of the oscillating shear [192].

$$c\dot{\alpha}_B(t) + \alpha_B(t) = \frac{\alpha_{B0}}{1 + \left(\frac{\gamma_s(t)}{\gamma_t}\right)^b} \tag{5.81}$$

A time-dependent equation for the instantaneous Bohm coefficient is assumed of the form given in Eqn. 5.81. This formulation has the desired features that the

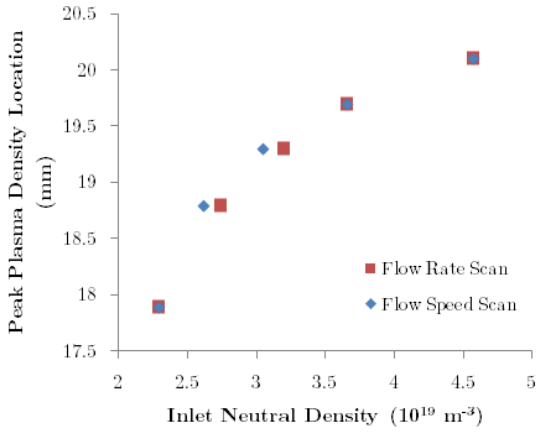

Figure 5-34: Model results for 180 V at either 5 mg/s and various neutral speeds (Flow speed scan) or 200 m/s neutral speed and various flow rates (Flow rate scan)

anomalous diffusivity is not altered instantaneously by a steady shear, but instead lags its application by a time delay, c, and the effect of oscillating components of shear on diffusivity is weakened if they oscillate faster than $1/c$. Equation 5.81 reduces to Eqn. 5.80 if a steady state shear rate is obtained.

Laplace transformation can be used to solve Eqn. 5.81 in terms of $\alpha_B(t)$, yielding,

$$\alpha_B(t) = \alpha_B(0)e^{-t/c} + \frac{1}{c}e^{-t/c}\int_0^t e^{\tau/c}\frac{\alpha_{B0}}{1+\left(\frac{\gamma_s(\tau)}{\gamma_t}\right)^b}d\tau \tag{5.82}$$

which can easily be implemented in our numerical scheme in the form,

$$\alpha_B^{n+1} = \alpha_B^n e^{-\Delta t/c} + \frac{\Delta t}{2c}\left(e^{-\Delta t/c}\frac{\alpha_{B0}}{1+\left(\frac{\gamma_s^n}{\gamma_t}\right)^b} + \frac{\alpha_{B0}}{1+\left(\frac{\gamma_s^{n+1}}{\gamma_t}\right)^b}\right) \tag{5.83}$$

where we use a central finite difference stencil to calculate the shear rate ($\gamma_s^n = dv_{e\theta}^n/dx$). The power, b, is a fit parameter, which we take to be 2, for ease of comparison with the results of Scharfe et al [189] as well as for its common occurrence in the fusion literature [188, 14, 193]. The value of the shear-free diffusion coefficient, α_{B0}, is also a fit parameter of sorts, which we take to be 1/8, unless otherwise noted, matching the value taken by Scharfe.

The delay time, c, is taken to equal the eddy turnover time for the reasons stated

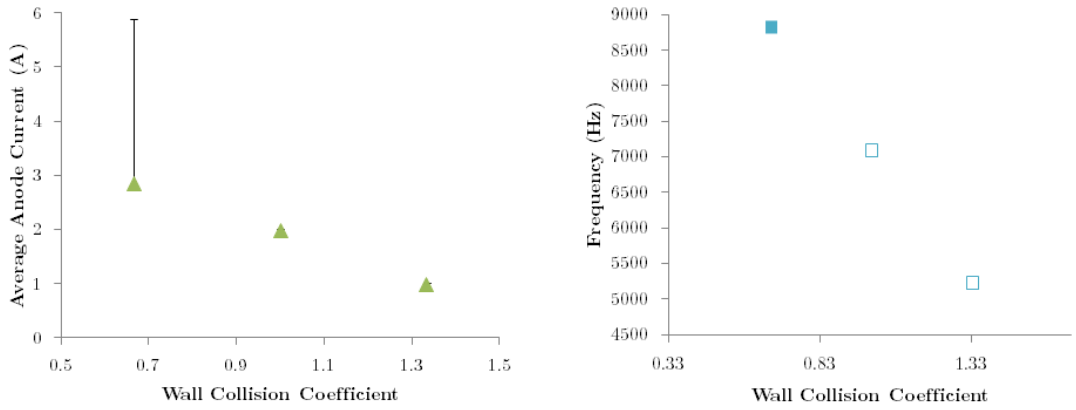

(a) (b)

Figure 5-35: Model results for 180 V and 5 mg/s at various ν_{iw} coefficients (nominally 4/3). (a) Time averaged anode current with error bar showing 1 standard deviation. (b) Anode current oscillation peak-to-peak frequencies. Empty markers represent conditions where oscillations are damped.

above, ensuring that the anomalous transport coefficient does not change much faster than the time scale of the turbulence responsible. It is easy to see that, within the framework of the sheared eddy model, eddy decorrelation may occur on shorter time scales than the shear-free eddy turnover time, however it may not proceed any slower. In this sense, $1/\gamma_t$ is an upper bound on c and offers a convenient choice for a parameter that is difficult to quantify otherwise.

The eddy turnover rate itself, γ_t, depends on details of the turbulence which may vary substantially from one device to the next, and at present has no universal expression. Ultimately, this is another fitting parameter for our model, and is varied at each set of thruster input conditions to gauge its effects. Typical values used are on the order of 10 MHz, which for typical time steps of several ns results in $c \sim 20\Delta t$.

In the hybrid Hall thruster code discussed by Scharfe, the 2-D shear rate data was distilled into a 1-D profile for the Bohm coefficient. In a similar manner we reduce our 1-D shear profiles to a single instantaneous shear rate, γ_s^n, which is used to find the global Bohm coefficient through Eqn. 5.83. The maximum value of the azimuthal electron velocity shear within the discharge channel at time step n is used for γ_s^n, though shear values within 3 mm of either end of the channel are neglected to avoid

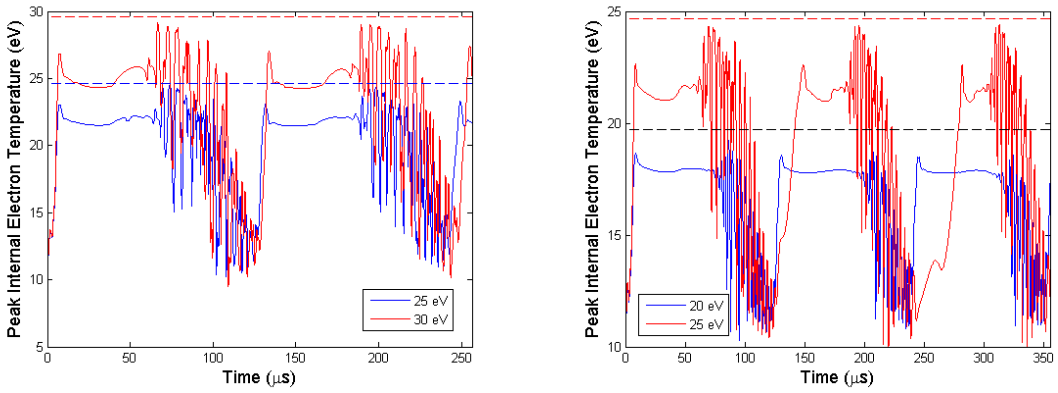

(a) (b)

Figure 5-36: Peak electron temperature upstream of the exit versus time for various values of the crossover energy with a flow rate of 5 mg/s and an anode potential of (a) 300 V (b) 280 V. The dashed lines indicate the temperature at which the sheath will become space charge saturated

spurious effects from discontinuities.

5.3.9.2 Shear Model Results

The eddy turnover time was varied for several different high voltage conditions until a stable spiral type solution was obtained. The turnover rate needed to obtain a stable focus solution is given for each voltage in Table 5.1, which also summarizes the resulting time averaged current and inverse Bohm coefficient, as well as the damped breathing mode frequency. In order for high voltage breathing modes to be extinguished through the quenching of Bohm diffusion, the eddy turnover time ($1/\gamma_t$) must increase along with the applied voltage.

Anode Voltage (V)	γ_t (MHz)	$< I_a >_t$	$< 1/\alpha_B >_t$	$\widetilde{I_a}$ Frequency (Hz)
220	8.75	1.27	268	14600
260	7.25	1.04	597	11800
300	5.25	1.10	1534	9300

Table 5.1: Model Properties For Stable Spiral Type Solutions at High Voltage (5 mg/s Flow Rate)

The breathing mode at 300 V is normally damped without the addition of the shear model, however the steady anode current is slightly higher than the time averaged

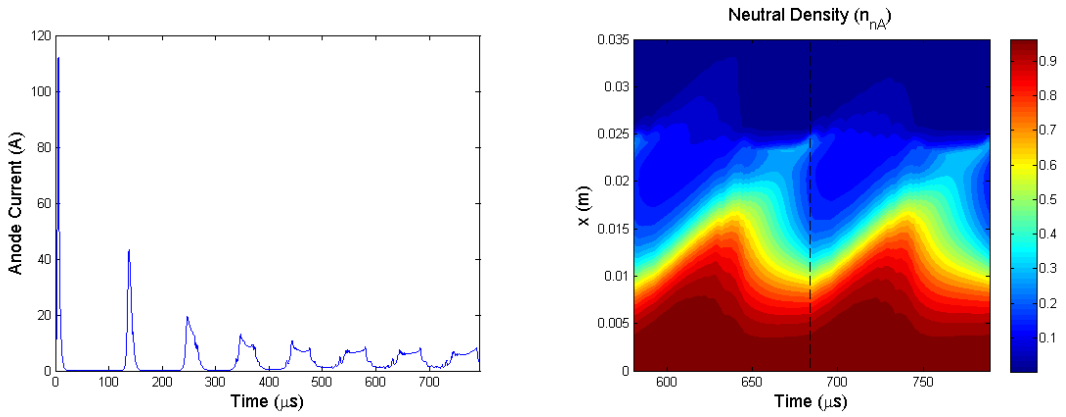

(a) (b)

Figure 5-37: Simulation results with at 300 V, 5 mg/s with a wall collision frequency coefficient of 2/3, showing (a) the anode current waveform (b) the neutral density profile versus time where the dashed line indicates the 7th current peak

current at lower voltages, so that it does not appear to resemble the high voltage transition seen in the DCFT, which involves a sharp drop in the anode current. When the shear model is applied the 300 V condition damps to 1 A (as opposed to 4 A), due to an order of magnitude reduction in the anomalous diffusion coefficient, mimicking the sought after bifurcation.

An unexpected result of the application of the quenching model is the appearance of simulated anode current waveforms with one or more 'stunted' peaks preceding the main burst of ionization. Similar waveforms are measured on the DCFT, such as the ones in Fig. 4-15, where the number of incomplete peaks tends to increase as the stable LC mode is approached. The model outputs for an anode potential of 220 V, a flow rate of 5 mg/s and a turnover rate of 9 MHz are shown in Fig. 5-41, where the anode current waveform contains two incomplete peaks before each main peak. The first stunted peak occurs roughly halfway into the cycle, while the second occurs about 3/4 of the way through.

A clear progression of anode current waveforms is obtained at 260 V and 5 mg/s of flow as the turnover rate is reduced from 11 Mhz to 7.25 MHz. At the highest γ_t used, a normal looking limit cycle is obtained (no stunted peaks) with slightly lower values of time averaged anode current (2.23 A) and breathing frequency (8350 Hz)

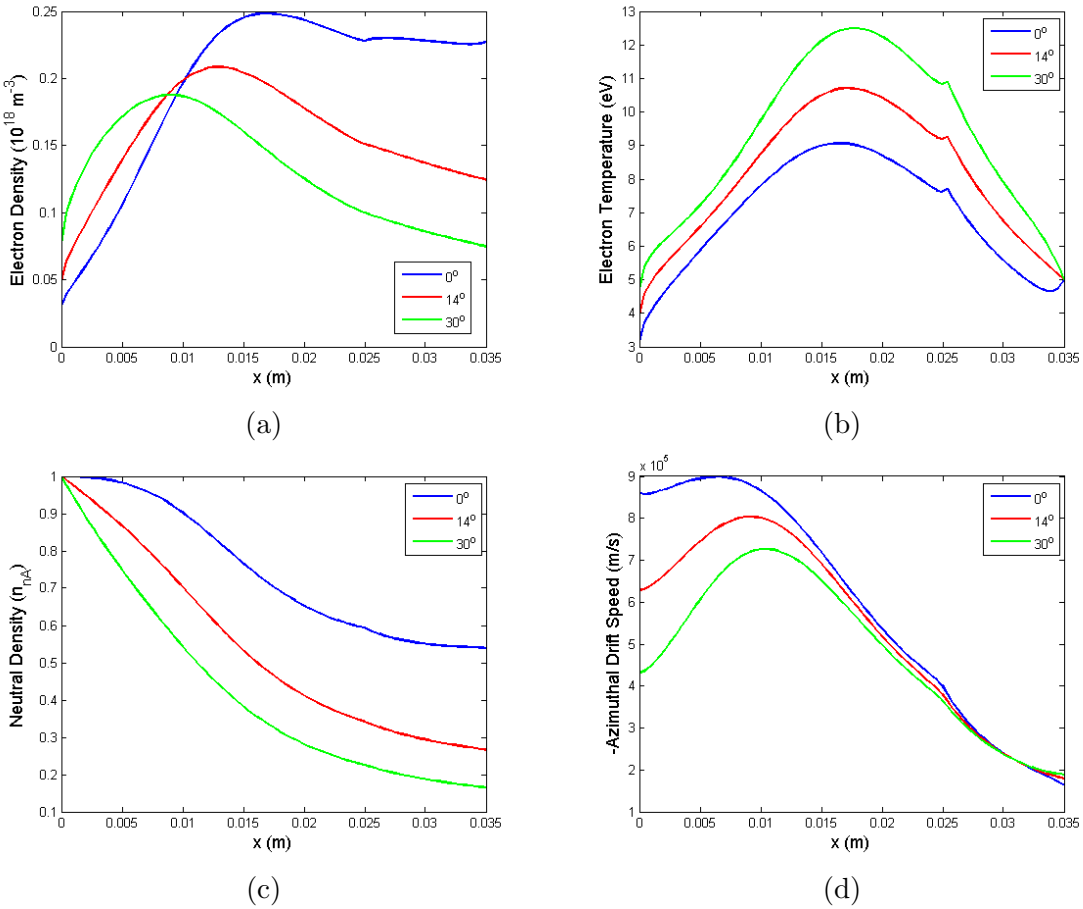

Figure 5-38: Model results for 180 V and 6 mg/s and various angles of channel divergence. (a) Time averaged plasma density (b) Time average electron temperature (c) Time averaged neutral density (d) Time averaged electron azimuthal drift speed profiles

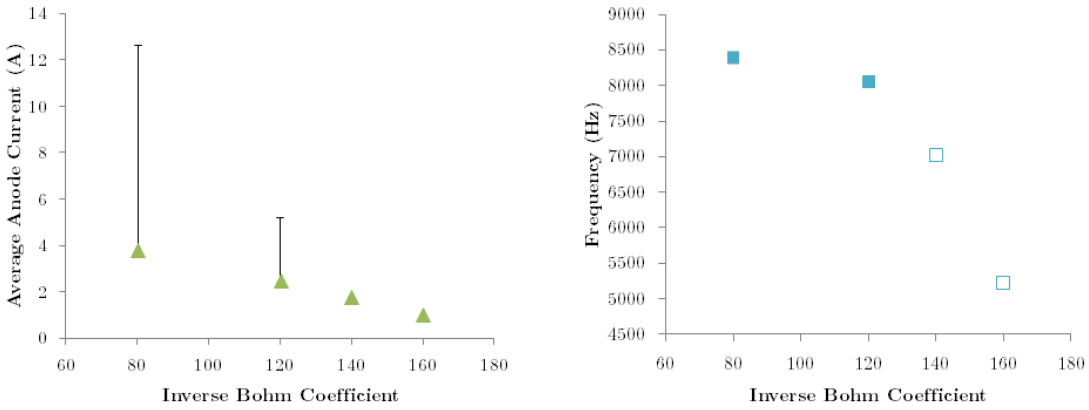

(a) (b)

Figure 5-39: Model results for 180 V, 5 mg/s and various values of the inverse Bohm coefficient (normally 160). (a) Time averaged anode current with error bar showing 1 standard deviation. (b) Anode current oscillation peak-to-peak frequencies. Empty squares represent conditions where oscillations are damped.

than observed when no turbulent shearing is imposed (3.19 A and 8490 Hz). A single stunted peak appears, preceding the main current spike by about 1/4 of a cycle, when an intermediate turnover rate of 8.25 MHz is applied, resulting in a time averaged current of 1.71 A and a peak-to-peak frequency of 5060 Hz. Finally, a stable sprial solution is found when the turnover rate is dropped to 7.25 MHz, with a time averaged inverse Bohm coefficient much lower than that for the cases which exhibit breathing oscillations.

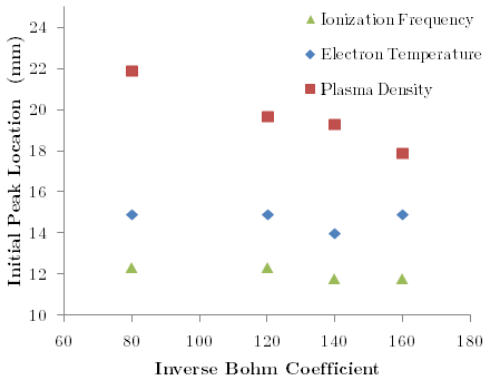

Figure 5-40: Location of variable peaks at start of current rise for 180 V, 5 mg/s and various values of the inverse Bohm coefficient (normally 160)

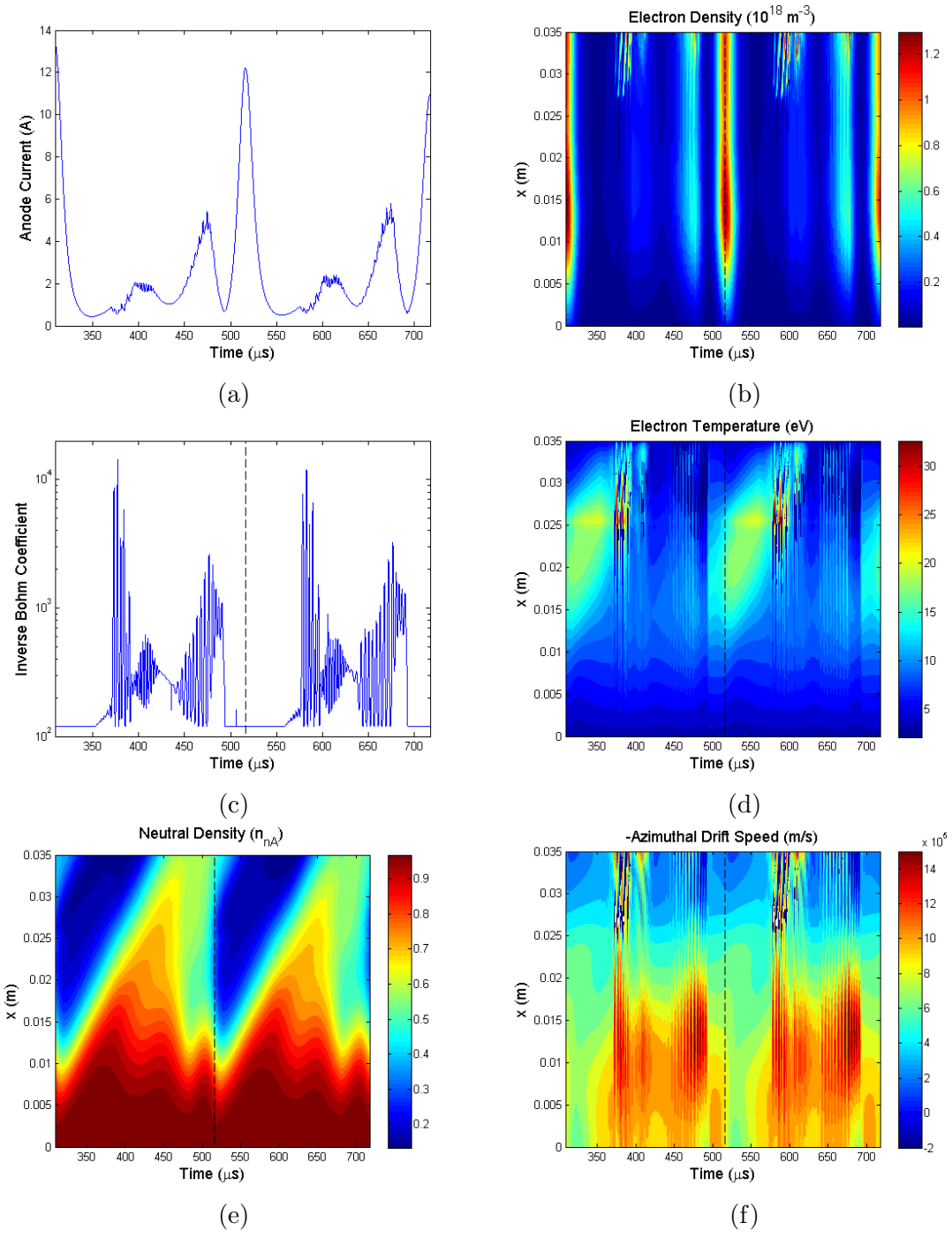

Figure 5-41: Model results for 220 V, 5 mg/s and γ_t=9 MHz. (a) Anode current (b) Plasma density profile (c) Inverse Bohm coefficient (d) Electron temperature profile (e) Neutral density profile (f) Azimuthal electron speed profile versus time. Dashed line indicates location of main current peak

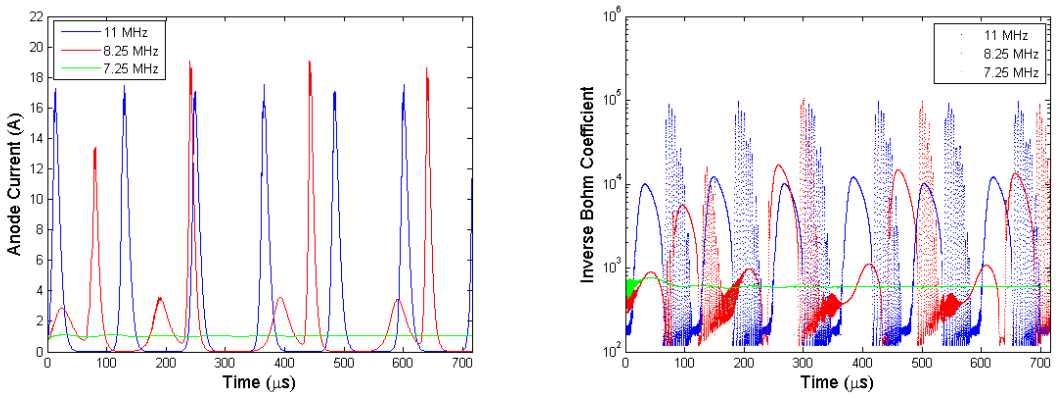

(a) (b)

Figure 5-42: Model results for 260 V, 5 mg/s and various values of γ_t. (a) Anode current (b) Inverse Bohm coefficient versus time

An anode current waveform with a single stunted peak is also obtained at a 300 V anode potential, with a 5 mg/s flow rate and a turnover rate of 7.25 MHz. The current is similar in appearance to Fig. 5-43a, however the stunted peak occurs closer to 60% into a period, rather than 75%. The time averaged current is 2.73 A with a peak-to-peak frequency of 5560 Hz. The current waveform approaches the normal, singly-peaked behavior at γ_t=8.25 MHz, with a DC current of 2.26 A and a peak frequency of 9460 Hz, though every second peak is gradually diminishing in amplitude and shifting further in time from the preceding peak. The progression of anode current and inverse Bohm coefficient waveforms towards a damped solution at a low turnover rate is shown in Fig. 5-44

A mechanism by which the turnover rate might decrease as the anode voltage increases in not presently obvious, however we note that Scharfe found a lower turnover rate to be necessary at higher voltages in order to best fit experimental profiles [189]. Scharfe's hybrid model best matched data at 160 V when a turnover rate of 10 MHz was used, while at 200 V a turnover rate of 6.25 MHz was more successful. A similar 37.5% decrease of the turnover rate in our 1-D model from 8.25 Mhz at 260 V to 5.16 MHz at 300 V would result in a mode transition from a high current, stunted peak, breathing mode to a low current, stable spiral solution.

The comparison of our model requiring a drop in turnover rate with voltage to

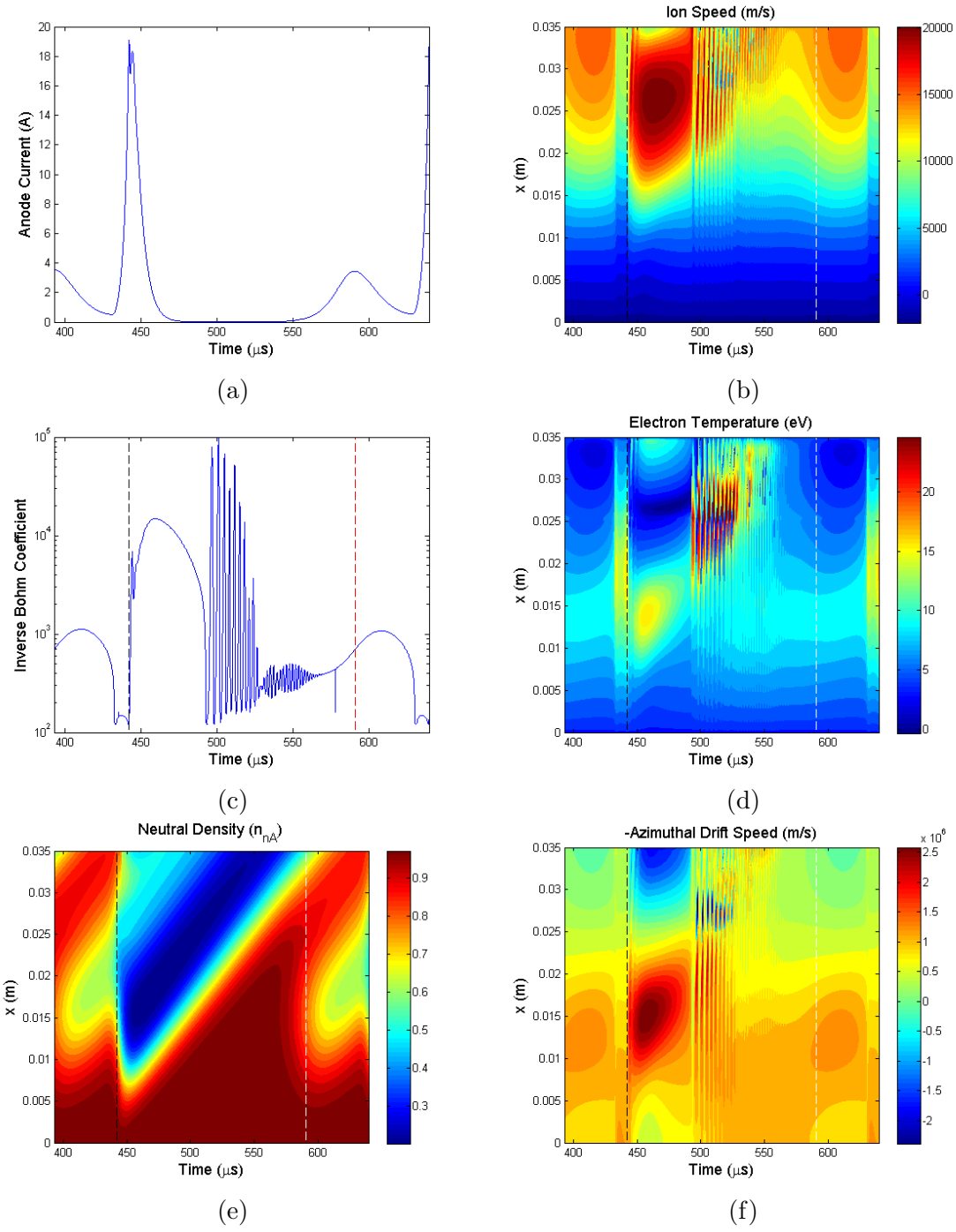

Figure 5-43: Model results for 260 V, 5 mg/s and γ_t=8.25 MHz. (a) Anode current (b) Ion speed profile (c) Inverse Bohm coefficient (d) Electron temperature profile (e) Neutral density profile (f) Azimuthal electron speed profile versus time. Dashed line indicates location of main current peak

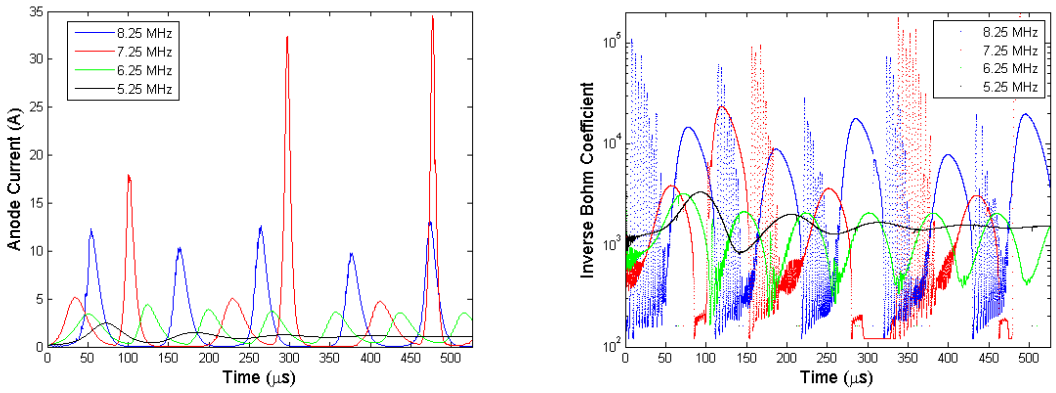

(a) (b)

Figure 5-44: Model results for 300 V, 5 mg/s and various values of γ_t. (a) Anode current (b) Inverse Bohm coefficient versus time

the somewhat similar result of Scharfe et al is not intended to suggest that a certain physical situation ought to exist. It is stressed that the reported turnover rates are just fitting parameters for an empirical model within a highly simplified set of equations used to describe fundamentally 3-dimensional processes. The corroboration in trends is meant only to signify that the present model does not discredit the hypothesis that high voltage transitions to low, quiescent anode currents may be due to a quenching of anomalous transport.

It should be noted that results were sometimes difficult to obtain with the quench model described above, as certain inputs of flow rate, voltage and turnover time would lead to a simultaneous runaway in the inverse Bohm coefficient and the azimuthal flow shear. It was found that results might diverge quickly when simulations were initialized with unrealistic conditions and so profiles from the constant Bohm coefficient runs described in previous sections were used. Also, in practice, the Bohm coefficient was not allowed to increase all the way to α_{B0} in low shear situations, but was instead capped at a maximum value of 1/120. High Bohm coefficients allow far too much electron conduction to the anode in this very basic model. The choice of 1/120 as a maximum is somewhat arbitrary, however, and was adopted to allow some leeway for the Bohm coefficient to increase past the normal 1/160, without going so far as to allow a short circuiting of the electron flow.

5.3.10 Ion Transit-Time Instability

The transit-time instability appears fairly common in Hall thruster simulations of both 1D fully fluid [12] and 2D hybrid-PIC types [182, 194]. Much mention of the transit-time instability is made in early Russian Hall thruster experiments [168, 195, 196] where it is described as a broadband fluctuation centered about a frequency related to the ion velocity leaving the accelerating channel divided by the length of the channel (rough inverse of the time for an ion to trasnsit the channel). In [195] they are described as turbulent potential oscillations in the discharge chamber of up to 30% of the anode voltage which occur synchronously throughout the channel volume, but are of much smaller amplitude in the low magnetic field near the anode. In [196] a dispersion relation for a cold (i.e. neglecting pressure terms), collisionless plasma with steady components of axial ion velocity, azimuthal electron drift and radial magnetic field is derived for frequencies between the ion cyclotron and electron cyclotron frequencies. The dispersion in the limit where the azimuthal drift speed is much greater than the ion speed is noted to predict frequencies and stability characteristics resembling those of the transit-time instability measurements.

These instabilities appear less prevalent in modern Hall thruster studies though several fairly recent experiments call upon the transit-time instability as a possible source for measured low-frequency, axially propagating fluctuations [197, 198]. Some recent literature has also been to devoted to improving its analytical framework [182, 199].

In [199] a WKB analysis is performed on the high frequency modes of a 1D plasma problem resembling the near-exit acceleration region of a Hall thruster which finds that quasineutral ion acoustic waves (which are superimposed on a standing discharge current wave) are amplified as they propagate downstream for a high enough ion-to-discharge current ratio. The analysis is also used to show how plasma potential oscillations may appear as standing waves in the upstream region despite perturbations in the plasma density and ion velocity having a phase speed equal to the time averaged ion speed decremented by the Bohm speed. A flaw in the analysis of [196]

is demonstrated to lead to an ambiguous stability relation.

Fernandez *et al* derive a new dispersion relation to describe the transit-time instability observed in their 2-D hybrid-PIC Hall thruster simulations based on the 1D two-fluid equations which, when neglecting electron pressure, predicts a resistive mode with a phase speed roughly equal to the axial ion speed [182]. The growth rate of the resistive mode is proportional to $\mu_{eff}^{-1/2}$, where μ_{eff} is the effective cross-field mobility of electrons, though perturbations evanesce when a function inversely proportional to the mobility is sufficiently high in comparison to the axial plasma species drift speeds. Including pressure effects results in the prediction of an ion acoustic wave which is unstable for the branch with phase speed $v_i - c_s$, as in [199], though the included results of the 2D hybrid simulations suggest the instability is more closely reproduced by the stable $v_i + c_s$ branch of the dispersion. It is also shown that the addition of a constant ionization rate to the fluid equations leads to an enhanced growth rate for the resistive mode, with ionization effects becoming prominent at low frequencies.

Interestingly, the dispersion relation derived by Chable and Rogier [161] in an attempt to define a stability criterion for Hall thruster breathing modes is identical to the resistive mode derived by Fernandez (in the limit of $v_{ez}/v_{iz} << 1$). The derivations run the same course, as both neglect ionization, which for Chable and Rogier is motivated by a linear stability analysis which suggests their 1D model only requires (and always requires) a perturbed electric field to become unstable. The linear model is assumed to describe the full nonlinear system well because of the similar trends found in positive linear growth rates with the occurrence of breathing mode cycles in the full solution when model parameters such as anode voltage, magnetic field strength and neutral flow speed were altered.

Many of the limit cycles presented above are also seen to contain ion transit-time oscillations, while none of the damped solutions exhibit them, suggesting the stability envelope for transit-time fluctuations (at least that predicted by the present crude model) might easily be very similar to that of the breathing mode. They appear, however, to be phenomenologically quite different with one requiring large swings in neutral and plasma densities and the other relying mainly on a strong impedance of

electron flow to the anode. A more focused study is required to properly assess the connection between the two instabilities.

Transit-time fluctuations are highlighted from our simulations at 180 V and 8 mg/s in Fig. 5-45, where the convective ion flux oscillations are shown along with their dispersion. The dispersion plot was obtained by first using a piecewise cubic spline interpolant to resample the ion flux data at regular time intervals. The 2D FFT of the evenly spaced cubic spline contour is taken using a built-in Matlab function and the amplitude plotted.

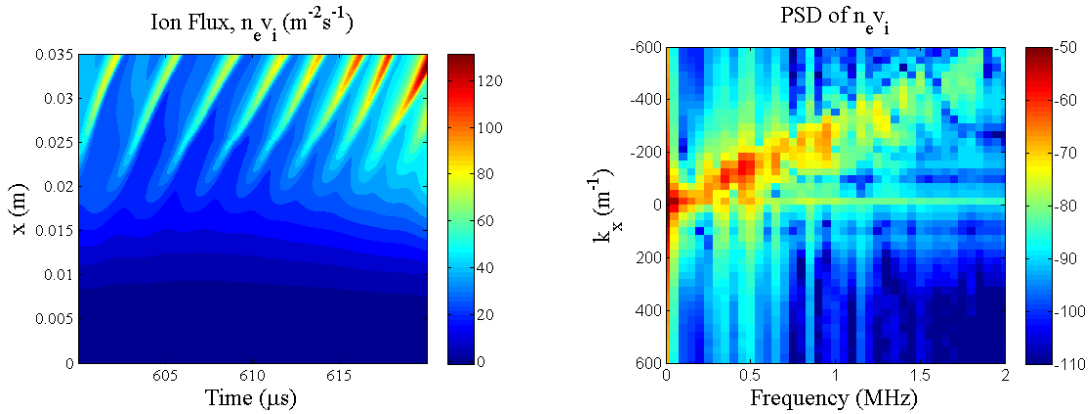

(a) (b)

Figure 5-45: Model results for 180 V, 8 mg/s highlighting the transit time oscillation. (a) Ion flux (b) Dispersion of ion flux oscillations

The peak frequency of the oscillations in this case is around 0.4 MHz. Figure 5-45b shows a clearly propagating wave with a group velocity ($\partial\omega/\partial k$) of approximately 3.3 km/s (this is also the phase velocity for the 0.4 MHz mode), which is on the order of the isothermal ion sound speed.

5.3.11 Applicability to the DCFT

The preceding results indicate that an anode current bifurcation is found, with the imposition of certain conditions, when an axial shear of the azimuthal electron flow is introduced to decorrelate turbulent flow and reduce collisionless cross-field transport. This bifurcation shares several qualitative similarities to the one measured in the DCFT, including a cessation of the breathing mode oscillations accompanying a sharp

drop in the steady component of the anode current as well as the existence of an intermediate state in which at least one abbreviated current peak is obtained prior to the main spike.

A question remains as to whether, though producing strikingly similar results, the present model, derived for an annular device with purely radial magnetic fields, is applicable to the DCFT. The differences are obvious, with no inner wall to bound the plasma radially, non-negligible azimuthal effects, a magnetic field which changes from largely radial to fully axial at different cross-sections, and an extreme radial gradient in field strength, to list a few. There are, however, some important aspects of similarity which allow some interpretation of the Hall thruster results to the cusped-field thruster.

The axial mobility of electrons is large both immediately upstream of the exit separatrix and upon approach of the anode in the DCFT. In this manner, the exit magnetic field cell (from point cusp to point cusp) may resemble a Hall thruster in terms of a cross-field mobility profile which experiences a minimum near the exit, but increases upstream of this point. Each magnetic cell upstream of the exit exhibits some axial impedance to electron motion, though LIF and emissive probe data suggest it is substantially less than the impedance of the exit cusp [6, 8]. The axial mobility of electrons is low for an electron entering the discharge chamber, since the path from cathode to exit separatrix requires the perpendicular crossing of a fairly strong magnetic field.

The main result of the simulations is a description of the key components needed to create a sustained breathing mode with a magnetic field mediated electron flow. Though the nature of electron transport may be different between the two devices the source of the impediment is always the magnetic field and the source of the oscillation a substantial, periodic depletion of the neutral propellant. The conclusion that electron mobility between the electrodes must be high (in a relative sense) to create an ionization avalanche strong enough to maintain a predator-prey type cycle is not expected to be limited to Hall thrusters.

5.4 Chapter Summary

This chapter presents a derivation of the equations and solution methods used for an unsteady, 1-D, three fluid (ion, electron, neutral) model of a Hall thruster which essentially follows the simplified model presented by Barral and Ahedo [12]. This particular model is chosen for its simplicity, allowing us to examine the routes to instability, with minimal interdependencies to sort through, using an already established method.

The results of a parametric scan of input conditions reveals several very general trends. The location of the region of high ionization frequency (which is the product of neutral density and an electron energy function) is set almost solely by the magnetic field, and is quite surprisingly observed to undergo a fairly low amplitude ($\sim 50\%$), nearly standing fluctuation during highly peaked current oscillations. The lack of a convective component in the ionization frequency (aside from that created by ion transit-time instabilities) during a breathing cycle in which both the neutral density and electron temperature are the most clearly convected parameters suggests an interesting balance between the two constituents of the ionization frequency.

A stable limit cycle solution can be obtained through essentially any parametric change which enhances the ionization rate. In all limit cycles the peak density and peak temperature are offset at the start of the exponential current growth, with intense upstream ionization causing the density peak to migrate towards the temperature peak. The motion of the density peak is joined by an increase in the electric field strength as continuity is maintained between a diminishing downstream and rising upstream plasma density perturbation, which further heats electrons and sustains ionization past the peak in anode current. If the depletion of neutrals is strong enough the ionization will abate and allow a complete refill of the neutral population in the chamber to its state prior to the ionization avalanche.

The various parameters which when raised allow the approach of a limit cycle solution in the presented model are the inlet neutral density (a combination of neutral speed and mass flow rate), anode voltage (up to the extent of the model's applicabil-

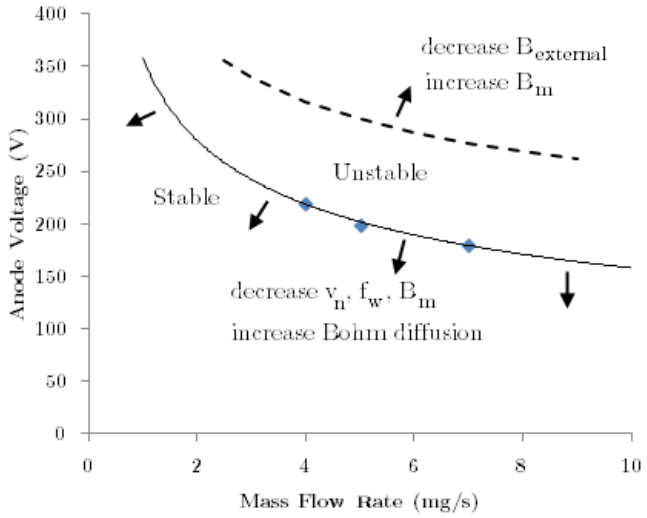

Figure 5-46: Notional stability map showing regions where limit cycle solutions are obtained (marked unstable). Dashed line indicates high voltage quenching of the breathing mode which may be an artifact of the simplifications in the model. Arrows suggest how the unstable region is broadened by the parametric changes listed.

ity), Bohm diffusion, and inverse wall collision frequency. Each of these parametric changes leads to the peak plasma density starting each exponential current growth period further downstream as the limit cycle is approached (closer to the peak electric field, the location of which is largely set by the magnetic field profile), while the peak electron temperature starts each cycle in the same general location.

A summary of how changes in the different model parameters affect the excitation of self-sustained breathing modes is made schematically in the notional stability map of Fig. 5-46. The solid line in the figure shows where normally damped modes become unstable in anode voltage-flow rate phase space. Parametric changes which expand the region of unstable solutions are listed in the figure, though the trends are not actually so monotonic. For example, an increase in the anomalous diffusion coefficient, α_B, will at first lead to limit cycles at conditions (such as 180 V and 5 mg/s) which are normally damped, but when α_B is high enough the anode current once again damps to a stationary value (perhaps due to an effect analogous to the high voltage, high current damping seen at 300 V and 5 mg/s). As the wall collision frequency coefficient drops to zero, on the other hand, we see no damped solutions

(other than the trivial case of no anode current) at any flow rates for a 180 V applied potential (though a stable focus can be found at $f_w = 0$ if α_B is sufficiently high or low). The values plotted in Fig. 5-46 are only loosely based on the results obtained here, as the purpose of the figure is purely to convey typical trends and not any quantitative predictions.

Interestingly, when the magnetic field is set to peak downstream of the channel exit or close to the anode a normally self-excited breathing mode is found to damp out. The upstream motion of the magnetic field is also found, unexpectedly, to lead to a decrease in the breathing frequency. Perhaps this effect is due to the ionization region effectively ending at the channel exit regardless, while its upstream boundary shifts with the peak magnetic field, thus extending the refill portion of the cycle when the maximum field is closer to the anode.

The strong dependence of the solution type on the degree of anomalous diffusion inserted in the model led to the idea that a bifurcation from a high current limit cycle to a low current stationary solution may be due to a self-consistent change in the transport characteristics. A self-consistent model of anomalous transport is of course not currently feasible, however there has been success in predicting bifurcations in plasma confinement due to turbulent shearing in the fusion community [14]. We have shown that an adaptation of turbulence shear models, which have been applied to Hall thrusters in the past [189], to the present 1D model can not only lead to the desired anode current bifurcation (in which high $V_a/\dot{m}_a$ leads to a sharp drop in DC anode current and current oscillations), but also, unexpectedly, reproduce the behavior of transitional waveforms observed in the DCFT. These transitional current traces, shown and described in Sec. 4.4, are marked by one or more aborted current peaks preceding the main burst in ionization.

Though the appearance of stunted peaks in the anode current waveforms obtained with the shear model is forwarded as a possible explanation for similar waveforms found in the DCFT, one might wonder if they are also found in SPT's, the devices which are actually being modeled here. There are in fact some anode current traces in the SPT-100 literature which bear some resemblance to those shown here (the 450

V condition on pg. 9 in [166], Fig. 6c in [4]), where the current reaches a small peak just after a minimum, but subsides for a period before a stronger current spike appears.

Another interesting feature of the simple 1D model demonstrated here is the appearance of ion-transit time type instabilities in a very similar parametric envelope as the high amplitude breathing mode. The conditions for the excitation of transit-time instabilities found in the literature appear to generally match those demonstrated here to lead to periodic solutions for the breathing mode: specifically, a high degree of ionization [199] and a high (but finite) electron cross-field mobility [182]. A similarly broad spectral peak in the DCFT anode current waveform (with an order of magnitude higher frequency than the fundamental breathing mode) appears at conditions close to the LC-to-HC mode transition, lending it some resemblance to the transit-time fluctuation found in Hall thrusters [195].

Chapter 6

Conclusions

In sum, there is far more left unknown about the workings of this device than there is understood, but some headway has been made in deciphering the underpinnings of its odd plume structure and sharp changes in operational mode. Some of the main conclusions drawn as to the nature of the fundamental phenomena are reiterated below.

6.1 Cusped Field Thruster Plumes

It is believed that the work described here answers the question of why the hollow plume common to cusped field thrusters is focused to a high divergence angle (at least in the case where the near-exit magnetic field is strong). This is due to the natural curvature of the exit separatrix when a pair of alternating polarity, permanent magnets is used to create a ring cusp. Techniques for reducing this curvature have been forwarded and one of these techniques (the external EM) is demonstrated to lessen divergence.

The potential structure has also been experimentally shown to largely follow the exit separatrix when the magnetic field is strong there. The on-axis, anode voltage normalized, floating probe potential experiences a large drop a roughly constant distance from the separatrix regardless of operating conditions. As the thruster is brought to conditions closer to the bifurcation into HC mode the floating probe po-

tential in the near field rises by several volts. This effect may be related to cathode coupling with the anode [105], with a higher near field potential belying a more difficult coupling.

The upstream motion of the on-axis potential profile when transitioning from LC to HC mode is also noted in LIF measurements by MacDonald *et al* [6] and may have some bearing on the more 'filled-in' structure of the HC mode plume. Their may also be a link to the bifurcation mechanism, discussed further below, which allows ionization further upstream as well. The precise nature of the increased ion flux on-axis in HC mode is not currently clear and may require further insight from numerical models before some resolution can be reached.

The reason for the hollow nature of the plume has yet to be rigorously validated. It is believed by the author that the strong magnetic field in the exit ring cusp is likely to play a dominate role. Electrons are funneled into the ring cusp, speeding by the null point on-axis then slowed in their motion along the field line by the strong magnetic mirror, while low energy ions are largely constrained electrostatically to follow. Perhaps an increase in ionization upstream of the exit separatrix follows the upstream motion of the potential structure which occurs as the exit magnetic field is weakened, with created ions becoming supersonic as they stream, on-axis, through the point cusp between C2 and C3, staying at a low angle from the thrust axis as they become a part of the plume.

6.2 Power Loss

Internal probing and thermal imaging of the thruster have been used to characterize the plasma heating of the discharge chamber walls. The dielectric is found to reach temperatures between about 100 and 300°C for power levels below 200 W, while the graphite anode is generally hotter by as much as 100°C. The amount of power deposited by the plasma on the anode appears to jump up in relation to the anode power when the thruster transitions into HC mode, with temperature profiles along the length of the cone exhibiting a stronger gradient (which points towards the up-

stream end). The increased gradient in the temperature profiles along the chamber wall in HC mode is thought to be at least somewhat attributable to reflected radiation from the anode, but may also be an indication of an increased proportion of ionization occurring internally, near C1 and C2. The portion of the anode power deposited near C2 and, to a lesser extent, C3 appears to increase with anode voltage when in a low voltage HC mode.

Estimates based on the thermal data presented here place the power lost to the walls at upwards of 30% of the input power. When combined with efficiency data obtained from other sources, this leaves roughly another third of the input power to be lost to inelastic collisions (excitation and ionization) which is a fairly high fraction, suggesting the electron temperature may be low in a large portion of the discharge.

Since the main potential drop occurs near the exit, the region of peak electron temperature may be expected to occur just upstream causing an area of high ionization somewhere between C3 and C2. The electric field appears to be fairly small internal to the discharge chamber, so electrons moving upstream of the main ionization region are likely relatively cold. A combination of very high neutral densities and a cold, dense electron population upstream of C2 may be the cause of the posited large inelastic losses. This is all very speculative, however.

6.3 Discharge Oscillations

Anode current oscillations in the DCFT have been found to be consistent with the breathing mode observed to dominate the power spectra of Hall thrusters. The frequency of these oscillations is demonstrated to increase with anode mass flow rate, EM current[a], and cathode distance from the beam edge, but appears to decrease slightly as the discharge voltage is raised.

A higher frequency oscillation, near 30 kHz for typical conditions, has also been observed in the low current mode of operation. This mode appears to share the spectral characteristics of the ion transit-time instability captured by the 1-D fluid code,

[a]EM current shifts exit separatrix upstream and strengthens external field; see Appendix A

though experimental verification of their association is required. In both the fluid code and experiments on the DCFT this oscillation becomes excited at operational points near those corresponding to the high amplitude breathing mode excitation. The similarity of excitation mechanisms for breathing and ion transit-time instabilities may be behind the results of Chable and Rogier [161] who find a low frequency (20 kHz) linearly unstable mode with high growth rates at the same general conditions which lead to non-linear breathing-type oscillations. The dispersion relation derived for the linearly unstable mode matches that of the resistive mode found by Fernandez *et al* to describe the ion transit time instabilities occurring in their hybrid-PIC Hall thruster code [182].

6.3.1 Suggested Bifurcation Mechanisms

In parametrically studying the excitation of non-linear breathing modes through the 1-D fluid code a general trend has been encountered. Essentially, any change promoting an enhanced net ionization rate may eventually lead to a stable limit cycle oscillation, provided there is some mechanism, such as the spatial separation of regions of high ionization frequency and high plasma density growth rate [180], which allows for a complete enough exhaustion of the neutral propellant to prevent collapse towards a spiral type solution.

The general excitation mechanism described does not in itself point towards a bifurcation in the time-averaged anode current however. For example, the breathing mode can be damped by lowering the anode flow rate, as found in the DCFT, but the DC anode current does not exhibit a sharp jump at the transition and higher anode voltages require even lower flow rates to damp oscillations, the opposite of the trend in the DCFT.

One method proposed here for the current bifurcation is a change in the character of electron cross-field transport. It was clear from the outset that an increase in the anomalous transport frequency would excite high-amplitude breathing oscillations in the 1-D simulations, so it was no surprise that by adding a semi-empirical model whereby a shear in the azimuthal current would lead to a non-linear decrease in

transport we could force a normally stable breathing mode condition to damp towards a steady state. The surprising outcome was that the introduction of the shear model also predicted the gradual suppression of one or more current peaks in a given cycle as the point of total oscillation damping was approached, in direct agreement with experiments on the DCFT.

The 1-D model reveals a possible scenario for the development of one or more stunted peaks into a large current spike: as the current initially begins to rise the gradients in plasma properties increase (this includes the azimuthal flow shear) until the plasma growth is eventually choked off by the sharp drop in turbulent transport. The azimuthal shear drops as the plasma gradients become smoothed out during plasma decay until turbulence becomes high enough to allow electrons to again access the region of peak ionization frequency. Since the plasma density is still significantly higher than it was at the beginning of the cycle the ionization avalanche begins at a faster rate and the eventual current peak is higher with such a cycle repeating until the current growth out-paces the shearing effect enough to completely ionize the neutral background, creating a much higher spike in current followed by a near complete extinguishing of the plasma.

In the paradigm suggested by the 1-D model results, the bifurcation occurs because of a sharp drop in electron transport as either the anode voltage is increased or the anode flow rate is decreased. Unfortunately, not much is currently known about the mechanisms for axial electron transport in the DCFT, making it difficult to assess (as opposed to speculate) how parametric changes might affect electron mobility. The region from the cathode to the exit separatrix is marked by cross-field electron transport, for which near-wall-conductivity and turbulence-induced transport are the leading candidates (the neutral densities are extremely low in this region, making classical diffusion unlikely to be a dominant effect) at this time. The strong electric field near the exit of the DCFT certainly drives an azimuthal electron flow, so that the azimuthal-shear-based suppression of turbulence in this region is a possible driver for the anode current bifurcation.

The internal ring cusps are suspected to have a high degree of azimuthal electron

current shear, due to the change in direction of density gradient and electric field driven drifts at the separatrix, as both of these forces drive electrons away from the center of the cusp to maintain quasineutrality with the unmagnetized ions. If turbulent transport is present in these regions then shear-based suppression may play a role in the internal plasma dynamics as well. The C1 and C2 regions are expected to have high enough neutral densities for classical diffusion to be a factor (perhaps dominant) and it is also possible that the plasma bypasses the cross-field transport problem at the internal separatrices by instead leaking through the magnetic nulls. The azimuthal flow shear itself may lead to a slip-stream (or 'diocotron') instability [201] which could also play a role in the plasma transport here.

Ion acoustic instabilities have been measured on either side of a line cusp in multidipole devices [71, 72] with frequencies from tens to hundreds of kHz. The ion acoustic instability is driven unstable by electron drifts (identified as gradient drifts in the cases cited) which exceed the ion sound speed when $T_e >> T_i$. This instability has been linked to the anomalous transport of electrons out of the field-free region of a spindle cusp device, leading to a Bohm-like diffusion with $\alpha_B \sim \sqrt{m_e/m_i}$ (which is 1/490 for xenon) [202]. The drift modified ion acoustic instability is thus another possible driver for electron diffusion in the DCFT.

The idea of the bifurcation being tied to a change in cross-field transport may be bolstered by the measured trends in the mode transition with cathode coupling: the high amplitude breathing mode is excited when the cathode is further from the ion beam edge or when the keeper current is low. Raitses *et al* have shown that increasing the keeper current eventually leads to the complete damping out of low frequency discharge current oscillations in both an annular Hall thruster (where the oscillation frequency is 20 kHz) and a CHT (where oscillations of 4 and 10 kHz are measured) [153]. Raitses also measures a decrease in the plasma potential at the CHT exit when the keeper current is raised (which is shown to occur on the DCFT in Ch. 3) and estimates that the cross-field mobility of electrons is cut in half when the thruster transitions from the mode of operation marked by high discharge current oscillations to a 'quiet' mode with high keeper current (which in this case appears

to be due to the damping of a spoke mode instability [155]). The cathode coupling may also be the reason why the HC mode is eventually excited at high EM currents (see Fig. 3-11), where increasing I_{mag} puts the cathode on a flux line of increasingly high vector potential, as does physically moving the cathode further from the thruster axis. The increase in EM current is also shown in Ch. 3 to lead to an increase in the near-field potential of a floating emissive probe.

An early idea of ours for how the anode current bifurcation might occur was based on the assumption that high anode voltage or low anode propellant flow rates would lead to high electron energies near the exit separatrix resulting in the main ionization occurring in this region. It was hypothesized that the relatively low neutral densities near the exit would not be enough to facilitate the large swings in ionization which mark the high amplitude breathing oscillations. As the voltage was decreased or flow rate increased the electron energies near C3 would decrease, reducing ionization there and perhaps allowing higher energy electrons to leak towards the internal cusps (C1 and C2) where the neutral densities are much higher. The crux of the hypothesis was that an increase in the internal ionization would lead to even lower densities at C3, lowering the ionization there even further and amplifying the dominance of the internal ionization, with this feedback mechanism leading to the bifurcation in modes. The high neutral densities expected near the upstream cusps would then allow the ionization avalanche necessary for a sustained breathing mode. A switch in the location of the main ionization region from C3 to C2 (or C1) during the transition from LC to HC modes in this heuristic picture may be supported by thermal measurements of the insulating cone shown in Sec. 4.5, but there is really no evidence otherwise to support this speculation. The location of the main ionization region is actually unknown for any operational mode at this time, with attempts to probe inside the discharge chamber being met with extreme perturbations to the thruster state and the physical well-being of the probes.

Another alternative explanation for the bifurcation is the existence of two roots for the electron temperature which lead to the same global power balance. The supplied anode power is mainly spent on inelastic collisions (ionization and excitation), plasma

loss to the walls and anode, and exhausting an energetic ion beam. Excitation losses become exponentially large as the electron temperature is lowered below around 5 eV, while the power deposited by electrons on the chamber walls grow rapidly at high temperatures (due to reduced confinement when the wall emits a large secondary electron current as well as the broadening of cusp leak widths at the walls) of around 20 eV, with the result being an equal total power loss (sum of inelastic losses and wall/anode losses) can be obtained with the plasma in two very different states. The low electron temperature state (where excitation losses dominate) is unstable however, since an increase in the electron temperature would lead to a decrease in the total power lost, so there is more power available to further heat the electrons, allowing the perturbation to feed on itself until the stable high temperature state (where wall losses dominate) is obtained. Though this consideration shows how the plasma may have two distinct modes, with one being unstable, its precise manifestation in the DCFT is unclear. It is noted that inclusion of the temperature dependence in the ion production cost term in the unsteady 1-D model appears only to shift the location of the stability envelope without changing its shape, in a manner similar to reducing the wall collision frequency coefficient for example.

6.4 Recommendations for Future Work

A comparison of magnetically shielded designs with flattened separatrix designs is needed to elucidate their differing effects. The clear drawback to using an external electromagnet or some other method to turn the exit separatrix in by increasing the external field strength is the measured drop in propellant utilization efficiency. A hollow plume is not intrinsically undesirable, however, with an idealized hollow cylindrical beam even allowing for some internal entrainment of plasma particles (e.g. charge-exchange ions caught in the potential well inside the beam) in the far plume. The low propellant utilization in the DCFT may be its largest source of inefficiency and if this can be remedied by a weaker external magnetic field (as is hinted at by the external EM experiments) a shielded configuration ought to be explored.

Faraday probe measurements of the DCFT plume described here demonstrate that a reliable measurement technique for determining the on-orbit structure of the plume is currently lacking for this type of device. The background pressure of the vacuum vessel is shown to have a noticeable effect on thruster operation and plume topography, with non-monotonic trends likely a byproduct of the complex potential structure in the DCFT plume. A focused study of the effects of background neutrals on a cusped-field thruster, perhaps aided by a numerical model such as AQUILA, is a possible avenue for future research. If instead the plume is made to resemble that of a Hall thruster then previously developed methods may be applied for correcting ion flux measurements in the plume [24].

Characterization of thruster oscillations has so far concentrated on the HC mode, where fluctuations are at their highest. However, there is a clear need for identifying the 20-100 kHz feature found in the LC mode, with some interesting spectral features also cropping up at lower frequencies. A link is made here between the 20-100 kHz modes and the transit-time fluctuation, however there has not yet been an attempt to experimentally characterize this mode. The 1-8 kHz oscillations found in LC mode are also far from being fully cataloged, though high speed camera footage suggests these share the standing wave pattern of brightening and dimming seen for the breathing oscillations in HC mode.

Time-resolved measurement of plasma fluctuations near the exit of the thruster, though difficult, is essential towards the validation or clarification of the bifurcation mechanism proposed here. One technique, which may be well-suited to the DCFT, is the use of optical emission spectroscopy to try to detect any changes in phase shift of emission intensity with respect to anode current waveforms using a high speed PMT and amplifier. The emission from the DCFT appears visually to be conveniently stratified to regions of higher radial distance from the thruster axis for each downstream cell. In this way, azimuthal variations detected at a 3 cm radius, by axially directed optics, may be reasonably expected to be due to fluctuations near the 3rd ring cusp, variations at a 2 cm radius would likely be due to emission from near the 2nd ring cusp and fluctuations at a radius of 1 cm more nearly due to radiation

from the most upstream ring cusp. This is a drastically oversimplified picture of the optical emission from the thruster, but it is believed that the extraordinary optical access afforded by the divergent discharge chamber shape can be utilized in some manner similar to that just described.

The convenient optical stratification of the internal plasma may also be more easily used as a steady state diagnostic, to measure changes in the broad spectral characteristics of each luminous ring individually. A comparison of emission from neutral atoms to emission from ions allows a simple, though rough, comparison of changes in the relative degree of ionization in the different regions as thruster conditions are varied. A collisional radiative model, or perhaps even a coronal equilibrium analysis, may provide some information on the relative temperature. In this manner it is possible that one could verify whether or not the region of ionization is shifting at all with changes in the thruster control parameters.

One question a reader may have taken through this entire work is: why do we use 3 ring cusps, when 1 or 2 or 20 might work as well or better? Obviously, this question is not regarded in the present work which seeks insight into why the DCFT operates the way it does without going into the kind of rapid prototyping which might provide a quicker (possibly more expensive) answer to the question of how to make a better DCFT. The question, of course, is an important one and it is strongly suggested that a study be performed which seeks its answer.

A thorough assessment of the effects of changing the number and relative strengths of the ring cusps can be made using a series of electromagnets. For example, 4 solenoids can be used to create a thruster with anywhere from 0 to 3 ring cusps with various permutations of cell length and cusp strength. The main difficulty in creating such a versatile testbed is the large number of amp-turns (and thus large solenoid size) necessary to create internal field strengths comparable to those found in the DCFT. It may be possible to create a somewhat scaled-up cusped-field thruster to accommodate the large electromagnets, though there is no assurance that the important physical processes will scale up with the thruster.

Appendix A

Magnetic Field Simulations and Measurements

Simulated magnetic field topographies are found using the ANSYS Maxwell 2D Student Version, with user input B-H curves for the SmCo magnets provided by the magnet manufacturer (Dexter Magnetic Technologies). The results of simulations at various values of applied EM currents are given in Figs. A-1 & A-2, focusing on the near-exit region where the electromagnet has an observable effect.

The magnetic field was measured using an AlphaLabs Inc. DC Gaussmeter and positioned using the 3-axis system used for probe positioning with the thruster in its experimental condition in ASTROVAC. The probe sensor area for the Gaussmeter is 4 mm by 1.5 mm with the uncertainty in probe angle being the largest contributor to errors in the measurements. Measured field strengths and flux line topology are shown in Fig. A-3 for 0 A, 10 A and 20 A supplied to the electromagnet. The expected effect of increased coil current reducing the convexity of the separatrix near the thruster axis is clearly verified by the measurements. Flux lines are interpolated from the measurements using Tecplot 360 software.

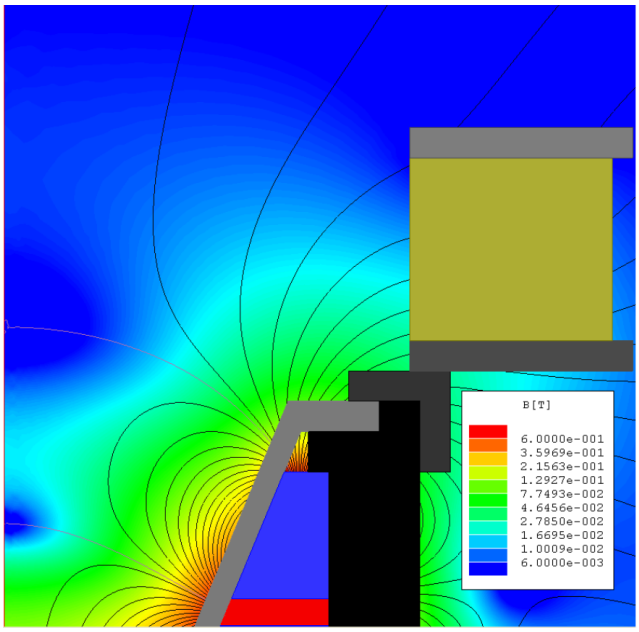

(a)

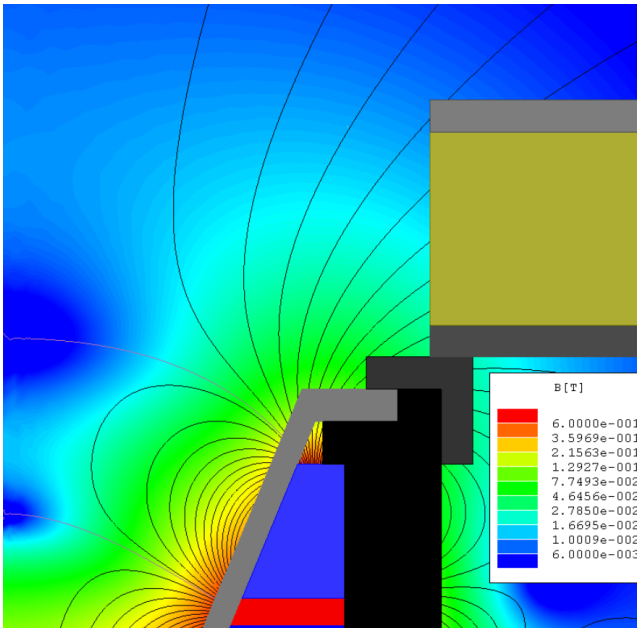

(b)

Figure A-1: Maxwell 2D simulations of DCFT magnetic field with external EM current of (a) -10 A (b) 0 A

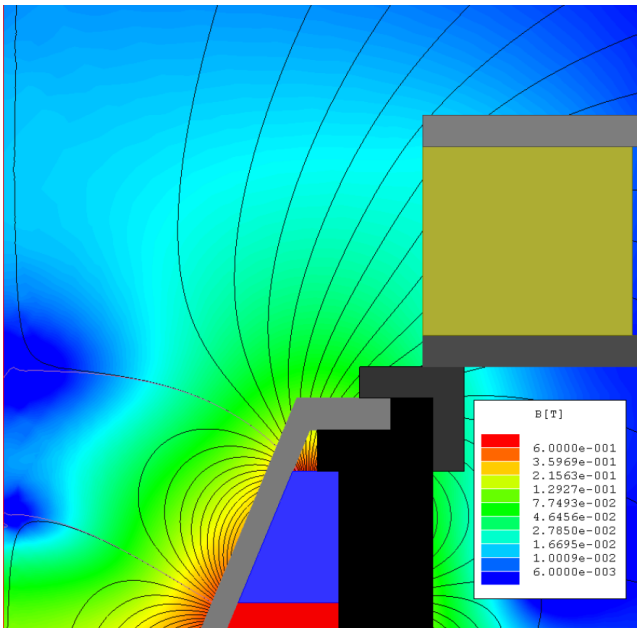

(a)

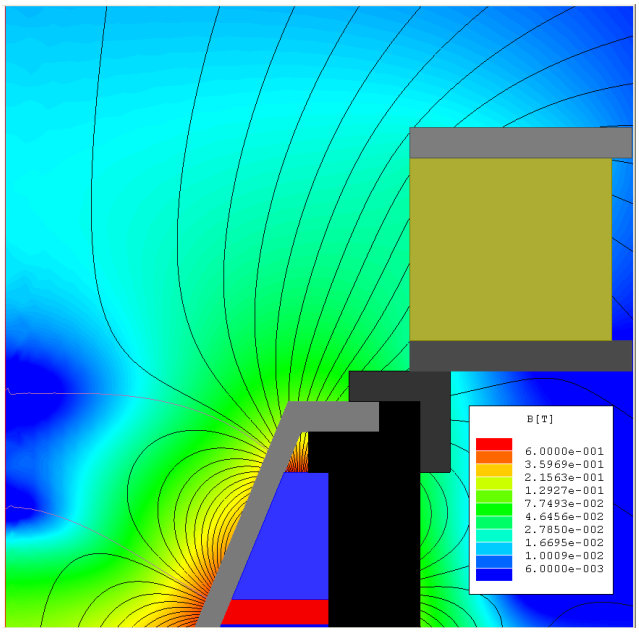

(b)

Figure A-2: Maxwell 2D simulations of DCFT magnetic field with external EM current of (a) 10 A (b) 20 A

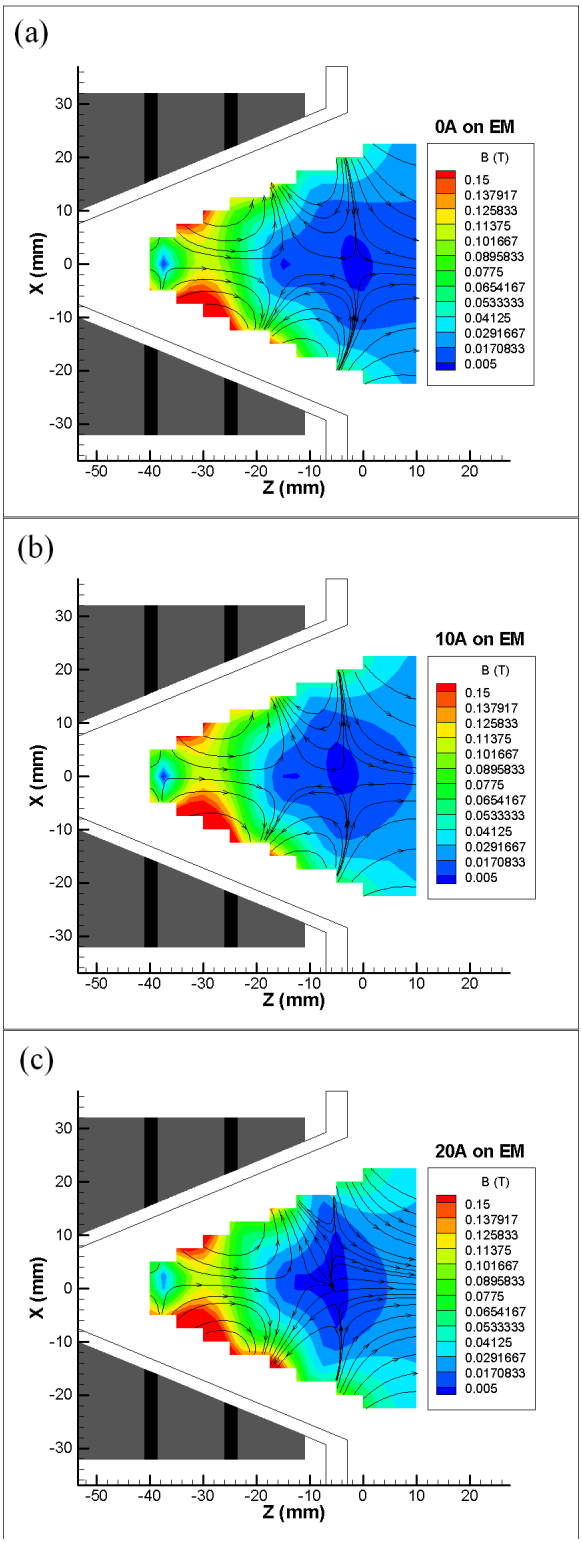

Figure A-3: DC Gaussmeter measurements on the DCFT outfitted with electromagnet. Field strength and flux lines are shown in (a) with 0 A (b) 10 A and (c) 20 A supplied to the magnet. The axial distance, Z, is zero at the exit plane defined by the edge of the cap which retains the BN insulating cone.

Appendix B

Cusp Leak Widths

Much of the early theoretical work on plasma interactions with a cusped magnetic field came from the fusion community where it was considered a promising method for ion confinement. Simple analysis taking the magnetic moment as invariant shows how strong parallel gradients in the magnetic field can lead to nearly complete confinement. This lead to the idea of using a magnetic bottle for plasma containment, with a point cusp at each end to reflect charged particles back to the mid plane of the device. Unfortunately, it was found that particles continually diffuse into the loss cone through Coulombic collisions, making substantial power gains virtually impossible[31]. A historical overview of mirror fusion development up to the 1980's is given by Damm[33], where the use of cusped fields to quell low frequency instabilities is presented.

The problem of mirror machine instabilities led to the examination of cusped geometries, the most basic of which being the spindle cusp shown if Figure B-1, due to the inherent macroscopic stability afforded by keeping the radius of curvature of the confining field everywhere outside of the plasma[34]. The spindle cusp, consisting of a ring cusp at the mid plane and point cusps along the axis on either side, is similar to the magnetic cells of the DCF and HEMP thrusters, though many of the early experiments utilized them to contain plasmas of pressures near the applied magnetic pressure[35]. Plasma pressures in the DCFT are expected to be much lower than that of the applied field, indeed around 1 Pa compared to the 4 kPa provided by a field of

1 kG.

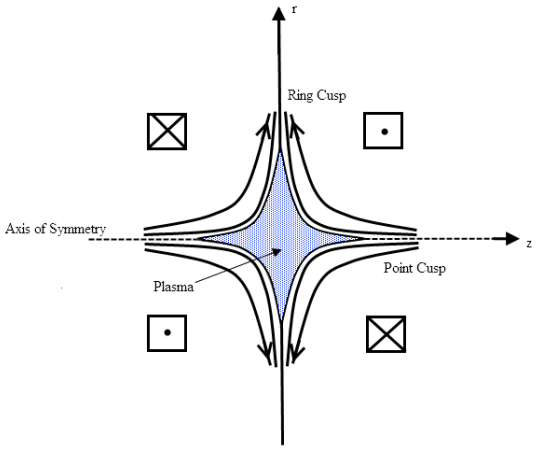

Figure B-1: Schematic of spindle cusp magnetic field confining a plasma

Much of the early literature on spindle cusp geometries considers the case of β, the ratio of plasma pressure to applied magnetic field pressure, near unity[34, 35, 36]. The high β spindle cusp is idealized by considering the central plasma as a field-free perfect conductor separated from the vacuum magnetic field by a transition layer often referred to as the sheath. This model, described by Berkowitz *et al* in a seminal 1958 paper, considers particle trajectories to be approximately line segments bouncing off of the sheath so that only on-axis particles with velocities towards the cusp are able to escape[34]. Escaping particles stream through a hole about the size of the transition layer, which Berkowitz *et al* derive for monoenergetic, isotropic electrons to be roughly the electron gyroradius. The authors maintain that a self consistent electric field then forces ions to leak through a hole about 1.7 times larger than that experienced by the electrons irrespective of the ion mass.

A review of cusped field confinement for thermonuclear fusion by Spalding in 1971 presents the results of several more complicated derivations of the particle loss widths[35]. These derivations rely on the conservation of canonical angular momentum and particle energy neglecting electric fields and result in leak half-widths scaling with the ion gyroradius at the cusp and, when the action integral is introduced as an adiabatic invariant, the inverse of the square root of the mirror ratio, $\lambda^{-1} = \sqrt{B_{min}/B_{max}}$, along the confining line of force. The latter, adiabatic case was

derived by Kaye assuming a Maxwellian velocity distribution[37]. In both cases the particle flux through the ring cusp is equal to that through a point cusp when the field strength at the cusps are the same and the derivation assumes $\beta = 1$, collisions can be neglected and the ion gyroradius at the sheath edge is much less than the radius of the ring cusp.

The review of Spalding also gathers data from various confinement experiments, showing that measured leak widths of high β plasmas were within a factor of 3 of the ion gyroradius evaluated at B_{min}. It was noted that no distinction could be made between the leak width scaling with ion gyroradius or with a Bohm diffusion based skin depth given by $\delta \sim \sqrt{LD_B\lambda/2c_s}$ where D_B is the Bohm diffusion coefficient and L the length of the plasma. Spalding briefly discusses the measurement in one experiment of a potential valley at the ring cusp of depth greater than kT_i/er_i (where r_i is the ion gyroradius) and a width of roughly $2r_i$, but does not make any statements about the impact such a well might have on the presented derivations of particle loss which neglect entirely any electric field. Oddly, a derivation of the Ferraro-Rosenbluth sheath is presented but it is not discussed in terms of applicability to any confinement experiment. The derivation assumes ions and electrons travel at a single velocity towards a transverse magnetic field which does not affect ion motion on the scale of the sheath length and thus results in a space charge electric field. The result is a sheath width scaling with the hybrid gyroradius, r_H, which is simply the geometric mean of ion and electron gyroradii.

A later, more general review of cusp containment by Haines [36] in 1977 touches on the topic of low-beta spindle cusps and discusses the first reported measurements of leak widths much smaller than the ion gyroradius, in fact closer to the geometric mean of ion and electron gyroradii. Haines posits that such small leak widths may arise from either the ion acoustic instability (predicting $\delta = r_H(T_e/T_i)^{1/4}$ when $\beta = 1$) or a viscoresistive sheath (for classical transport $\delta = 0.67r_H(T_i/T_e)$) arising from consideration of non-negligible viscosity in an MHD model.

Hershkowitz *et al* [49] were among the first to find loss widths on the order of $4r_H$, doing so in a picket fence experiment within a cylindrical device with multidipole

confinement near the walls. The 'picket fence' label refers to a lateral array of current carrying loops that are used to create a row of controllable line cusps, which in this case separate a driver multidipole chamber (where a biased hot filament drives the primary electron current) from a target multidipole chamber. A cylindrical Langmuir probe measured electron densities and temperatures in the target chamber, 5 mm behind the picket fence plane, and was scanned laterally across the array of line cusps. The measured current profiles were nearly Gaussian and peaked at the center of each cusp, allowing a leak width to be described by the full-width at half-maximum (FWHM) of a given profile.

The authors were able to determine a plasma electron leak width (taken from the electron saturation current of the Langmuir probe) approximately equal to four times the hybrid gyroradius by varying the field strength at the cusp from around 100 to 250 G and changing the working gas between Helium, Argon and Xenon. The typical driver-side densities measured were around 1-5$\times 10^{16}$ m^{-3} with neutral densities around 5×10^{18} m^{-3} (1×10^{-4} Torr). The ion leak widths (from the ion saturation current to the probe) were found to be a little larger (roughly 1.5 times the plasma electron width) and the primary electrons (from a linear, electron-dominated portion of the probe I-V curve) were found to exhibit a FWHM about equal to twice their gyroradius. The authors point out that due to a near constant ratio of electron to ion temperature they cannot differentiate between a loss half-width scaling with $2r_H$ or with $r_H(T_e/T_i)^{1/4}$ as predicted for a high-beta plasma with the ion acoustic instability. Also of note is their measurement of plasma noise at the cusps near the lower hybrid frequency, $\omega_{LH}^2 = \omega_{pi}^2/(1 + \omega_{pe}^2/\omega_{ce}^2)$, along with a lag of about 30 μs ($\sim 10\tau_{pi} \sim 1/3\tau_{ci}$) between Argon plasma initiation and relaxation of the plasma constituent leak widths from their own gyrodiameters to a hybrid one.

Work by Leung *et al* [47] on the same configuration expands the results of Hershkowitz *et al* to magnetic field strengths of up to 560 G and a broader range of neutral pressures, with an emphasis on determining the ability of the line cusp to increase the primary electron confinement time. Ion current to a negatively biased plate was measured along with the bulk plasma density before and after insertion of

the plate into the multidipole chamber in order to indirectly measure the total ion current lost to the chamber walls. The lost ion current, I_i, is then used to estimate the effective primary electron path length, L, which describes the average distance a primary travels before encountering a wall by $L/\lambda_i = I_i/I_p$, where λ_i is the mean free path for ionization and I_p is the emitted primary electron current.

This method is based on one used by Limpaecher [66] in an earlier multidipole device and relies on a simplified particle balance. The production of ions is assumed purely by primary electrons, which will not be valid if a significant proportion of plasma electrons are present, and the primaries only produce singly charged ions, which breaks down at high primary energies. The inserted plate is also assumed to have no impact on the ion production rate or the local plasma properties compared to those intercepted by the chamber walls.

An analytical model by Knorr and Willis [51] estimates the width of a potential valley centered at a line cusp to be on the order of the hybrid diameter. The model considers the conservation of canonical momentum and energy for both ions and electrons and a potential that only varies in the direction pointing from cusp to current loop, in the plane of the current loop of a picket fence. Asymptotic limits of the equations are taken in order to find an analytical form which gives the potential half-width as about 1-2 hybrid gyroradii, with the constant being a function of ion temperature over ion density to the one fourth power. Numerical solutions to the boundary value problem are also shown which predict a half-width of around 60-100 times the electron gyroradius for Xenon when the gyroradius is around half of the Debye length. The hybrid radius for expected conditions near the DCFT cusp is around 6 times the electron Larmor radius for comparison.

A follow-on analysis by Knorr and Merlino [53] suggests that the hybrid leak width is only possible with a population of fast primary electrons present to collisionally depopulate the region outside of the hybrid leak area of trapped plasma electrons. The authors surmise that without a population of high energy (60 eV compared to a 2 eV main plasma in the case depicted) primary electrons, electron collisions with the background neutral gas will allow them to diffuse across field lines effectively enough

to drastically increase the leak width above the hybrid gyrodiameter. They claim the existence of primaries with energies of around 50 eV is the reason Hershkowitz and Leung find hybrid leak widths while many others don't. The relative density of fast electrons to slow in order to obtain a hybrid scaling, though is quite small, in fact only 0.06% for the Argon plasma they describe.

A multidipole experiment by Nihei *et al* found a hybrid gyroradius scaling using a microwave plasma source operating on either Argon or Oxygen.[74] The plasma densities and temperatures in the experiment were on the order of 10^{17} m^{-3} and 2 eV respectively, the field strength at the line cusp varied from 9 kG to 22 kG, and the background pressure was kept below about 2 mTorr. The plasma leak widths reported in [74] were not measured directly by electrostatic probes at the wall, but rather inferred from matching power balance results assuming hybrid leak widths to experimental density profiles as well as by measuring the width of irradiation to the walls of the device. Both methods of inference yield only order of magnitude results, and no parametric sweeps were reported to further validate scaling relations.

A spindle cusp experiment using a CO2 laser to ionize a vaporized Deuterium pellet was performed by Pechacek *et al* [75] in which they report a time-independent leak width on the order of the ion gyrodiameter. In their experiment the working gas is almost fully ionized leading to a value β, the ratio of plasma pressure to applied magnetic field pressure, of unity despite a ring cusp field of 2 kG, unlike the work of Hershkowitz *et al* or Leung *et al* in which partial ionization leads to $\beta \sim 2 \times 10^{-5}$. The authors note that previous work finding leak widths near the hybrid radius use electrostatic probes which perturb the plasma and therefore choose to use a Thompson scattering measurement to determine the plasma density profile. Unfortunately, the spatial resolution of the system is larger than the hybrid gyroradius, which makes there conclusions about the FHWM of the density profile somewhat dubious. They offer burn patterns on the chamber wall as corroborating evidence, however, and it is worth noting that the pulsed laser ionization of the D_2 pellet leads to plasma lifetimes around 10 μsec, which leads to a much different problem than the steady-state diffusion of the low-β experiments.

Bosch *et al* [46] find leak widths for ions, primaries and plasma electrons in a ring cusp that show different scalings for different operational conditions. An increase in the electron density by almost four orders of magnitude found the ion leak width converge from about 15 times to 1.5 times the electron leak width, while the electron leak width roughly doubled. Bosch *et al* also find a rough dependence of the electron leak width on the square root of the background neutral pressure and an inverse proportionality with magnetic field for neutral pressures above 70 μTorr or cusp fields below 70 Gauss. For lower pressures and fields above 70 G the electron leak width scales roughly with the inverse of the square root of magnetic field strength. The authors outline a simple derivation of the leak width based on cross-field diffusion of electrons which neglects ionization in the cusp and assumes the plasma flow is choked (i.e. reaches the ion acoustic speed) at the cusp, in a manner analogous to a Laval nozzle. The resulting leak width,

$$d = \sqrt{2\overline{D}R/c_s} \tag{B.1}$$

where R is the distance from ring cusp to axis, c_s is the ion acoustic speed and $\overline{D}$ is an effective perpendicular electron diffusion coefficient. If classical diffusion dominates and the electron gyrofrequency, ω_e, is much greater than the electron-neutral collision frequency, $\nu_{en} = 1/\tau_H$, then $\overline{D} \simeq \frac{r_e^2}{\tau_H}$ and the leak width scaling inversely with magnetic field and with the square root of neutral pressure is recovered. If instead Bohm diffusion dominates then $\overline{D} \simeq \frac{kT_e}{16eB}$ and the leak width scales with $1/\sqrt{B}$ as measured with low background pressures. The authors note that the ratio of primary electrons to plasma electrons decreases as the neutral pressure is increased, but ignore this observation when discussing the scaling of leak width with pressure. The primaries are measured to leak over their own gyrodiamter. The measurements of primary electron currents by Bosch *et al* and Leung *et al* are both made at a single Langmuir probe bias, which is not a good indicator of the primary density if their is any change in the particle energies, but this is not expected to be a large effect in these particular experiments.

The same type of scaling is derived in a similar manner by Fukano *et al* [77] who use a linearly repeating cusp geometry to find $d = 2\sqrt{D_\perp L/c_s}$, where the differing factor of $\sqrt{2}$ with Eqtn. (B.1) comes from their definition of loss width as twice the e-folding length as opposed to the the FWHM used by [46]. The length L measures the distance along a flux tube connecting a cusp to a point of symmetry with the next cusp where the parallel electron fluxes cancel. The authors find the scaling compares favorably (in terms of proportionality with the various gyroradial lengths) for weakly, strongly and fully ionized plasmas with experimental results from the literature in each regime by matching the expression for the perpendicular diffusion coefficient, $D_\perp$, with the particular conditions. The main distinction between [46] and [77] is that the latter presents a case they call short circuiting where the ambipolar perpendicular diffusion is roughly equivalent to the ion perpendicular diffusion resulting in a loss width scaling with the ion gyroradius.

Kumar and Senecha [78] note that the analysis of Fukano *et al* (which is essentially the same as the earlier work of [79, 46]) is hampered by the assumption that the diffusion coefficient is constant along the cusp connecting flux tube, while it will clearly vary substantially in practice. They perform there own derivation of the leak width using a conformal mapping of the magnetic vector potential, which has the same form as Eqtn. (B.1) with the length scale R replaced by $l = (n/\frac{\partial n}{\partial r})|_{cusp}$, where the coordinate r points towards a radial cusp.

Early derivations of the loss width were made by Simon [79] in general terms, but for application to an arc plasma flowing along a magnetic field applied perpendicularly to an end wall. He derives an e-folding length for free-streaming plasma to the end wall of $d/2 = \sqrt{(D_{i\perp}L)/(2v_i)}$ where L is the length of the arc column, v_i is the ion speed and $D_{i\perp} = (kT_i)/(m_i\nu_{iH}[1 + \omega_{ci}^2/\nu_{iH}^2])$ is the perpendicular diffusion coefficient for ions. Simon shows that perpendicular plasma diffusion is dominated by the perpendicular ion diffusion coefficient when the perpendicular current due to the electric field is negligible and the parallel electron mobility is much higher than that of the ions. These assumptions also result in ambipolar diffusion of both species along the magnetic field, where $D_\parallel \simeq c_s^2/\nu_{iH}$.

Alternatively, the perpendicular ambipolar electric field can be calculated by setting the parallel current, $e(\Gamma_{i\|} - \Gamma_{e\|})$, to zero separately from the perpendicular current[79]. In this case the perpendicular diffusion coefficient, $D_\perp \simeq D_{e\perp}(1 + T_i/T_e)$, is roughly equal to that of the electrons as assumed by Fukano *et al* for weakly ionized plasmas. The parallel diffusion coefficient is unchanged under these considerations.

Gautheraeau and Matthieussent [70] have shown analytically that the density profiles measured in their multidipole confinement experiment are matched well by the ambipolar diffusion equations assuming a sharp jump in ionization near the walls by primary electrons trapped in the cusp fields. In a later article they ascribe the preponderance of a large population of trapped primaries in the cusps to the existence of an ion acoustic instability caused by the electron diamagnetic drift exceeding the local ion sound speed[72].

It is clear that the electron flux to the wall with a cusp field is the same as it would be in the magnetic field-free case, but the area over which the flux impinges is greatly decreased, meaning lower electron currents to the wall. The wall material in our case, and in SPT-type Hall thrusters, is an insulator so the ion current to the walls is equally decreased and the total charged particle losses to discharge chamber walls will lessen when a cusped field is used rather than a purely radial one if the bulk plasma density and temperature remains the same. The effect of the field shape on wall erosion rates and power losses is less obvious as the energy of the particles comes into play, but ultimately a steady state can only be reached if the temperature and density are just such that ionization gains equal loss rates into the cusps, anode and beam.

Appendix C

Wall Loss Estimates from IR Camera Data

A simple method for estimating the power deposited by the plasma on the discharge chamber walls is presented here, which is based on the analysis of Mazouffre *et al* [200]. The boron nitride wall is segregated into differential volume elements to which the energy equation,

$$\rho c \frac{\partial T}{\partial t} dV = \mathbf{q_p} \cdot \mathbf{dS} - \sum_j F_{1-j} \epsilon \sigma (T^4 - T_j^4) dS + k \nabla T \cdot \mathbf{dS} \tag{C.1}$$

is applied, where ρ is the mass density of the wall material (2 g/cc for BN), c is its specific heat (1.5 J/g/K for BN), q_p is the power density input from the plasma to the wall element, F_{1-j} is the radiative view factor between the considered wall element and element j, ϵ the thermal emissivity (about 0.85 from thermal camera calibration) and k the thermal conductivity (27 W/m/K for BN at room temperature). The thermal and mass properties of the HP-grade BN used for the chamber wall are taken from the data sheet provided by the material supplier, Saint-Gobain Advanced Ceramics.

Mazouffre proposes that a rough estimate of q_p can be obtained by taking the difference of the temperature rate changes just before and just after the thruster is shut down [200]. This method neglects any changes in the net power brought into each element by radiative or conductive heat transfer in between temperature

rate change measurements. Neglecting changes in conduction may be reasonable if thermal camera images are obtained at a rate which exceeds the inverse timescale for conduction.

The 1-D characteristic time for conductive heat transfer is $t = (L/2)^2/D$ where L is the length scale and D the thermal diffusion coefficient, $D = k/(\rho c) \sim 8 \times 10^{-6}$ m^2/s. The characteristic time is then about 3 seconds for conduction over a length of 1 cm. Adjacent pixels on our thermal images of the cone are typically imaging physical locations separated by only about 3 mm and our imaging rate is typically once per 4 seconds, suggesting conduction is more nearly instantaneous between rate measurements and certainly not negligibly slow. Our slightly revised method for obtaining rough estimates is then,

$$(q_{p+} - q_{p-})dS \sim \rho c(\frac{\partial T}{\partial t}|_+ - \frac{\partial T}{\partial t}|_-)dV - k\left(\frac{\partial T}{\partial x}S_e + \frac{\partial T}{\partial x}S_w + \frac{\partial T}{\partial y}S_n + \frac{\partial T}{\partial y}S_s\right)_-^+ \quad \text{(C.2)}$$

where x refers to the distance between laterally adjacent pixels, separated by cross-sectional areas of S_w to the left and S_e to the right, and y the distance between those vertically adjacent, separated by cross-sectional areas of S_n above and S_s below. Here t_- and t_+ refer to the times just before and just after a large change in the anode power. Conduction normal to the cone surface is neglected for convenience only, since the outer wall temperature of the cone is not known to high accuracy. The thermal conductivity of boron nitride is relatively high and the cone wall is fairly thin, so this may ultimately be a reasonable approximation.

Implementation of Eqn. C.2 to estimate changes in plasma power to the walls with changes in anode power requires some straightforward but time consuming transformations from 2D pixelated images to 3D geometric data. First, a comparison of the lateral pixel distance between the upstream and downstream edges of the cone taken on the left and right side of the anode is used to estimate the yaw of the BN cone with respect to the camera, with similar estimates obtained for the cone pitch through vertical pixel distances. A large set of pixel coordinates are tabulated for

points which visually appear to correspond to certain locations on the thruster exit face and a least squares fit is performed to find the cone vertex in pixel coordinates which minimizes error in the distance to the tabulated coordinates.

Armed with the yaw, pitch and vertex coordinate of the BN cone it is then simple to transform between IR camera coordinates and a coordinate system bound to the cone. The 3D coordinates of each corner of a pixel can be estimated by finding the intersection of a line perpendicular to the pixel coordinate (along the IR line of sight, neglecting perspective) and the cone function, $F = (x_c^2 + y_c^2)\cos^2\alpha - z_c^2\sin^2\alpha = 0$, where (x_c, y_c, z_c) are the coordinates in the cone frame and α is the angle of the cone's divergence. The surface area of each pixel is taken as the area of the parallelogram defined by the four corner coordinates and the differential volume estimated by finding the magnitude of the cross product of the parallelogram surface with an outward normal vector to the cone surface with a 2.31 mm magnitude (the cone thickness in this direction).

The time derivate of the temperature in each pixel is taken as the centered difference between camera images before and after. The thermal state at t_- is taken as the average of the that found in the four frames preceding a large anode power change, while the thermal state at t_+ is taken as either the first frame after the power change or the second, with estimates obtained using both shown in Figs. 4-31 and 4-32.

To avoid the influence of stray signals from a visibly glowing probe lead near 11 o'clock on the exit face of the cone, and to minimize errors in the volume and surface area estimates for cone regions nearly parallel to camera line-of-sight, the thermal state of the cone is only taken from a swath within 20 degrees of 3 o'clock, where the cone surface is most nearly normal to the IR camera view.

Estimates of the change in power radiated from the cone surface (assuming the temperature of the secondary body receiving the radiation does not change much from t_- to t_+) do not change estimates of the plasma deposited power by any more than 10% at the highest cone temperatures. Neglecting conduction between pixels, however, results in an estimate of q_p which is approximately double what is reported here.

Appendix D

Damped Breathing Cycle

A damped breathing cycle, near the transition to a limit cycle solution, is presented in the following figures. The general characteristics are quite similar to the self-sustained oscillations, though the final neutral density is higher than the initial density, as a stationary solution is approached.

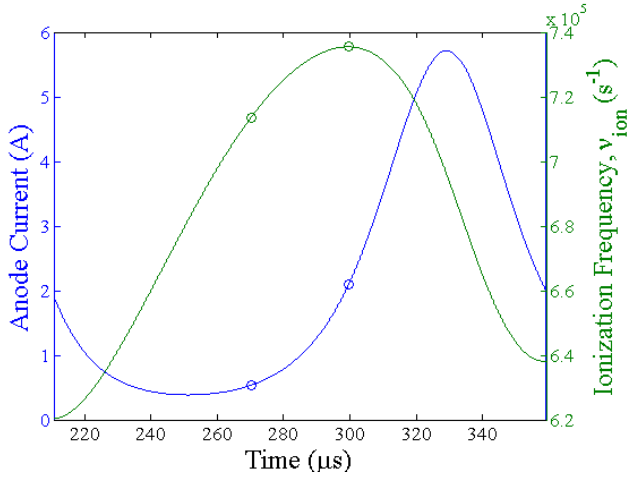

Figure D-1: Anode current and ionization frequency versus time. Circles indicate sections of cycle in terms of ν_{ion}: from minimum to end of linear growth portion, then to peak and back to minimum.

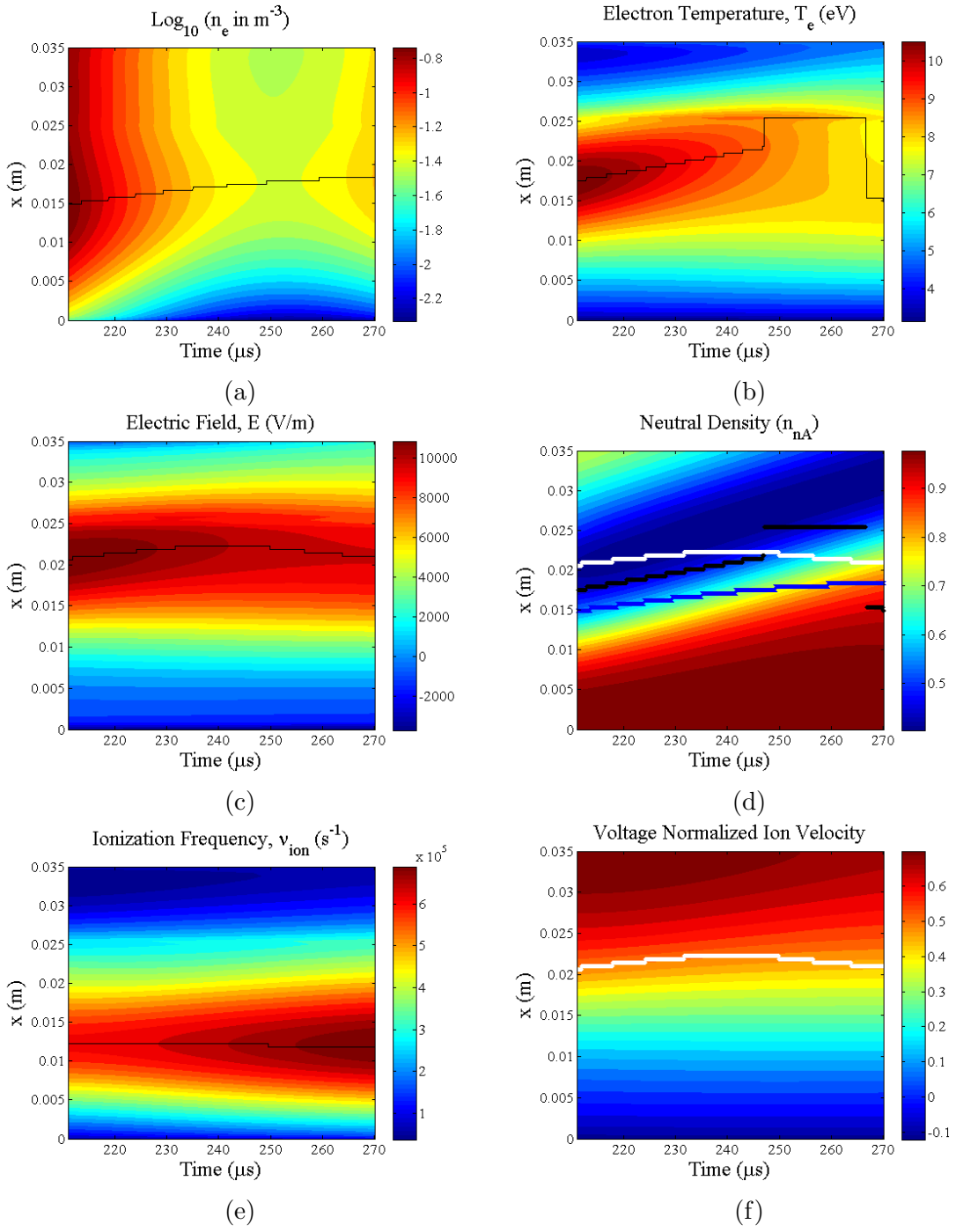

Figure D-2: Model results for 180 V and 6 mg/s during linear growth of ionization frequency. (a) Log_{10} of plasma density profile (b) Electron temperature profile (c) Electric field profile (d) Neutral density profile (e) Ionization frequency profile (f) Ion speed normalized by anode voltage speed profile versus time. (a)-(c), (e) Thin black line traces location of peak of plotted variable. (d),(f) Blue line traces location of peak n_e, black line is peak T_e, white line is peak E.

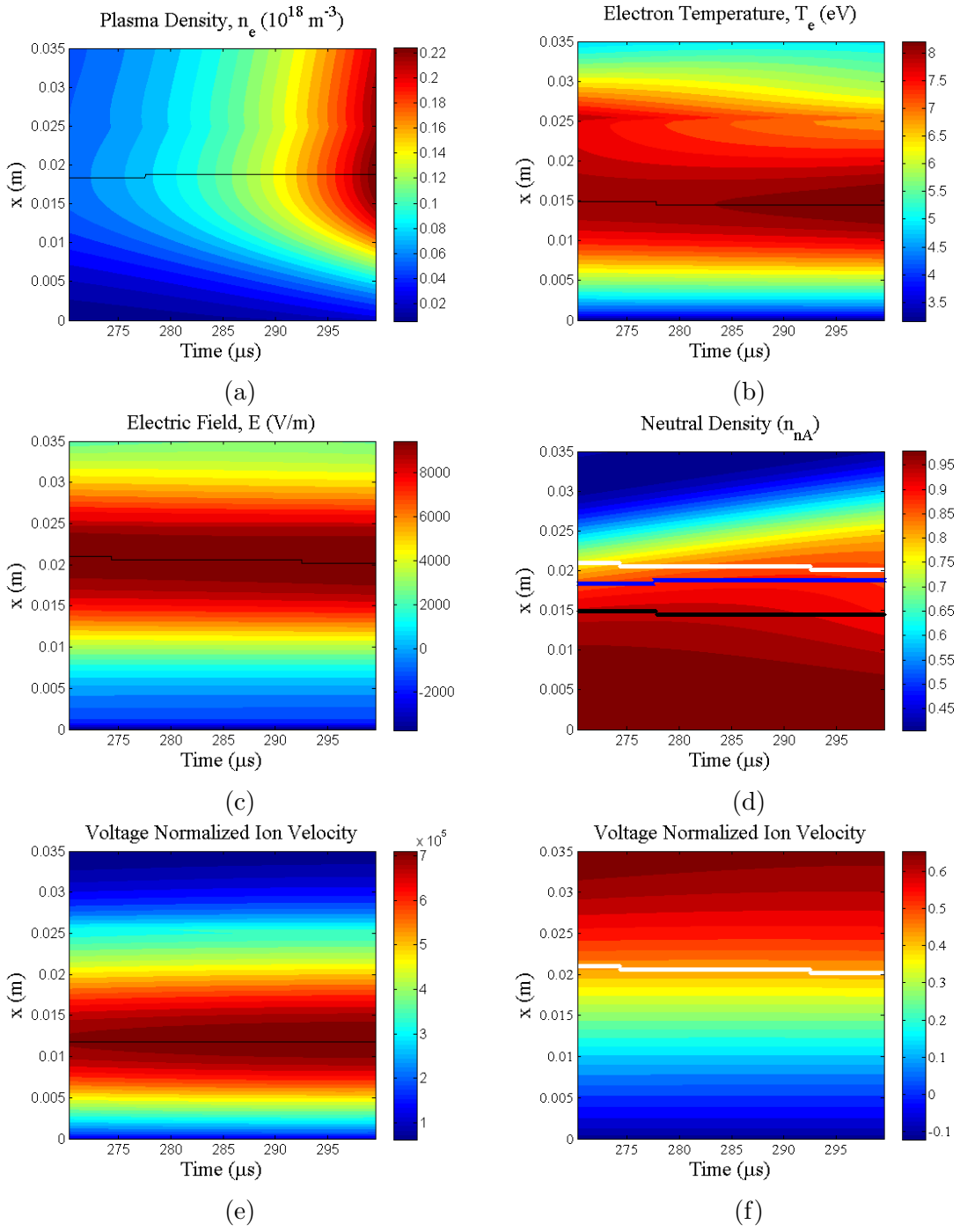

Figure D-3: Model results for 180 V and 6 mg/s during exponential growth of plasma density. (a) Log_{10} of plasma density profile (b) Electron temperature profile (c) Electric field profile (d) Neutral density profile (e) Ionization frequency profile (f) Ion speed normalized by anode voltage speed profile versus time. (a)-(c), (e) Thin black line traces location of peak of plotted variable. (d),(f) Blue line traces location of peak n_e, black line is peak T_e, white line is peak E.

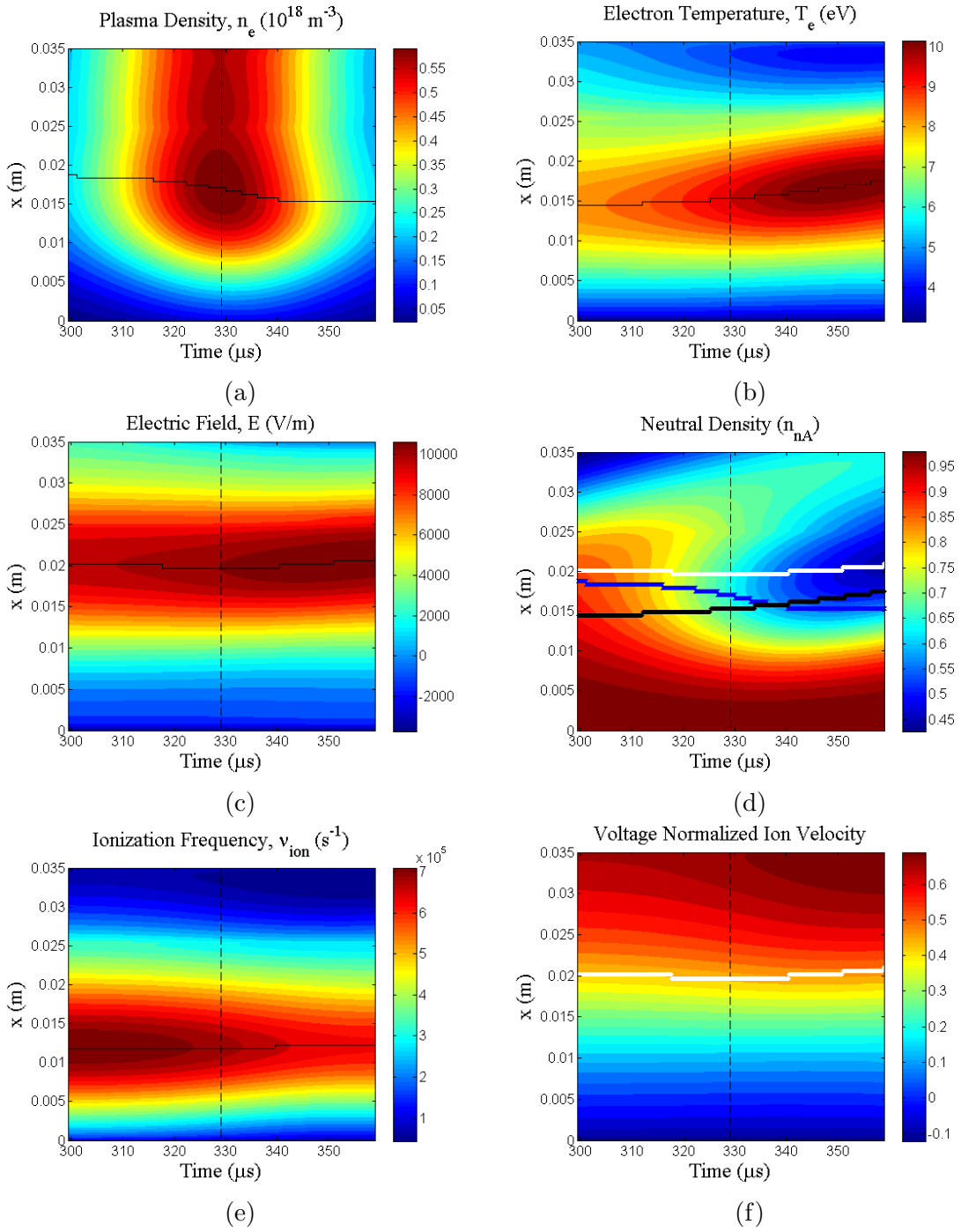

Figure D-4: Model results for 180 V and 6 mg/s during current peak and decay. (a) plasma density profile (b) Electron temperature profile (c) Electric field profile (d) Neutral density profile (e) Ionization frequency profile (f) Ion speed normalized by anode voltage speed profile versus time. (a)-(c), (e) Thin black line traces location of peak of plotted variable. (d),(f) Blue line traces location of peak n_e, black line is peak T_e, white line is peak E.

Appendix E

Fluid Description of a Magnetic Mirror

The concept of magnetic mirroring was introduced in Sec. 2.2, but only in a single particle sense. This section begins with our own derivation of the mirror force on an electron fluid, with the result matching that found elsewhere in the literature [62, 63]. The presented derivation begins in general terms in an attempt to elucidate the assumptions which result in the well known simplified form.

We begin with the Boltzmann equation (Eqn. 2.13) recast into electron guiding center coordinates. The electron guiding center refers to the point about which an electron gyrates in a magnetic field, which may migrate along a magnetic field line and also drift perpendicular to the field in the presence of electric fields or gradients. The position of the guiding center is denoted $\mathbf{R}$, which moves along a given field line with parallel velocity $v_{||}$ and has an energy of gyration $y = 1/2mv_{\perp}^2$. The third variable describing a particles coordinates in gyro-centered velocity-space is the phase of its gyrorotation, α, which integrates out of the following equations but is included for completeness. The Boltzmann equation may be rewritten as,

$$\frac{\partial f}{\partial t} + \dot{\mathbf{R}} \cdot \nabla f + \dot{v}_{||} \frac{\partial f}{\partial v_{||}} + \dot{y} \frac{\partial f}{\partial y} + \dot{\alpha} \frac{\partial f}{\partial \alpha} = \sum \mathbb{C} \tag{E.1}$$

where the collision integral on the right hand side is retained, but left in its

general form. The rate change in guiding center position and parallel velocity can be expressed (following Porcelli [64]) as,

$$\dot{\mathbf{R}} = v_{||}\mathbf{b} - \frac{1}{eB}\mathbf{b} \times (\mu\nabla\mathbf{B} + m_e v_{||}^2 \kappa + e\mathbf{E}) \tag{E.2}$$

$$\dot{v}_{||} = -\frac{\mu}{m_e}\mathbf{b}\cdot\nabla\mathbf{B} - \frac{e}{m_e}\mathbf{b}\cdot\mathbf{E} + v_{||}\kappa\cdot\dot{\mathbf{R}} \tag{E.3}$$

where μ is the magnetic moment, $\kappa \equiv (\mathbf{b}\cdot\nabla)\mathbf{b}$ is the unit curvature of the field line and $\mathbf{b} \equiv \mathbf{B}/B$ is the parallel unit vector. The parenthetic terms in Eqn. E.2 account for the $\nabla\mathbf{B}$, curvature and $\mathbf{E}\times\mathbf{B}$ drifts. The guiding center does not move in the direction of the curvature vector barring collisions or a gradient in either the magnetic field or electrostatic potential in the $\mathbf{b}\times\kappa$ direction (which we take here as the azimuthal direction in a cylindrically symmetric system). Assuming azimuthal symmetry results in $\kappa\cdot\dot{\mathbf{R}} = 0$, so the rate change of $v_{||}$ is due to the magnetic mirror force and the parallel component of the electric field.

The rate change in y is simple in the limit where the magnetic moment is conserved and the applied magnetic field is static, consisting only of a convective component,

$$\dot{y} = \frac{d}{dt}(\mu\mathbf{B}) = \mu(\dot{\mathbf{R}}\cdot\nabla)\mathbf{B} = \mu v_{||}\mathbf{b}\cdot\nabla\mathbf{B} \tag{E.4}$$

which is clearly the effect of the mirror force on the perpendicular electron energy. The rate change of the gyrophase is just the gyrofrequency, ω_{ce}. The Boltzmann equation may now be written,

$$\frac{\partial f}{\partial t} + v_{||}\frac{\partial f}{\partial \xi} - (\frac{\mu}{m_e}\frac{\partial B}{\partial \xi} + \frac{eE_{||}}{m_e})\frac{\partial f}{\partial v_{||}} + \mu v_{||}\frac{\partial B}{\partial \xi}\frac{\partial f}{\partial y} + \omega_{ce}\frac{\partial f}{\partial \alpha} = \sum \mathbb{C} \tag{E.5}$$

where we take ξ as the coordinate parallel to the field line and assume the electron distribution function is independent of the azimuthal direction, so that $\mathbf{u}_D\cdot\nabla f = 0$, where $\mathbf{u}_D$ is the electron drift velocity.

The fluid equation for the parallel electron momentum is then obtained in the

same manner as the momentum equation of Sec. 2.3.1. In this case we take the moment of $mv_{||}$ which results in,

$$\frac{\partial m_e n_e u_{e||}}{\partial t} + \frac{\partial}{\partial \xi}(m_e n_e \left\langle v_{||}^2 \right\rangle) + n_e \frac{\partial B}{\partial \xi} \left\langle \mu \right\rangle + e n_e E_{||} - \frac{m_e n_e}{B} \frac{\partial B}{\partial \xi} \left\langle v_{||}^2 \right\rangle = \sum \Delta[m v_{||}] \tag{E.6}$$

where we define $u_{e||} = \left\langle v_{||} \right\rangle$ as normal. We then apply the definitions $T_{||} = \left\langle m c_{||}^2 \right\rangle$ and $T_\perp = \langle 1/2 m c_\perp^2 \rangle$ to find,

$$\frac{\partial m_e n_e u_{e||}}{\partial t} + \frac{\partial}{\partial \xi}(m_e n_e u_{e||}^2 + n_e T_{||}) + \frac{n_e}{B} \frac{\partial B}{\partial \xi} \left[T_\perp - T_{||} - m_e u_{||}^2 \right] + e n_e E_{||} = \sum \Delta[m v_{||}] \tag{E.7}$$

where all averages over c to an odd power are zero by definition. This equation is equivalent to that found in [62] and [63] and suggests that the mirror force goes to zero when the electrons are isotropic (in the absence of a parallel drift), which is somewhat counterintuitive since an isotropic distribution necessarily has a large population of particles experiencing the mirror force. The reason for this effect, as explained by Comfort [62], is that the repelling force felt by the electrons entering a cusp is precisely balanced, in the case of isotropic electrons, by the uneven parallel pressure gradient forces on either side of the fluid element caused by the restriction in area through which the electrons flow.

Note that the ensemble average of μ is just $nT_\perp/B$ with no inclusion of the perpendicular drift energy. This is clear from our choice of phase-space coordinates which describe a particle's velocity in reference to its guiding center. The guiding center itself may drift perpendicular to the magnetic field line, but the velocity coordinates are independent of this motion, and since the distribution function is assumed homogeneous in the drift direction the inclusion of drifts has no effect on the present analysis. The guiding center analysis must be applied with care, as the equations are

only valid when the parallel motion is slow compared to a gyro-rotation and gradient length scales are much smaller than a gryo-radius [65].

The above equation is interesting in its implications for low density plasma loss to a normal wall cusp. The presence of the wall tends to cool the component of electron temperature perpendicular to the wall (parallel to the magnetic field in this case) as electrons with high parallel energy are lost to the boundary, and possibly replaced by secondaries. The presence of a strong electric field perpendicular to the magnetic field (parallel to the wall) can preferentially increase $T_{\perp}$, which when combined with the effect of $T_{||}$ cooling from the wall can lead to $T_{\perp}$ being several times as large as $T_{||}$, as has been observed in kinetic Hall thruster simulations [183]. Equation E.7 suggests that such a large anisotropy favoring the perpendicular temperature component ought to increase plasma confinement from magnetic mirroring (as one might expect from a simple pitch angle analysis as well), which in turn would increase $T_{||}$ from the arguments above, decreasing the mirror force term until some balance is struck.

Bibliography

[1] Courtney, D., *Development and Characterization of a Diverging Cusped Field Thruster and a Lanthanum Hexaboride Hollow Cathode*,Masters Thesis, Massachusetts Institute of Technology, 2008.

[2] Daspit, R., *Performance Characterization and Optimization of a Diverging Cusped Field Thruster with a Calibrated Counter-Weighted Millinewton Thrust Stand*,Masters Thesis, Massachusetts Institute of Technology, 2012.

[3] Brown, D., Gallimore, A. *Investigation of Low Discharge Voltage Hall Thruster Operating Modes and Ionization Processes* 31st International Electric Propulsion Conference, 2009.

[4] Gascon, N., Dudeck, M., Barral, S. *Wall material effects in stationary plasma thrusters: I. Parametric studies of an SPT-100* Phys of Plasmas 10(10), 2003.

[5] Young, C., Smith, A., Cappelli, M. *Preliminary Characterization of a Diverging Cusped Field (DCF) Thruster*, 31st International Electric Propulsion Conference, 2009.

[6] MacDonald, N.A., Cappelli, M.A., Gildea, S.R., Martinez-Sanchez, M., Hargus Jr., W.A. *Laser-induced flourescence velocity measurements of a diverging cusped-field thruster* J Phys D: Appl Phys 44(295203), 2011.

[7] Gildea, S.R., Martinez-Sanchez, M., Hargus, W.A. Jr., Matlock, T.S., *Erosion Measurements in a Low-Power Cusped-Field Plasma Thruster*, accepted for publication in Journal of Propulsion and Power, 2012.

[8] Matlock, T., Gildea, S., Hu, F., Becker, N., Lozano, P., Martinez-Sanchez, M. *Magnetic Field Effects on the Plume of a Diverging Cusped-Field Thruster*, 46th AIAA/ASME/SAE/ASEE Joint Propulsion Conference, 2010.

[9] Kornfeld, G., Koch, N., Harmann, H. *Physics and Evolution of HEMP-Thrusters*, 30th International Electric Propulsion Conference, 2007.

[10] Ahedo, E., Martinez-Cerezo, P., Martinez-Sanchez, M. *One-dimensional model of the plasma flow in a Hall thruster* Phys of Plasmas 8(6), 2001.

[11] Kornfeld, G., Harmann, H., Koch, N. *Status and limited life test results of the cylindrical HEMP 3050 thruster*, 41st AIAA/ASME/SAE/ASEE Joint Propulsion Conference, 2005.

[12] Barral, S., Ahedo, E. *Low-frequency model of breathing oscillations in Hall discharges* Phys Rev E 79(046401) 2009.

[13] Biglari, H., Diamond, P.H., Terry, P.W. *Influence of sheared poloidal rotation on edge turbulence*, Phys. Fluids B 2(1), 1990.

[14] Shaing, K.C., Crume, E.C., Houlberg, W.A. *Bifurcation of poloidal rotation and suppression of turbulent fluctuations: A model for the L-H transition in tokamaks*, Phys. Fluids B vol. 2, (1492) 1990.

[15] Waltz, R.E., Dewar, R.L., Garbet, X. *Theory and simulation of rotational shear stabilization of turbulence* Phys. Plasmas 5(5), 1998.

[16] Courtney, D., Martinez-Sanchez, M. *Diverging Cusped-Field Hall Thruster (DCHT)*, 30th International Electric Propulsion Conference, 2007.

[17] Courtney, D., Lozano, P., Martinez-Sanchez, M. *Continued Investigation of Diverging Cusped Field Thruster*, 44th AIAA/ASME/SAE/ASEE Joint Propulsion Conference, 2008.

[18] Gildea, S., Martinez-Sanchez, M., Nakles, M., Hargus, W. *Experimentally Characterizing the Plume of a Divergent Cusped-Field Thruster*, 31st International Electric Propulsion Conference, 2009.

[19] Gildea, S., Matlock, T., Lozano, P., Martinez-Sanchez, M., *Low Frequency Oscillations in the Diverging Cusped-Field Thruster*, 46th AIAA/ASME/SAE/ASEE Joint Propulsion Conference, 2010.

[20] Matlock, T., Daspit, R., Batishchev, O., Martinez-Sanchez, M. *Spectroscopic and Electrostatic Investigation of the Divergent Cusped Field Thruster*, 45th AIAA/ASME/SAE/ASEE Joint Propulsion Conference, 2009.

[21] Raitses, Y., Merino, E., Parker, J., Fisch, N. *Operation and plume measurements of miniaturized cylindrical Hall thrusters with permanent magnets*, 45th AIAA/ASME/SAE/ASEE Joint Propulsion Conference, 2009.

[22] Raitses, Y., Merino, E., Fisch, N.J. *Cylindrical Hall thrusters with permanent magnets*, Journ Appl Phys Vol. 108 (093307), 2010.

[23] Hutchinson, I.H *Principles of Plasma Diagnostics*, Cambridge University Press, Cambridge, UK, 2002, pp.97-98.

[24] Azziz, Y. *Experimental and Theoretical Characterization of a Hall Thruster Plume* Doctoral Dissertation, Department of Aeronautics and Astronautics, Massachusetts Institute of Technology, Cambridge, MA, 2007.

[25] Morozov, A.I., Savelyev, V.V. *Fundamentals of Stationary Plasma Thruster Theory* Reviews of Plasma Phys Vol. 21, 2000.

[26] Gavryshin, V.M., Kim, V., Kozlov, V.I., Maslennikov. *Physical and Technical Bases of the Modern SPT Development* IEPC1995-38, 1995.

[27] Hofer, R.R *Development and characterization of high-efficiency, high-specific impulse xenon hall thrusters* Doctoral Dissertation, University of Michigan, 2004.

[28] Larson, C.W., Brown, D.L., Hargus Jr., W.A. *Thrust Efficiency, Energy Efficiency and the Role of VDF in Hall Thruster Performance Analysis* AIAA 2007-5270, 2007.

[29] Brown, D.L. P *Investigation of Low Discharge Voltage Hall Thruster Characteristics and Evaluation of Loss Mechanisms* PhD Dissertation, University of Michigan, 2009.

[30] Linnell, J.A., Gallimore, A.D. *Hall Thruster Electron motion Characterization Based on Internal Probe Measurements* IEPC-2009-105, 2009.

[31] Freidberg, J. **Plasma Physics and Fusion Energy**, Cambridge University Press, 2007.

[32] Mitchner, M., Kruger, C.H. Jr., **Partially Ionized Gases**, Wiley, 1973.

[33] Damm, C.C. *Evolution of the Mirror machine*, J. Vac. Sci. Technol. A 2(2), 1984.

[34] Berkowitz, J., Friedrichs, K.O., Goertzel, H., Grad, H., Killeen, J., Rubin, E. *Cusped geometries*, 2nd Geneva Conf. on Peaceful Uses of Atomic Energy, 1958.

[35] Spalding, I. *Cusp Containment*, Advances in Plasma Physics Vol.4, 1971.

[36] Haines, M.G. *Plasma containment in cusp-shaped magnetic fields* Nucl Fusion 17(4), 1977.

[37] Kaye, A.S. *Plasma losses through an adiabatic cusp* J. Plasma Physics 11(1),1974.

[38] Coensgen, F.H., Sherman, A.E., Nexsen, W.E., Cummins, W.F. *Plasma injection into a Magnetic Field of Cusped Geometry*, Phys Fluids 3(5), 1960.

[39] Schmidt, G. *Nonadiabatic Particle Motion in Axialsymmetric Fields*, Phys Fluids 5(8), 1962.

[40] Luk'yanov, S.Y., Podgornyi, I.M. *Cusped Geometry Magnetic Traps*, Journ Nucl Energy C. 4(135-142), 1962.

[41] Schuurman, W., De Kluiver, H. *Non-adiabatic Motion of a Particle in a Cusped Magnetic Field*, Journ Nucl Energy C. 7(245-262), 1965.

[42] Shinano, K., Ito, H. *Behavior of a Charged Particle in a Cusp Field*, Journ of Phys Soc Japan 21(9), 1966.

[43] Strijland, W. *Injection and Containment of Charged Particles in a Cusp Magnetic Field*, Physica 44(241-259), 1969.

[44] Jaroensutasinee, K., Rowlands, G. *Charged-particle orbits near a magnetic null point*, J. Plasma Physics 64(3), 2000.

[45] Jones, R. *Leak Width Scaling of a Turbulent Magnetoplasma Line Cusp*, Lettere al Nuovo Cimento 34(6), 1982.

[46] Bosch, R.A., Merlino, R.L. *Confinement properties of a low-beta discharge in a spindle cusp magnetic field*, Phys. Fluids Vol.29(6), 1986.

[47] Leung, K.N., Hershkowitz, N., MacKenzie, K.R. *Plasma confinement by localized cusp*, Phys. of Fluids Vol.19 No.7, 1976.

[48] Christensen, T., Hershkowitz, H., Leung, K.N. *Mass scaling of permanent magnet line cusp plasma leaks*, IEEE Transactions on Plasma Science, Vol. PS-5, No. 1, 1977.

[49] Hershkowitz, N., Smith, J.R., Kozima, H. *Electrostatic self-plugging of a picket fence cusped magnetic field*, Phys. Fluids 22(1), 1979.

[50] Marcus, A.J., Knorr, G., Joyce, G. *Two-Dimensional Simulation of Cusp Confinement of a Plasma*, Plasma Physics, Vol 22(1015-1027), 1980.

[51] Knorr, G., Willis, D. *Leak Width of a Cusp-Confined Plasma*, Zeitschrift Naturforschung Teil A, Vol. 37, 1982.

[52] Koch, C., Matthieussent, G. *Collisional diffusion of a plasma in multipolar and picket fence devices*, Phys Fluids 26(2), 1983.

[53] Knorr, G., Merlino, R.L. *The role of fast electrons for the confinement of plasma by magnetic cusps*, Plasma Phys. and Contr. Fusion Vol.26 No.2, 1984.

[54] Sullivan, K., Fox, J., Martinez-Sanchez, M., Batishchev, O. *Kinetic Study of Wall Effects in SPT Hall Thrusters* AIAA 2004-3777, 2004

[55] Viel-Inguimbert, V. *Secondary electron emission of ceramics used in the channel of SPT* IEPC-258-03, 2003.

[56] Dawson, P.H. *Secondary Electron Emission Yields of some Ceramics* J. Appl. Phys. 37(3644), 1966.

[57] Choueiri, E.Y. *Fundamental difference between the two Hall thruster variants* Phys of Plasmas 8(11), 2001.

[58] Bugeat, J.P., Koppel, C. *Development of a second generation of SPT* IEPC-95-35, 1995.

[59] Jolivet, L., Roussel, J.F. *Effects of the secondary electron emission on the sheath phenomenon in a Hall thruster* 3rd International Conference on Spacecraft Propulsion, 2000.

[60] Dunaevsky, A., Raitses, Y., Fisch, N.J. *Secondary electron emission from dielectric materials of a Hall thruster with segmented electrodes* Phys of Plasmas 10(6), 2003.

[61] Barral, S., Makowski, K., Peradzynski, Z., Gascon, N., Dudeck, M. *Wall material effects in stationary plasma thrusters. II. Near-wall and in-wall conductivity* Phys of Plasmas 10(10), 2003.

[62] Comfort, R.H. *The magnetic mirror force in plasma fluid models* Geophysical Monograph Series 44, 1988.

[63] Lampe, M., Joyce, G., Manheimer, W.M., Slinker, S.P. *Quasi-Neutral Particle Simulation of Magnetized Plasma Discharges: General Formalism and Application to ECR Discharges* IEEE Trans on Plasma Sci 26(6), 1998.

[64] Porcelli, F., Stankiewicz, R., Kerner, W., Berk, H.L. *Solution of the drift-kinetic equation for global plasma modes and finite particle orbit widths* Phys. Plasmas 1(3), 1994.

[65] Northrop, T.G., *Adiabatic charged-particle motion* Rev. of Geophys. Vol 1 No 3, 1963.

[66] Limpaecher, R., MacKenzie, K.R. *Magnetic Multipole Containment of Large Uniform Collisionless Quiescent Plasmas*, Rev. of Sci. Instr. 44, 726, 1973.

[67] Leung, K.N., Kribel, R.E., Goede, A.P.H., Green, T.S. *Primary electron confinement measurement in a multidipole device*, Phys Lett 66A(2), 1978.

[68] Hershkowitz, N., Hendricks, K., Carpenter, R.T. *Electrostatic plugging of leaks in a multidipole device*, J. Appl. Phys. 53(6), 1982.

[69] Hershkowitz, N., Goettsch, R.L., Chan, C., Hendricks, K., Carpenter, R.T. *Detection of secondary electrons in a multidipole plasma*, J. Appl. Phys. 53(7), 1982.

[70] Gauthereau, C., Matthieussent, G. *Plasma density profiles in discharges surrounded by magnetic multipole walls*, Phys. Lett. A Vol.102A(5), 1984.

[71] Kozima, H., Yamagiwa, K., Kawaguchi, M. *Plasma instabilities excited around a line cusp magnetic field*, Phys Lett 106A(5,6), 1984.

[72] Gauthereau, C., Matthieussent, G. *Ion acoustic instability and plasma uniformity in multipolar discharges*, Phys. Lett. A Vol.121(7), 1987.

[73] Cho, M-H., Hershkowitz, N., Intrator, T. *Particle and power balances of hot-filament discharge plasmas in a multidipole device*, J. Appl. Phys. 67(7), 1990.

[74] Nihei, H., Enomoto, H., Inoue, N. *Analyses of plasma flux and density distribution in plasma sources surrounded by magnetic multipole fields*, Jpn. J. Appl. Phys Vol.34, 1995.

[75] Pechacek, R.E., Greig, J.R., Raleigh, M., Koopman, D.W., DeSilva, A.W. *Measurement of the plasma width in a ring cusp* Phys Rev Lett 45(4), 1980.

[76] Takekida, H., Nanbu, K. *Particle modelling of plasma confinement by a multipolar magnetic field*, J. Phys. D: Appl. Phys. 37, 2004.

[77] Fukano, A., Mizuno, T., Hatayama, A., Ogasawara, M. *Estimation of the cusp loss width in negative-ion sources*, Rev. of Sci. Instr. 77(3), 2006.

[78] Kumar A., Senecha V.K. *Cusp leak width computation and optimization for H- Ion source*, Indian Particle Accelerator Conference, 2009 .

[79] Simon, A. *Diffusion of Arc Plasmas across a Magnetic Field* Geneva Conference P/366, 1958.

[80] Martinez-Sanchez, M., Ahedo, E. *Magnetic mirror effects on a collisionless plasma in a convergent geometry*, Phys of Plasmas 18(033509), 2011.

[81] Goebel, D.M., Katz, I. **Fundamentals of Electric Propulsion: Ion and Hall Thrusters**, New Jersey: John Wiley and Sons, 2008.

[82] Goebel, D., Wirz, R., Katz, I. *Analytical Ion Thruster Discharge Performance Model* Journ Prop Power 23(5), 2007.

[83] Buzzi, J.M., Snow, J., Hirshfield, J.L. *Primary electron reflections in discharges surrounded by magnetic multipole walls*, Phys. Lett. Vol. 54A No. 4, 1975.

[84] Moore, D.R. *Magneto-electrostatically contained plasma ion thruster*, AIAA Paper 69-260, 1969.

[85] Beattie, J.R., Wilbur, P.J. *Cusped magnetic field mercury ion thruster*, Phd Dissertation, Colorado State University, 1976.

[86] Sovey, J.S. *Improved Ion Containment Using a Ring-Cusp Ion Thruster*, Journal of Spacecraft and Rockets, 1984.

[87] Wirz, R. E. *Discharge plasma processes of ring-cusp ion thrusters*, PhD Dissertation, California Institute of Technology, 2005.

[88] Kornfeld, G., Koch, N., Coustou, G. *First test results of the HEMP thruster concept*, 28th International Electric Propulsion Conference, 2003.

[89] Koch, N., Kornfeld, G., Harmann, H. *Status of the THALES High Efficiency Multi Stage Plasma Thruster Development for HEMP-T 3050 and HEMP-T 30250*, 30th International Electric Propulsion Conference, 2007.

[90] Harmann, H., Koch, N., Kornfeld, G. *The ULAN Test Station and its Diagnostic Package for Thruster Characterization*, 30th International Electric Propulsion Conference, 2007.

[91] Jankovsky, R., Tverdokhlebov, S., Manzella, D. *High Power Hall Thrusters* AIAA 99-2949, 1999.

[92] Kaufman, H.R., Robinson, R.S., Day, M.L., Haag, T.W. *End-Hall Thrusters* AIAA 90-2595, 1990.

[93] Raitses, Y., Fisch, N.J. *Parametric investigations of a nonconventional Hall thruster* Phys of Plasmas 8(5), 2001.

[94] Smirnov, A., Raitses, Y., Fisch, N.J. *Plasma measurements in a 100 W cylindrical Hall thrusters* Journ Appl Phys 95(5), 2004.

[95] Smirnov, A., Raitses, Y., Fisch, N.J. *Parametric investigation of miniaturized cylindrical and annular Hall thrusters* Journ Appl Phys 92(10), 2002.

[96] Hruby, V., Monheiser, J., Pote, B., Freeman, C., Connolly, W. *Low Power, Hall Thruster Propulsion System* IEPC 99-092, 1999.

[97] Raitses, Y., Gayaso, J.C., Merino, E., Fisch, N.J. *Effect of the Magnetic Field on the Plasma Plume of the Cylindrical Hall Thruster with Permanent Magnets* AIAA 2010-6621, 2010.

[98] Kang, S., Kim, Y., Jeong, Y., Seon, J., Lee, J., Seo, M., Choe, W. *Performance characteristics of cylindrical Hall thrusters* IEPC 2009-094, 2009.

[99] Shirasaki, A., Tahara, H. *Operational characteristics and plasma measurements in cylindrical Hall thrusters* Journ Appl Phys 101(073307), 2007.

[100] Raitses, Y., Gayoso, J.C., Fisch, N.J. *Effect of magnetic shileding on plasma plume of the cylindrical hall thrusters* IEPC-2011-175, 2011.

[101] Spektor, R., Diamant, K.D., Beiting, E.J., Swenson, K.A., Goddard, D.T. *Characterization of a cylindrical hall thruster with permanent magnets* IEPC-2011-264, 2011.

[102] Keller, A., Kohler, P., Gartner, W., Lotz, B., Feili, D., Dold, P., Bere, M., Braxmaier, C. *Feasibility of a down-scaled HEMP-Thruster* IEPC-2011-138, 2011.

[103] Koch, N., Schirra, M., Weis, S., Lazurenko, A., van Reijen, B., Haderspeck, J., Genovese, A., Holtmann, P., Schneider, R., Matyash, K., Kalentyev, O. *The HEMPT concept - a survey on theoretical considerations and experimental evidences* IEPC-2011-236, 2011.

[104] Matlock, T., Lozano, P., Martinez-Sanchez, M. *Discharge chamber wall flux measurements in a diverging cusped-field thrsuter*, ESA/A3F Space Propulsion Conference, San Sebastián 2010.

[105] Sommerville, J.D., King, L.B., *Hall-effect thruster -cathode coupling part I: efficiency improvements from an extended outer pole*, 45th AIAA/ASME/SAE/ASEE Joint Propulsion Conference, 2009.

[106] Gildea, S., Batishchev, O., Martinez-Sanchez, M. *Fully Kinetic Modeling of Divergent Cusped Field Thrusters*, 45th AIAA/ASME/SAE/ASEE Joint Propulsion Conference, 2009.

[107] Gildea, S., Martinez-Sanchez, M. *Improvements in Divergent Cusped-Field Thruster Modeling*, ESA/A3F Space Propulsion Conference, San Sebastián 2010.

[108] Linnell, J., Gallimore, A. *Efficiency Analysis of a Hall Thruster Operating with Krypton and Xenon* Journ Prop Power 22(6), 2006.

[109] Birdsall, C.K., Langdon, A.B. **Plasma Physics via Computer Simulation** McGraw-Hill Inc., 1985.

[110] Bittencourt, J.A. **Fundamentals of Plasma Physics** Springer, 2004.

[111] Bhatnagar, P.L., Gross, E.P., Krook, M. *A Model for Collision Processes in Gases. I. Small Amplitude Processes in Charged and Neutral One-Component Systems* Phys Rev 94(3), 1954.

[112] Golant, V.E., Zhilinsky, A.P., Sakharov, I.E. **Fundamentals of Plasma Physics** John Wiley and Sons, Inc., 1980.

[113] Bohm, D. in *The Characterestics of Electrical Discharges in Magnetic Fields* edited by Guthrie, A. and Wakerling, R.K., McGraw-Hill, 1949.

[114] Chen, F.F. **An Indispensable Truth: How Fusion Power Can Save the Planet** New York: Springer, 2011.

[115] Spitzer Jr., L. *Particle Diffusion across a Magnetic Field* Phys Fluids 3(659), 1960.

[116] Yoshikawa, S., Rose, D.J. *Anomalous Diffusion of a Plasma across a Magnetic Field* Phys Fluids 5(3), 1962.

[117] Janes, G.S., Lowder, R.S. *Anomalous Electron Diffusion and Ion Acceleration in a Low-Density Plasma* Phys Fluids 9(6), 1966.

[118] Hoh, F.C. *Low-Temperature Plasma Diffusion in a Magnetic Field* Reviews of Modern Phys 34(2), 1962.

[119] Boeschoten, F. *Review of Experiments on the Diffusion of Plasma Across a Magnetic Field* Journ Nucl Energy C 6(339), 1964.

[120] Meezan, N.B., Hargus Jr., W.A., Cappelli, M.A. *Anomalous electron mobility in a coaxial Hall discharge plasma* Phys Review E 63(026410), 2001.

[121] Haas, J. *Low Perturbation Interrogation of the Internal and Near-Field Plasma Structure of a Hall Thruster Using a High-Speed Probe Positioning System* PhD Dissertation, University of Michigan, 2001.

[122] Reid, B.M. *The Influence of Neutral Flow Rate in the Operation of Hall Thrusters* PhD Dissertation, University of Michigan, 2009.

[123] Morozov, A.I., Savelev, V.V. *Theory of the Near-Wall Conductivity* Plasma Physics Reports 27(7), 2001.

[124] Yu, D., Liu, H., Fu, H. *Effect of Magnetic Mirror on the Asymmetry of the Radial Profile of Near-Wall Conductivity in Hall Thrusters* Plasma Sci and Tech 11(3), 2009.

[125] Makowski, K., Peradzynski, Z., Kolanowski, M., Barral, S., Kurzyna, J., Dudeck, M. *Near Wall Conductivity in Hall Thrusters. Cylindrical geometry effect* IEPC-2007-246, 2007.

[126] Yu, D., Li, H., Wu, Z., Mao, W. *Effect of oscillating sheath on near-wall conductivity in Hall thrusters* Phys Plasmas 14(064505), 2007.

[127] Raitses, Y., Kaganovich, I.D., Khrabrov, A., Sydorenko, D., Fisch, N.J., Smolyakov, A. *Effect of Secondary Electron Emission on Electron Cross-Field Current in ExB Discharges* IEEE Trans on Plasma Sci 39(4), 2011.

[128] Fossum, E.B., King, L.B. *An Unexamined Collision-less Mechanism for Electron Mobility in Hall Thrusters* AIAA-2009-5366, 2009.

[129] Garrigues, L., Hagelaar, G.J.M., Boniface, C., Boeuf, J.P. *Anomalous conductivity and secondary electron emission in Hall effect thrusters* Journ Appl Phys 100(123301), 2006.

[130] Smith, A.W., Cappelli, M.A. *On the role of fluctuations, cathode placement, and collisions on the transport of electrons in the near-field of Hall thrusters* Phys of Plasmas 17(093501), 2010.

[131] Kemp, R.F., Sellen, J.M. *Plasma potential measurements by electron emissive probes*, Rev. Sci. Instrum. Vol.37(455), 1966.

[132] Ye, M., Takamura, S. *Effect of space-charge limited emission on measurements of plasma potential using emissive probes*, Physics of Plasmas, Vol.7, 2000.

[133] Fujita, H., Nowak, S., Hoegger, BA., Schneider, H. *Potential measurements by an emissive probe in a magnetized plasma*, Physics Letters, Vol.78A, 1980.

[134] Sheehan, J.P., Raitses, Y., Hershkowitz, N., Kaganovich, I., Fisch, N.J. *A comparison of emissive probe techniques for electric potential measurements in a complex plasma*, Phys. of Plasmas, Vol.18 (073501), 2011.

[135] Hargus, W.A., Cappelli, M.A. *Interior and Exterior Laser-Induced Fluorescence and Plasma Potential Measurements on a Laboratory Hall Thruster* AIAA-99-2721, 1999.

[136] Haas, J.M., Gallimore, A.D. *Characterization of the internal plasma structure of a 5 kW Hall thruster* IEPC-99-078, 1999.

[137] Hobbs, G.D., Wesson, J.A. *Heat flow through a Langmuir sheath in the presence of electron emission* Plasma Phys Vol. 9, 1967.

[138] Azziz, Y. *Experimental and Theoretical Characterization of a Hall Thruster Plume* Doctoral Dissertation, Department of Aeronautics and Astronautics, Massachusetts Institute of Technology, Cambridge, MA, 2007.

[139] Csiky, G.A. *Investigation of a Hollow Cathode Discharge Plasma* AIAA Journal 69-258, 1969.

[140] Fearn, D.G., Philip, C.M., *An Investigation of Physical Processes in a Hollow Cathode Discharge* AIAA Journal 72-416, 1972.

[141] Fearn, D.G., Singfield, A., Wallace, N.C., Gair, S.A., Harris, P.T. *The Operation of Ion Thruster Hollow Cathodes using Rare Gas Propellants* AIAA Journal 90-2584, 1990.

[142] Jack, T.M., Patterson, S.W., Fearn, D.G. *The Effect of the Keeper Electrode on Hollow Cathode Discharge Characteristics* AIAA Journal 2000-3533, 2000.

[143] Mandell, M.J., Katz, I. *Theory of Hollow Cathode Operation in Spot and Plume Modes* 30th AIAA/ASME/SAE/ASEE Joint Propulsion Conference, 1994.

[144] Goebel, D.M., Jameson, K.K., Katz, I., Mikellides, I.G. *Plasma Potential Behavior and Plume Mode Transitions in Hollow Cathode Discharges* 30th International Electric Propulsion Conference, 2007.

[145] Goebel, D.M., Jameson, K.K., Katz, I., Mikellides, I.G. *Potential fluctuations and energetic ion production in hollow cathode discharges* Phys of Plasmas 14(103508), 2007.

[146] Fitzgerald, D.J. *Plasma Fluctuations in Ion Thrusters Utilizing Hollow Cathodes* PhD Dissertation, Colorado State University 1983.

[147] Walker, M.L. *Effects of Facility Backpressure on the Performance and Plume of a Hall Thruster* Doctoral Dissertation, University of Michigan, 2005.

[148] Book, C.F., Walker, M.L. *Effect of Anode Temperature on Hall Thruster Performance* Jour Prop Power Vol. 26(5), 2010.

[149] Hargus, W.A., Pote, B. *Examination of a Hall thruster start transient* 38th AIAA/ASME/SAE/ASEE Joint Propulsion Conference, 2002.

[150] Han, K., Wei, L., Ding, Y., Ji, Y., Yu, D. *Unstable discharge phenomenon and stabilization of Hall thruster operating in self-excited mode* Journ. Prop. Power Vol 28 No 1, 2012.

[151] Cartier, S.L., Merlino, R.L. *Observations of nonlinear behavior in a low-pressure discharge column* IEEE Trans. Plasma Sci. Vol PS-12 No 1, 1984.

[152] Raitses, Y., Parker, J.B., Fisch, N.J. *Plume narrowing and suppression of low frequency oscillations in cylindrical hall thrusters* 31st International Electric Propulsion Conference, 2009.

[153] Raitses, Y., Smirnov, A., Fisch, N.J. *Effects of enhanced cathode electron emission on Hall thruster operation* Phys of Plasmas 16, 057106, 2009.

[154] Granstedt, E.M, Raitses, Y., Fisch, N.J. *Cathode effects in cylindrical Hall thrusters* Journ Appl Phys 104(103302), 2008.

[155] Parker, J.B., Raitses, Y., Fisch, N.J. *Transition in electron transport in a cylindrical Hall thruster* Appl Phys Lett 97(091501) 2010.

[156] Matlock, T. Hu, F., Martinez-Sanchez, M., *Controlling Plume Divergence in a Cusped-Field Thruster*, IEPC 2011-178, 2011.

[157] Fife, J., Martinez-Sanchez, M., Szabo, J. *A Numerical Study of Low-Frequency Discharge Oscillations in Hall Thrusters* AIAA-1997-3052, 1997.

[158] Darnon, F., Lyszyk, M., Bouchoule, A. *Optical Investigation on Plasma Oscillations of SPT Thrusters* AIAA-1997-3051, 1997.

[159] Meezan, N.B., Hargus, W.A., Cappelli, M.A. *Optical and Electrostatic Characterization of Oscillatory Hall Discharge Behavior* AIAA-1998-3502, 1998.

[160] Boeuf, J.P., Garrigues, L. *Low frequency oscillations in a stationary plasma thruster* Journ Appl Phys 84(7), 1998.

[161] Chable, S., Rogier, F. *Numerical investigation and modeling of stationary plasma thruster low frequency oscillations* Phys of Plasmas 12(033504), 2005.

[162] Chesta, E., Meezan, N.B., Cappelli, M.A. *Stability of a magnetized Hall plasma discharge* Journ Appl Phys 89(6), 2001.

[163] Yamamoto, N., Komurasaki, K., Arakawa, Y. *Discharge current oscillation in Hall thrusters* Journ Prop and Power 21(5), 2005.

[164] Barral, S., Peradzyski, Z. *Ionization oscillations in Hall accelerators* Phys of Plasmas 17(014505), 2010.

[165] Verhulst, F. **Nonlinear Differential Equations and Dynamical Systems**, Springer, 1996.

[166] Gascon, N., Perot, C., Bonhomme, G., Caron, X., Bechu, S., Lasgorceix, P., Izrar, B., Dudeck, M. *Signal Processing and Non-linear Behavior of a Stationary Plasma Thruster: First Results* AIAA-99-2427, 1999.

[167] Lobbia, R., Gallimore, A. *Two-dimensional Time-resolved Breathing Mode Plasma Fluctuation Variation with Hall Thruster Discharge Settings*, 30th International Electric Propulsion Conference, 2009.

[168] Tilinin, G.N. *High-frequency plasma waves in a Hall accelerator with an extended acceleration zone* Sov Phys Tech Phys 22(8), 1977.

[169] Choueiri, E.Y. *Plasma Oscillations in Hall Thrusters* Phys of Plasmas 8(4), 2001.

[170] Barral, S., Makowski, K., Peradzynski, Z., Gascon, N., Dudeck, M. *Wall material effects in stationary plasma thrusters. II. Near-wall and in-wall conductivity* Phys of Plasmas 10(10), 2003.

[171] Morozov, A.I., Esipchuck, Y.V., Kapulkin, A.M., Nevrovskii, V.A., Smirnov, V.A. *Effect of the Magnetic Field on a Closed-Electron-Drift Accelerator* Sov Phys Tech Phys 17(3), 1972.

[172] Marotta, E.E., Fletcher, L.S., Dietz, T.A. *Thermal constact resistance modeling of non-flat, roughened surfaces with non-metallic coatings* Journ. Heat Transfer Vol 123, 2001.

[173] Nishino, K., Yamashita, S., Torii, K. *Thermal contact conductance under low applied load in a vacuum environment* Exp. Thermal and Fluid Sci., 1995.

[174] MacDonald, M.S., Gallimore, A.D., *Parametric investigation of the rotating spoke instability in hall thrusters* IEPC-2011-242, 2011.

[175] Barral, S., Makowski, K., Peradzyski, Z., Gascon, N., Dudeck, M. *Numerical Study of the Current-Voltage Characteristic of Hall Thrusters* IEPC-01-27, 2001.

[176] Harten, A., Lax, P.D., van Leer, B. *On upstream differencing and Godunov-type schemes for hyperbolic conservation laws*, SIAM Rev., Vol. 25 No. 1, 1983.

[177] Davis, S.F. *Simplified second-order Godunov-type methods*, SIAM J. Sci. Stat. Comput., Vol. 9 No. 3, 1988.

[178] Ahedo, E. *Radial macroscopic model of a plasma flowing along annular dielectric walls*, Phys of Plasmas vol. 9 no. 7, (3178) 2002.

[179] Dugan, J.V. Jr, Sovie, R.J. *Volume ion production costs in tenuous plasmas: a general atom theory and detailed results for helium, argon, and cesium*, NASA Technical Note D-4150, 1967.

[180] Barral, S., Peradzyski, Z. *A new breath for the breathing mode* 31st International Electric Propulsion Conference, 2009.

[181] Mazouffre, S., Bourgeois, G. *Spatio-temporal characteristics of ion velocity in a Hall thruster discharge* Plasma Sources Sci. Tech. 19, (065018) 2010.

[182] Fernandez, E., Scharfe, M.K., Thomas, C.A., Gascon, N., Cappelli, M.A. *Growth of resistive instabilities in ExB plasma discharge simulations* Phys. of Plasmas vol. 15, (0121012) 2008.

[183] Sydorenko, D., Smolyakov, A., Kaganovich, I., Raitses, Y. *Modification of electron velocity distribution in bounded plasmas by secondary electron emission* IEEE Trans. Plasma Sci. Vol 34 No 3, 2006.

[184] Barral, S. *Theoretical analysis of the influence of the power supply on breathing oscillations in Hall thrusters* IEPC-2007-261, 2007.

[185] Koo, J., Boyd, I.D. *Modeling of anomalous electron mobility in Hall thrusters* Phys. Plasmas 13(033501), 2006.

[186] Azziz, Y., Warner, N.Z., Martinez-Sanchez, M., Szabo, J. *High voltage plume measurements and internal probing of the BHT-1000 Hall thruster* AIAA-2004-4097, 2004.

[187] Burrell, K.H. *Effects of ExB velocity shear and magnetic shear on turbulence and transport in magnetic confinement devices* Phys. Plasmas 4(5), 1997.

[188] Terry, P.W. *Suppression of turbulence and transport by sheared flow*, Rev. Modern Phys. vol. 72 no.1, (109) 2000.

[189] Scharfe, M.K., Thomas, C.A., Scharfe, D.B., Gascon, N., Cappelli, M.A., Fernandez, E. *Shear-based model for electron transport in hybrid hall thruster simulations*, IEEE Trans. on Plasma Sci. vol. 36 no. 5, (2058) 2008.

[190] Fox, J.M. *Advances in fully-kinetic PIC simulation of a near-vacuum hall thruster and other plasma systems* Doctoral Dissertation, Department of Aeronautics and Astronautics, Massachusetts Institute of Technology, Cambridge, MA, 2007.

[191] Zhang, Y.Z., Xie, T., Mahajan, S.M. *Analysis on the exclusiveness of turbulence suppression between static and time-varying shear flow* Phys. of Plasmas 19(020701), 2012.

[192] Hahm, T.S., Beer, M.A., Lin, Z., Hammett, G.W., Lee, W.W. *Shearing rate of time-dependent ExB flow*, Phys. Plasmas vol. 6, (922) 1999.

[193] Benkadda, S., Beyer, P., Bian, N., Figarella, C.F., Garbet, X., Garcia, O., Voitsekhovitch, I. *The physics of ExB shear, zonal flows and streamers in tokamak edge turbulence*, Contrib. Plasma Phys. vol. 42, (362) 2002.

[194] Bareilles, J., Hagelaar, G.J.M., Garrigues, L., Boniface, C., Boeuf, J.P., Gascon, N. *Critical assessment of a two-dimensional hybrid Hall thruster model: Comparisons with experiments* Phys. Plasmas 11(6), 2004.

[195] Esipchuk, Morozov, Tilinin, Trofimov *Plasma oscillations in closed-drift accelerators with an extended acceleration zone* Sov. Phys. Tech. Phys. Vol 18 No 7, 1974.

[196] Esipchuk, Tilinin *Drift instability in a Hall-current plasma accelerator* Sov. Phys. Tech. Phys. Vol 21 No 4, 1976.

[197] Gascon, N., Cappelli, M.A., *Plasma instabilities in the ionization regime of a Hall thruster* AIAA-2003-4857, 2003.

[198] Kurzyna, J., Mazouffre, S., Lazurenko, A., Albarede, L., Bonhomme, G., Makowski, K., Dudeck, M., Peradzynski, Z. *Spectral analysis of Hall-effect thruster plasma oscillations based on the empirical mode decomposition* Phys. Plasmas 12(123506), 2005.

[199] Barral, S., Makowski, K., Peradzynski, Z., Dudeck, M. *Transit-time instability in Hall thrusters* Phys. Plasmas 12(073504), 2005.

[200] Mazouffre, S., Dannenmayer, K., Perez-Luna, J. *Examination of plasma-wall interactions in Hall effect thrusters by means of calibrated thermal imaging*, Journ. of Appl. Physics 102(023304), 2007.

[201] Dolan, T.J. *Magnetic electrostatic plasma confinement* Plasma Phys Control Fusion 36 (1539-1593), 1994.

[202] Pastukhov, V.P. *Anomalous electron transport in the transition layer of an electrostatically plugged magnetic mirror* Sov. J. Plasma Phys. 6(5), 1980.